Technical Physics, Vol. 49, No. 8, 2004, pp. 1004–1011. Translated from Zhurnal Tekhnicheskoĭ Fiziki, Vol. 74, No. 8, 2004, pp. 51–57.
Original Russian Text Copyright © 2004 by Alekseev.

SOLID-STATE ELECTRONICS

On the Mechanism of Carbon Nanotube Formation: II. The Kinetics of Explosive Condensation of Carbon Molten Drops in a Metallic Catalyst

N. I. Alekseev

Ioffe Physicotechnical Institute, Russian Academy of Sciences,
Politekhnicheskaya ul. 26, St. Petersburg, 194021 Russia
e-mail: g.dyuzhev@pop.ioffe.rssi.ru

Received September 22, 2003; in final form, January 5, 2004

Abstract—The preliminary stage of the formation of carbon nanotubes by the vapor–liquid–drop mechanism is considered as applied to the condensation of drops from carbon and metal vapors. The problem of the condensation of molten drops is solved for a wide concentration range for both vapors at a condensation temperature. It is shown that, at very high concentrations of the metal vapor (10^{18}–10^{19} cm^{-3}) and high temperatures (about 0.3 eV), peculiar heterogeneous condensation of the drops can occur at huge supersaturation of the carbon vapor and the saturated metal vapor. This problem of the condensation of the binary vapor is of methodical interest. This condensation is shown to be unrealizable in real experiment at the parameters of the carbon and metal vapors; it virtually merges with the homogeneous condensation of the metal vapor. The maximum concentration of the carbon vapor below which carbon condenses into drops and above which carbon condenses into amorphous soot particles is calculated. The calculation makes it possible to propose a new approach to the controlled growth of carbon nanotubes. *© 2004 MAIK "Nauka/Interperiodica".*

INTRODUCTION

This work is a continuation of the study [1] dealing with the condensation of carbon molten drops in a catalytic metal. This problem is associated with the search for an optimum method for producing fine metallic drops that can serve as nucleation centers for carbon nanotubes (NTs) during further supersaturation of the drops with carbon.

A binary gas mixture of metal–carbon vapors is assumed to cool during its expansion from the source of the vapors (arc discharge or a laser target) in a buffer-gas flow. It is also assumed that the concentration of metal vapor N_K is significantly higher than the carbon concentration N_C so that the carbon–metal clusters being formed acquire the properties of metallic drops. The opposite case ($N_C \gg N_K$), which is usually occurs upon the arc production of NTs, is not considered, since this method cannot provide controlled growth of high-quality NTs.

We assume that, in an arc or laser method for synthesizing NTs, the initial stage of condensation of vapor drops is explosive [2, 3]. For the case of condensation of drops of a pure substance, this term has the following meaning. Upon cooling, the vapor goes through the point $S = 1$, where supersaturation ($S > 1$) or undersaturation ($S < 1$) is defined as the ratio of the concentration of atomic vapor N_1 to the concentration of saturated vapor $N_1^{(S)}$. The number of clusters (nucleation centers) is small because of the very strong dependence of the steady-state nucleation rate J (or the flux of drops in the space of the number of atoms in a drop or in the space of sizes) on S:

$$J = -\frac{1}{S}\frac{N_1^2}{N_L}A_{\mathrm{rot}}g_*^4\sqrt{\frac{2\sigma}{\pi m}}\exp\left(-\frac{\beta}{\ln^2 S}\right), \qquad (1)$$

where $\beta = 16\pi\sigma^3/3n_L^2T^3$; the parameters σ, m, and A_{rot} and the critical drop size g_* were determined in [1].

When S reaches a certain threshold value, the flux J increases by many orders of magnitude as compared to the before-threshold value and the drops that are formed begin to rapidly absorb vapor. This condensation stage is called explosive condensation. Vapor absorption causes a decrease in J and, simultaneously, supersaturation; however, the former factor is more pronounced than the latter. After the termination of the explosive stage and the "disappearance" of the source of drops, the supersaturation decreases due to the growth of the formed drops. This stage is called rapid growth [4].

In the case of the condensation of carbon molten drops in a metal, the process of explosive condensation has certain peculiar features.

When a metal is introduced into the vaporized electrode in the form of a sintered carbon–metal powder, the electrode temperature under the conditions of arcing is between the temperatures of purely metallic and purely graphite vaporized electrodes. According to the

1063-7842/04/4908-1004$26.00 © 2004 MAIK "Nauka/Interperiodica"

reasons given in [1], it is more reasonable to start consideration from the case of an “almost metallic” electrode with a small addition of carbon. In this case, the initial concentration of carbon vapor over the electrode is substantially higher than the concentration of the saturated vapor at the vaporization temperature and the metal-vapor concentration is close in order of magnitude to the concentration of the saturated vapor at an electrode temperature of 1500–1800 K.

The carbon vapor has a higher evaporation heat q_C than the metal vapor (q_K), and, when moving from the arc, it reaches saturation much earlier than the metal vapor. However, at a high concentration of the metal vapor, carbon cannot condense according to the “fullerene path,” since metal–carbon molten drops may begin to condense when the metal vapor reaches its saturation. By this time, the carbon vapor is strongly supersaturated. This condensation should have characteristics other than those of the condensation of a purely metal vapor and is, hereafter, called heterogeneous condensation, although it is not heterogeneous in the classical sense [1].

Heterogeneous condensation can occur if the size and concentration of the drops formed in the explosive stage are sufficiently large. Then, the drops can effectively absorb the metal vapor and stop the growth of its supersaturation. Otherwise, the heterogeneous condensation is followed by secondary condensation, which is similar to homogeneous condensation of a purely metal vapor. The criterion of the fact that heterogeneous condensation can stop an increase in the supersaturation of the metal vapor S_K and form a spectrum of drop sizes has the form

$$\frac{dS_K}{dt} > 0, \tag{2}$$

where $S_K = N_K/N_K^{(S)}$ and N_K and $N_K^{(S)}$ are the actual concentration and the concentration of the saturated metal vapor, respectively. The derivative is calculated for the end of the explosive condensation stage.

Apart from criterion (2), we also impose the condition that, at the end of the explosive condensation stage, the number of carbon atoms in a drop $g = g_d$ is substantially higher than the initial drop size g_*: $g_d/g_* \gg 1$; e.g.,

$$g_d/g_* = 10. \tag{3}$$

CALCULATION OF THE EXPLOSIVE STAGE OF HOMOGENEOUS CONDENSATION

(1) Formulation of the Problem

When considering the explosive condensation, we specify the following parameters: the temperature T_0 at the instant of saturation of the carbon vapor (saturation temperature); the spatial velocity V of the gas flow; the spatial scale L of the decrease in the carbon–vapor temperature for the linear dependence $T = T_0(1 - y/L)$ of temperature T on the space coordinate y ($V = dy/dt$); and the undersaturation of the metal vapor $S_K^{(0)}$ at T_0.

In calculation, we determine the condensation temperature T_1, the effective time of explosive condensation δt, the initial supersaturation of the metal vapor $S_K^{(1)}$ at which condensation can occur, the supersaturation $S_C^{(1)}$ of the carbon vapor at this time instant (or at this space point), and the maximum supersaturation of the carbon vapor $S_C^{(\max)}$ during explosive condensation. In addition, we determine the following parameters of the drops being formed: the drop concentration N_d; and the total (g_d and g_*) and the partial (c_d, k_d, c_*, and k_*) numbers of carbon and catalyst atoms in a drop at the end and beginning of explosive condensation, respectively.

Our calculation shows that, as $S_K^{(0)}$ decreases, the values of $S_C^{(1)}$ and $S_C^{(\max)}$ increase (Fig. 1); however, the maximum supersaturation of explosive condensation $S_C^{(\max)}$ (Fig. 1, curves *1*, *2*) increases faster than $S_C^{(1)}$ does (Fig. 1, curves *1*', *2*'). At a certain critical level of undersaturation, the initial supersaturation $S_C^{(1)}$ becomes greater than $S_C^{(\max)}$. This means that, at the beginning of condensation, the supersaturation of the carbon vapor is already at its maximum and is known. Therefore, the calculations of condensation at $S_C^{(1)} > S_C^{(\max)}$ (“delayed condensation”) and at $S_C^{(1)} < S_C^{(\max)}$

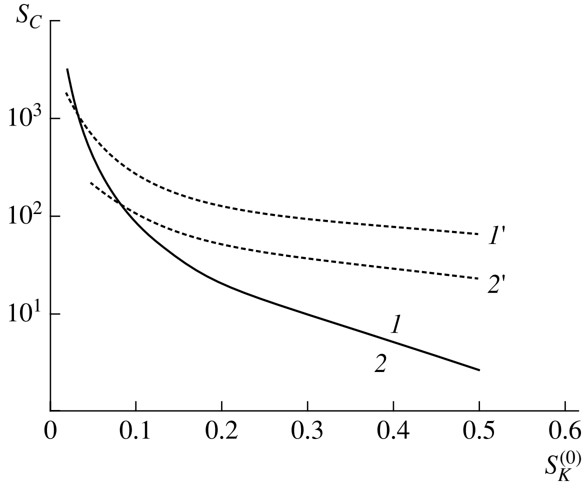

Fig. 1. Effect of the initial undersaturation of the metal vapor on (dotted curves) the maximum supersaturation of the carbon vapor in the stage of explosive condensation $S_C^{(\max)}$ and (solid curve) the initial supersaturation $S_C^{(1)}$ at which the explosive condensation begins. The saturation temperature of the carbon vapor is (*1*, *1*') 0.32 and (*2*, *2*') 0.3 eV.

("overdelayed condensation") are completely different. We first describe the procedure of calculation at $S_C^{(1)} < S_C^{(\max)}$, which is used to understand whether this inequality is valid in reality.

(2) Calculation of the Explosive Condensation: The Case of Delayed Condensation

The optimum composition of a critical drop is determined by the fact that, at $S_C \gg S_K$, the mole fraction of carbon X is close to $X = \gamma X_{\text{sat}}$, where $\gamma = 0.7$ [1].

Unlike a pure substance, the transition of a drop through the critical size does not cause the subsequent rapid growth of the drop in any direction in the (c, k) plane, where k and $c = kX/(1 - X)$ are the numbers of metal and carbon atoms in the drop ($g = c + k$), respectively. Apart from an increase in the total number of atoms, the Gibbs free energy must decrease along the trajectory of the drop in the (c, k) plane. The boundary trajectories at which the Gibbs energy of a subcritical drop is equal to this energy at the critical size of the drop are shown in Fig. 2 for carbon-depleted (curve *3*) and carbon-saturated (curve *4*) drops. Curves *3* and *4* are seen to be rather close to each other; that is, the mole fraction of carbon in a supercritical drop, as in a subcritical one, can vary over rather narrow limits. In the nearest supercritical region, none of the drop components can be evaporated so that the drop is simultaneously saturated with the other component.

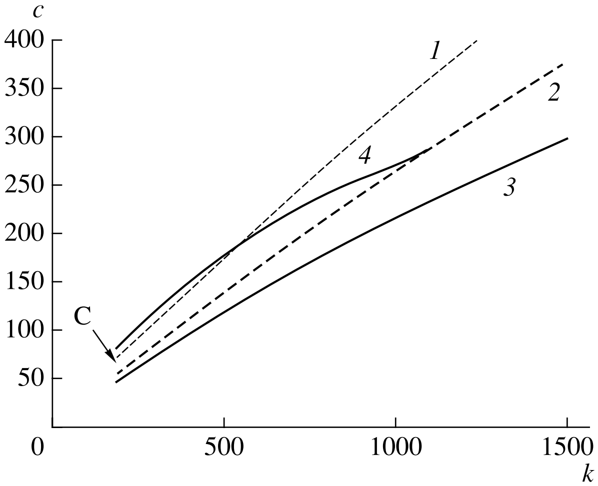

Fig. 2. Possible trajectories for a subcritical drop in the (c, k) space of the number of atoms in the drop: (*1*) trajectory of the drop saturated with carbon ($X = X_{\text{Sat}}$); (*2*) trajectory of the drop saturated with the optimum ratio of the components ($X = \gamma X_{\text{Sat}}$); and (*3*, *4*) trajectories of the drop with a carbon content such that $G(X, g(X)) = G_m$, where G_m is the potential condensation barrier. *C* is a critical point.

At $N_K \gg N_C$, the optimal mole fraction of carbon is retained during the explosive condensation due to the fact that the metal vapor component balances at the saturation level and that the carbon vapor can be strongly supersaturated. Therefore, the carbon and metal fluxes to the drop turn out to be of the same order of magnitude. If the concentrations of the vapors are comparable, the rates of increase in the number of carbon and metal atoms in the drop,

$$\frac{dk}{dt} = 4\pi r_L^2 V_T g^{2/3} N_K(1 - a_K/S_K), \tag{4}$$

and

$$\frac{dc}{dt} = 4\pi r_L^2 V_T g^{2/3} N_C(1 - a_C/S_K) \approx 4\pi r_L^2 V_T g^{2/3} N_C, \tag{5}$$

should be connected during the explosive condensation by the relation

$$\frac{dc}{dt} = \frac{X}{1 - X}\frac{dk}{dt}. \tag{6}$$

The activities a_C and a_K relate the equilibrium concentrations of the vapor components over the melt to the concentrations of the saturated vapors of the pure substances: $N_{C,\,\text{sol}}^{(S)} = a_C N_C^{(S)}$ and $N_{K,\,\text{sol}}^{(S)} = a_K N_K^{(S)}$. As follows from [1], at the optimal carbon content in the drop, the activities are equal to the corresponding mole fractions, $a_C = X$ and $a_K = 1 - X$, just as in an ideal solution. Then, it follows from Eqs. (4) and (5) that, at the beginning of condensation, the supersaturation $S_K^{(1)}$ is

$$S_K^{(1)} = \frac{N_K X(1 - X)}{N_K X - N_C(1 - X)}. \tag{7}$$

The saturation temperature T_0 and the undersaturation $S_K^{(0)}$ determine the concentrations N_C and N_K, which are taken to be constant in the following calculation. This means that the actually specified quantities are the concentrations of the vapors at the instant of condensation. Explosion conditions (7) along with the temperature dependence of saturation [1]

$$X_{\text{sat}} = \exp(-\eta/T - \psi) \tag{8}$$

(for iron, $\eta = 0.112$ and $\psi = 0.8635$) and the condition $X = \gamma X_{\text{sat}}$ allow us to determine the temperature of explosive condensation $T_1 < T_0$ and the quantity X using an iteration procedure. The initial saturation of the carbon vapor is

$$\ln S_C^{(1)} = \frac{q_C}{q_K}\ln\frac{S_K^{(1)}}{S_K^{(0)}}. \tag{9}$$

For the following calculation, we use the technique that was proposed by Raizer to solve the problem of vapor expanding into vacuum [2] and then developed in

[3] as applied to the condensation of a slag in the channel of an MHD generator.

We assume that, during the explosive condensation, drops grow so fast that the size distribution of the drops in the near-critical region is insignificant. Then, the balance equation for the number of carbon atoms in the drops and gas [2],

$$N_C^{(0)} - N_C(t) = \int_0^t dt' J(t') c(t, t') \tag{10}$$

can approximately be integrated by expanding the exponent in $J(t')$ into a series in powers of the difference $\zeta - \zeta_{\max}$ (where $\zeta = \ln S$ and $\zeta_{\max} = \ln S_{\max}$) in the vicinity of the logarithm of the maximum saturation $\zeta_{\max}$, which is reached at a certain time instant $t_{\max}$, and then, the difference $(\zeta - \zeta_{\max})$ into a power series

$$\begin{gathered} t - t_{\max} : \zeta' - \zeta_{\max} = -\frac{\alpha_{\max}}{2}(t' - t_{\max})^2, \\ \exp\left(-\frac{\beta}{\zeta^2}\right) = \exp\left(-\frac{\beta}{\zeta_{\max}}\right)\exp\left(\frac{\alpha_{\max}\beta}{\zeta_{\max}^3}(t' - t_{\max})^2\right). \end{gathered} \tag{11}$$

As follows from the results obtained in [1], when the size effects are ignored, the flux J has the form

$$J = \chi \exp\left(-\frac{\beta}{\zeta^2}\right),$$

$$\chi = \frac{N_C}{N_L} g_*^{9/2} B \left(\frac{N_C X}{S_C}\right)^X \left(\frac{N_K(1 - X)}{S_K}\right)^{1 - X} \sqrt{\frac{2\sigma}{\pi M_C}}, \tag{12}$$

$$B = A_{\mathrm{rot}}\left(\frac{A_C X + A_K(1 - X)}{A_C^X A_K^{1 - X}}\right)^{3/2},$$

and the role of the logarithm of the effective supersaturation is played by the quantity

$$\zeta = X\zeta_C + (1 - X)\zeta_K - X\ln X - (1 - X)\ln(1 - X). \tag{13}$$

Since the supersaturation of the metal vapor increases much more slowly than that of the carbon vapor, the procedure for the subsequent solution is identical to that for the case of a pure substance. We doubly differentiate Eq. (10) and reject the integrated terms on the right-hand side in both cases; then, we have

$$\begin{gathered} -\frac{dN_C}{dt} = \int_0^t dt' J(t') \frac{dc(t', t)}{dt}, \\ -\frac{d^2 N_C}{dt^2} = \int_0^t dt' J(t') \frac{d^2 c(t', t)}{dt^2}. \end{gathered} \tag{14}$$

An increase in the number of carbon atoms in a drop is described by Eq. (5). If the mole fraction of carbon in the drop only weakly depends on the drop size, we can use the identity $dX/dt = (1/g)dc/dt - (X/g)dg/dt = 0$ to obtain the equation for the rate of increase in the total number of atoms in the drop:

$$\frac{dg}{dt} = 4\pi r_L^2 V_T g^{2/3} N_C \left[1 - \frac{X}{S_C}\right] \frac{1}{X}\left(1 + \frac{g}{X}\frac{dX}{dg}\right)^{-1}. \tag{15}$$

At X = const, the solution to Eq. (15) is

$$g(t', t) = Q_C(t - t')^3 / X, \quad c = Q_C(t - t')^3, \tag{16}$$

where

$$Q_C = \frac{1}{X^2\theta^3}\left(1 - \frac{X}{S_C}\right)^3, \quad \theta^{-1} = \frac{4}{3}\pi r_L^2 V_T N_C.$$

Taking into account Eq. (14), at the instant $t_{\max}$, we can easily find

$$-\frac{dN_C}{dt} = 3Q_C\chi\exp\left(-\frac{\beta}{\zeta_{\max}^2}\right)\frac{\sqrt{\pi}}{4}\frac{\zeta_{\max}^{9/2}}{(\beta\alpha_{\max})^{3/2}}, \tag{17}$$

$$-\frac{d^2 N_C}{dt^2} = 3Q_C\chi\exp\left(-\frac{\beta}{\zeta_{\max}^2}\right)\frac{\zeta_{\max}^3}{\alpha_{\max}\beta}. \tag{18}$$

On the other hand, from the definition of the supersaturation and the relation between the saturated-vapor pressure and the temperature through the evaporation heat, it follows that

$$\frac{N_C'}{N_C} = \frac{q_C}{T}\frac{T'}{T}, \tag{19}$$

$$-\frac{\alpha_{\max}}{X} = \frac{N_C''}{N_C} - \left(\frac{N_C'}{N_C}\right)^2 + \frac{2q_C}{T}\left(\frac{T'}{T}\right)^2. \tag{20}$$

In Eqs. (19) and (20), we took into account the fact that $\zeta_{\max} = X\zeta_{\max}^{(C)} - \mu_{\max}/T$ and $\alpha_{\max} = X\alpha_{\max}^{(C)}$.

Finally, the set of two equations with two unknowns ($\alpha_{\max}$ and $\zeta_{\max}$) that follows from Eqs. (17)–(20) has the form

$$-\frac{qN_C}{T}\frac{d\ln T}{dt} = 3Q_C\chi\frac{\sqrt{\pi}}{4}\frac{\zeta_{\max}^{9/2}}{(\beta\alpha_{\max})^{3/2}}\exp\left(-\frac{\beta}{\zeta_{\max}^2}\right), \tag{21}$$

$$\begin{gathered} \alpha_{\max} + \left(\frac{4X}{\sqrt{\pi}}\frac{q_C}{T}\frac{d\ln T}{dt}\frac{\sqrt{\beta}}{\zeta_{\max}^{3/2}}\right)\sqrt{\alpha_{\max}} \\ -X\left(\frac{d\ln T}{dt}\right)^2\left(\left(\frac{q_C}{T}\right)^2 - \frac{2q_C}{T}\right) = 0. \end{gathered} \tag{22}$$

As noted above, we assumed that, after the point of saturation of the carbon vapor was reached, the temperature T decreased linearly with the spatial scale L. The value of L and the flow velocity, which specifies the relation between the derivatives $T' = dT/dt$ and dT/dy, were varied.

The set of equations (21) and (22) was solved by an iteration procedure. The only technical difference in solution from the problem of the homogeneous condensation of vapor was that we took $eXS_C^{(1)}$ and not e as the initial approximation to calculate the unknown value of the maximum supersaturation $S_C^{(\max)}$.

The values of $\alpha_{\max}$ and $\zeta_{\max}$ allow us to determine changes in the concentrations of the vapors by the end of the explosive condensation. By analogy with the expression

$$\Delta N_1 = \frac{N_1^2}{SN_L}\sqrt{\frac{2\sigma}{\pi m}}\frac{3}{\theta^3}\left(1-\frac{1}{S}\right)^3\frac{1}{\alpha_{\max}^2}\left(\frac{\zeta_{\max}^3}{\beta}\right)^2\exp\left(-\frac{\beta}{\zeta_{\max}^2}\right)$$

we can easily obtain

$$\Delta N_C = \chi Q_C\left(\frac{\zeta_{\max}^3}{\alpha_{\max}\beta}\right)^2\exp\left(-\frac{\beta}{\zeta_{\max}^2}\right) \tag{23}$$

for the case of the condensation of a pure substance from the solution.

The total concentration of the drops formed during the explosive condensation, which is

$$N_d = \int\limits_{-\infty}^{+\infty}J(t')dt' = \frac{1}{S}\frac{N_1^2}{N_L}\sqrt{\frac{2\sigma}{\pi m}}g_*^4A_{\text{rot}}$$
$$\times\exp\left(-\frac{\beta}{\zeta_{\max}^2}\right)\left(\frac{\pi\zeta_{\max}^3}{\alpha_{\max}}\right)^{1/2}$$

in the case of a pure substance, is now defined by the expression

$$N_d = \chi\sqrt{\frac{\pi\zeta_{\max}^3}{\alpha_{\max}\beta}}\exp\left(-\frac{\beta}{\zeta_{\max}^2}\right). \tag{24}$$

All the formulas given above are written for the case when the size effects are neglected, which is due to the fact that the condition of the delayed condensation $S_C^{(1)} > S_C^{(\max)}$ sets a high condensation temperature and a large critical drop size.

(3) The Case of Overdelayed Condensation

At $S_C^{(1)} > S_C^{(\max)}$, the maximum supersaturation is reached at the beginning of condensation and is unknown. Two variants can occur in this case.

(a) The second derivative is

$$\zeta''_{\max} = \frac{d^2\zeta}{dt^2}(t_{\max}) < 0$$

and, when expanding the supersaturation $\zeta(t')$ into a power series of the difference $t' - t_{\max}$ in Eqs. (10) and (11), we have to take into account both the first and second derivatives. Then, N_d is calculated in the same approximation that for the delayed condensation:

$$N_d = \chi\exp\left(-\frac{\beta}{\zeta_{\max}^2}\right)\exp\left(\frac{a^2}{4b}\right)$$
$$\times\left(\sqrt{\frac{\pi}{\beta}} - \int\limits_{+a/2b}^{\infty}dt\exp(-bt^2)\right), \tag{25}$$

where

$$a = -\frac{\beta\zeta'_{\max}}{\zeta_{\max}^3} > 0, \quad b = -\frac{\beta}{\zeta_{\max}^2}\left(\frac{\zeta''_{\max}}{\zeta_{\max}} - 3\left(\frac{\zeta'_{\max}}{\zeta_{\max}}\right)^2\right) > 0.$$

Numerical estimations show that, as $S_K^{(0)}$ decreases, the drop size and the number of atoms in the drops vary identically to the case of delayed condensation. There are no qualitatively new results in this case.

(b) $S_K^{(0)} \ll 1$, the supersaturation $S_C^{(1)}$ is very high, the derivative $\zeta''_{\max} > 0$, and it is sufficient to take into account only the term with the first derivative in $\exp(-\beta/\zeta^2)$. In this case, the condensation parameters are as follows: the drop concentration is

$$N_d \approx \chi\exp\left(-\frac{\beta}{\zeta_{\max}^2}\right)\int\limits_0^{+\infty}\exp\left(\frac{\beta\zeta'_{\max}}{\zeta_{\max}^3}t'\right)dt'$$
$$= \chi\exp\left(-\frac{\beta}{\zeta_{\max}^2}\right)\frac{\zeta_{\max}^3}{\beta(-2\zeta'_{\max})}, \tag{26}$$

the reciprocal condensation time is $\Gamma = 1/\delta t$, $\Gamma = \beta\zeta'_{\max}/\zeta_{\max}^3$; the change in the concentration of the carbon vapor after completion of the explosive condensation is

$$\delta N_C = \int\limits_0^{1/\Gamma}dt'J(t')c(t,t')$$
$$= Q_C\chi\exp\left(-\frac{\beta}{\zeta_{\max}^2}\right)\frac{1}{\Gamma^4}\left(\frac{6}{e}-2\right), \tag{27}$$

and the number of atoms in the drop is

$$g_d = \frac{\delta N_C}{XN_d} = \frac{Q_C}{X}\left(\frac{\zeta_{\max}^3}{-\beta\zeta'_{\max}}\right)^3\left(\frac{6}{e}-2\right). \tag{28}$$

In cases (a) and (b), the calculation can give any values of N_d and g_d. A qualitative conclusion about the possibility of heterogeneous condensation can only be drawn using criterion (2), which can be rewritten as

$$N_K\frac{q_K}{L}V - N_d\left(\frac{dg}{dt}\right)_0 < 0, \tag{29}$$

where

$$\left(\frac{dg}{dt}\right)_0 = 4\pi r_L^2 V_T g_d^{2/3} N_K \left[1 - \frac{N_d g_d}{N_K} - \frac{1-X}{S_K^{(1)}}\right].$$

CALCULATION RESULTS AND THEIR DISCUSSION

Figure 3 shows the dependence of the critical drop size g_* on the temperature T_0. The relative role of the size effects is seen to decrease with increasing T_0 (Fig. 3, curves *1*, *2*); however, these effects become weak (about 20%) only at $T_0 \geq 0.3$ eV, where the Frenkel model can be applied.

Figure 4 shows the analogous dependence for the drop concentration N_d. The dependence on the initial undersaturation $S_K^{(0)}$ is seen to be insignificant. For the curves given in Fig. 4, we have $S_K^{(0)} = 0.1$. The drop concentration is very high ($N_d \sim (10^{10}–10^{12})$ cm^{-3}), and the characteristic size is small and decreases sharply with temperature. This circumstance gives the minimum temperature $T_0^{\min}$ at which the heterogeneous condensation can become noticeable (Fig. 5). As a concentration criterion, we chose condition (3). When constructing the velocity dependence of $T_0^{\min}$, we chose the velocity range from the typical values of the velocity of a buffer gas under the conditions of a fullerene arc at temperatures near T_0 [5].

These calculations indicate that the delayed condensation occurs only at a high temperature T_0 and, correspondingly, at a very high concentration of the metal vapor ($N_K \sim (10^{19}–10^{20})$ cm^{-3}). It is virtually impossible to provide such a concentration by the evaporation of an electrode at any ratios of carbon and metal in the electrode. In a nearly graphite electrode, at $T \sim 4000$ K, the concentration N_K cannot exceed fractions of the concentration of carbon vapor, which is $N_C \sim (10^{17}–10^{18})$ cm^{-3}. On the contrary, the concentration over a fusible metal electrode with a melting temperature of less than 2000 K cannot exceed $10^{15}–10^{16}$ cm^{-3}. Therefore, of practical importance is the case of overdelayed condensation ($S_C^{(1)} > S_C^{(\max)}$), i.e., the case of a relatively high carbon concentration and a relatively low metal concentration.

We calculated the maximum concentration $N_K^{(\max)}$ of a catalyst at which conditions (2) and (3) were met. Figure 6 shows the $N_K^{(\max)}$ versus T_0 dependence, and Fig. 7 shows the $N_K^{(\max)}$ versus N_C dependence. Curve *A* (with a vapor concentration $N_K^{(A)}$) meets condition (2), and curve *D* (with a concentration $N_K^{(D)}$) meets the condition $S_K^{(1)} > 0$. Formally, curve *D* indicates infinite supersaturation of the metal vapor.

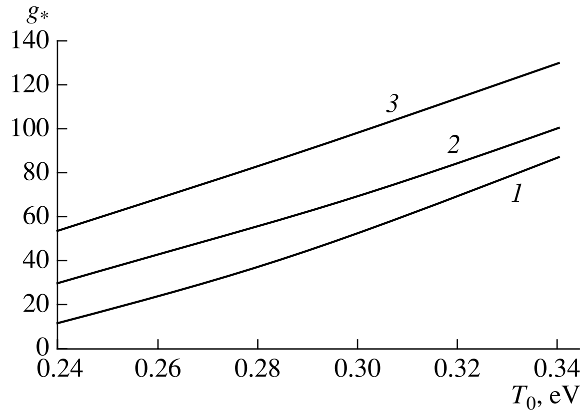

Fig. 3. Dependence of the critical drop size on T_0. The flow velocity is $V = 10^4$ cm/s. (*1*) The melt without regard for the size effects, (*2*) the melt with allowance for the size effects, and (*3*) purely metal vapor.

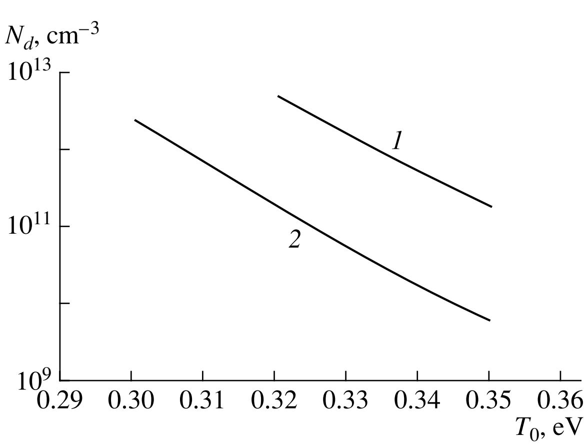

Fig. 4. Concentration N_d of the drops formed within the explosive condensation depending on the saturation temperature. The undersaturation of the metal vapor at the point of saturation of the carbon vapor is $S_K^{(0)} = 0.1$. The flow velocity V is (*1*) 3×10^3 and (*2*) 10^4 cm/s.

Curve *A* bounds the metal-vapor concentration from above, and curve *D* bounds this concentration from below. It is seen that, at low condensation temperatures, the curves are very close to each other (the case of low N_K). This means that the region of heterogeneous condensation virtually disappears. The condensation develops as the homogeneous condensation of the metal vapor from the very beginning.

At $N_C > N_C^{(D)}$, the heterogeneous condensation is impossible. In this case, the formation of lumps of amorphous carbon is most probable. However, the concentration of free metal, which can condense, is

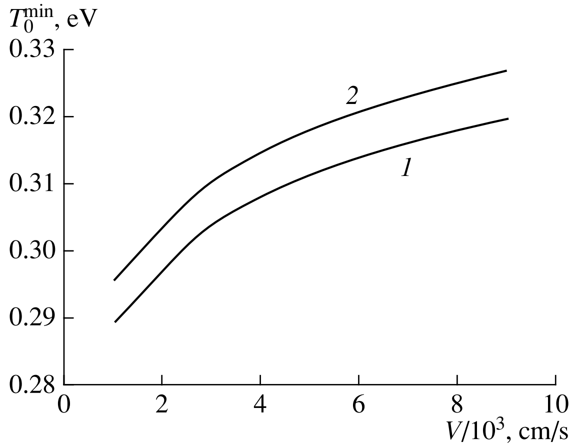

Fig. 5. Minimum temperature at which condition (3) of the heterogeneous condensation is met, depending on the flow velocity. The scale L is (*1*) 8 and (*2*) 5 cm.

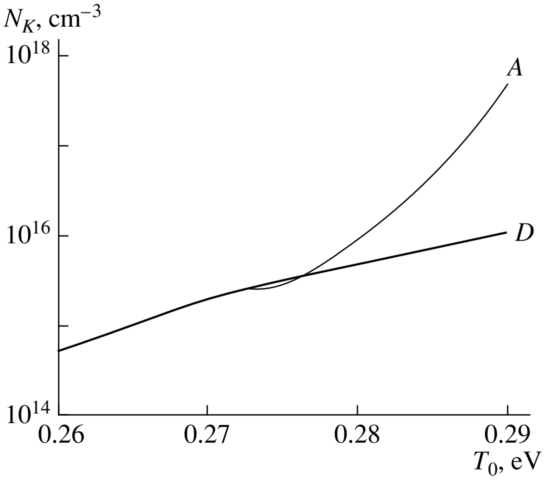

Fig. 6. Maximum catalyst concentration $N_K^{\max}$ at which condition (2) of the heterogeneous condensation is met. $V = 3 \times 10^3$ cm/s. Curve A corresponds to condition (2), and curve D is the minimum metal concentration at which the heterogeneous condensation is possible.

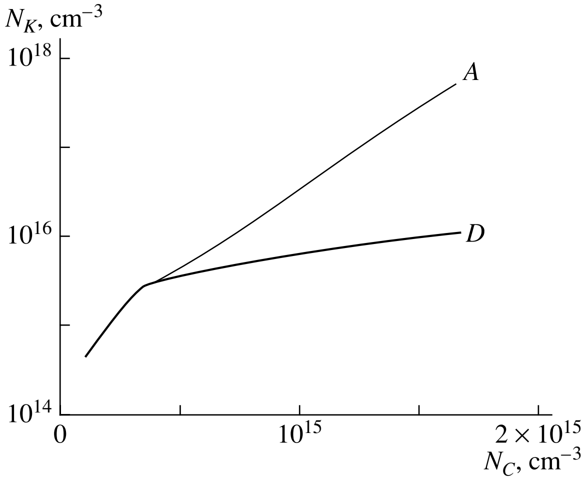

Fig. 7. The same as in Fig. 6 but depending on the carbon-vapor concentration. The flow velocity $V = 3 \times 10^3$ cm/s.

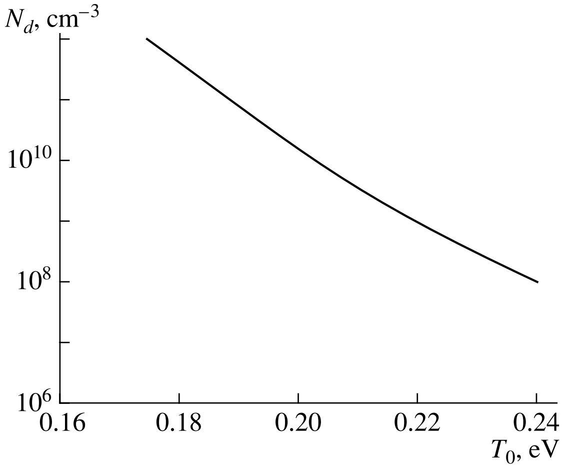

Fig. 8. Concentration of the metallic drops formed during the homogeneous condensation of the metal vapor. $V = 3 \times 10^3$ cm/s.

strongly decreased. Therefore, the metal vapor can condense only at a very low temperature, and the drops formed contain much amorphous carbon long before the stage of nanotube growth.

Based on the considerations given above, we can conclude that the pulse evaporation of a metallic electrode or an electrode with a low carbon content can provide the required concentration of metallic drops on a substrate. For a proper pulse duration, metal vapor exists in the discharge for the time it takes for the creation of nucleation centers for the nanotube growth.

The time of evaporation of an electrode, τ, should be chosen so that the number of drops that diffuse toward the substrate in the time τ does not exceed one monolayer; that is, the surface per drop of radius R_g should be about $\pi(2R_g)^2$. Correspondingly, the pulse duration can be determined from the relation

$$\tau^{-1} \sim D 4\pi R_g^2 \nabla N_d, \qquad (30)$$

where D is the coefficient of diffusion of drops toward the surface and ∇N_d is the radial gradient of the drop concentration from the flux axis toward the substrate.

The diffusion of heavy particles in a light buffer gas with a concentration N_B is determined by the relation [6]

$$D = \frac{0.68}{4\sqrt{2}} \frac{V_T}{R_d^2 N_B} [6],$$

where the thermal velocity of a particle of the buffer gas with a mass m_B is $V_T = (2T/m_B)^{1/2}$.

Then, the pulse duration is estimated as $\tau = (R/3V_T)(N_B/N_d)$, where R is the chamber radius, which coincides with the characteristic distance to the substrate.

The concentration N_d of the metal drops formed during homogeneous condensation is plotted as a function of the saturation temperature T_0 in Fig. 8.

The value of τ is on the order of milliseconds; however, generally speaking, it can vary over wide limits and should be determined experimentally.

CONCLUSIONS

An arc with a low concentration of metallic-catalyst vapor as compared to carbon vapor cannot provide the controlled growth of high-quality NTs; therefore, we have considered the kinetics of condensation of carbon–metal molten drops at arbitrary ratios of the concentrations of the vapors. The result is as follows.

If the concentration of the metal vapor is significantly higher than the carbon concentration, peculiar heterogeneous condensation of the drops can occur in theory. It begins under the conditions where the carbon vapor is strongly supersaturated and the metal vapor has just reached saturation. However, this condensation cannot be realized in practice because of a large difference in the concentrations of the saturated vapors. This is due to the fact that the possibility of heterogeneous condensation puts upper and lower limits on the carbon-vapor concentration. The upper limit is determined by the flux of carbon atoms to a drop, at which the drop composition is optimal for condensation. Under an intense carbon flux, condensation is impossible and a cluster can develop only as an amorphous soot particle.

The lower limit is related to the fact that the amount of vapor condensed in the explosive stage of the heterogeneous condensation is determined by the concentration of the carbon rather than the metal vapor. If this amount is negligible, the heterogeneous condensation is impossible.

The actual condensation temperature of the metal vapor is limited by the temperature of an electrode and cannot be high. Under these conditions, the upper and lower limits virtually merge. Therefore, at any relation between carbon and metal, the metal vapor condenses homogeneously.

The calculation shows that, at a relative carbon concentration below the upper limit, the most portion of carbon should enter into molten drops rather than soot particles. Therefore, when drops are used as nucleation centers for NTs, which are preliminarily deposited onto a substrate, the material of the evaporated electrode can contain a small amount of carbon (e.g., conventional stainless steel).

Thus, the process of production of NTs can contain, as the first stage, the formation of metallic drops on a substrate as a result of the evaporation of a metallic target with a laser beam or of a metallic electrode with an arc discharge.

The calculation of the concentration of the drops that are formed during the homogeneous condensation of the metal vapor allows us to determine the time of arcing in the pulse mode.

REFERENCES

1. N. I. Alekseev, Zh. Tekh. Fiz. **74** (8), 45 (2004) [Tech. Phys. **49**, 998 (2004)].
2. Yu. P. Raĭzer, Zh. Éksp. Teor. Fiz. **37**, 1741 (1959) [Sov. Phys. JETP **10**, 1229 (1960)].
3. D. I. Zhukhovitskiĭ, A. G. Khrapak, and I. T. Yakubov, Teplofiz. Vys. Temp., No. 5, 982 (1983).
4. D. I. Zhukhovitskiĭ, A. G. Khrapak, and I. T. Yakubov, Teplofiz. Vys. Temp., No. 6, 1197 (1983).
5. N. I. Alekseev, F. Chibante, and G. A. Dyuzhev, Zh. Tekh. Fiz. **71** (6), 122 (2001) [Tech. Phys. **46**, 761 (2001)].
6. L. D. Landau and E. M. Lifshitz, *Course of Theoretical Physics*, Vol. 10: *Physical Kinetics* (Pergamon, New York, 1981; Nauka, Moscow, 1989).

Translated by K. Shakhlevich

Technical Physics, Vol. 49, No. 8, 2004, pp. 1012–1015. Translated from Zhurnal Tekhnicheskoĭ Fiziki, Vol. 74, No. 8, 2004, pp. 58–61.
Original Russian Text Copyright © 2004 by M. Aliev, B. Aliev, Alieva, Velikhanov, Mutalibov, Seleznev.

SOLID-STATE ELECTRONICS

The Effect of Special Features of Forming the Imperfect Structures in Germanium Crystals on Plastic Properties of These Crystals

M. A. Aliev, B. G. Aliev, Kh. O. Alieva, A. R. Velikhanov,
Sh. R. Mutalibov, and V. V. Seleznev

Institute of Physics, Dagestan Scientific Center, Russian Academy of Sciences, Makhachkala, 367003 Russia
e-mail: kamilov@datacom.ru

Received December 9, 2003

Abstract—A new technology for forming the structures in semiconductor crystals using plastic deformation in an electric field is suggested. A setup making it possible to implement the suggested method and study the idea of self-organization of dislocation-related dissipative structures is described. *© 2004 MAIK “Nauka/Interperiodica”.*

INTRODUCTION

Practical use of the high strength of atomic semiconductors is restricted owing to brittleness of these materials at low temperatures [1]. Germanium belongs to the class of materials with the largest values of theoretical breaking and shear strength, which is caused by a high degree of directivity of covalent bonds that link atoms and gives rise to a high resistance of the lattice to the dislocation glide [2]. Because of this consideration and other reasons, a search for various methods for increasing the plasticity at the lowest possible temperatures and a study of interrelation between the structure and properties of semiconductor crystals is a task that is extremely important from both theoretical and application-oriented standpoints [3].

It is well known that a single crystal is an example of structural organization, i.e., a process that carries no information on the evolution of the crystal structure as a whole. The criterion for a transition from organization to self-organization amounts to the requirements that conditions under which the process occurs are far from equilibrium and that there are indications of instability and openness [4].

In this study, we use a synergistic method for affecting a crystal; this method ensures the nonequilibrium conditions by providing the natural gradients of pressure, temperature, and concentration. These conditions are satisfied in a plastically deformed solid in which a constant current flows (in an electric field) and electrodiffusion of atoms occurs simultaneously with deformation. The energy spectrum of electrons in semiconductor crystals can be easily affected by applying a constant or variable electric field to the crystal with ensured simultaneous interaction of the lattice and impurity atoms with generated dislocations. Moving dislocations interact with the atomic and electronic subsystems in single crystals and, as a result, change the dynamics of their glide and affect the characteristics of plastic strain in the crystal. The combined multiparameter effect on the crystal in the presence of a catalyst reveals unique characteristics of this phenomenon [5].

EXPERIMENTAL

Germanium crystals were deformed using three methods. These included (i) thermoplastic deformation (TPD) that occurred under conditions of external heating of the sample in a resistance furnace; (ii) electroplastic deformation (EPD) that was accomplished under conditions of a high-density current flowing through the sample; and (iii) the electrotransport–plastic deformation (ETPD) conducted in the situation where the sample was deformed with simultaneous electrotransport of the lattice and impurity atoms in the anode–cathode regions of the sample [6].

The samples were deformed in a pressure chamber, which made it possible to attain all kinds of strains in the dynamic and static conditions and record the results using a plotter. The forces were recorded using a tensodynamometer as the sensor, and displacements were recorded using an inductive transducer. The setup also made it possible to deform the crystals in a wide range of temperatures, forces, and loading rates both in the dynamic and static conditions. The main objective of experiments was to determine the dependence of plastic properties of germanium single crystals on the methods of deformation and clarify the trends in variation of these properties under various strain rates. The new methods of plastic deformation of the material made it possible to reveal important differences in the results obtained using different methods and conditions of deformation. The new EPD and ETPD methods have a

1063-7842/04/4908-1012$26.00 © 2004 MAIK “Nauka/Interperiodica”

number of advantages compared to the well-known TPD method. First, the possibility of contaminating the sample with impurities released by structural components and the furnace material is reduced appreciably. Second, it is well known that electrons acquiring directional motion in a constant electric field can affect the motion of dislocations and their interaction with impurities. A new complex consideration of an impurity–electron–dislocation system can give rise to the effects of practical interest. Another important advantage of the new method is the possibility of studying and combining several (previously developed) methods using the same setup and the same sample. There are indications that other advantages of the new approach to structure formation in crystalline solids will be found, including a controlled coherent rearrangement of particles at the microlevel, which would offer very high energy gains.

We studied Ge single crystals that were compensated with Au to the concentration of 1×10^{15} cm^{-3}; were oriented along the $[1\bar{1}0]$, [001], and [110] crystallographic axes; and had dimensions of 5 × 10 × 15 mm.

The density of current flowing through the sample was varied in the range of 2.0×10^6–2.5×10^6 A/cm^2, depending on the deformation temperature. The voltage drop across the sample was 1.0–0.6 V. The power released in the sample was as high as 100 W.

RESULTS

In this paper, we report the results of studying the dependences of the strengthening coefficient, the strain, the strain rate, and the elastic-strain region on the loading rate of the crystal under deformation in dynamic and static conditions of loading. In Figs. 1 and 2 (curves *1*–*3*), we show the stress–strain σ(ε) and strain–time ε(*t*) dependences for three samples of single-crystal *p*-Si for three different loading rates. As can be seen from Figs. 1 and 2 (curves *1*–*3*), not only the duration of overcoming the elasticity region but also the yield stress itself decrease as the loading rate increases. The deformation-process parameters calculated from curves *1*–*3* (Figs. 1, 2) are listed in the table. Analyzing the run of the curves in the dynamic loading region (Fig. 1), we can find the dependence of the strengthening coefficient on the loading rate. At low loading rates, the strengthening coefficient is largest in the first portion of its steplike behavior and is smallest in the second portion of softening. It is worth noting that there are no strengthening–softening portions in curve *3* (Fig. 1) obtained at the highest loading rate. The strengthening in this case is characterized by the coefficient that is intermediate between those corresponding to two portions in curves *1* and *2*.

It is noteworthy that the absence of steplike behavior in curve *3* (Fig. 1) can be also related to two factors other than those mentioned above. First, the dynamic-loading time (*t* = 150 s) was short, and, second, the force (σ = 1.7 kg/mm^2) was small. We note a high pliability of the sample among other special features of such samples deformed with a high rate. As can be seen from Fig. 1 (curve *3*), the strain ε = 1% at a force σ = 1.5 kg/mm^2, whereas ε = 0.5% for curves *1* and *2*.

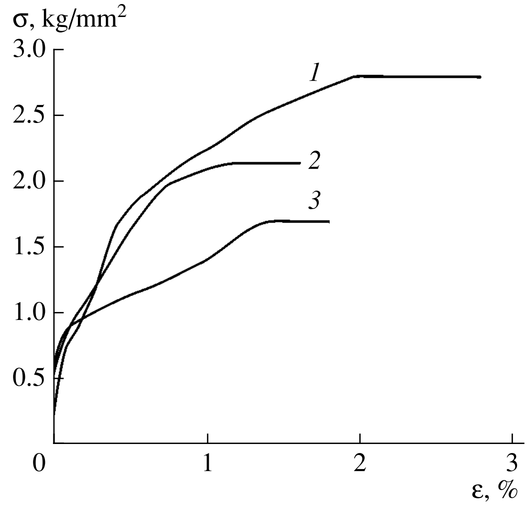

Fig. 1. Dependences of the shear stress on the strain σ(ε) at T_D = 650°C and the loading rates equal to (*1*) 71, (*2*) 150, and (*3*) 590 g/s.

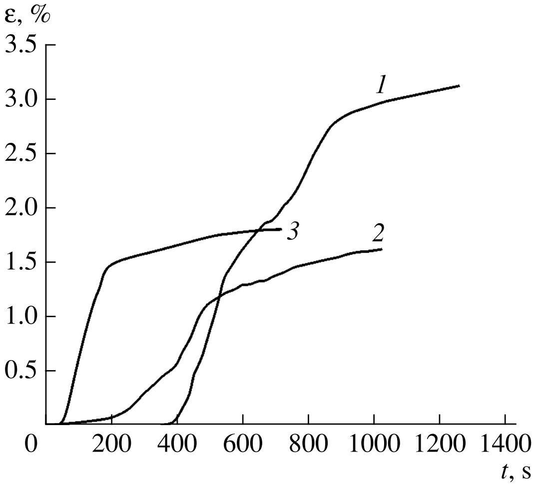

Fig. 2. Dependences of the strain on time ε(*t*) in the dynamic and static conditions of deformation at the shear stresses σ = (*1*) 2.8, (*2*) 2.1, and (*3*) 1.7 kg/mm^2.

In Fig. 2, we show the dependences ε(*t*) recorded using a plotter and encompassing all three deformation regions in the sequence: elastic, dynamic, and static. The dynamic region is characterized by the force that varies in time, whereas the force in the static region of deformation is time-independent. It can be seen from Fig. 2 (curves *1*–*3*) that, despite small values of force, incompleteness of the deformation process is observed in all cases. It also follows from Fig. 2 (curves *1*–*3*) that

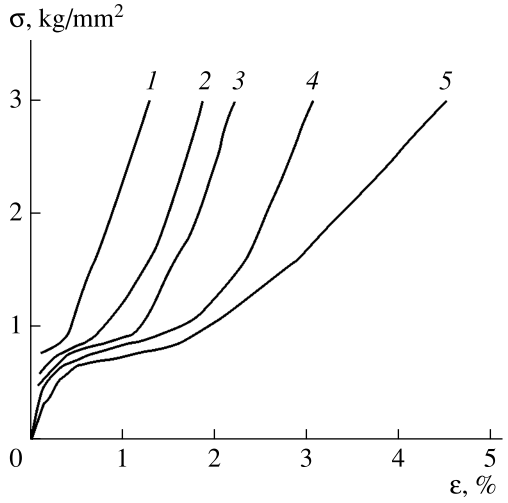

Fig. 3. Dependences of the shear stress on the strain σ(ε) for several methods and conditions of deformation of *p*-Ge single crystals at T = 750°C: (*1*) thermoplastic deformation, (*2*) thermoplastic deformation with simultaneous In diffusion, (*3*) electroplastic deformation, (*4*) electroplastic deformation with simultaneous In diffusion, and (*5*) plastic deformation with electrotransport.

the strain is affected greatly by external factors. In the dynamic region, the strain rate $\dot{\varepsilon} = \partial\varepsilon/\partial t$ is equal approximately to $\dot{\varepsilon} = 1.5$ μm/s in absolute units and to $\dot{\varepsilon} = 1.3 \times 10^{-4}$ s^{-1} in relative units at both low and high loading rates. True, the loading rates in the dynamic region do not differ to the same extent as in the elastic region (see table). A variation in the inclination with respect to the time axis characterizes the steplike character (discontinuity) of the process and confirms the fact that strengthening is replaced with softening. Even in the static region, for which small forces and long deformation times are characteristic, two steps with different strain rates are observed (see table and Fig. 2, curve *1*).

In Fig. 3, we show the characteristic curves σ(ε) for germanium single crystals deformed using different methods: the TPD method (curves *1*, *2*), the EPD method (curves *3*, *4*), and the ETPD method (curve *5*). As can be seen from Fig. 3 (curve *2*), the elasticity region is characteristic of the TPD method, although the deformation temperature in this case is higher than that in the EPD method since the crystal is not practically deformed in the case of TPD at lower temperatures. Curves *2*, *4*, and *5* obtained in the case of simultaneous diffusion of nickel represent a clear illustration of differences in the methods and conditions of deformation. As can be seen from Fig. 3 (curve *5*), the ETPD method is found to be the best for deformation; in this method, the deformation and electrodiffusion processes occur simultaneously. In the conditions of steady-state creep, the strain rate at the TPD method differs from that at the ETPD method by several orders of magnitude.

Summing up the above-listed special features of the behavior of mechanical properties of germanium single crystals, we note that the structure formation in these crystals is affected by any external factor, especially if this factor is multiparameter (synergistic). In our experiments, a high-density electric current flowing through the sample, electrodiffusion of the lattice and impurity atoms, and various loading rates were additional factors that perturbed the dislocation system.

DISCUSSION

The application of unconventional new technological method to the plasticity problem in the studies of interrelation between the structure, composition, and

Table

Sample no.	Loading rate in the regions (V_H, g/s)		Shear stress in the regions (σ, g/mm^2)			The deformation time in the regions (t, s)			Strain in the regions (ε, %)		Strengthening coefficient $\gamma = \frac{d\sigma}{d\xi}$	Strain rate in the regions ($\dot{\varepsilon}$, m/s)	
	elastic	dynamic	elastic	dynamic	static	elastic	dynamic	Static	dynamic	static		dynamic	static
1	71	180	0.87	2.8	2.8	360	360	540	1.9	1.1	Curve *1*: 2.48 Curve *2*: 0.66	Curve *1*: 1 Curve *2*: 0.42	Curve *1*: 1.55 Curve *2*: 0.12
2	150	162	0.74	2.1	2.1	195	340	480	1.12	0.4	Curve *1*: 2.43 Curve *2*: 0.92	Curve *1*: 0.42	Curve *1*: 0.1
3	590	220	0.5	1.7	1.7	60	150	510	1.4	0.3	Curve *1*: 0.804	Curve *1*: 2	Curve *1*: 0.093

properties of diamond-like semiconductors made it possible to obtain results that differed appreciably from those obtained by the thermoplastic method of deformation. In particular, the EPD and ETPD methods made it possible to significantly decrease the deformation temperature, starting stresses, and the upper yield point and also led to an increase in the total magnitude of plasticity at much smaller values of external factors. We observed the appearance of steplike behavior in the deformation process and also the appearance of new regions of strengthening and softening. The diversity of the structures formed in nonequilibrium conditions is greater than that of the structures formed in equilibrium conditions, especially in the case of a multiparameter (synergistic) approach to the deformation processes. In discussing the results obtained, we must give special attention to an appreciable difference between the compression curves shown in Figs. 1–3. Naturally, this difference is related to special features of the loading conditions and, possibly, to resulting special features of the defect structure in the crystals subjected to loading. The results obtained are qualitative and do not allow for direct quantitative comparison of theoretical results with experimental data. In our experiments, we observed the combined effect of two competing mechanisms that affected the origination of internal stresses in the crystal. The first mechanism is temperature-related and tends to decrease the internal stresses, whereas the second mechanism tends to increase these stresses as a result of an increase in the strain rate. As a result, the velocity of a group of dislocations exceeds that of an individual dislocation, which can give rise to collective kinetic effects. In our experiments, an athermal method of overcoming the obstacles to the motion of dislocations was predominant. It should be emphasized that the static mode of loading was implemented simultaneously with the dynamic mode. The electron–phonon and electron–dislocation interactions are present in the course of thermoplastic deformation of semiconductor crystals as independent factors, whereas all structure carriers rearrange into dynamic fluxes and forces with certain directions. If crystals are deformed in an electric field, an additional force (along with stresses) affects charged dislocation; this force is equal to $F = e^*E$, where e^* is the effective charge of dislocation and E is the electric-field strength [7]. If the aforementioned experimental conditions are realized, the following situation apparently takes place: dislocations are charged and acquire a preferential direction of motion with a mobility higher than that of neutral dislocations [8]. If there is a diffusive electrotransport, a redistribution of impurity ions can occur in the vicinity of dislocations and can affect the dynamics of dislocations owing to preferential location of the above ions near the anode [9]. At high densities of current flowing through the samples subjected to deformation ($j > 1.5 \times 10^6$ A/m^2) that stimulate the motion of charged defects, the strain rate can easily increase, which is observed experimentally. Finally, at certain intensities of the energy and material fluxes (in the case of a dopant impurity), the processes that support the active modes of self-consistent autocatalytic or coherent collective motion can occur in the crystals deformed by the ETPD method [10].

CONCLUSIONS

It is established as a result of studies performed that it is impossible to attain a significant plasticity magnitude in the TPD process in the same conditions load and temperature as in the EPD and ETPD modes. We found that it was possible experimentally to reduce the starting shear stress appreciably by decreasing the extent of the elasticity region in relation to the size-related factors and the degree of compensation. We showed that indications of softening appeared in compensated germanium crystals in the situation where a high-density electric current flowed through these crystals at constant values of the shear stress and temperature. We studied experimentally trends in the effect of various conditions of deformation (dynamic or static) on elastic properties of germanium in relation to the loading and strain rates. The simplicity of control and small value of energy expenditure make highly nonequilibrium systems very promising for future technologies.

REFERENCES

1. V. I. Trefilov, Yu. V. Mil’man, and I. V. Gridneva, Izv. Akad. Nauk SSSR, Neorg. Mater. **30**, 958 (1984).
2. W. Ebeling, A. Engel, and R. Feistel, *Physik der Evolutionsprozesse* (Akademie-Verlag, Berlin 1990; Editorial URSS, Moscow, 2001).
3. V. S. Ivanova, A. S. Balankin, and I. Zh. Bunin, *Synergetics and Fractals in Materials Science* (Nauka, Moscow, 1994) [in Russian].
4. T. Suzuki, H. Yosinaga, and S. Takeucti, *Dislocation Dynamics and Plasticity* (Syokabo, Tokyo, 1986; Mir, Moscow, 1989).
5. G. A. Malygin, Usp. Fiz. Nauk **69**, 979 (1999) [Phys. Usp. **42**, 887 (1999)].
6. M. A. Aliev and V. V. Seleznev, Preprint IF DNTS RAN (Russian Institute of Physics, Dagestan Scientific Center, Russian Academy of Sciences, Makhachkala, 1989).
7. G. A. Kontorova, Fiz. Tverd. Tela (Leningrad) **9**, 1235 (1967) [Sov. Phys. Solid State **9**, 961 (1967)].
8. V. B. Fiks, Zh. Éksp. Teor. Fiz. **80**, 2313 (1981) [Sov. Phys. JETP **53**, 1209 (1981)].
9. V. Ya. Kravchenyuk, Zh. Éksp. Teor. Fiz. **51**, 1676 (1966) [Sov. Phys. JETP **24**, 1135 (1967)].
10. A. I. Olemskiĭ and I. A. Sklyar, Usp. Fiz. Nauk **162** (6), 29 (1992) [Sov. Phys. Usp. **35**, 455 (1992)].

Translated by A. Spitsyn

Technical Physics, Vol. 49, No. 8, 2004, pp. 1016–1020. Translated from Zhurnal Tekhnicheskoĭ Fiziki, Vol. 74, No. 8, 2004, pp. 62–66.
Original Russian Text Copyright © 2004 by Bryushinin.

OPTICS, QUANTUM ELECTRONICS

Nonlinear Interaction of Moving Space-Charge and Photoconductivity Gratings in $Bi_{12}SiO_{20}$ Crystal

M. A. Bryushinin
Ioffe Physicotechnical Institute, Russian Academy of Sciences, St. Petersburg, 194021 Russia
e-mail: mb@mail.ioffe.ru

Received January 29, 2004

Abstract—A nonlinear interaction of moving space-charge and photoconductivity gratings is experimentally investigated. In the presence of a dc electric field, a crystal is irradiated with an oscillating interference pattern with a spatial frequency K and an oscillation frequency ω. An ac electric field with a frequency Ω is also applied to the sample. At certain frequencies ω and Ω, the crystal exhibits two types of interacting oscillations: the space-charge grating moving with velocity $|\omega - \Omega|/K$ and the photoconductivity grating moving with velocity $-\omega/K$. The effect is studied using the method of the nonstationary photoelectromotive force in a photorefractive $Bi_{12}SiO_{20}$ crystal. *© 2004 MAIK “Nauka/Interperiodica”.*

INTRODUCTION

The dynamics of photoelectric processes determines the working principles and technical characteristics of the majority of optoelectronic devices (photoresistors, photodiodes, adaptive interferometric sensors, and pattern recognition and holographic memory devices based on photorefractive materials). In this connection, the study of relaxation processes in semiconductors remains one of the most important problems of solid-state physics.

In semiconductors, the evolution of photoinduced charges consists of two stages: the buildup of the photoconductivity distribution and the formation of the space charge [1, 2]. In the presence of an external electric field, the photoconductivity and space-charge distributions can exhibit oscillating relaxation. The existence of two types of oscillations in semiconductors (moving photoconductivity gratings and the waves of the space recharging of traps) was predicted in [3]. For the first time, the oscillations of an optically induced space charge representing moving holograms were experimentally observed in $Bi_{12}SiO_{20}$ photorefractive crystals [4, 5]. Later, the time-of-flight method was used in [6] to study the moving photoconductivity gratings in the same crystal. Similar methods were used to study the waves of space charge and photoconductivity in [7–13]. One of these is the method of the nonstationary photoelectromotive force (PEMF) [14, 15].

The nonstationary PEMF (or the nonstationary holographic photocurrent) manifests itself as an ac current emerging in a semiconductor illuminated by an oscillating interference pattern. The photocurrent is induced by relative periodic displacements of the photoconductivity and electric field distributions. This mechanism for signal excitation makes it possible to use this method to study both photoconductivity and space charge. Specifically, the frequency response function of the signal emerging in crystals in the presence of an electric field exhibits two resonance maxima, one of which is related to the excitation of space charge waves and another is determined by the excitation of moving photoconductivity gratings [15].

In spite of a large number of works devoted to the aforesaid problem, it is still unclear if it is possible to simultaneously excite two types of the above natural oscillations and to observe their interaction. In the existing methods (including the nonstationary PEMF technique), the interference pattern with the spatial frequency K and the oscillation frequency ω induces either a space charge wave or a moving photoconductivity grating. The reason for this is the fact that the natural oscillation frequency of the space charge grating in high-resistance crystals (e.g., $Bi_{12}SiO_{20}$) is $\omega_{sc}/2\pi = 10$–100 Hz, whereas the oscillation frequency of the photoconductivity grating with the same spatial period is as high as $\omega_{pc}/2\pi = 0.01$–1 MHz. The phenomenon is similar to the light scattering by acoustic waves involving the particles with comparable momenta (wave vectors) and substantially different energies (frequencies). To simultaneously excite the space-charge grating (ω_{sc}, K) moving along the dc electric field with the velocity ω_{sc}/K and the electron photoconductivity grating (ω_{pc}, $-K$) moving in the opposite direction with the velocity $-\omega_{pc}/K$, and to effect their interaction, we need the third oscillation (Ω, 0) ensuring the conditions similar to the energy and momentum conservation laws: $\omega_{sc} + \omega_{pc} = \Omega$ and $K - K = 0$. As the third oscillation, we use an external electric field with frequency Ω. In our experiment, the space charge wave is excited owing to the nonlinear interaction of the moving photoconductivity grating and an ac electric field. To observe the effect, we employ the modified nonstationary PEMF technique.

EXPERIMENTAL SETUP

Figure 1 demonstrates the scheme of the experimental setup. A helium–cadmium laser (λ = 442 nm and $P_{out} \simeq$ 3 mW) serves as a coherent light source. The laser beam is split into two beams, one of which is phase-modulated using an ML-102A electrooptical modulator. A sine voltage with frequency ω is applied to the modulator. The phase modulation depth is Δ = 0.8. The laser beams are expanded and directed to the surface of the crystal. The resulting interference pattern exhibits the mean intensity I_0 = 84 W/m^2, contrast m = 0.92, and spatial frequency K = 25 mm^{-1}. A combination of dc and ac voltages is applied to the crystal: $U_{ext} = U_0 + U_A \cos\Omega t$. The dc voltage U_0 is needed for the excitation of moving gratings. The ac voltage with an amplitude U_A and frequency Ω makes it possible to effect the interaction between the moving charge and photoconductivity gratings. A nonstationary holographic photocurrent emerging in the sample causes a corresponding voltage drop at load resistance R_L = 18 kΩ. Then, the signal is amplified, filtered out, and measured using a Unipan-232B lock-in nanovoltmeter. To measure the harmonic of the nonstationary photocurrent at the difference frequency $|\omega - \Omega|$, we form a reference voltage with the same frequency. To do so, we multiply the voltages applied to the electrooptic modulator and the crystal in a balanced mixer based on a K174PS1 chip. The harmonics of the reference voltage at frequencies ω, Ω, and $\omega + \Omega$ are suppressed using a low-pass filter.

For the conventional excitation of the nonstationary PEMF in the crystal, we use only the dc voltage U_0 and detect the signal at the phase modulation frequency ω [15]. For the measurements, we employ an SK4-56 spectrum analyzer and a Unipan-232B lock-in nanovoltmeter.

Experiments employ a photorefractive $Bi_{12}SiO_{20}$ crystal. The sample represents a single crystal with the sizes 10 × 3 × 1 mm. The front and back surfaces (10 × 1 mm) are polished to optical quality. Using a silver paste, we deposit electrodes (3 × 3 mm) on the side surfaces. The interelectrode distance is L = 1 mm. The crystal is mounted between two Styrofoam layers that serve as mechanical vibration dampers (mechanical vibrations are induced owing to the piezoelectric effect).

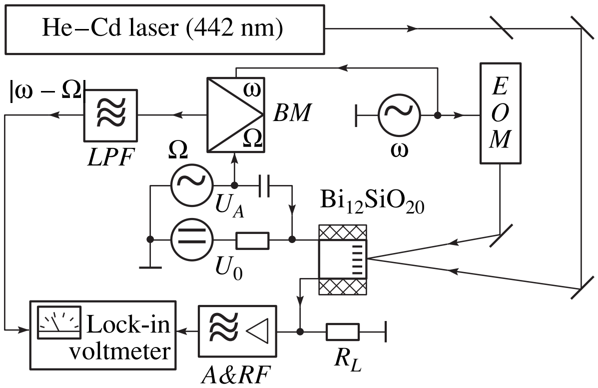

Fig. 1. Experimental setup for the study of the nonstationary holographic photocurrent excited at the difference (heterodyne) frequency: *EOM* electrooptic modulator, *BM* balanced mixer, *LPF* low-pass filter, and A&RF preamplifier with a rejector filter.

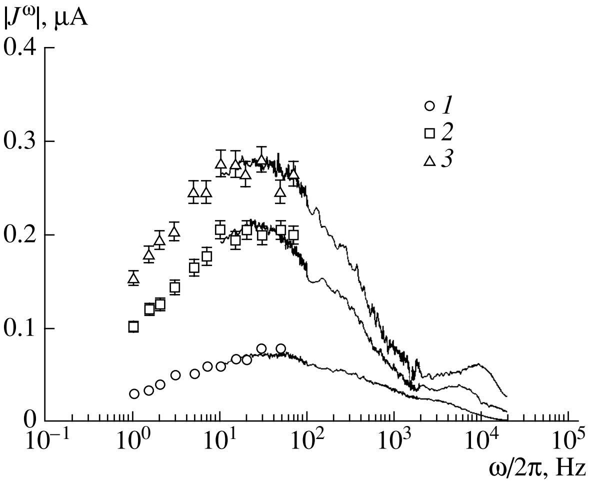

Fig. 2. Frequency response functions of the nonstationary holographic photocurrent excited in $Bi_{12}SiO_{20}$ with the conventional method: E_0 = (*1*) 6, (*2*) 10, (*3*) 14 kV/cm (E_A = 0).

EXPERIMENTAL RESULTS

Prior to analyzing the nonlinear interaction of the space-charge and photoconductivity gratings, we briefly outline the results on the nonstationary holographic photocurrent measured using the conventional method for the signal excitation. Figure 2 shows the frequency response functions of the nonstationary PEMF signal measured in $Bi_{12}SiO_{20}$ crystal at three values of the dc field $E_0 = U_0/L$. The increase in the field leads to the growth of the signal amplitude. At the lowest field strength, the frequency response function exhibits a maximum at low frequencies ($\omega/2\pi \sim$ 100 Hz). When the field increases to $E_0 \simeq$ 6 kV/cm, we observe a shoulder at the frequency $\omega/2\pi \sim$ 3 kHz. The further increase in the field gives rise to the second maximum. It follows from the frequency dependences that the increase in the external field results in the shift of the first (second) maximum towards lower (higher) frequencies. Specifically, at a dc field strength of E_0 = 10 (14) kV/cm, the resonance frequencies are $\omega_{sc}/2\pi \simeq$ 25 (20) Hz and $\omega_{pc}/2\pi \simeq$ 5.6 (9.1) kHz. It is demonstrated in [15] that this evolution of the signal is related to the resonant

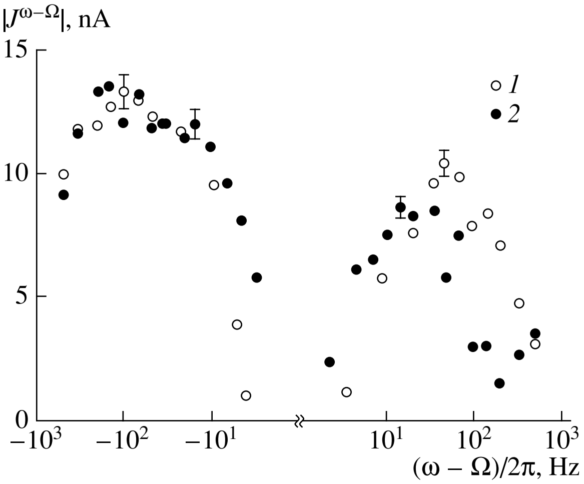

Fig. 3. Frequency response functions of the nonstationary holographic photocurrent excited in $Bi_{12}SiO_{20}$ at the difference (heterodyne) frequency: (*1*) E_0 = 10 kV/cm and $\Omega/2\pi$ = 5.9 kHz and (*2*) E_0 = 14 kV/cm and $\Omega/2\pi$ = 8.8 kHz (E_A = 3.5 kV/cm).

excitation of moving space charge and electron photoconductivity gratings. The corresponding dispersion relations are written as

$$\omega_{sc} = (\tau_M K L_0)^{-1}, \qquad (1)$$

$$\omega_{pc} = K\mu E_0, \qquad (2)$$

where τ_M is the Maxwell relaxation time, $L_0 = \mu\tau E_0$ is the drift length, μ is the mobility, and τ is the electron lifetime.

Apparently, the significant broadening of the first maximum is related to the nonlinearity of the holographic recording observed at a high contrast of the interference pattern [16]. The broadening of the resonance maximum can also be caused by the illumination nonuniformity: at high absorption coefficients ($\alpha \sim 30$ cm^{-1} [2]), the space-charge grating relaxation time in the surface layer is significantly shorter than the relaxation time in deep layers.

It is known that the nonstationary PEMF technique is a unique method enabling one to directly measure the drift mobility of carriers. Indeed, knowing the frequency of the second resonance maximum at the given K and E_0, we can easily estimate the mobility: $\mu \simeq 0.015$ cm^2/Vs. This value is in agreement with the value $\mu = 0.016$ cm^2/V s measured at a wavelength of 458 nm in [15].

Consider the results on the nonlinear interaction of the moving space-charge and photoconductivity gratings obtained with the modified nonstationary PEMF method. In experiments, the frequency of the external ac field must be approximately equal to the second resonance frequency: $\Omega/2\pi$ = 5.9 (8.8) kHz for E_0 = 10 (14) kV/cm. The frequency Ω of the external field can slightly (by approximately 300 Hz) differ from the resonance frequency ω_{pc}, since the width of the second resonance peak is 5–10 kHz (Fig. 2). The amplitude $E_A = U_A/L$ = 3.5 kV/cm of the external ac field is substantially less than the dc field. Therefore, the possible shifts of the resonance frequencies must be insignificant.

Figure 3 demonstrates the frequency response function of the nonstationary holographic photocurrent excited at the difference (heterodyne) frequency $\omega - \Omega$. For E_0 = 10 (14) kV/cm, we observe maxima at the negative and positive frequency differences: $(\omega - \Omega)/2\pi \simeq$ –100 (–80) Hz and $(\omega - \Omega)/2\pi$ = 50 (30) Hz. When the external dc field increases, the signal amplitude increases and the maxima shift towards lower frequencies. This is typical of space-charge waves [2]. The resonance peaks are relatively broad. Note that the strongly broadened and distorted maximum at $\omega - \Omega < 0$ is characterized by a higher resonance frequency. As in the case of the conventional measurements, possible reasons for this are the nonlinear limitations on the amplitude of the space-charge grating observed at high contrasts of the interference pattern and the nonuniformity of illumination with respect to the depth in the crystal.

In addition, note that the amplitude of the maximum at $\omega - \Omega < 0$ is greater than the amplitude of the maximum at $\omega - \Omega > 0$. This is a consequence of the fundamental difference between the mechanisms for the photocurrent excitation at the frequencies under consideration. At a negative frequency difference ($\omega - \Omega < 0$), a space-charge wave emerges owing to the interaction of the external field and the photoconductivity grating that moves in the direction opposite to the external electric field. When the motion of the interference pattern is matched with the motion of electrons in the conduction band, we observe a resonant enhancement of the photoconductivity wave. Thus, we observe the simultaneous excitation and interaction of two types of oscillations (the moving space-charge and photoconductivity gratings). At the positive frequency difference ($\omega - \Omega > 0$), the space-charge wave is related to the interaction of the external field and the photoconductivity grating that moves along the external field. In this case, the photoconductivity grating does not represent natural oscillations of the semiconductor. This grating nonresonantly reproduces the motion of the oscillating interference pattern along the external field. For clarity, consider the diagram illustrating the interaction of the space charge wave, the photoconductivity wave, and the external field (Fig. 4). It is seen that in the first case, the ac electric field is involved in the coupling of two types of natural oscillations in the semiconductor and the following relationships are satisfied: $\omega_{sc} + \omega_{pc} = \Omega$ and $K - K = 0$. In the second case, only one type of the natural oscillations (the space-charge wave) is excited. Evidently, the signal amplitude is higher when the conditions of the resonant excitation are satisfied for both the space-

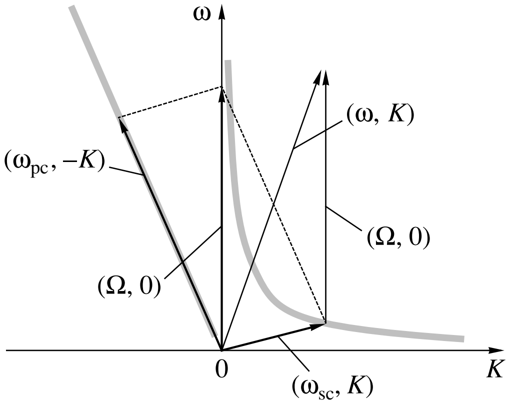

Fig. 4. Diagram of the interaction of the moving space-charge and photoconductivity gratings and the external ac electric field. Arrows show the space charge grating (ω_{sc}, K) moving at the velocity ω_{sc}/K along the dc electric field, the photoconductivity grating (ω_{pc}, $-K$) moving at the velocity $-\omega_{sc}/K$ in the direction opposite to the dc electric field, the photoconductivity grating (ω, K) moving at the velocity ω/K along the dc electric field, and the ac electric field (Ω, 0) with the frequency Ω. Halftone lines show the dispersion relations of the space-charge waves $\omega_{sc}(K)$ and photoconductivity $\omega_{pc}(-K)$.

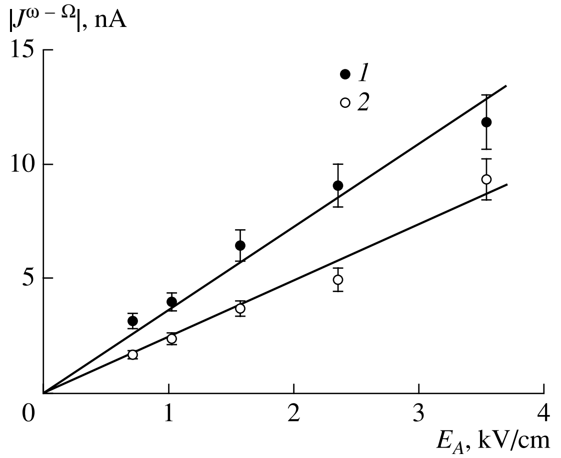

Fig. 5. Plots of the amplitude of the nonstationary holographic photocurrent $|J^{\omega-\Omega}|$ vs. the external field amplitude: (*1*) $(\omega-\Omega)/2\pi = -20$ Hz and (*2*) $(\omega-\Omega)/2\pi = +20$ Hz ($E_0 = 14$ kV/cm and $\Omega/2\pi = 8.8$ kHz).

charge grating and the photoconductivity grating. Apparently, the difference between the amplitudes of the resonance peaks must be determined by the factor KL_0 characterizing the Q factor of the space-charge and photoconductivity oscillations. In our experiment, this difference is relatively small owing to the aforementioned nonlinear limitations on the grating of the space-charge field appearing at high contrasts of the interference pattern.

Figure 5 shows the dependences of the resonance amplitudes on the amplitude of the external ac field. For the range of external field amplitudes under study, these dependences are virtually linear. The limitations on the signal amplitude can be observed at an ac field strength E_A corresponding to $KL_A \sim 1$ ($L_A = \mu\tau E_A$ is the electron drift length). For $\mu\tau \sim 10^{-10}$ m^2/V [17] and $K = 25$ mm^{-1}, this limitation must be observed at $E_A \sim 4$ kV/cm.

CONCLUSIONS

We report the first study of the simultaneous excitation and interaction of the moving space-charge and photoconductivity gratings, which represent two types of natural oscillations in a semiconductor. A new method for the excitation of the nonstationary PEMF at the difference (heterodyne) frequency makes it possible to detect a space-charge wave related to the nonlinear interaction of the moving photoconductivity grating and the ac electric field. A distinctive feature of the method proposed is the difference between the spatial and temporal characteristics of the space-charge wave and the corresponding characteristics of the external action on the crystal (illumination and electric field). In this sense, the effect under study is similar to another interesting effect consisting in the excitation of the spatial harmonics of the space charge field in photorefractive crystals [10, 11].

The nonlinear interaction of the moving space-charge and photoconductivity gratings and the modified nonstationary PEMF method based on this effect can be used to study fast processes in high-resistance semiconductors. One of the problems involving the detection of high-frequency signals is the measurement of the true drift mobility of carriers in wide-band-gap semiconductors with a complex structure of impurity levels. For $Bi_{12}SiO_{20}$ crystals, the resonance frequency of the photoconductivity grating used to estimate the true electron mobility can be as high as 100 MHz [18]. At such frequencies, it is extremely difficult to match a high-resistance crystal with the input circuits of measuring devices. Since the nonstationary holographic photocurrent at the difference frequency $\omega-\Omega$ depends on the amplitude of the moving photoconductivity grating excited at the high frequency ω, we can assume that the frequency response function $J^{\omega-\Omega}(\omega)$ measured using the modified method will be similar to the frequency response function $J^{\omega}(\omega)$ measured using the conventional method. Therefore, we will be able to determine the same material parameters. In the method under consideration, the high-frequency signal is transformed into a low-frequency signal in the crystal rather than in the measuring device.

Apparently, the nonlinear interaction of the moving space charge and photoconductivity gratings cannot be comprehensively characterized using the results presented. We need to theoretically analyze the effect in details, to perform additional experimental investigation using similar methods, and to analyze the prospects for practical applications.

ACKNOWLEDGMENTS

This work was supported by Russian Federation Presidential grant no. MK-2744.2003.02.

REFERENCES

1. S. M. Ryvkin, *Photoelectric Phenomena in Semiconductors* (Fizmatgiz, Moscow, 1963) [in Russian].
2. M. P. Petrov, S. I. Stepanov, and A. V. Khomenko, *Photorefractive Crystals in Coherent Optics* (Nauka, St. Petersburg, 1992) [in Russian].
3. R. F. Kazarinov, R. A. Suris, and B. I. Fuks, Fiz. Tekh. Poluprovodn. (Leningrad) **7**, 149 (1973) [Sov. Phys. Semicond. **7**, 102 (1973)].
4. J. P. Huignard and A. Marrakchi, Opt. Commun. **38**, 249 (1981).
5. S. I. Stepanov, V. V. Kulikov, and M. P. Petrov, Pis'ma Zh. Tekh. Fiz. **8**, 527 (1982) [Sov. Tech. Phys. Lett. **8**, 229 (1982)].
6. J. P. Partanen, J. M. C. Jonathan, and R. W. Hellwarth, Appl. Phys. Lett. **57**, 2404 (1990).
7. G. Hamel de Montchenault, B. Loiseaux, and J. P. Huignard, Electron. Lett. **22**, 1030 (1986).
8. J. M. Heaton and L. Solymar, IEEE J. Quantum Electron. **24**, 558 (1988).
9. M. P. Petrov, V. M. Petrov, V. V. Bryksin, *et al.*, J. Opt. Soc. Am. B **15**, 1880 (1998).
10. S. Mallick, B. Imbert, H. Ducollet, *et al.*, J. Appl. Phys. **63**, 5660 (1988).
11. H. C. Pedersen and P. M. Johansen, Opt. Lett. **20**, 689 (1995).
12. M. P. Petrov, V. V. Bryksin, H. Vogt, *et al.*, Phys. Rev. B **66**, 085107 (2002).
13. U. Haken, V. V. Hundhausen, and L. Ley, Phys. Rev. B **51**, 10579 (1995).
14. S. I. Stepanov and G. S. Trofimov, Fiz. Tverd. Tela (Leningrad) **28**, 2785 (1986) [Sov. Phys. Solid State **28**, 1559 (1986)].
15. I. A. Sokolov and S. I. Stepanov, J. Opt. Soc. Am. B **10**, 1483 (1993).
16. S. Mansurova, S. Stepanov, N. Korneev, *et al.*, Opt. Commun. **152**, 207 (1998).
17. M. Bryushinin, V. Kulikov, and I. Sokolov, Phys. Rev. B **65**, 245204 (2002).
18. M. A. Bryushinin and I. A. Sokolov, Phys. Rev. B **63**, 153203 (2001).

Translated by A. Chikishev

Technical Physics, Vol. 49, No. 8, 2004, pp. 1021–1027. Translated from Zhurnal Tekhnicheskoĭ Fiziki, Vol. 74, No. 8, 2004, pp. 67–73.
Original Russian Text Copyright © 2004 by Tyukhtin.

Energy Characteristics of Radiation of Oscillating Dipoles Moving in a Nondispersive Medium and a Cold Plasma

A. V. Tyukhtin
Scientific Research Institute of Radiophysics, St. Petersburg State University, St. Petersburg, 198504 Russia
e-mail: tyukhtin@niirf.spbu.ru

Received August 20, 2003; in final form, January 23, 2004

Abstract—We consider radiation of moving oscillating electric and magnetic dipoles, whose moments are oriented along their velocity. We have derived general expressions for field components and radiation power, which are valid for isotropic homogeneous nonabsorbing media. Special cases of a nondispersive medium and a cold plasma are considered. In these cases, the dependences of energy spectral distributions and radiation powers are analyzed as a function of the velocity of the sources and the parameters of media. *© 2004 MAIK “Nauka/Interperiodica”.*

INTRODUCTION

Radiation of sources moving in homogenous steady-state media has been actively investigated for many decades. The main attention has been paid to analysis of radiation of charged particles and their flows as well as of sources having any multipole moments. The results have been widely published (see, for example, [1–10] and references therein). However, it should be noted that in the problems considered earlier a source was usually assumed to be static in the intrinsic reference system (i.e., it had no eigenfrequency). If nonuniformity of the source movement can be neglected, the radiation at a preset frequency occurs only in the case when the velocity of the source is higher than the phase velocity of electromagnetic waves of this frequency (Cherenkov radiation).

In the case of a moving source oscillating in its quiescence system, the situation changes radically. Naturally, such a source emits at any velocity but radiation characteristics essentially depend on the velocity. Similar problems are of interest to theory as well as to various experiments. An emitting moving atom is an example of sources of this kind. Another example is antennas of space vehicles, which can be influenced by the flow of the ambient plasma.

Problems with moving oscillators were seldom considered (see, for example, [1, 2, 11–15]). For example, the Doppler effect was studied in [1, 11, 12]; the case of a moving oscillating electric dipole was partly considered in [11, 13]; and radiation of moving sources in chiral media was studied in [15]. In some works, similar problems were considered in a different formulation: a harmonic source was assumed to be fixed, while the medium was moving [16–19]. However, in such a formulation, which is undoubtedly of independent interest, the spectral characteristics of radiation are automatically not considered: in a quiescence system of a harmonic source, the field is also a harmonic function of time. Meanwhile, when considering the problem in the quiescence system of the medium, the spectral distribution of radiation power is one of the key factors. In addition, the solution of the problem of the total radiation power of a source of one kind or another also essentially depends on the choice of a reference system; this was mentioned in [16].

This paper is devoted to analysis of energy characteristics in problems with oscillating dipoles, which move in some isotropic homogenous media. As was mentioned above, a number aspects of the theory of radiation of moving oscillators was studied in the scientific literature; however, some important questions were not considered or considered only fragmentarily. Among them are questions concerning the behavior of spectral energy distributions in media with various dispersion properties, the dependence of radiation power on the dipole kind and dipole velocity in different media, and others.

Section 1 of the paper presents some general expressions valid for a medium with any frequency dependence of the refractive index. We note that these expressions were obtained for an electric dipole in [13], but there are no similar results for a magnetic dipole in the available literature. Hence, it seems reasonable to write out the corresponding formulas for both sources with minimum comments only. The special cases of nondispersive medium and cold plasma are studied in Sections 2 and 3.

1. GENERAL EXPRESSIONS FOR FIELDS AND RADIATION POWERS IN AN ISOTROPIC HOMOGENOUS MEDIUM

Let a source having an electric or magnetic dipole moment in the intrinsic reference system move with velocity $\mathbf{v} = v\mathbf{e}_z$ relative some isotropic medium with permittivity ε and permeability μ. We do not define concretely the properties of the medium so far. The medium is just assumed to be homogenous, stationary, and without spatial dispersion and absorption. Let us suppose that a dipole moment of one kind or another is oriented along the velocity vector of the source. In the source quiescence system, we write the densities of the electric and magnetic dipole moments, respectively, in the form

$$\begin{aligned} \mathbf{P}' &= p_0'\mathbf{e}_z'\exp(-i\omega_0't')\delta(x')\delta(y')\delta(z'), \\ \mathbf{M}' &= m_0'\mathbf{e}_z'\exp(-i\omega_0't')\delta(x')\delta(y')\delta(z'), \end{aligned} \tag{1}$$

where $\delta(\xi)$ is the delta function. Here and below, the values and operators related to the intrinsic reference system of a source are designated with prime. The volume current densities are expressed by

$$\mathbf{j}'^p = \partial\mathbf{P}'/\partial t', \quad \mathbf{j}'^m = c\,\mathrm{curl}'\mathbf{M}', \tag{2}$$

where the superscript indicates the source type (everywhere below, the values marked with superscripts p and m are related to the electric and magnetic dipoles, respectively).

The charge density ρ' is determined by the charge conservation law (for a magnetic dipole, $\rho'^m = 0$).

We substitute each of Eqs. (1) into the corresponding formula from (2) and pass on to a "laboratory" reference system (quiescence system of the medium). To do that, one should apply the Lorentz transformations for derivatives, as well as for current and charge density [20, 21]. As a result, we obtain for nonzero current density components

$$\begin{aligned} j_z^p &= p_0'\sqrt{1-\beta^2}\frac{\partial}{\partial t}[\mathbf{e}^{-i\omega_0 t}\delta(z - vt)]\delta(x)\delta(y), \\ j_\varphi^m &= -cm_0'\sqrt{1-\beta^2}\mathbf{e}^{-i\omega_0 t}\delta(z - vt)\delta(x)\delta(y), \end{aligned} \tag{3}$$

where $\beta = v/c$ and $\omega_0 = \omega_0'\sqrt{1-\beta^2}$ is the frequency of the source in the laboratory system (cylindrical coordinate system r, φ, z is used here).

An expression for the electrical dipole charge density can easily be obtained using the equation of continuity. We stress that, in the case considered (dipole moments are parallel to their velocity vector), a source having only an electric (or only magnetic) dipole moment in its quiescence system is characterized also by the moment of the same kind in the laboratory system (values of the moments are linked through the relations $p_0 = p_0'\sqrt{1-\beta^2}$, $m_0 = m_0'\sqrt{1-\beta^2}$).

A further course of solution is standard for the problems with moving sources (see, for example, [1–5, 7, 8, 13]). In this case, one can use either Hertz vectors (electric or magnetic) or vector $\mathbf{A}$ and scalar Φ potentials introduced in the standard way. The solution is sought in the form of Fourier integrals. When the expressions for potentials are found, the formulas for field components can easily be obtained. Omitting all the intermediate transformations, we give straightaway the expressions for nonzero components of electric and magnetic fields in the cylindrical coordinate system:

(i) in the case of an electric dipole, we have

$$\begin{aligned} E_z^p &= \frac{i}{c}\int_{-\infty}^{\infty} a^p\omega\left[1 - \left(\frac{\omega-\omega_0}{\omega\beta n}\right)^2\right]\mathbf{e}^{i\psi}d\omega, \\ E_r^p &= -\int_{-\infty}^{\infty}\frac{\partial a^p}{\partial r}\frac{\omega-\omega_0}{\omega\beta n^2}\mathbf{e}^{i\psi}d\omega, \\ H_\varphi^p &= -\int_{-\infty}^{\infty}\frac{1}{\mu}\frac{\partial a^p}{\partial r}\mathbf{e}^{i\psi}d\omega; \end{aligned} \tag{4}$$

(ii) in the case of a magnetic dipole, we have

$$\begin{aligned} E_\varphi^m &= \frac{i}{c}\int_{-\infty}^{\infty}\omega a^m\mathbf{e}^{i\psi}d\omega, \\ H_r^m &= -\frac{i}{v}\int_{-\infty}^{\infty}\frac{(\omega-\omega_0)a^m}{\mu}\mathbf{e}^{i\omega}d\omega, \\ H_z^m &= \int_{-\infty}^{\infty}\frac{1}{\mu r}\frac{\partial(ra^m)}{\partial r}\mathbf{e}^{i\psi}d\omega. \end{aligned} \tag{5}$$

Here, the following notation is introduced,

$$\begin{aligned} \psi(\omega) &= \frac{\omega-\omega_0}{v}z - \omega t, \\ a^p(\omega, r) &= \frac{p_0'\sqrt{1-\beta^2}\omega\mu(\omega)}{2cv}H_0^{(1)}(rs(\omega)), \\ a^m(\omega, r) &= -\frac{im_0'\sqrt{1-\beta^2}\mu(\omega)}{2v}\frac{\partial}{\partial r}H_0^{(1)}(rs(\omega)), \end{aligned} \tag{6}$$

where,

$$\begin{aligned} s(\omega) &= \frac{\omega}{c}\sqrt{n^2(\omega) - \left(\frac{\omega-\omega_0}{\omega\beta}\right)^2}, \\ n^2\omega &= \varepsilon(\omega)\mu(\omega), \end{aligned} \tag{7}$$

and the radical in the formula for $s(\omega)$ is positive for the positive radicand; if, however, it is negative, we have $s = i|s|$. Such a fixation of the root branch is caused by the fact that, at a long distance form the z axis, the Fourier component of the field has to be either a wave propagating away from the z axis or a nonhomogenous wave exponentially decreasing with increasing r.

Let us now obtain general expressions for the power of sources averaged over a radiation period. To do that, we calculate the averaged energy flux Σ through an infinitely large cylindrical surface, which surrounds the source trajectory. The surface radius R can be arbitrary (including infinitely large values) since there is no absorption in the medium. This method leads to evaluation of the integral

$$\Sigma = \frac{cR}{16\pi}\int_{-\infty}^{\infty} dz \int_{0}^{2\pi} d\varphi(\mathbf{e}_r, [\mathbf{E}, \mathbf{H}^*] + [\mathbf{E}^*, \mathbf{H}]). \tag{8}$$

We note that other ways can also be used [1, 4]. A widespread method among them involves the calculation of the work done by field over a source.

The calculation technique of integrals like Eq. (8) was developed in investigating the Cherenkov radiation (CR) [1–5, 7, 8]. Omitting intermediate steps, we give the final expressions for the power of sources

$$\begin{Bmatrix}\Sigma^p \\ \Sigma^m\end{Bmatrix} = \int\limits_{\substack{-\infty \\ (\omega n\beta)^2 > (\omega - \omega_0)^2}}^{\infty} \begin{Bmatrix} d\Sigma^p/d\omega \\ d\Sigma^m/d\omega \end{Bmatrix} d\omega, \tag{9}$$

where

$$\frac{d\Sigma^p}{d\omega} = \frac{p_0'^2(1-\beta^2)}{4c^2 v}\mu|\omega|^3\left[1-\left(\frac{\omega-\omega_0}{\omega n\beta}\right)^2\right], \tag{10}$$

$$\frac{d\Sigma^m}{d\omega} = \frac{m_0'^2(1-\beta^2)}{4c^2 v}\varepsilon\mu^2|\omega|^3\left[1-\left(\frac{\omega-\omega_0}{\omega n\beta}\right)^2\right]. \tag{11}$$

As is seen, integration is performed over part of the real axis, where

$$(\omega n\beta)^2 > (\omega - \omega_0)^2, \tag{12}$$

and, hence, the value of $s(\omega)$ is real. We emphasize that the corresponding expression for an electric dipole was obtained in [13], where integration was carried out only over the positive part of the frequency axis. It is easy to show that the expression for Σ^p is equivalent to that given in [13]; for this purpose, it is sufficient to replace ω with $-\omega$ in the integral along a negative semiaxis and to take into account the evenness of the functions $\varepsilon(\omega)$ and $\mu(\omega)$ (the latter is valid due to the absence of absorption in the medium).

The results obtained turn into the formulas for CR of nonoscillating (i.e., static in the intrinsic reference system) dipoles [1–4] if we set $\omega_0 = 0$ and replace the averaged value of dipole moment $p_0'/\sqrt{2}$ by the static moment $p_{\rm st}'$ ($m_0'/\sqrt{2}$ by $m_{\rm st}'$, respectively). We stress that, as in the case of nonoscillating dipoles, Eq. (10) is not transformed into Eq. (11) when changing $p_0' \longrightarrow m_0'$, $\varepsilon \rightleftarrows \mu$ (extra multiplier μ^2 appears in Eq. (11)). As is known from the theory of CR of nonoscillating dipoles [1], this asymmetry is caused by the asymmetry of the sources: the electric dipole is a model of the Hertz dipole, while the magnetic dipole is associated with a small current loop. Symmetric expressions for fields and energy characteristics could be obtained if the so-called "true" magnetic dipole designed using hypothetical magnetic charges by analogy with the Hertz dipole were taken instead of the current loop.

2. RADIATION OF OSCILLATORS IN A NONDISPERSIVE MEDIUM

Let us apply the results obtained to the case of a nondispersive medium. In this case, inequality Eq. (12) has the following solutions: (i) if $n\beta < 1$, we have $\omega_1 < \omega < \omega_2$; (ii) if $n\beta > 1$, we have $\omega < \omega_2$ and $\omega > \omega_1$, where $\omega_{1,2} = \omega_0'\sqrt{1-\beta^2}(1 \pm n\beta)^{-1}$. Obviously, a correct expression for radiation power can be obtained in case (i) only ("subluminal" regime of source movement), since the radiation spectrum in case (ii) becomes unlimited and integrals (9) diverge (it should be recalled that this paradox also takes place for moving nonoscillating sources, which do not emit electromagnetic waves at $n\beta < 1$, while at $n\beta > 1$, the radiation power is infinitely large). For this very reason, we consider only the case of "subluminal" velocity of the dipoles.

For convenience of further analysis, it is reasonable to introduce the dimensionless frequencies normalized to the source eignefrequency,

$$\begin{gathered}\Omega = \omega/\omega_0', \\ \Omega_{1,2} = \omega_{1,2}/\omega_0' = \sqrt{1-\beta^2}/(1 \pm n\beta).\end{gathered} \tag{13}$$

Taking into account this notation, we express Eqs. (9)–(11) as

$$\begin{gathered}\Sigma^p = \frac{p_0'^2\omega_0'^4}{3c^3}\tilde{\Sigma}^p, \quad \Sigma^m = \frac{m_0'^2\omega_0'^4}{3c^3}\tilde{\Sigma}^m; \\ \tilde{\Sigma}^p = \int_{\Omega_1}^{\Omega_2}\sigma^p(\Omega)d\Omega, \quad \tilde{\Sigma}^m = \int_{\Omega_1}^{\Omega_2}\sigma^m(\Omega)d\Omega;\end{gathered} \tag{14}$$

$$\begin{gathered}\sigma^p(\Omega) = \frac{3(1-\beta^2)\mu}{4\beta}\Omega^3\left[1-\left(\frac{\Omega-\sqrt{1-\beta^2}}{\Omega n\beta}\right)^2\right], \\ \sigma^m(\Omega) = n^2\sigma^p(\Omega).\end{gathered} \tag{15}$$

The dimensionless values $\tilde{\Sigma}^p$, $\tilde{\Sigma}^m$ were introduced in such a way that they become 1 at $\varepsilon = \mu = 1$ and $\beta = 0$ (however, as will be shown below, these values equal 1 even at $\varepsilon = \mu = 1$ regardless of the source velocity).

Let us emphasize the main features of the obtained expressions. First of all, we stress that the dependence of radiation power on the velocity of the medium becomes apparent only when the values quadratic in β are taken into account; i.e., it is a relativistic effect. The dependence of the spectral density of the radiation power σ^p on the frequency Ω is shown in Figs. 1a–1c (for σ^m, the corresponding dependences are of the same form since these quantities differ only by the constant multiplier n^2). It is taken throughout that $\mu = 1$: (a) belongs to a case of $n = 0.7$, (b), to a case of vacuum ($n = 1$), and (c), to $n = 1.3$. The curves for several values of the velocity are shown in Figs. 1a–1c.

As is seen, the width of the radiation spectrum is defined as

$$\Omega_2 - \Omega_1 = 2n\beta\sqrt{1-\beta^2}(1-n^2\beta^2)^{-1}. \qquad (16)$$

For $n > 1$ the width increases monotonically as the velocity increases from zero at $\beta = 0$ to infinity at $\beta \longrightarrow 1/n$. However, if $n < 1$, this regularity is violated: it is easy to show that the spectrum width is maximal at $\beta = (2 - n^2)^{-1/2}$ and equal to zero at $\beta \longrightarrow 0$ and $\beta \longrightarrow 1$.

For $n = 0.7$, the maximum value of the spectral power density decreases with increasing velocity for both considered sources (Fig. 1a). We note that the position of the maximum depends on the velocity only slightly if the latter is not too close to 1. For $n = 1$, with increasing velocity, the maximum value σ^p also decreases and its position is appreciably shifted towards higher frequencies. For $n > 1$, the behavior of σ^p is more complicated (Fig. 1c). For a small velocity, the maximum of the frequency distribution of power decreases with increasing β but, starting with some value of the velocity, the decrease is changed by the increase and the value of the maximum approaches infinity at $\beta \longrightarrow 1/n$.

The total radiation powers of the considered sources can easily be determined calculating integrals (14):

$$\tilde{\Sigma}^p = \mu n\left(\frac{1-\beta^2}{1-n^2\beta^2}\right)^3, \quad \tilde{\Sigma}^m = n^2\tilde{\Sigma}^p. \qquad (17)$$

We note that for an electric dipole in nonmagnetic medium, the corresponding result was first obtained in [11].

The dependence of the radiation power on the velocity of the source is shown in Fig. 2. As before, we assume that $\mu = 1$; the values of $n = \sqrt{\varepsilon}$ are given in the figure caption. For $n < 1$, the radiation power is a monotonically decreasing function of the source velocity, while for $n > 1$, it is a monotonically increasing function and at $\beta \longrightarrow 1/n$ it becomes infinitely large. We emphasize that in vacuum the radiation powers of both sources do not depend on their velocities $\tilde{\Sigma}^p = \tilde{\Sigma}^m = 1$ (although, as has been shown above, even in vacuum the radiation spectrum substantially changes with velocity).

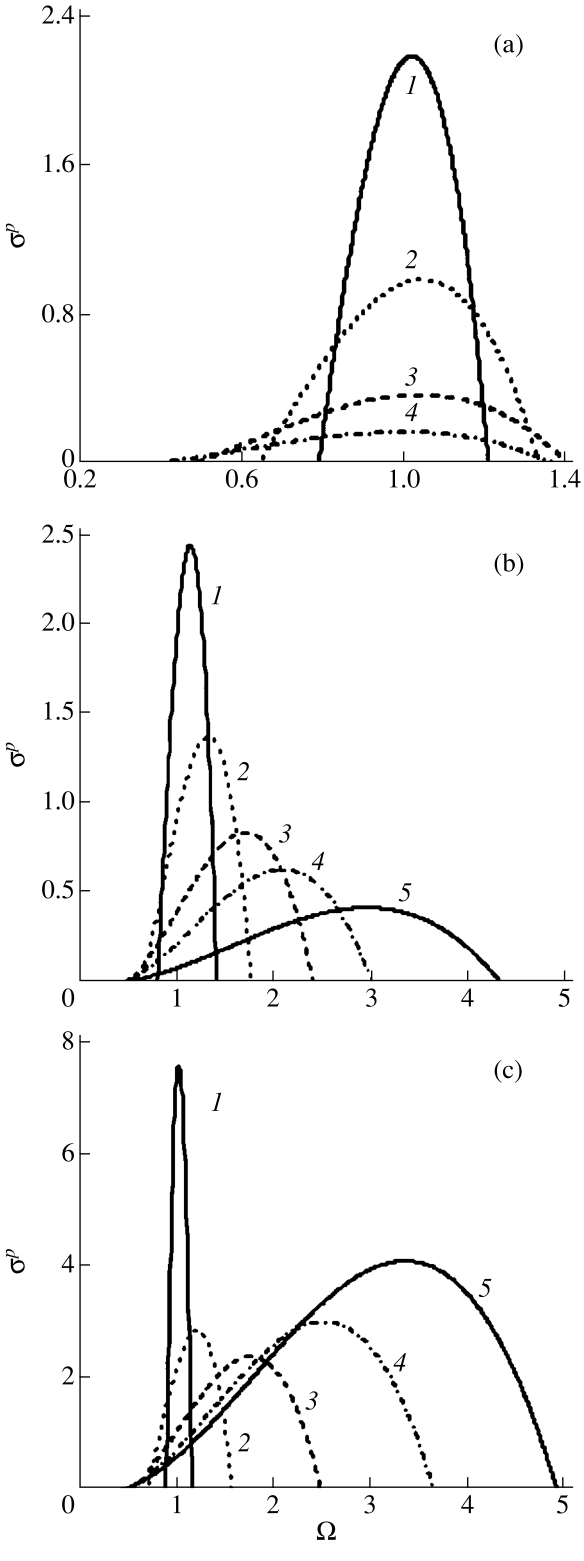

Fig. 1. Frequency distributions of the radiation power in the case of (a) a nondispersive medium with $n = 0.7$; $\beta = 0.3$ (*1*), 0.5 (*2*), 0.7 (*3*), 0.8 (4); (b) vacuum: $\beta = 0.3$ (*1*); 0.5 (*2*), 0.7 (*3*), 0.8 (*4*); 0.9 (*5*); (c) a nondispersive medium with $n = 1.3$; $\beta = 0.1$ (*1*), 0.3 (*2*), 0.5 (*3*), 0.6 (*4*), 0.65 (*5*).

3. RADIATION OF OSCILLATORS IN A COLD PLASMA

Let us pass to analysis of radiation of longitudinal moving oscillating dipoles in the cold plasma characterized by permittivity $\varepsilon = 1 - \omega_p^2/\omega^2$ and permeability $\mu = 1$. In such a situation, the solution of inequality (12), determining the range of frequencies of the emitted waves, has the form

$$\omega_1 < \omega < \omega_2,$$

$$\omega_{1,2} = \frac{\omega_0 \mp \beta\sqrt{\omega_0^2 - \omega_p^2(1-\beta^2)}}{1-\beta^2} = \frac{\omega_0' \mp \beta\sqrt{\omega_0'^2 - \omega_p^2}}{\sqrt{1-\beta^2}}. \tag{18}$$

Radiation occurs only when $\omega_{1,2}$ are real-valued; i.e., the source eigenfrequency ω_0' is higher than the plasma frequency ω_p (it should be stressed that the source frequency in the laboratory system, $\omega_0 = \omega_0'\sqrt{1-\beta^2}$, may be lower that the plasma frequency). It is easy to see that the width of the radiation spectrum increases with the source velocity and decreases with increasing plasma frequency.

As before, we introduce dimensionless frequencies normalized to the source eigenfrequency,

$$\Omega = \omega/\omega_0', \quad \Omega_p = \omega_p/\omega_0',$$
$$\Omega_{1,2} = \omega_{1,2}/\omega_0' = \left(1 \mp \beta\sqrt{1-\Omega_p^2}\right)/\sqrt{1-\beta^2}. \tag{19}$$

Taking into account these designations, the integrals for the total powers can be expressed in the form (14), and the spectral distributions of power are written as

$$\sigma^p(\Omega) = \frac{3}{4}\frac{(1-\beta^2)^2}{\beta^3}\frac{\Omega^3(\Omega-\Omega_1)(\Omega_2-\Omega)}{\Omega^2-\Omega_p^2},$$
$$\sigma^m(\Omega) = \frac{3}{4}\frac{(1-\beta^2)^2}{\beta^3}\Omega(\Omega-\Omega_1)(\Omega_2-\Omega). \tag{20}$$

Thus, the spectral distribution of power for an electric dipole is the ratio of fifth- and second-degree polynomials, while for a magnetic dipole this distribution is a third-degree polynomial. The frequency dependences of normalized spectral densities are shown in Figs. 3a and 3b for different values β and Ω_p: (a) for $\Omega_p = 0.7$ and (b) for $\Omega_p = 0.95$. The curves with identical numbers relate to the same velocity given in the caption to Fig. 3a. Comparing Figs. 3a and 1b, we see that for small plasma frequencies the spectral distributions are similar to that in vacuum. An important difference is that values σ^p and σ^m are somewhat less than that in vacuum. If $\Omega_p \approx 1$ (Fig. 3b), the frequency distributions of power acquire an interesting feature: for a rather high velocity, the radiation spectrum of any source is within the range $\Omega > 1$; i.e., an observer will record only frequencies higher than the oscillator eigenfrequency.

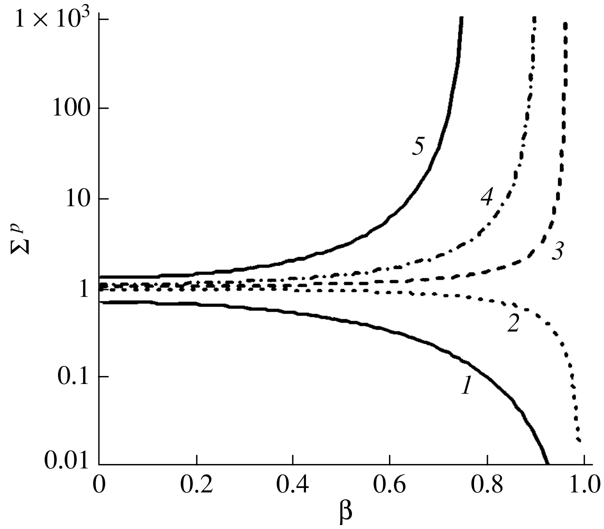

Fig. 2. Velocity dependences of the power of an electric dipole at $\mu = 1$: $n = 0.7$ (*1*), 0.97 (*2*), 1.03 (*3*), 1.1 (*4*), 1.3 (*5*).

Let us pass to analysis of total radiation powers of the oscillators moving in a plasma. Calculating analytically integrals (14) with integrands (20), we obtain

$$\tilde{\Sigma}^p = \frac{3}{4\beta^3}\Bigg\{2\beta\sqrt{1-\Omega_p^2}\left[\Omega_p^2 + \frac{\beta^2}{3}(2-5\Omega_p^2)\right]$$
$$-\frac{\Omega_p^2}{2}(1-\beta^2)\left[\left(\Omega_p + \sqrt{1-\beta^2}\right)^2 \ln\frac{\Omega_2+\Omega_p}{\Omega_1+\Omega_p}\right. \tag{21}$$
$$\left. + \left(\Omega_p - \sqrt{1-\beta^2}\right)^2 \ln\frac{\Omega_2-\Omega_p}{\Omega_1-\Omega_p}\right]\Bigg\},$$

$$\tilde{\Sigma}^m = (1-\Omega_p^2)^{3/2}. \tag{22}$$

It is interesting to note that the total radiation power of a magnetic oscillator does not depend on its velocity regardless of the substantial dependence of spectral composition of radiation. On the other hand, it can be shown that the radiation power of an electric oscillator is a monotonically decreasing function of the oscillator velocity as well as of the plasma frequency. For small velocities, this power coincides with the radiation power of a fixed source with an accuracy on the order of β^2,

$$\tilde{\Sigma}^p \approx (1-\Omega_p^2)^{1/2}. \tag{23}$$

In the ultrarelativistic regime, when $1 - \beta^2 \ll 1$, one can obtain

$$\tilde{\Sigma}^p \approx (1-\Omega_p^2)^{3/2}. \tag{24}$$

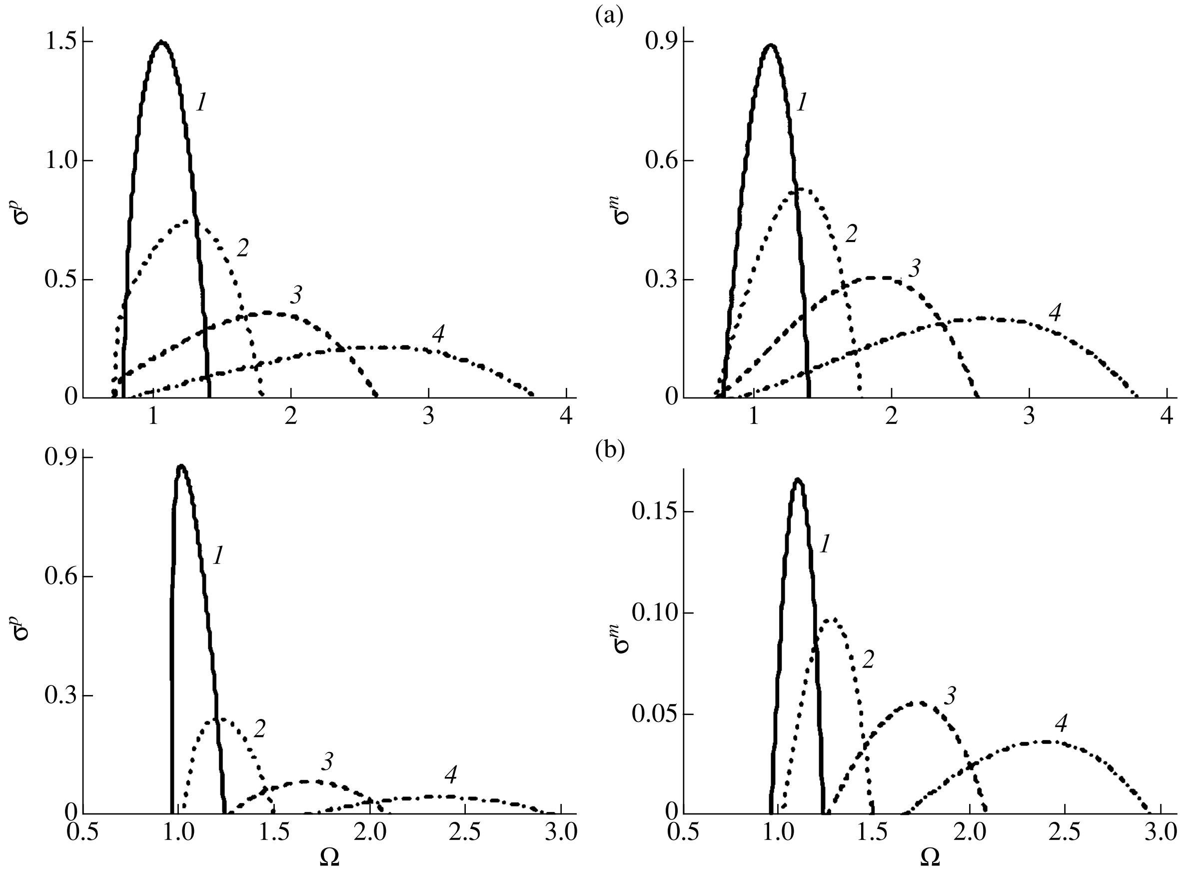

Fig. 3. Frequency distributions of radiation power in plasma at (a) $\Omega_p = 0.7$: $\beta = 0.4$ (*1*), 0.6 (*2*), 0.8 (*3*), and 0.9 (*4*); (b) the same at $\Omega_p = 0.95$.

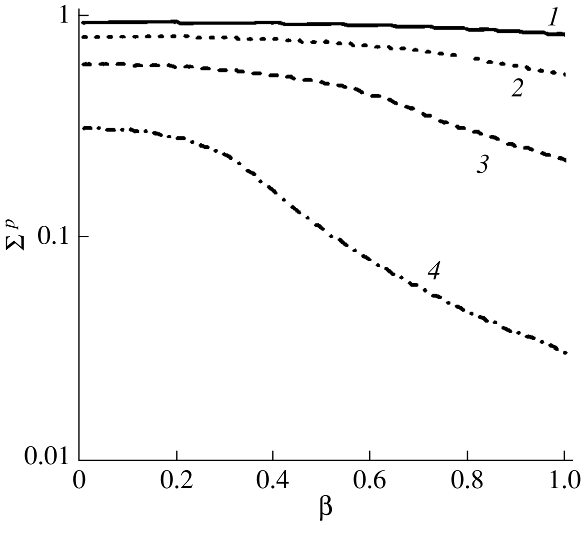

Fig. 4. Velocity dependence of the power of an electric dipole: $\Omega_p = 0.4$ (*1*), 0.6 (*2*), 0.8 (*3*), 0.95 (*4*).

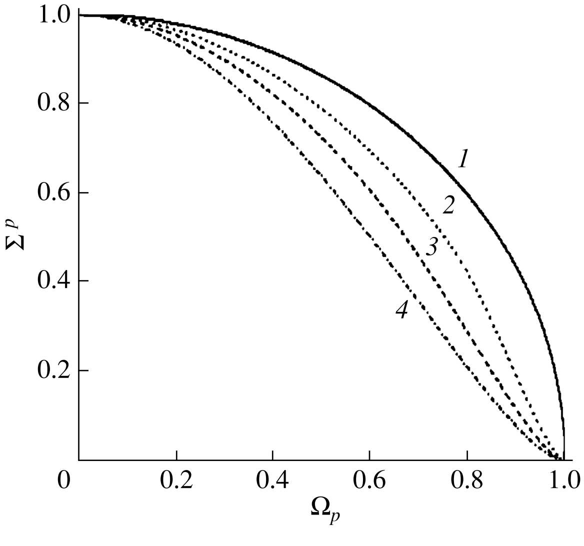

Fig. 5. Power of an electric dipole as a function of the plasma frequency: $\beta = 0$ (*1*), 0.6 (*2*), 0.8 (*3*), $\beta \longrightarrow 1$ (*4*). Curve *4* also relates to a magnetic dipole for any its velocity.

As velocity β increases from 0 to 1, the value of $\tilde{\Sigma}^p$ decreases monotonically from the value given by Eq. (23) to a value following from Eq. (24), while the value of $\tilde{\Sigma}^m$ remains constant. Thus, for equal dipole moments and eigenfrequencies, an electric dipole is found to be a more effective oscillator than a magnetic dipole (equality $\tilde{\Sigma}^m = \tilde{\Sigma}^p$ is reached only in the limit $\beta \longrightarrow 1$).

The velocity dependences of the radiation power of an electric dipole are shown in Fig. 4 for several values of a plasma frequency, while the dependences of the radiation power of both sources on the plasma frequency are shown in Fig. 5 for various values of velocity. As is seen, even for the electric dipole, the velocity dependence of radiation power is weak if the plasma frequency ω_p is not too close to the source eigenfrequency ω_0'. We emphasize that, in spite of this fact, the radiation spectra of both sources change substantially with the velocity, as has been mentioned.

CONCLUSIONS

This paper considers radiation of moving oscillating dipoles of the electric and magnetic kinds in certain media. It was assumed that the corresponding dipole moments are oriented along the velocity of the source. The main results are as follows.

(1) We analyzed the energy characteristics of the radiation fields of dipoles moving in a medium without dispersion with a velocity smaller than the velocity of light in the medium. In particular, it is shown that for $n > 1$, an increase in the source velocity results in the following effects: the width of the radiation spectrum increases monotonically and unlimitedly; the peak in the radiation spectrum first decreases, reaching the minimum value, and then increases; and the radiation power monotonically increases. For $n < 1$, the behavior of the corresponding regularities changes: the width of the radiation spectrum reaches maximum at a certain velocity, while for $\beta \longrightarrow 1$ this width equals zero; and the maximum in the radiation spectrum and total radiation power are monotonically decreasing functions of β. All the mentioned regularities are valid for both electric and magnetic dipoles.

(2) We analyzed the energy characteristics of the radiation fields of dipoles moving in a cold plasma. In particular, we showed that the radiation is emitted only in the case when the oscillator eigenfrequency ω_0' is higher than the plasma frequency (but the oscillator frequency in the laboratory system, ω_0, may be lower than the plasma frequency). The radiation spectra are similar to those in vacuum if the plasma frequency is not too close to the oscillator eigenfrequency. If, however, these frequencies are close, for a high velocity the radiation spectrum is within the range higher than ω_0'. The radiation power of an electric dipole is a monotonically decreasing function of its velocity, while the radiation power of a magnetic dipole is independent of the velocity (although, the radiation spectrum changes substantially with the velocity). In a cold plasma, an electric dipole is a more effective oscillator than a magnetic dipole if their dipole moments, eigenfrequencies and velocities are equal in value.

REFERENCES

1. I. M. Frank, *Cherenkov Radiation* (Nauka, Moscow, 1988) [in Russian].
2. V. P. Zrelov, *Cherenkov Radiation and Its Applications in High-Energy Physics* (Atomizdat, Moscow, 1968), Part 1 [in Russian].
3. V. L. Ginzburg, *Theoretical Physics and Astrophysics* (Nauka, Moscow, 1987; Pergamon, Oxford, 1979).
4. B. M. Bolotovskiĭ, Usp. Fiz. Nauk **62**, 201 (1957).
5. B. M. Bolotovskiĭ, Usp. Fiz. Nauk **75**, 295 (1961) [Sov. Phys. Usp. **4**, 781 (1961)].
6. V. L. Ginzburg, Usp. Fiz. Nauk **172**, 373 (2002).
7. G. N. Afanasiev and V. G. Kartavenko, J. Phys. D **31**, 2760 (1998).
8. G. N. Afanasiev, V. G. Kartavenko, and E. N. Magar, Physica B **269**, 95 (1999).
9. I. Carusotto, M. Artoni, G. C. La Rocca, and F. Bassani, Phys. Rev. Lett. **87**, 064801 (2001).
10. T. E. Stevens, J. K. Wahlstrand, J. Kuhl, and R. Merlin, Science **291**, 627 (2001).
11. I. M. Frank, Izv. Akad. Nauk SSSR **6** (1–2), 3 (1942).
12. V. L. Ginzburg and I. M. Frank, Dokl. Akad. Nauk SSSR **56**, 583 (1947).
13. V. L. Ginzburg and I. M. Frank, Dokl. Akad. Nauk SSSR **56**, 699 (1947).
14. G. M. Garibyan and F. A. Kostanyan, Izv. Vyssh. Uchebn. Zaved. Radiofiz. **14**, 1857 (1971).
15. A. A. Smirnova, Author's Abstract of Candidate's Dissertation (St. Petersburg, 2002).
16. P. Daly, K. S. H. Le, and C. H. Papas, IEEE Trans. Antennas Propag. **13**, 583 (1965).
17. B. M. Bolotovskiĭ and S. N. Stolyarov, in *Einstein Studies 1978–1979* (Nauka, Moscow, 1983), pp. 173–277.
18. É. G. Doil'nitsina, Yu. B. Zhuravlev, and A. V. Tyukhtin, Vestn. S-Peterb. Univ., Ser. 4: Fiz., Khim., No. 4 (28), 44 (2001).
19. É. G. Doil'nitsina and A. V. Tyukhtin, Izv. Vyssh. Uchebn. Zaved. Radiofiz. **46**, 21 (2003).
20. W. Pauli, *The Theory of Relativity* (Pergamon, Oxford, 1958; Nauka, Moscow, 1983) [translated from German].
21. V. A. Ugarov, *Special Theory of Relativity* (Nauka, Moscow, 1977) [in Russian].

Translated by M. Astrov

Technical Physics, Vol. 49, No. 8, 2004, pp. 1028–1034. Translated from Zhurnal Tekhnicheskoĭ Fiziki, Vol. 74, No. 8, 2004, pp. 74–80.

RADIOPHYSICS

A Possibility to Produce Elliptically Polarized Transition Radiation

B. M. Bolotovskiĭ and A. V. Serov

Lebedev Physical Institute, Russian Academy of Sciences, Moscow, 119991 Russia

Received January 23, 2004

Abstract—Transition radiation produced when a charged particle successively crosses two anisotropically conducting planes is considered. The first plane has the form of a two-dimensional array (grating) made of thin metal wires parallel to the *x* and *y* axes. The second plane is a one-dimensional array whose wires are parallel to the *y* axis. The planes are parallel to each other and perpendicular to the particle trajectory. Transition radiation is shown to be elliptically polarized, the degree of ellipticity and rotation direction being dependent on the direction of radiation, the distance between the arrays, and the particle velocity. *© 2004 MAIK “Nauka/Interperiodica”.*

INTRODUCTION

Transition radiation in isotropic media is known to be linearly polarized [1]. At the normal incidence of a particle onto the interface, the polarization vector lies in the plane that passes through the particle trajectory and the wave vector of the emitted wave. Transition radiation on an anisotropically conducting plane is also linearly polarized [2]. The anisotropically conducting plane was modeled in [2] by a system of thin parallel wires perpendicular to the particle trajectory. It is clear that, if the distance between the wires is much smaller than the radiation wavelength, this system of wires can be regarded as a plane whose conductance is high along the wires and low in the orthogonal direction. It was assumed in [2] that the conductance of the plane is infinitely high along the wires and is equal to zero in the orthogonal direction; an exact solution to the problem under these conditions was obtained. In this case, the electric vector of the transition radiation lies in the plane that passes through the wave vector and the wires.

It is of practical interest to obtain elliptically or circularly polarized radiation. Transition radiation produced when a relativistic charged particle successively crosses two parallel one-dimensional arrays was considered in [3]. The arrays were assumed to consist of parallel metal wires. The array planes were parallel to each other and perpendicular to the charged particle trajectory. The wires of one array were perpendicular to the wires of the other array. It was shown that transition radiation produced in this case is elliptically polarized, the ellipticity and rotation direction being dependent on the direction of the radiation, the distance between the arrays, and the particle velocity.

In this paper, we also consider the radiation produced by a relativistic charged particle successively crossing two anisotropically conducting planes (Fig. 1). However, in contrast to the case considered in [3], the first plane has the form of a two-dimensional array (grating) made of thin metal wires and its conductance is infinitely high in two mutually orthogonal directions (in the *x* and *y* directions), and not in one direction. The second plane is a one-dimensional array whose conductance is infinite in the *y* direction as in [3]. The charged particle moves perpendicular to the array (along the *z* axis) and crosses the first array, producing transition radiation. This radiation can be regarded as the radiation of currents induced in the array by the charged particle flying through it. Because each wire of the array is parallel to the *x* or *y* axis, the induced currents are also parallel to these axes. Consequently, the vector potential that describes radiation of the induced currents also has components parallel to the *x* and *y* axes. Let us place the second diffraction grating at a distance *d* from the first one. Planes of the two gratings are parallel and the wires of the second grating are parallel to the *y* axis. Incident on the second grating are the field of the charged particle and the field produced by the currents induced in the first grating. The currents induced on the

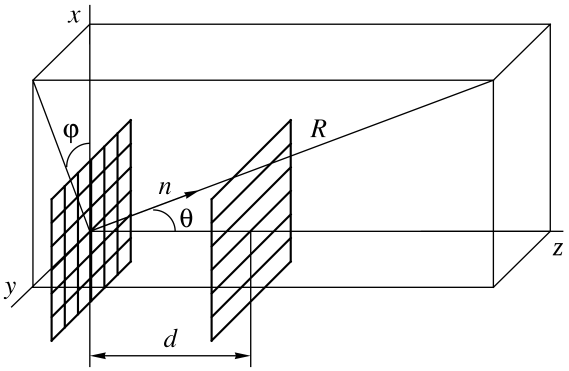

Fig. 1. Geometry of the problem.

second grating by these fields are parallel to the y axis and the radiation produced by these currents is described by the vector potential, which is polarized parallel to the y axis. Thus, after the charge passes through the two gratings, two waves are emitted whose phase difference depends on distance between the gratings and the transit time. Below, we will determine the parameters of these waves. We will show that radiation produced when a charged particle successively crosses the planes is elliptically polarized. The polarization characteristics depend on the particle energy and the distance between the planes.

RADIATION PRODUCED BY A CHARGE WHEN IT CROSSES THE FIRST PLANE

As is known, the field produced by a moving particle is determined by the vector **A** and scalar φ potentials, which can be found from the equations [4]

$$\left(\Delta - \frac{1}{c^2}\frac{\partial^2}{\partial t^2}\right)\mathbf{A} = -\frac{4\pi}{c}\mathbf{j}, \tag{1}$$

$$\left(\Delta - \frac{1}{c^2}\frac{\partial^2}{\partial t^2}\right)\varphi = -4\pi\rho. \tag{2}$$

Let us calculate the field produced after the charge crosses the first array, which lies in the xy plane. The conductance of the $z = 0$ plane in the x and y directions will be assumed to be infinitely high. The conductance in the z direction will be assumed to be zero. Let the charge q move alone the z axis with a velocity v. As follows from Eq. (1), the direction of the vector potential coincides with the direction of the particle motion. Therefore, the vector potential of a particle that moves along the z axis has only one component A_z. The current corresponding to the moving charge is described by

$$j_z = qv\delta(z - vt)\delta(y)\delta(x). \tag{3}$$

Using the Fourier integral expansion of the δ function,

$$\delta(\eta) = \frac{1}{2\pi}\int_{-\infty}^{\infty}\exp i(\xi\eta)d\xi, \tag{4}$$

we rewrite Eq. (1) as

$$\begin{aligned}\left(\Delta - \frac{1}{c^2}\frac{\partial^2}{\partial t^2}\right)A_z &= -\frac{4\pi}{c}qv\delta(z - vt)\delta(y)\delta(x)\\ &= -\frac{qv}{2\pi^2 c}\int\exp i[k_x x + k_y y + k_z(z - vt)]dk_x dk_y dk_z,\end{aligned} \tag{5}$$

where k_x, k_y, and k_z are the projections of the wave vector onto the coordinate axes.

The solution to Eq. (5) is

$$A_z = \frac{qv}{2\pi^2 c}\int\frac{\exp i[k_x x + k_y y + k_z(z - vt)]}{k_x^2 + k_y^2 + k_z^2(1 - \beta^2)}dk_x dk_y dk_z, \tag{6}$$

where $\beta = v/c$ is the reduced particle velocity.

For a uniformly moving charge, the projection of the wave vector onto the direction of motion is $k_z = \omega/v$, where ω is the radiation frequency. Therefore, expression (6) can be written as

$$\begin{aligned}A_z &= \frac{q}{2\pi^2 c}\int\frac{\exp i[k_x x + k_y y + (\omega/v)(z - vt)]}{k_x^2 + k_y^2 + (\omega/v)^2(1 - \beta^2)}dk_x dk_y d\omega\\ &= \int\left[\frac{q}{2\pi^2 c}\int\frac{\exp i[k_x x + k_y y + (\omega/v)z]}{k_x^2 + k_y^2 + (\omega/v)^2(1 - \beta^2)}dk_x dk_y\right]\\ &\quad\times\exp(-i\omega t)d\omega.\end{aligned} \tag{7}$$

The term in the brackets in the integrand is the spectral density $A_{z\omega}$ (Fourier expansion) of the vector potential A_z. Expansions of $A_{z\omega}$ and φ_ω in plane waves $\exp i(k_x x + k_y y + k_z z)$ have the form

$$A_{z\omega} = \frac{q}{2\pi^2 c}\int\frac{\exp i[k_x x + k_y y + (\omega/v)z]}{k_x^2 + k_y^2 + (\omega/v)^2(1 - \beta^2)}dk_x dk_y, \tag{8}$$

$$\varphi_\omega = \frac{q}{2\pi^2 v}\int\frac{\exp i[k_x x + k_y y + (\omega/v)z]}{k_x^2 + k_y^2 + (\omega/v)^2(1 - \beta^2)}dk_x dk_y. \tag{9}$$

The field defined by formulas (8) and (9) is incident on the array and induces currents on the wires. Since the wires of the first array are parallel to the x and y axes, the currents are induced by the E_x and E_y components of the electric field of the uniformly moving charge. Let us write the $E_{x\omega}$ and $E_{y\omega}$ components. The spectral density components $A_{x\omega}$ and $A_{y\omega}$ of the vector potential are equal to zero. Therefore, the electric field components can be obtained by taking derivatives of the scalar potential φ_ω with respect to the corresponding coordinates:

$$\begin{aligned}E_{x\omega}^{(1)} &= -\frac{\partial\varphi_\omega}{\partial x}\\ &= -\frac{iq}{2\pi^2 v}\int\frac{k_x\exp i[k_x x + k_y y + (\omega/v)z]}{k_x^2 + k_y^2 + (\omega/v)^2(1 - \beta^2)}dk_x dk_y,\end{aligned} \tag{10}$$

$$\begin{aligned}E_{y\omega}^{(1)} &= -\frac{\partial\varphi_\omega}{\partial y}\\ &= -\frac{iq}{2\pi^2 v}\int\frac{k_y\exp i[k_x x + k_y y + (\omega/v)z]}{k_x^2 + k_y^2 + (\omega/v)^2(1 - \beta^2)}dk_x dk_y.\end{aligned} \tag{11}$$

The superscript indicates that these formulas refer to the first array. The fields induce currents in the wires. We denote the densities of these currents as $j_x^{(1)}(x, y)$

and $j_y^{(1)}(x, y)$. Let us also represent the currents in the form of the Fourier expansion,

$$j_x^{(1)}(x, y) = \frac{1}{(2\pi)^2} \times \int_{-\infty}^{\infty} j_{x\omega}^{(1)}(k_x, k_y)\exp i(k_x x + k_y y)\,dk_x dk_y, \tag{12}$$

$$j_y^{(1)}(x, y) = \frac{1}{(2\pi)^2} \times \int_{-\infty}^{\infty} j_{y\omega}^{(1)}(k_x, k_y)\exp i(k_x x + k_y y)\,dk_x dk_y, \tag{13}$$

where $j_{x\omega}^{(1)}(k_x, k_y)$ and $j_{y\omega}^{(1)}(k_x, k_y)$ are to be determined from boundary conditions on the array surface.

Let us calculate vector potentials $A_x^{'(1)}$ and $A_y^{'(1)}$ of the radiation field produced by currents $j_x^{(1)}$ and $j_y^{(1)}$. Equations for the vector potentials $A_x^{'(1)}$ and $A_y^{'(1)}$ have the following form:

$$\left(\Delta - \frac{1}{c^2}\frac{\partial^2}{\partial t^2}\right)A_x^{'(1)} = \frac{4\pi}{c}j_x^{(1)} = -\frac{2}{c} \times \int \exp i(k_x x + k_y y + k_z z - \omega t)\, j_{x\omega}^{(1)}(k_x, k_y)\,dk_x dk_y dk_z d\omega, \tag{14}$$

$$\left(\Delta - \frac{1}{c^2}\frac{\partial^2}{\partial t^2}\right)A_y^{'(1)} = \frac{4\pi}{c}j_y^{(1)} = -\frac{2}{c} \times \int \exp i(k_x x + k_y y + k_z z - \omega t)\, j_{y\omega}^{(1)}(k_x, k_y)\,dk_x dk_y dk_z d\omega. \tag{15}$$

Solutions to these equations can be represented as

$$A_x^{'(1)} = \frac{2}{c} \times \int \frac{\exp i(k_x x + k_y y + k_z z - \omega t)}{k_x^2 + k_y^2 + k_z^2 - (\omega/v)^2}\, j_{x\omega}^{(1)}(k_x, k_y)\,dk_x dk_y dk_z d\omega, \tag{16}$$

$$A_y^{'(1)} = \frac{2}{c} \times \int \frac{\exp i(k_x x + k_y y + k_z z - \omega t)}{k_x^2 + k_y^2 + k_z^2 - (\omega/v)^2}\, j_{y\omega}^{(1)}(k_x, k_y)\,dk_x dk_y dk_z d\omega. \tag{17}$$

Denominators of integrands in Eqs. (16) and (17) can be written in the form

$$k_x^2 + k_y^2 + k_z^2 - (\omega/v)^2 = \left(k_z - \sqrt{(\omega/v)^2 - k_x^2 - k_y^2}\right)\left(k_z + \sqrt{(\omega/v)^2 - k_x^2 - k_y^2}\right),$$

which shows that the integrands have poles at the points $k_z = \pm\sqrt{(\omega/v)^2 - k_x^2 - k_y^2}$. Let us integrate with respect to k_z, passing around the poles of the integrands in compliance with the radiation condition (i.e., the solutions must consist of waves that travel away from the array). Then, we obtain

$$A_{x\omega}^{'(1)} = i\frac{2\pi}{c}\int \exp i\left(k_x x + k_y y + \sqrt{(\omega/c)^2 - k_x^2 - k_y^2}\,|z| - \omega t\right) \times j_{x\omega}^{(1)}(k_x, k_y)\frac{dk_x dk_y d\omega}{\sqrt{(\omega/c)^2 - k_x^2 - k_y^2}}, \tag{18}$$

$$A_{y\omega}^{'(1)} = i\frac{2\pi}{c}\int \exp i\left(k_x x + k_y y + \sqrt{(\omega/c)^2 - k_x^2 - k_y^2}\,|z| - \omega t\right) \times j_{y\omega}^{(1)}(k_x, k_y)\frac{dk_x dk_y d\omega}{\sqrt{(\omega/c)^2 - k_x^2 - k_y^2}}. \tag{19}$$

Knowing $A_{x\omega}^{'(1)}$ and $A_{y\omega}^{'(1)}$, we can determine the $E_{x\omega}^{'(1)}$ and $E_{y\omega}^{'(1)}$ components of the electric field produced by the first array:

$$E_{x\omega}^{'(1)} = -2\pi\int \exp i\left(k_x x + k_y y + \sqrt{(\omega/c)^2 - k_x^2 - k_y^2}\,|z|\right) \times \{[(\omega/c)^2 - k_x^2]j_{x\omega}^{(1)}(k_x, k_y) - k_x k_y j_{y\omega}^{(1)}(k_x, k_y)\} \times \frac{dk_x dk_y}{\omega\sqrt{(\omega/c)^2 - k_x^2 - k_y^2}}, \tag{20}$$

$$E_{y\omega}^{'(1)} = -2\pi\int \exp i\left(k_x x + k_y y + \sqrt{(\omega/c)^2 - k_x^2 - k_y^2}\,|z|\right) \times \{[(\omega/c)^2 - k_y^2]j_{y\omega}^{(1)}(k_x, k_y) - k_x k_y j_{x\omega}^{(1)}(k_x, k_y)\} \times \frac{dk_x dk_y}{\omega\sqrt{(\omega/c)^2 - k_x^2 - k_y^2}}. \tag{21}$$

The x and y electric field components must turn to zero on the array surface:

$$E_{x\omega}^{'(1)} + E_{x\omega}^{(1)} = 0, \quad E_{y\omega}^{'(1)} + E_{y\omega}^{(1)} = 0, \quad z = 0.$$

If we take expressions (10) and (11) for $E_{x\omega}^{(1)}$ and $E_{y\omega}^{(1)}$ and expressions (20) and (21) for $E_{x\omega}^{'(1)}$ and $E_{y\omega}^{'(1)}$, the following system of two equations will be obtained:

$$-\frac{iq}{2\pi^2 v}\frac{k_x}{k_x^2 + k_y^2 + (\omega/v)^2(1 - \beta^2)} = \frac{[(\omega/c)^2 - k_x^2]j_{x\omega}^{(1)} - k_x k_y j_{y\omega}}{\omega\sqrt{(\omega/c)^2 - k_x^2 - k_y^2}}, \tag{22}$$

$$-\frac{iq}{2\pi^2 v}\frac{k_y}{k_x^2+k_y^2+(\omega/v)^2(1-\beta^2)} = \frac{[(\omega/c)^2-k_y^2]j_{y\omega}^{(1)}-k_xk_yj_{x\omega}}{\omega\sqrt{(\omega/c)^2-k_x^2-k_y^2}}, \tag{23}$$

from these equations, we can determine the Fourier components $j_{x\omega}^{(1)}$ and $j_{y\omega}^{(1)}$ of currents induced in the array. By solving this system, we obtain

$$j_{x\omega}^{(1)} = -\frac{iq}{4\pi^3 v} \times\frac{\omega k_x}{[k_x^2+k_y^2+(\omega/v)^2(1-\beta^2)]\sqrt{(\omega/c)^2-k_x^2-k_y^2}}, \tag{24}$$

$$j_{y\omega}^{(1)} = -\frac{iq}{4\pi^3 v} \times\frac{\omega k_y}{[k_x^2+k_y^2+(\omega/v)^2(1-\beta^2)]\sqrt{(\omega/c)^2-k_x^2-k_y^2}}. \tag{25}$$

By substituting the expressions for $j_{x\omega}^{(1)}$ and $j_{y\omega}^{(1)}$ into expressions (18) and (19), we obtain the vector potentials

$$A'^{(1)}_{x\omega} = -\frac{q}{2\pi c v} \times\int\frac{k_x\omega\exp i(k_xx+k_yy+\sqrt{(\omega/c)^2-k_x^2-k_y^2}|z|)}{[k_x^2+k_y^2+(\omega/v)^2(1-\beta^2)]((\omega/c)^2-k_x^2-k_y^2)}dk_xdk_y, \tag{26}$$

$$A'^{(1)}_{y\omega} = -\frac{q}{2\pi c v} \times\int\frac{k_y\omega\exp i(k_xx+k_yy+\sqrt{(\omega/c)^2-k_x^2-k_y^2}|z|)}{[k_x^2+k_y^2+(\omega/v)^2(1-\beta^2)]((\omega/c)^2-k_x^2-k_y^2)}dk_xdk_y. \tag{27}$$

Formulas (26) and (27) determine the radiation produced by a charge passing through the array located in the plane $z = 0$. The total field in the space between the first and second arrays (i.e., in the space between the planes $z = 0$ and $z = d$) is a superposition of radiation $A'^{(1)}_{x\omega}$ and $A'^{(1)}_{y\omega}$ and the fields $A^{(1)}_{x\omega}$ and $A^{(1)}_{y\omega}$ produced by the uniformly moving charge. This total field is incident on the second array and excites currents on it.

Let us consider the field at a long distance from the array. The electric field is related to the vector potential as [4]

$$\mathbf{E}_\omega = \frac{c}{i\omega}[\mathbf{k}[\mathbf{k}\mathbf{A}_\omega]].$$

After some transformations, we obtain the following formulas for the electric field components:

$$E'^{(1)}_{x\omega} = \frac{c}{i\omega}\{-[(\omega/c)^2-k_x^2]A'^{(1)}_{x\omega}+k_xk_yA'^{(1)}_{y\omega}\}, \tag{28}$$

$$E'^{(1)}_{y\omega} = \frac{c}{i\omega}\{-[(\omega/c)^2-k_y^2]A'^{(1)}_{y\omega}+k_xk_yA'^{(1)}_{x\omega}\}, \tag{29}$$

$$E'^{(1)}_{z\omega} = \frac{c}{i\omega}\sqrt{(\omega/c)^2-k_x^2-k_y^2}\{k_xA'^{(1)}_{x\omega}+k_yA'^{(1)}_{y\omega}\}. \tag{30}$$

Let us calculate the integrals in expressions (26) and (27) by the stationary phase method. This method for evaluating integrals of rapidly oscillating functions yields the formula [5]

$$\int_{-\infty}^{\infty}F(\xi,\eta)\exp if(\xi,\eta)d\xi d\eta = \frac{2\pi i}{\sqrt{\alpha_1\alpha_3-\alpha_2^2}}F(\xi_0,\eta_0)\exp if(\xi_0,\eta_0), \tag{31}$$

where ξ_0, η_0 is the root of equation $df(\xi,\eta) = 0$ and $\alpha_1 = f''_{\xi^2}$, $\alpha_2 = f''_{\xi\eta}$, and $\alpha_3 = f''_{\eta^2}$ at $\xi = \xi_0$ and $\eta = \eta_0$.

After calculating the vector potentials and substituting them into expressions (28)–(30), we obtain the following formulas for the electric field components

$$E'^{(1)}_{x\omega} = \frac{q}{c}\frac{\beta\sin\theta\cos\theta\cos\varphi}{1-\beta^2\cos^2\theta}\frac{\exp\left(i\frac{\omega}{c}\right)R}{R}, \tag{32}$$

$$E'^{(1)}_{y\omega} = \frac{q}{c}\frac{\beta\sin\theta\cos\theta\sin\varphi}{1-\beta^2\cos^2\theta}\frac{\exp\left(i\frac{\omega}{c}\right)R}{R}, \tag{33}$$

$$E'^{(1)}_{z\omega} = \frac{q}{c}\frac{\beta\sin^2\theta}{1-\beta^2\cos^2\theta}\frac{\exp\left(i\frac{\omega}{c}\right)R}{R}; \tag{34}$$

here, R is the distance from the origin to the observation point, $x = R\sin\theta\cos\varphi$, $y = R\sin\theta\cos\varphi$, $z = R\cos\theta$, θ is the angle between the wave vector and the z axis, and φ is the azimuth angle.

A comparison of expressions (32)–(34), which describe the angular spectrum distributions of the electric field of transition radiation, with the results obtained earlier [6], shows that the field produced by a particle that crosses the two-dimensional array (grating) is the same as the field excited by a particle emitted from a conducting plane. Further calculations are therefore also valid for the case when the first plane is a metal foil whose conductance is independent of direction.

RADIATION PRODUCED BY CURRENTS ON THE SECOND PLANE

Because the conductance of the second array is nonzero only in the y direction, the induced currents have the $j_y^{(2)}$ component alone. In turn, currents $j_y^{(2)}$ produce the field, which can be described by the vector potential $A_y^{\prime(2)}$,

$$A_{y\omega}^{\prime(2)} = i\frac{2\pi}{c}$$

$$\times\int \exp i\left(k_x x + k_y y + \sqrt{(\omega/c)^2 - k_x^2 - k_y^2}|z-d|\right) \quad (35)$$

$$\times j_{y\omega}^{(2)}(k_x, k_y)\frac{dk_x dk_y}{\sqrt{(\omega/c)^2 - k_x^2 - k_y^2}}.$$

This formula is completely similar to formulas (18) and (19) for the field excited by the first array with the only difference that, in the first case, the field is produced by the currents that flow in the first array in the x and y directions and the vector potential has the components $A_{x\omega}^{\prime(1)}$ and $A_{y\omega}^{\prime(1)}$, while in the second case, the field is produced only by the current that flows in the y direction and, hence, the vector potential has the component $A_{y\omega}^{\prime(2)}$ alone. Recall that the second array lies in the plane $z = d$.

On the surface of the second array, the y component of the total electric field must turn to zero; i.e., the following equality must be valid:

$$E_{y\omega}^{\prime(1)} + E_{y\omega}^{(1)} + E_{y\omega}^{\prime(2)} = 0, \quad z = d.$$

This condition makes it possible to determine the currents induced on the array. Indeed, if the currents induced in the second array have only one Fourier component $j_{y\omega}^{(2)(k_x, k_y)}$, the electric field $E_{y\omega}^{\prime(2)}$ excited by these currents can be written as

$$E_{y\omega}^{\prime(2)} = -2\pi$$

$$\times\int \exp i\left(k_x x + k_y y + \sqrt{(\omega/c)^2 - k_x^2 - k_y^2}|z-d|\right) \quad (36)$$

$$\times j_{y\omega}^{(2)}(k_x, k_y)\frac{[(\omega/c)^2 - k_y^2]dk_x dk_y}{\omega\sqrt{(\omega/c)^2 - k_x^2 - k_y^2}}.$$

Let us also write the y component of the electric field excited by the field of the uniformly moving charge and by the field of the first array. The superposition of these fields can be written as

$$E_{y\omega}^{\prime(1)} + E_{y\omega}^{(1)} = -\frac{q}{2\pi^2 v}\int\frac{k_y \exp i(k_x x + k_y y)dk_x dk_y}{[k_x^2 + k_y^2 + (\omega/v)^2(1-\beta^2)]}$$

$$\times\left[\exp i\frac{\omega}{v}z + \frac{-(\omega/c)^2 + k_x^2 + k_y^2}{k_z^2} \quad (37)\right.$$

$$\left.\times \exp i\sqrt{(\omega/c)^2 - k_x^2 - k_y^2}|z|\right].$$

Here, the first term in the brackets refers to the field of the uniformly moving charge, and the second term, to the field of the first array. Clearly, a sum of expressions (36) and (37) must turn to zero at $z = d$. This condition yields the currents induced in the second array:

$$j_{y\omega} = -\frac{q}{4\pi^3 v}\frac{ik_y\sqrt{(\omega/c)^2 - k_x^2 - k_y^2}}{[k_x^2 + k_y^2 + (\omega/v)^2(1-\beta^2)]((\omega/c)^2 - k_y^2)} \quad (38)$$

$$\times\left[\exp i\frac{\omega}{v}d - \exp i\sqrt{(\omega/c)^2 - k_x^2 - k_y^2}d\right].$$

By substituting expression (38) into (35), we find the vector potential of the radiation field produced by the second array:

$$A_{y\omega}^{\prime(2)} = -\frac{q}{2\pi c v}$$

$$\times\int\frac{k_y\omega \exp i\left(k_x x + k_y y + \sqrt{(\omega/c)^2 - k_x^2 - k_y^2}|z-d|\right)}{[k_x^2 + k_y^2 + (\omega/v)^2(1-\beta^2)]((\omega/c)^2 - k_x^2)} \quad (39)$$

$$\times\left[\exp i\frac{\omega}{v}d - \exp i\sqrt{(\omega/c)^2 - k_x^2 - k_y^2}d\right]dk_x dk_y.$$

The field in the space behind the second array consists of three components: the field produced by the uniformly moving charge; the field produced by charges on the second array, which is described by the vector potentials $A_{x\omega}^{\prime(1)}$ and $A_{y\omega}^{\prime(1)}$; and the field excited by currents flowing in the second array, which is described by the vector potential $A_{y\omega}^{\prime(2)}$.

Let us consider the field at long distances ($z \gg d$) from the array. We consider the distances at which the field of the uniformly moving charge does not interfere with the fields radiated by the arrays. We calculate the potentials by the stationary phase method and use expressions (28)–(30) for the electric field components to obtain

$$E_{x\omega}^{\prime(1+2)} = \frac{q}{c}\frac{\beta\sin\theta\cos\theta\cos\varphi}{1-\beta^2\cos^2\theta}$$

$$\times\left(1 + \frac{\sin^2\theta\sin^2\varphi}{1-\sin^2\theta\sin^2\varphi}C\right)\frac{\exp\left(i\frac{\omega}{c}R\right)}{R}, \quad (40)$$

$$E'^{(1+2)}_{y\omega} = \frac{q}{c}\frac{\beta\sin\theta\cos\theta\sin\varphi}{1-\beta^2\cos^2\theta}$$

$$\times\exp i\frac{\omega}{v}d(1-\beta\cos\theta)\frac{\exp\left(i\frac{\omega}{c}R\right)}{R}, \tag{41}$$

$$E'^{(1+2)}_{z\omega} = \frac{q}{c}\frac{\beta\sin^2\theta}{1-\beta^2\cos^2\theta}$$

$$\times\left(1+\frac{\cos^2\theta\sin^2\varphi}{1-\sin^2\theta\sin^2\varphi}C\right)\frac{\exp\left(i\frac{\omega}{c}R\right)}{R}. \tag{42}$$

Expressions (40)–(42) describe a spherical wave. The components of this wave are seen to be inversely proportional to $(1 - \beta^2\cos^2\theta)$; i.e., when the charge moves at a relativistic velocity, radiation is concentrated in a narrow range of angles θ, approximately $1/\gamma$ wide, where $\gamma = 1/\sqrt{1-\beta^2}$. The second array exerts no influence on the amplitude of the angular spectrum distribution of the E_y field component, but shifts its phase by $\alpha = (\omega/v)d(1 - \beta\cos\theta)$. As the distance d between the arrays decreases, the effect of the second array on the field distribution becomes weaker. In the limiting case of $d = 0$, the field described by expressions (40)–(42) is the same as the transition radiation field excited by the particle when it crosses the first array.

In the relativistic case, when $\gamma \gg 1$ and radiation is considered at angles $\theta \le 1/\gamma$, the terms proportional to $\sin^2\theta$ in the expressions for the field can be neglected. In this case, expressions (40)–(42) are transformed to

$$E'^{(1+2)}_{x\omega} = \frac{q}{c}\frac{\beta\sin\theta\cos\theta\cos\varphi}{1-\beta^2\cos^2\theta}\frac{\exp\left(i\frac{\omega}{c}R\right)}{R}, \tag{43}$$

$$E'^{(1+2)}_{y\omega} = \frac{q}{c}\frac{\beta\sin\theta\cos\theta\sin\varphi}{1-\beta^2\cos^2\theta}$$

$$\times\exp i\frac{\omega}{v}d(1-\beta\cos\theta)\frac{\exp\left(i\frac{\omega}{c}R\right)}{R}. \tag{44}$$

These expressions show in particular that, at the azimuth angle of $\varphi = \pm(\pi/4)$ and $\pm(3\pi/4)$, fields E_x and E_y are equal in magnitude and shifted in phase relative to each other by $\alpha = (\omega/v)d(1 - \beta\cos\theta)$. Radiation is circularly polarized when the field E_x is shifted in phase with respect to the field E_y by $\alpha = (\pi/2) + \pi n$ (where $n = 0, 1, 2, \ldots$) and is linearly polarized when $\alpha = \pi + \pi n$. At other phase shifts, radiation is polarized elliptically.

At $\varphi = 0$ or π, the electric field of radiation lies in the xz plane; at $\varphi = \pm\pi/2$, this field lies in the yz plane. At these azimuth angles, the radiation field is linearly polarized at any distance between the arrays.

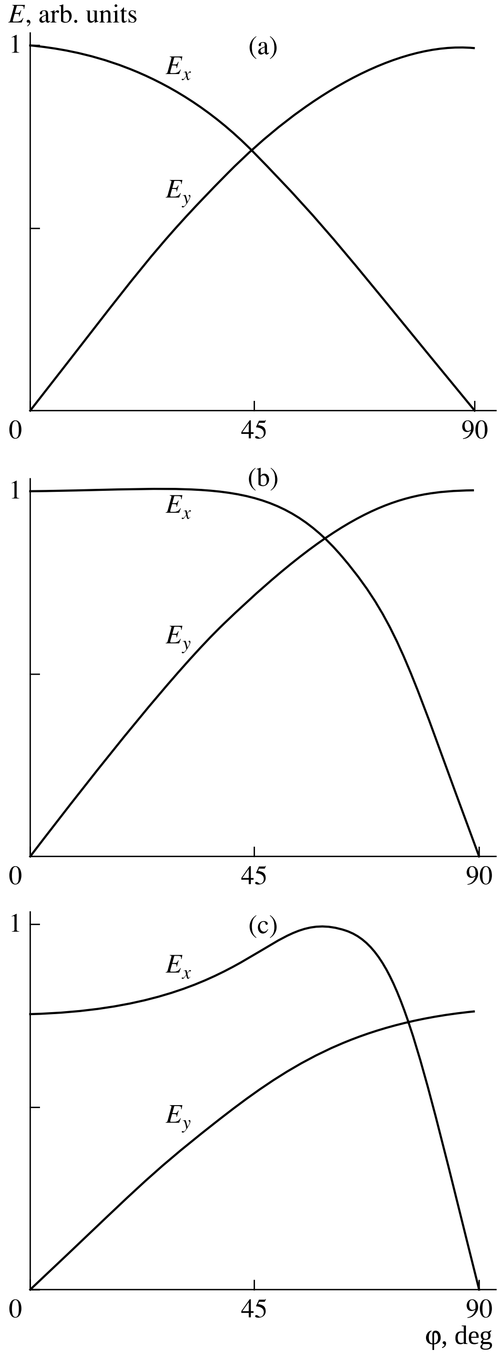

Fig. 2. Electric field intensities E_x and E_y of the wave versus azimuth angle φ at the angle $\theta = 1/\gamma =$ (a) 6°, (b) 45°, and (c) 60°. The reduced particle energy is $\gamma = 10$.

Because the phase shift between the fields E_x and E_y depends on angle θ, at given electron energy $\gamma = 1/\sqrt{1-\beta^2}$, distance d between the arrays, and wavelength λ, circularly polarized transition radiation will be observed at the angles

$$\varphi = \pm(\pi/4), \pm(3\pi/4),$$

$$\theta = \arccos\left[\frac{\gamma}{\sqrt{\gamma^2 - 1}} - \frac{\lambda}{2d}\left(\frac{1}{2} + n\right)\right].$$

As follows from expressions (40) and (42), at large observation angles $\theta \gg 1/\gamma$, a significant contribution to the electric field intensities E_x and E_y comes from the second terms. Figure 2 plots E_x versus azimuth angle φ calculated from formula (40) for various angles θ at a reduced particle energy of $\gamma = 10$. For the sake of comparison, the figure also plots the sine curves $E_y(\varphi)$. Figures 2a–2c refer to $\theta = 1/\gamma = 6°$, 45°, and 60°, respectively. As the angle increases, the difference between the $E_x(\varphi)$ curve and the cosine function is seen to become more and more pronounced.

CONCLUSIONS

Expressions that describe the field produced by a relativistic particle when it crosses two anisotropically conducting planes are obtained. The field of radiation emitted when the particle crosses the plane with a higher conductance in two mutually perpendicular directions is found. At certain wavelengths, this field coincides with the field of transition field emitted by a charged particle that exits from a metal foil, which has an isotropic conductance. In the case when the second plane has an anisotropic conductance, transition radiation is polarized elliptically.

REFERENCES

1. V. L. Ginzburg and I. M. Frank, Zh. Éksp. Teor. Fiz. **16**, 15 (1946).
2. K. A. Barsukov and L. G. Naryshkina, Izv. Vyssh. Uchebn. Zaved. Radiofiz. **8**, 936 (1965).
3. B. M. Bolotovskiĭ and A. V. Serov, Kratk. Soobshch. Fiz., No. 7, 29 (2003).
4. L. D. Landau and E. M. Lifshitz, *Course of Theoretical Physics*, Vol. 2: *The Classical Theory of Fields* (Nauka, Moscow, 1988; Pergamon, Oxford, 1975).
5. M. I. Kontorovich and Yu. K. Murav'ev, Zh. Tekh. Fiz. **22**, 394 (1952).
6. V. L. Ginzburg and V. N. Tsytovich, *Transient Radiation and Transient Scattering* (Nauka, Moscow, 1984) [in Russian].

Translated by A. Khzmalyan

Technical Physics, Vol. 49, No. 8, 2004, pp. 1035–1039. Translated from Zhurnal Tekhnicheskoĭ Fiziki, Vol. 74, No. 8, 2004, pp. 81–85.
Original Russian Text Copyright © 2004 by Banishev, Golubev, Kremnev.

SURFACES, ELECTRON AND ION EMISSION

Effect of the Ambient Atmosphere and the Gas Type on Generation of Defects and Destruction of Silicon Surface under the Action of Laser Pulses

A. F. Banishev, V. S. Golubev, and A. Yu. Kremnev

Institute for Problems in Laser and Information Technology, Russian Academy of Sciences,
Shatura, Moscow oblast, 140700 Russia
e-mail: banishev@laser.nictl.msk.su

Received November 10, 2003

Abstract—Solid-phase destruction of the silicon surface under the action of submicrosecond laser pulses in the atmosphere of various active (oxygen, nitrogen, carbon dioxide) and inert gases (helium, argon, krypton) is studied. It is found that the surface destruction threshold (the threshold of formation of inhomogeneities in the surface relief) is lowest in helium atmosphere and highest in krypton atmosphere. A mechanism for inhomogeneity growth and relaxation is proposed. *© 2004 MAIK "Nauka/Interperiodica".*

INTRODUCTION

It is well known that the action of high-power laser radiation on semiconductors leads to a substantial increase in the diffusion coefficients of atoms [1]. Two aspects (thermal and athermal) can be singled out in the effect of laser radiation on diffusion. The thermal effect is associated with the possibility of creating huge temperature gradients and thermal stresses; according to a number of authors [2–7]), this is the reason for enhanced diffusion. The athermal effect of laser radiation is associated with the excitation of electronic states such as excitons and electron–hole plasmas localization of excitations of these states at an impurity may substantially increase the impurity diffusion rate [8–12]. Some authors associate high diffusion rates during laser annealing with local melting of the surface [13].

In spite of the fact that laser-stimulated diffusion was studied by many authors, the nature of anomalous enhancement of diffusion is not quite clear. The effect of laser-induced nonequilibrium structural defects on the diffusion rate of impurities has been studied insufficiently. The high concentration of laser-induced vacancies and interstices ($\sim 10^{21}$–10^{22} cm^{-3}) attained at the instant of action of a laser pulse may noticeably change the diffusion of impurity atoms, which is governed by the vacancion or interstitial mechanism. It is also known [14, 15] that dislocations (grain and phase boundaries) are the routes for enhanced diffusion for intrinsic defects and impurity atoms. The coefficients D_d of diffusion over dislocations may exceed the bulk diffusion coefficients by several orders of magnitude.

Solid-phase destruction of the silicon surface under the action of submicrosecond laser pulses in air was studied in [16]. It was found that a laser pulse initiates a jump in the intensity of scattered radiation from a probe laser. The duration (at half-amplitude) of the anomalous scattering signal was ~0.5 s, which is six orders of magnitude higher than the duration of the acting laser pulse. However, it was shown in [17] that the action of solitary pulses on a sample in vacuum does not lead to visible (according to the results of diagnostic methods used) structural changes of the surface. Surface destruction is observed only in the case of action of many pulses, is of accumulation type, and is associated with the generation and growth of dislocations.

The results of these experiments unambiguously indicate that the presence of the surrounding gas atmosphere stimulates the formation of scattering inhomogeneities in the silicon surface layer under the action of laser pulses.

In this study, we analyze the effect of the ambient atmosphere and the type of the gas on the threshold of intense defect formation and destruction of the silicon surface under the action of laser pulses. The anomalies observed in the scattering of probe radiation are associated with the formation of local inhomogeneities (scattering centers) in the silicon surface layer, which represent the system dislocation + cloud of impurity atoms.

EXPERIMENTAL RESULTS AND DISCUSSION

The experiments were carried out on the setup shown in Fig. 1. A sample of monocrystalline dislocation-free silicon with a mirror-polished surface oriented along the (100) crystallographic axis was placed into a vacuum chamber in which the pressure could be varied from 10^{-2} Torr to 1 atm. The experiments were made in vacuum and in the atmosphere of various gases, both active (oxygen, nitrogen, or carbon dioxide) and inert (helium, argon, and krypton), and the gas pressure was

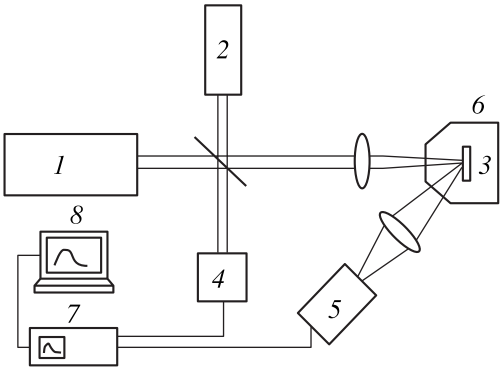

Fig. 1. Block diagram of experimental setup: (*1*) Nd : YAG laser, (*2*) He–Ne probe laser; (*3*) sample, (*4*) photodetector, (*5*) monochromator, (*6*) vacuum chamber, (*7*) oscilloscope, and (*8*) computer.

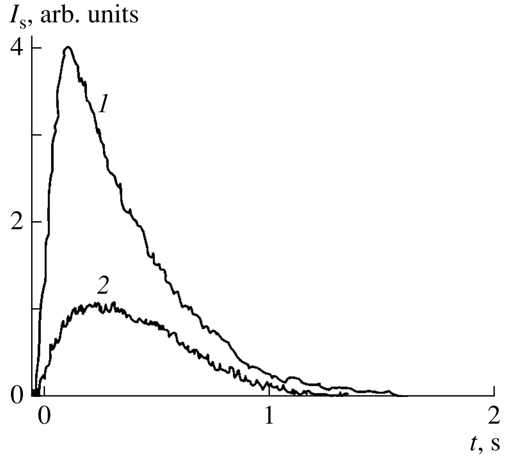

Fig. 2. Variation of scattering of a probe beam emitted by a He–Ne laser at the silicon surface, caused by the action of a Nd : YAG laser pulse ($I = 2.25 \times 10^6$ W cm^{-2}, $P \approx 1$ atm): in helium atmosphere (*1*) and in krypton atmosphere (*2*).

$P_1 \approx 1$ atm. The sample surface was exposed to pulses from a Nd : YAG laser with a pulse energy of $E \approx 0.5$–1.0 mJ and a pulse duration of $\tau \approx 3 \times 10^{-7}$ s. Laser radiation was focused as a spot $d \approx 0.3$–1.0 mm in diameter at the sample surface. Irradiation was carried out by pulses with a power density below the surface-melting threshold. Probing of the exposed area was carried out by a He–Ne probe laser beam. Scattered radiation from the probe laser was detected at an angle $\alpha \approx 45°$ sample surface.

By way of example, Fig. 2 shows oscillograms describing the variation of the radiation intensity of the He–Ne probe laser scattered by the silicon surface exposed to the Nd : YAG laser pulses in atmospheres of helium and krypton. It can be seen from the figure that, the action of a laser pulse results in a jumpwise increase in scattering intensity I_s; the duration of the scattering signal amounts to $t \approx 0.2$–0.5 s, which is almost six orders of magnitude larger than the duration of a Nd : YAG laser pulse acting on the surface. The peak of the scattering signal is attained $t^+ \approx 0.1$–0.2 s after the termination of the Nd : YAG laser pulse. The pulse decay time is $t^- \approx 0.2$–0.3 s after the termination of the Nd : YAG laser pulse. According to [16], each next exposure of the same area of the surface leads to a rapid decrease in the amplitude of the scattered radiation signal. With decreasing pressure in the chamber, the intensity of scattered radiation also decreases rapidly and the signal disappears almost completely at $P \approx 10^{-1}$ Torr [16].

The enhancement of scattering indicates the emergence of inhomogeneities in the surface relief (which was initially flat and mirror finished) as a result of action of the Nd : YAG laser pulse. The main reason for the change in the surface relief in the solid phase can be associated with thermal deformation and deformation due to generation of a considerable concentration of structural defects in the surface layer. Thermal deformation is due to heating of the surface layer; since the temperature of the surface rapidly decreases (the cooling time $t_1 \sim \alpha^{-2}\chi^{-1} \approx 10^{-7}$ s, which is much smaller than the duration of the scattering signal) after the termination of a laser pulse, the thermal deformations must also rapidly decrease after the termination of the laser pulse. Consequently, the existence of such a long scattering signal is difficult to explain by thermal deformations of the surface. The changes in the surface relief associated with the generation of defects and their subsequent slow recombination in all probability cannot be a reason for the observed effect since no scattering jump is observed in vacuum, while heating and generation of defects take place. It was noted in [17] that an increase in the intensity of radiation scattered from the silicon surface in vacuum is observed only in the case of multiple action of laser pulses and is associated with the generation and growth of dislocations. Consequently, the jump in the scattering intensity under the action of a solitary pulse in air is probably associated with the diffusion of gas atoms to the surface layer. For this reason, it is interesting to study the effect of various gases (such as oxygen, nitrogen, and carbon dioxide) contained in air and capable of forming chemical compounds with silicon at high temperatures as well as inert gases (such as helium, argon, and krypton), which do not form any compounds.

Figure 3 shows the variation of the scattered radiation amplitude as a result of irradiation of the silicon surface with submicrosecond laser pulses in the atmosphere of different gases. According to the data from the literature, all the gases chosen here (except nitrogen) occupy interstitial positions in silicon and diffuse in accordance with the direct interstitial mechanism. It is known that interstitial atoms in silicon are characterized by a high mobility.

It can be seen that, the irradiation conditions being the same, the scattering amplitude in the helium atmosphere is 3–4 times higher than in the remaining gases. For other gases, a tendency of the scattering amplitude to decrease is observed in the following sequence: O_2, N_2, CO_2, Ar, and Kr. Figure 4 shows the thresholds $I_{\text{th.las}}$ for the emergence of scattering signals in increasing order. It can be seen from the figure that the value of $I_{\text{th.las}}$ in the helium atmosphere is much lower (by 25–35%) than in the remaining gases. It should be recalled that the chosen gases differ from one another in atomic size (by a factor of several units), chemical activity, solubility (by several orders of magnitude), and diffusion coefficient (by several orders of magnitude).

The above results show that the threshold for the formation of inhomogeneities in the surface relief and the "scattering" properties of these inhomogeneities depend on the type of surrounding gas. The most probable reason for the growth of inhomogeneities may be diffusion of the surrounding gas to the surface layer enriched in defects. We can propose the following model to explain the observed phenomenon. The action of a laser pulse leads to heating of the surface layer. Gas diffusion to the surface layer and intense generation of structural defects (vacancies and interstices) are activated simultaneously. At the same time, generation and growth of dislocations and gas diffusion along dislocation tubes to the bulk of the crystal take place. Thus, as a result of action of laser radiation, an elevated concentration of defects (impurities, vacancies, and interstices) is formed in the surface layer of thickness Δz as well as the corresponding gradients of temperature and concentration directed to the bulk of the crystal.

The heating and high concentration of point defects lead to a deformation (bulging) of the surface. In addition, the formation and growth of macrodefects (pores, dislocations, and microcracks) are also possible. Consequently, the scattering of probe radiation in this case can be caused by both the bulging of the surface as a result of joint action of heating and accumulation of point defects and the growth of local inhomogeneities in the surface layer, viz., macrodefects of diameter $d \sim \lambda$, where $\lambda = 0.63$ μm is the wavelength of the probe laser. However, in our detection geometry ($\alpha \approx 45°$), scattered radiation from the bulged surface is not detected since the scattering angles $\varphi_s \sim \alpha h(t)\Delta T/r_0$ (α represents the thermal expansion coefficient, ΔT is the temperature of the surface, and h and r_0 are the thickness and the radius of the heated area, $h \ll r_0$) are much smaller than the detection angle; i.e., $\varphi_s \ll \varphi \approx 45°$. It is important to note that, irrespective of the object scattering the probe beam, a jump in scattering is observed only in the presence of an ambient atmosphere, indicating the decisive role of diffusion of gas atoms to the surface layer. In our opinion, the elevated concentration of intrinsic defects in the surface layer is a factor of fundamental importance, which facilitates an increase in the flux of diffusing gas (impurities) to the surface layer.

After the termination of the laser pulse, the temperature of the surface rapidly decreases; as a result, the surface layer is supersaturated with impurity (gas) atoms and structural defects. The relaxation of density of defects begins due to their mutual annihilation and well as their flow to dislocations and to the surface. It can be seen from Fig. 2. That the scattering signal continues to increase for a certain time period following the laser pulse and then decreases. Such an increase in scattering supports the opinion that local inhomogeneities grow and serve as scattering centers for radiation. Dislocations may serve as centers for nucleation of inhomogeneities, while the growth of inhomogeneities can be caused by the flow of impurity atom and defects to them. It is well known that a dislocation possesses long-range forces and interacts with impurity atoms and defects located in its neighborhood. For this reason, the concentration of impurity and, hence, local deformations are higher in the vicinity of the dislocation, especially in the part of the dislocation that is closer to the surface (or emerges at the surface). An increase in the concentration of impurity atoms leads to an increase in elastic stresses that may either relax via the forma-

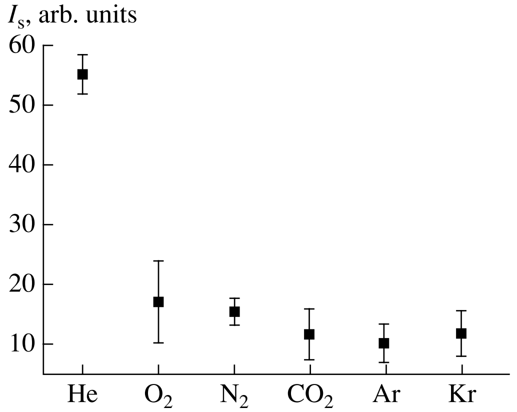

Fig. 3. Variation of the amplitude of scattered radiation in the atmosphere of various gases at a constant power density of a Nd : YAG laser pulse.

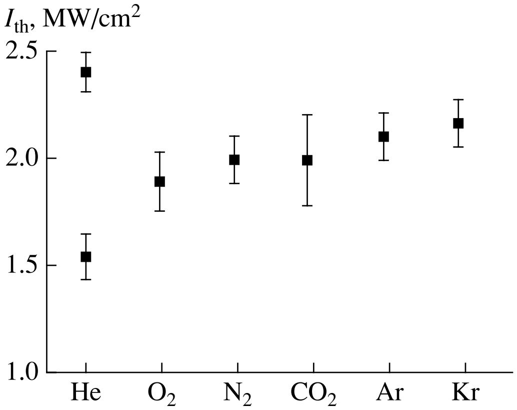

Fig. 4. Variation of the threshold for the emergence of radiation of a probe He–Ne laser beam scattered from the silicon surface in the atmosphere of various gases.

tion of new dislocations or stimulate the growth of the initial dislocation. We can assume that it is the system "dislocation + impurity atmosphere" that determines local inhomogeneity (local deformation) in the surface layer, where scattering of probe laser radiation takes place. Conditionally, we can assume that local inhomogeneity is a result of deformation of the medium induced by the dislocation and impurity atoms; i.e., $\varepsilon = \varepsilon_d + \varepsilon_{im}$.

If we assume that scattering occurs at the local inhomogeneities described above, the decrease in the scattering intensity indicates the relaxation of these inhomogeneities. It should be noted that the above-mentioned relaxation processes occur in the surface layer cooled practically to room temperature, in which the diffusion coefficients for impurities, vacancies, and interstices are negligibly small; for this reason, the observed changes in the scattering intensity can hardly be explained by relaxation of the defect density due to conventional diffusion. This gives grounds to assume that low-threshold diffusion channels exist in the defect-saturated silicon layer in question. It was noted above that such channels might be dislocations. It was found [14] that the energy of migration E_{md} of impurity atoms over dislocations in semiconductors amounts to $E_{md} \approx (0.4–0.6)E_v$, where E_v is the vacancy migration energy and the diffusion coefficient is 3–5 orders of magnitude higher than in the bulk of the crystal. Then the size of inhomogeneities decreases as a result of diffusion of impurity atoms over dislocations, which in turn must be manifested in a decrease in the amplitude of scattered radiation. The experimentally observed changes in the intensity of scattered radiation completely agree with the model of formation, growth, and relaxation of scattering inhomogeneities proposed above. Since the surface initially contains a large number of various defects and experiences the highest stresses under the action of a laser pulse, the generation of dislocations begins in all probability at the surface. Subsequently, their growth in the direction to the bulk of the crystal takes place; in this way, the low-threshold accelerated diffusion of impurity atoms occurs via dislocations. At the instant when a laser pulse is acting, diffusion of impurity atoms proceeds to the bulk of the crystal via dislocation tubes. The fraction of impurity having diffused in this way may be as high as 10–15% of the total mass of diffused impurity [14, 15].

After the termination of a laser pulse, the reverse flow of impurities along a dislocation tube to the surface takes place; simultaneously, impurities flow towards dislocations. At the initial instant after the termination of the laser pulse, the inflow J_Σ^+ of impurity atoms to a dislocation exceeds the outflow J_Σ^- to the surface via dislocation cores; as a result, impurities are accumulated in the upper part of a dislocation core and the local inhomogeneity increases. With increasing impurity concentration in the area surrounding an inhomogeneity, the outflow of impurities begins to prevail over the inflow; i.e., $J_\Sigma^- > J_\Sigma^+$, and the size of the inhomogeneity decreases.

The decrease in the amplitude of scattered radiation under multiple irradiation can then be explained by the fact that new dislocations are generated in the surface layer after each pulse; as a result of flow of impurities to these dislocations according to the mechanism described above, they also become scattering centers. In addition, a part of impurity atoms is accumulated after each pulse in the surface layer. Thus, after several irradiation pulses, a high density of dislocations is formed in the surface layer, leading to averaging of the amplitude of local inhomogeneities, i.e., "homogenization" of the surface layer and, hence, to a suppression of diffuse scattering. As a result, the action of a laser pulse leads to uniform bulging of the surface. Scattering from this surface occurs at small angles and cannot be detected in the experimental geometry of scattered radiation detection.

According to experimental results, an increase in the intensity of diffuse scattering of a probe laser beam is observed during the time interval $t^+ \approx 0.1–0.2$ s after termination of the action of the main (pump) laser pulse, while a decrease is observed during time $t^- \approx 0.2–0.3$ s. The characteristic relaxation time for dislocations estimated in [17] at $\tau_r \approx 1.2$ s was obtained as a fitting parameter from a comparison of the experimental results with the estimates of the growth of dislocation loop as a result of laser action. It can be seen that $t^- < \tau_r$; i.e., the time of decrease in anomalous scattering is shorter than the dislocation relaxation time. This means that the relaxation of scattering inhomogeneities in this case is determined in all probability by the emergence of impurity atoms at the surface via dislocation cores rather than by the decrease in the dislocation size.

CONCLUSIONS

(1) It is found that the action of a submicrosecond laser pulse on silicon in the atmosphere of an ambient gas initiates the emergence of an anomalously protracted spike in the scattering of the probe beam by the surface. The duration of the anomalous scattering is ~0.5 s, which is almost six orders of magnitude longer than the acting laser pulse.

(2) It is shown that the threshold (in I) of the emergence of the anomalous peak of scattering by silicon depends on the type of the ambient gas: the lowest threshold is observed in the atmosphere of helium and the highest threshold takes place in the krypton atmosphere. The observed anomalies in the scattering of probe radiation are associated with laser-induced accelerated diffusion of atoms of the ambient gas (impurity atoms) to the surface layer and the formation of unstable local inhomogeneities (scattering centers) in the surface layer, which form the system "dislocation +

cloud of impurity atoms," which slowly relaxes after the termination of the laser pulse due to the emergence of impurity atoms to the surface via dislocation cores (low-threshold diffusion).

REFERENCES

1. I. B. Khaĭbullin and L. S. Smirnov, Fiz. Tekh. Poluprovodn. (Leningrad) **19**, 569 (1985) [Sov. Phys. Semicond. **19**, 353 (1985)].
2. *Laser Annealing of Semiconductors*, Ed. by J. M. Poate and J. W. Mayer (Academic, New York, 1982).
3. A. M. Chaplanov and E. L. Tochitsky, Thin Solid Films **116**, 117 (1984).
4. V. A. Bushuev and A. P. Petrakov, Zh. Tekh. Fiz. **70** (5), 92 (2000) [Tech. Phys. **45**, 613 (2000)].
5. A. P. Petrakov and E. A. Golubev, Fiz. Tverd. Tela (St. Petersburg) **40**, 156 (1998) [Phys. Solid State **40**, 140 (1998)].
6. V. A. Bushuev and A. P. Petrakov, Fiz. Tverd. Tela (St. Petersburg) **35**, 355 (1993) [Phys. Solid State **35**, 181 (1993)].
7. V. I. Fistul' and A. M. Pavlov, Fiz. Tekh. Poluprovodn. (Leningrad) **17**, 854 (1983) [Sov. Phys. Semicond. **17**, 535 (1983)].
8. V. L. Komolov, Zh. Tekh. Fiz. **64** (7), 64 (1994) [Tech. Phys. **39**, 667 (1994)].
9. M. I. Klinger, Ch. B. Lushchik, T. V. Moshavets, *et al.*, Usp. Fiz. Nauk **147**, 523 (1985) [Sov. Phys. Usp. **28**, 994 (1985)].
10. V. N. Strekalov, Fiz. Tekh. Poluprovodn. (Leningrad) **20**, 361 (1986) [Sov. Phys. Semicond. **20**, 225 (1986)].
11. V. N. Strekalov, Zh. Tekh. Fiz. **67** (12), 59 (1997) [Tech. Phys. **42**, 1426 (1997)].
12. V. L. Vinetskiĭ and G. E. Chaĭka, Fiz. Tverd. Tela (Leningrad) **24**, 2170 (1982) [Sov. Phys. Solid State **24**, 1236 (1982)].
13. A. M. Pristrem, A. V. Demchuk, and N. I. Danilov, Zh. Tekh. Fiz. **56**, 1220 (1986) [Sov. Phys. Tech. Phys. **31**, 717 (1986)].
14. D. Shaw, *Atomic Diffusion in Semiconductors* (Plenum, London, 1973; Mir, Moscow, 1975).
15. I. Kaur and W. Gust, *Fundamentals of Grain and Interphase Boundary Diffusion* (Ziegler, Stuttgart, 1988; Mashinostroenie, Moscow, 1991).
16. A. F. Banishev, V. S. Golubev, and A. Yu. Kremnev, Pis'ma Zh. Tekh. Fiz. **26** (2), 8 (2000) [Tech. Phys. Lett. **26**, 49 (2000)].
17. A. F. Banishev, V. S. Golubev, and A. Yu. Kremnev, Zh. Tekh. Fiz. **71** (8), 33 (2001) [Tech. Phys. **47**, 962 (2001)].

Translated by N. Wadhwa

Technical Physics, Vol. 49, No. 8, 2004, pp. 1040–1043. Translated from Zhurnal Tekhnicheskoĭ Fiziki, Vol. 74, No. 8, 2004, pp. 86–89.
Original Russian Text Copyright © 2004 by Loginov, Shrednik.

Field Evaporation of Carbonized Molybdenum

M. V. Loginov and V. N. Shrednik
Ioffe Physicotechnical Institute, Russian Academy of Sciences,
Politekhnicheskaya ul. 26, St. Petersburg, 194021 Russia

Received January 23, 2004

Abstract—Field evaporation of a carbonized molybdenum crystal is studied using an atomic probe. In the flow of ions being evaporated, various radical ions containing Mo and C, as well as pure Mo ions, are observed. Analysis of mass spectra of field evaporation and corresponding accumulation curves leads to the conclusion about the composition and complex ordering of the surface layers of the crystal. © *2004 MAIK "Nauka/Interperiodica".*

INTRODUCTION

Molybdenum is a chemical analogue of tungsten, actively interacting with hydrocarbons (as well as with atomic carbon) and forming various crystallographic forms of carbon-containing chemical compounds completely analogous to W. When Mo points are heated in a vacuum containing hydrocarbons (methane, benzene, etc.) in residual gas, sharp faceting of a previously rounded crystal without a change in their symmetry is observed. These "ribbed" crystals differ only slightly from similar crystals in the case of carbonized molybdenum. Field evaporation of carbidized tungsten was thoroughly studied in at least three publications [1–3]. As regards molybdenum, which is chemically more active than tungsten, no such studies have been carried out, although such experiments (as well as any experiments on field evaporation of non-one-component surfaces) are of considerable interest. Ribbed tungsten crystals did not correspond to a stable chemical compound and were distinguished by a varying composition, which was measured in the direction from the surface to the bulk [2, 3]. The same behavior could be expected for carbonized Mo points. As usual, the following two aspects of the experiment were of special interest: the composition of the flow of evaporating ions and the composition of the surface being evaporated as well as its physical and chemical processes. The goal of this first publication devoted to the field evaporation of carbonized molybdenum is to study the phenomenon, bearing in mind these two aspects.

EXPERIMENTAL TECHNIQUE

A method adequate to the posed problem was the time-of-flight atomic probing technique [4]. We used a probe with a low mass-spectrometric resolution [5, 6] but with a high luminosity. A resolution of about 30 made it possible to determine the elemental (but not isotopic) composition of ions, while the high luminosity provided for a large number of detailed mass spectra from the same point prior to its rounding. A distinguishing feature of our atomic probe was the fixation of its point to a bracket heated by electric current. This enabled us to carry out the thermal and temperature-field treatment of the object, to analyze field emission images in the cold and hot states, and also to obtain mass spectra at elevated temperatures in the cases when the useful signal was considerably stronger than the noise mainly generated by evaporation under a constant base voltage V_b. The base voltage could be varied from 0 to 20 kV, while the pulsed evaporating voltage V_p varied from 3 to 6.2 kV.

The system of experimental data processing enabled us not only to obtain the field-evaporation mass spectra, but also to plot the curves of successive accumulation of ions from their entire aggregate (integral accumulation curves) as well as ions belonging to selected mass peaks (differential curves). These curves provided important information on the evaporation rate, the sequence of ion evaporation, etc.

The object was a carbonized Mo crystal prepared according to the following technology. A Mo point etched in a dilute solution of NaOH and thoroughly washed was fixed in the probe chamber in a vacuum of 10^{-7}–5×10^{-8} Torr and was heated to a temperature T of 2200–2500 K for a few seconds. To prevent the sharp point from blunting, heating was carried out under a positive potential of 1.5 kV applied to the point. The residual gases in the chamber contained methane and other hydrocarbons formed during the operation of pumps: an electric discharge NORD pump and an oil-vapor pump TsVL-100. As a result of such a standard treatment, a ribbed crystal was formed at the tip of the point. The typical field emission patterns of the point are shown in Fig. 1. The diaphragm of an atomic probe 3 mm in diameter (circular aperture in a microchannel plate, a screen, and a mirror at a distance of 100 mm from the point) was directed at one of the bright ribs between the {001} and {110} faces (Fig. 1b). In the course of obtaining the spectrum, the crystal rib became blunted. On the electron pattern, the rib appeared blurred and a higher voltage (1.3–1.8 times the previous value) was required to observe the emission pattern of the previous brightness. After several cycles of crystal growth and obtaining of the spectrum, the point was blunted (in spite of the application of a “backward” voltage of 1.5 kV) and the base voltage V_b had to be increased for obtaining subsequent spectra (in our work, this increase was from 4 to 15 kV at V_p = 6.2 kV). At the same time, as a result of intense heating cycles required for the formation of the crystal, the amount of carbon on its surface and in the surface region decreased down to complete purification, when the spectrum of virtually pure Mo was obtained for $V_b + V_p = (15 + 6.2)$ kV with a clearly manifested Mo3+ peak. This spectrum was used for the additional calibration of the probe parameters. All spectra were obtained for the point at room temperature.

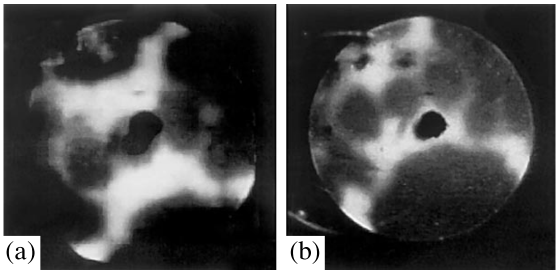

Fig. 1. Autoemission images of a carbonized molybdenum, obtained after heating at T = 2400 K for 10 s under a positive potential of 1.2 kV at the point: (a) room temperature, V = –1.9 kV; (b) room temperature, V = 1.7 kV. The aperture of the diaphragm is directed to the central part of the lower “bracket.”

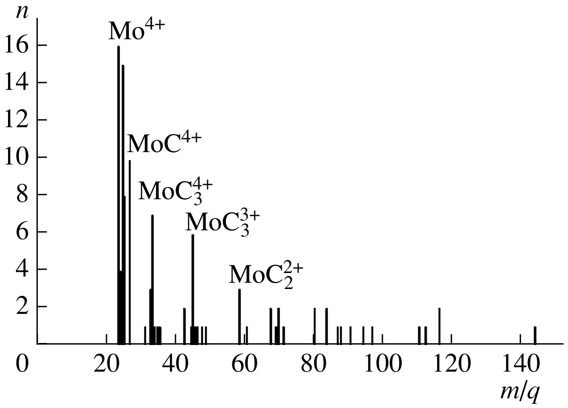

Fig. 2. Mass spectrum obtained for a ribbed Mo crystal for $V_b + V_p = (10 + 6.2)$ kV. The number n of detected ions and the ratio m/q of the mass of the ion to its charge are laid along the ordinate and abscissa axes, respectively.

EXPERIMENTAL RESULTS AND DISCUSSION

In all, we obtained eight satisfactory spectra. The conditions for obtaining some of these spectra were the same as in the previous measurement (the spectra were obtained twice for $V_b + V_p = (7 + 6.2)$ kV and thrice for $V_b + V_p = (10 + 6.2)$ kV), demonstrating good reproducibility. The initial situations (naturally prior to complete purification from carbon) corresponded to the crystals whose emission images are shown in Fig. 1. As in the case of carbonated W [3], the spectra exhibited noticeable peaks of Mo–C and purely Mo ions with charges +4, +3, and (less frequently) +2. The approximate list of these ions in the decreasing order of frequencies at which the ions appear in the spectrum is Mo^{4+}, MoC^{4+}, MoC$_3^{4+}$, MoC$_3^{3+}$, MoC$_2^{2+}$, Mo$_2$C^{3+}, Mo^{3+}, Mo^{2+}, and Mo$_2$C^{2+}. These ions were accumulated during evaporation from the same area (crystal rib; see Fig. 1b). After purification from carbon, Mo^{3+} ions mainly evaporated from the central face {110}. As small impurities, Mo$_2$C^{2+}, (MoC$_3$)$_2^{3+}$, etc., ions were also encountered in the latter case.

Let us consider one of the most interesting field evaporation mass spectra shown in Fig. 2. The crystal was grown by heating to 2500 K for 30 s under a potential of +1.5 kV at the point. In such a regime, a rather sharp rib to which the diaphragm was directed was formed. At a voltage of (10 + 6.2) kV, only 234 ions accumulated as a result of 10 000 evaporating pulses. Figure 2 reflects the main part of the spectrum for values of the m/q ratio (of the ion mass to the ion charge) to 150, although ions were detected up to m/q = 2000. However, a large number of peaks of single and double frequency were detected for high values of this ratio; a part of these peaks should be attributed to noise (in general, we identified peaks with a height starting from three, although many peaks with a height of two ions corresponded to a quite probable composition). The spectrum depicted in Fig. 2 contains an intense peak at $m/q \approx 24$, which corresponds to the Mo^{4+} ion. A sharp individual peak corresponding to m/q of about 27 is identified with MoC^{4+}; the peaks representing MoC$_3^{4+}$, MoC$_3^{3+}$, and MoC$_2^{2+}$ can also be clearly seen. All the clearly pronounced peaks in Fig. 2 were successfully reproduced in the next two spectra for the same value of $V_b + V_p = (10 + 6.2)$ kV, the only difference being that the point was blunted and the number of ions decreased. For the peaks corresponding to Mo^{4+}, MoC^{4+}, MoC$_3^{4+}$, and MoC$_3^{3+}$, the differential accumulation curves were plotted. Such curves for the first two ions are shown in Fig. 3a. The “antiphase” nature of data collection is obvious, especially for the first half of collection (to be more precise, up to 6000 pulses): when Mo^{4+} ions appear, there are no MoC^{4+} ions, and vice versa. After the 6000th pulse, the same tendency persists, but is pronounced less clearly. This may be for two reasons. The process of evaporation decays and proceeds at a lower rate since the area of the sharp rib is rapidly blunted. In addition, the amount of carbon

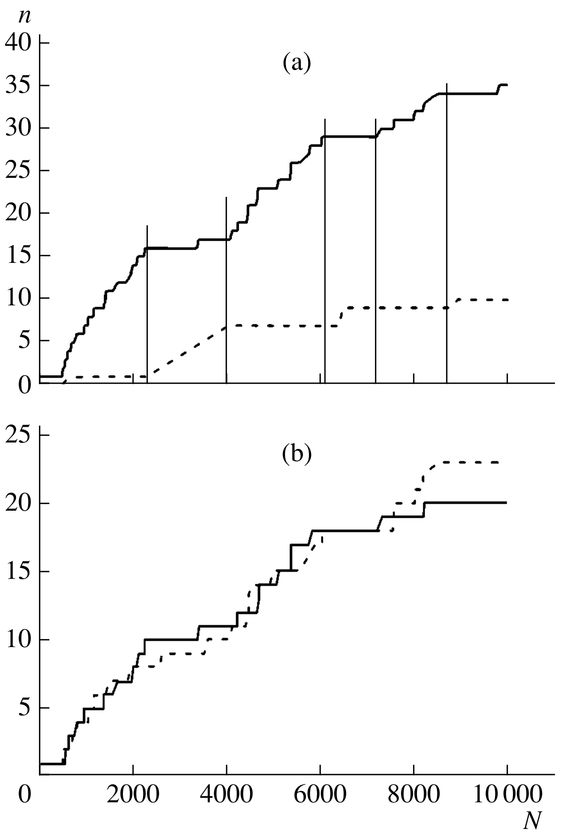

Fig. 3. Differential curve of ion accumulation (the number *n* of detected ions as a function of the number *N* of supplied pulses) (a) for Mo^{4+} peaks (solid curve) and MoC^{4+} peaks (dashed curve); (b) for two branches of the Mo^{4+} peak: $m/q = 24$ (solid curve) and 24.5–25.5 (dashed curve).

decreases as a result of "digging." In our case (in contrast to many cases described for W [2, 3]), the carbidized crust is very thin. For this reason, we did not observe a negative image [1, 2] of "brackets" after an evaporation cycle. The indisputable obviousness of the emergence of ions can be explained by evaporation of Mo with accumulation of carbon to a certain critical state, after which it is removed in the form of MoC or by layer-by-layer evaporation, when the layers of Mo and C atoms alternate in the structure of the crystal itself. In the former case, the "antiphase" nature of the process should not be manifested so clearly (for constant V_b and V_p). Along with Mo ions, MoC ions could also evaporate since these ions evaporate in the same field. The pattern would be such as if the numbers of ions of both species increase synchronously (e.g., as shown in Fig. 3b). The peak of Mo^{4+} is split and we decided to analyze separately the increase in the number of ions on both branches of this peak. It was found (see Fig. 3b) that the ions from both branches accumulate synchronously (with a statistical spread), which confirms the same physical nature of ions corresponding to the peak at $m/q \approx 24$. The spread and separation of ions into two thin subpeaks are explained primarily by the ionization not only at the top of a bell-shaped pulse, but also on its slopes. To a lesser extent (due to a low mass resolution), this can also be associated with a wide set of stable isotopes of Mo (from 92 (15.1%) to 100 (9.7%) with a maximum at 98 (24%) [7]). By the way, a thin (one-channel) peak like that corresponding to MoC^{4+} with 10 ions in a channel of the analyzer indicates ionization precisely at the top of the pulse (i.e., for the maximal possible field).

Thus, we must assume that Mo ions lie at the top of a rib of the ribbed crystal prepared in the standard way; it is these ions that are the first to evaporate. A layer of C atoms is located in an orderly way under the Mo layer. As soon as this layer outcrops, carbon atoms escape, each C atom entraining a Mo atom. Such evaporation is obviously more advantageous from the energy standpoint. It is well known that evaporation of carbon from carbon (e.g., in graphite) requires extremely high fields [8]. The next layer is again a layer of Mo atoms, and it is only under this layer that a layer of C atoms (insufficiently thick in our case) may lie. We also plotted the accumulation curves for not very high, but still noticeable peaks of (triply and quadruply charged) MoC_3; these curves indicated the instants of time (measured in the number of pulses supplied to the point) when such ions appear (these times are not shown in Fig. 1a). According to their emergence, these ions were found to be statistically distributed over the regions of increase in the number of Mo^{4+} and MoC^{4+} ions. In the first region, six MoC_3 ions appeared (4 quadruply charged and 2 triply charged ions). In the second region (i.e., for increasing number of MoC^{4+}), seven MoC_3 ions were produced (3 quadruply charged and 4 triply charged). No regularity can be observed in this case. The emergence of MoC_3 ions is apparently associated with the nonideal character of the layered structure of carbon atoms, whose number is slightly greater and which may also be located in a layer of Mo atoms. Apparently, the evaporation of a Mo atom with three carbon atoms is also advantageous from the energy point of view. These ions reflect fluctuations in the composition of the carbidized surface region. If we take into account only the ions corresponding to the first four peaks in the spectrum (it is these ions that play the leading role), it will turn out that the layers enriched by molybdenum contain 40 Mo atoms and 18 C atoms, which is close to the composition of Mo_2C; the layers rich in carbon contain 17 Mo atoms and 31 C atoms, which is close to the composition of MoC_2. On the average, over all four peaks, we can count 57 Mo atoms and 49 C atoms; taking into account a large number of small peaks containing more C atoms than the number of Mo atoms, we can assume that the average composition of the surface region is close to MoC.

CONCLUSIONS

(1) The surface region of a carbonized ribbed Mo crystal is close in composition to monocarbide MoC.

(2) However, a detailed analysis of the peaks in the mass spectra and the differential accumulation curves reveals a tendency to an atomic ordering in the crystal (grown in the standard way), so that a Mo layer is at the surface, followed by a carbon layer under which at least two Mo layers are located (this is observed to within certain fluctuations in the arrangement of C atoms).

(3) Taking into account the aforementioned fluctuations, the layered structure is preserved, but we must ascribe a composition of Mo_2C and MoC_2 to the alternating layers.

(4) The ion flow contains both pure Mo ions (Mo^{4+}, Mo^{3+}, and sometimes Mo^{2+}) and various radical ions containing Mo and C atoms (first of all, MoC^{4+}, MoC_3^{4+}, MoC_3^{3+}, MoC_2^{2+}, etc.).

ACKNOWLEDGMENTS

This study was supported by the Russian Foundation for Basic Research (project no. 01-01-17803) and the program of the Ministry of Science and Technology of the Russian Federation (contract no. 40.012.1.1.1152).

REFERENCES

1. O. L. Golubev, B. M. Shaĭkhin, and V. N. Shrednik, Pis'ma Zh. Tekh. Fiz. **1** (15), 714 (1975) [Sov. Tech. Phys. Lett. **1**, 313 (1975)].
2. M. V. Loginov and V. N. Shrednik, Pis'ma Zh. Tekh. Fiz. **24** (11), 45 (1998) [Tech. Phys. Lett. **24**, 432 (1998)].
3. M. V. Loginov and V. N. Shrednik, Pis'ma Zh. Tekh. Fiz. **29** (13), 1 (2003) [Tech. Phys. Lett. **29**, 529 (2003)].
4. M. K. Miller and G. D. W. Smith, *Atom Probe Microanalysis: Principles and Applications to Material Problems* (Materials Research Society, Pittsburgh, 1989; Mir, Moscow, 1993).
5. M. V. Loginov, O. G. Savel'ev, and V. N. Shrednik, Zh. Tekh. Fiz. **64** (8), 123 (1994) [Tech. Phys. **39**, 811 (1994)].
6. V. N. Gurin, M. M. Korsukova, M. V. Loginov, and V. N. Shrednik, Zh. Tekh. Fiz. **71** (9), 97 (2001) [Tech. Phys. **46**, 1161 (2001)].
7. G. W. C. Kaye and T. H. Laby, *Tables of Physical and Chemical Constants and Some Mathematical Functions*, 16th ed. (Longman, New York, 1995; Fizmatgiz, Moscow, 1962).
8. N. M. Blashenkov and G. Ya. Lavrent'ev, Pis'ma Zh. Tekh. Fiz. **22** (7), 57 (1996) [Tech. Phys. Lett. **22**, 293 (1996)].

Translated by N. Wadhwa

Technical Physics, Vol. 49, No. 8, 2004, pp. 1044–1049. Translated from Zhurnal Tekhnicheskoĭ Fiziki, Vol. 74, No. 8, 2004, pp. 90–94.
Original Russian Text Copyright © 2004 by Golubev, Shrednik.

SURFACES, ELECTRON AND ION EMISSION

Temperature- and Field-Induced Changes in the Form of the Mo–Hf Alloy

O. L. Golubev and V. N. Shrednik

Ioffe Physicotechnical Institute, Russian Academy of Sciences,
St. Petersburg, 194021 Russia

e-mail: V.Shrednik@mail.ioffe.ru

Received January 23, 2004

Abstract—Simultaneous action of strong electric fields and high temperatures on point field emitters made of the Mo–15%Hf alloy is studied by field emission methods. Such alloys enriched with an emission-active component and containing the Mo_2Hf intermetallide exhibit basically the same stages of temperature- and field-induced changes in their form as for pure metals, although a number of peculiarities associated with the surface segregation of Hf also exist. Thermal-field processing of emitters was accompanied with high-temperature field evaporation and emission of predominantly Hf (both atomic and cluster-type) ions. Thermal-field processing also enhances emission localization, but to a smaller extent as compared to that in alloys with a low Hf concentration. *© 2004 MAIK “Nauka/Interperiodica”.*

INTRODUCTION

The thermal-field effect, i.e., the simultaneous action of strong electric fields F from tenths of V/Å to several V/Å and high temperatures T sufficient for an intense surface diffusion of the emitter atoms is an effective tool for a controlled change in the shape of a point field emitter of electrons and ions. The main stages of such a change have been comprehensively studied for pure (mainly refractory) metals [1–3] and have been reduced to the following. First, at the lowest values of T and F, the initial point rounded by heating is transformed into a ribbed polyhedron with a noticeable expansion of densely packed faces of the pointed single crystal; this is the rearrangement stage of the point. Subsequently, for higher values of T and F, the next stages of the field-induced crystal growth are observed. At first, small outgrowths (microprotrusions) appear at the edges and vertices of the rearranged point, which facilitate the formation (mainly in the densely packed faces) of large outgrowths (macroprotrusions) whose vertices and edges are covered with microprotrusions. However, in contrast to pure metals, such experiments have not been carried out at full scale with alloys and only an insignificant number of alloys among the huge variety of modern alloys have been studied.

In this study, we analyzed the Hf–Mo alloy (15 wt% Hf). This alloys was studied previously only in [4, 5], where field evaporation was analyzed with the help of an atomic probe and a considerable segregation of Hf at the surface was demonstrated; however, the morphology of the surface was not studied at all. In our previous publication [6], we considered in detail the effect of temperature and field on the allied Hf–W alloy, which contained, however, a very small amount of Hf (less than 3%). For this reason, it would undoubtedly be of interest to study the change in the form of the present alloy rich in emission-active adsorbate. The diagram of states of this alloy is not available to our knowledge; however, the known diagrams of allied Hf–W and Zr–Mo alloys [7, 8] indicate that the solubility of Hf in the bulk of Mo is not less than 3–5%; at higher concentrations of Hf, the intermetalide Mo_2Hf is formed. Such alloys containing components like Zr and Hf are characterized by a much smaller work function of the surface. In addition, the emission of electrons is localized in a narrow solid angle, which leads to the formation of small brightly emitting islands, e.g., on W in the vicinity of the {001} faces even in the case of heating in zero field [9, 10]. Such alloys are very promising as regards the obtaining of point sources of electrons and ions. Alloys rich in an active adsorbate are of special importance since these alloys can ensure a long working life of the ion source due to continuous evaporation of the adsorbate from the emitter surface, as well as electron sources used in the Schottky cathode regime (i.e., with cathode heating [10]), and require a large volume concentration of the emission-active element.

EXPERIMENTAL TECHNIQUE

Experiments were made using the classical methods of field emission spectroscopy. We used as the objects of investigation small bars made of the bulk Mo–15%Hf alloy, from which point emitters with a radius r equal to a fraction of a micrometer were prepared by electrolytic etching. The values of field F and work function φ were determined by the conventional method from the slopes of the Fowler–Nordheim characteristics under the assumption that a change in the slope corresponds to a change in either F or φ. The initial value of φ for the Hf–Mo alloy with the given composition is unknown and its absolute value cannot be correctly determined in this particular case; for this reason, we used as the initial value φ = 3.70 eV, which is equal to the value of φ for the Mo–15%Zr alloy obtained by the thermoemission method and is given in [11]. As regards the experimentally determined values of F, the shape of the emitter changes under the action of heat and field at a constant applied voltage U; consequently, the field F also changes. We must distinguish between the initial field F_{tr} of treatment, which is determined relative to the initial rounded shape of the point, and the final field F_{fin} emerging at the surface after variation in the emitter shape and the attainment of steady state.

EXPERIMENTAL RESULTS

Figure 1a shows the electron field image of the initial surface of a point single crystal made of the given alloy and rounded by prolonged heating in vacuum at $T = 2000$ K in zero external field (so-called annealing shape). Extended brightly emitting regions near the {001} faces of the cube and weakly emitting regions near the {111} faces can be clearly seen. The formation of such regions around {001} is not surprising since Hf may form a densely packed square lattice in these regions [12] since the atomic diameter of Hf (3.18 Å [13]) is close to the atomic spacing on the {001} face of Mo (3.15 Å). The formation of such brightly emitting regions is also typical of the adsorption of Zr and Hf at W [9, 10]. The thermal and field effect exerted on the emitter up to $T = 1700$ K does not lead to any appreciable change in its shape even for high values of $F_{tr} = 0.6$ V/Å; the field factor β slightly increases from the initial value of $\beta = 5800$ to 6300 cm^{-1}. Figure 1b corresponds to treatment at $T = 1700$ K and $F_{tr} = 0.6$ V/Å. It can be seen that the regions near the cube have been slightly rearranged and have become smaller in area; the regions near the {111} faces have vanished in the images. Regions near {001} are noticeably rearranged with the formation of acute angles along the contour of the emitting narrow ring only when the temperature increases to $T = 1750$ K and $F_{tr} = 0.43$ V/Å (Fig. 1c). The value of β increases to 9520 cm^{-1} and the field increases as a result of treatment to $F_{fin} = 0.76$ V/Å. Finally, for the maximal possible treatment field $F_{tr} = 0.65$ V/Å (point emitters had a fairly large radius of curvature $r \sim 0.6$–0.7 μm and a voltage U required for attaining high values of F_{tr} exceeded 15 kV, which could cause a breakdown); at the same temperature $T = 1750$ K (Fig. 1d), the regions with cubes were trans-

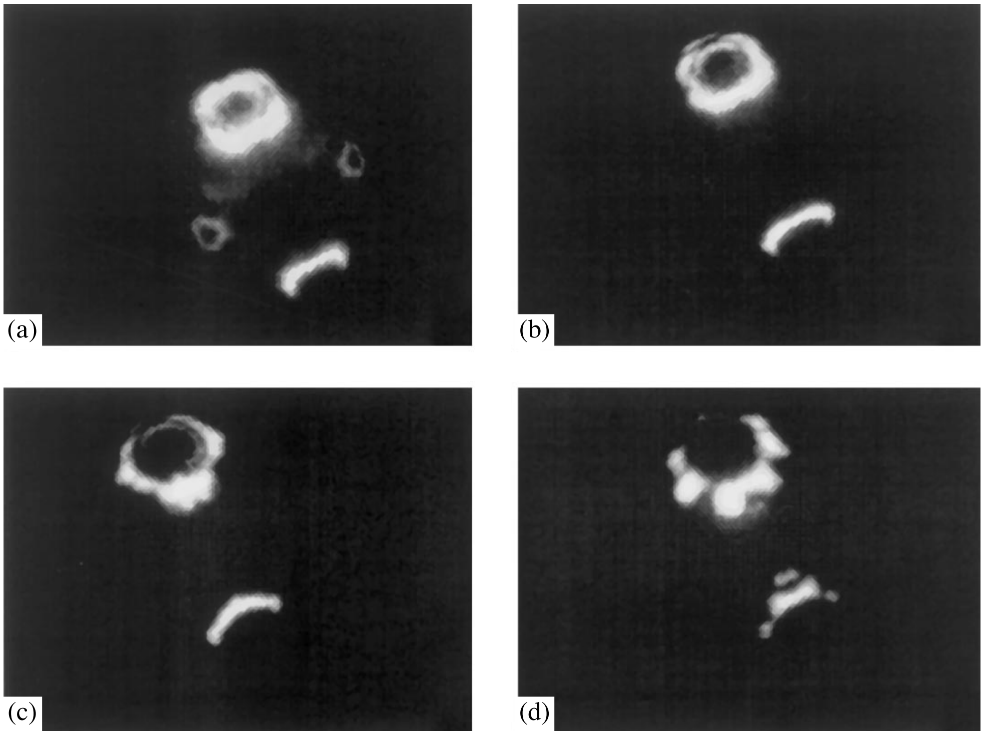

Fig. 1. Field electron images of the surface of an emitter made of the Mo–15%Hf alloy under the thermal effect in the field. The initial stages of change in the emitter shape: (a) after heating the emitted at $T = 2000$ K in zero field; (b) after heating the emitter at $T = 1700$ K and $F_{tr} = 0.60$ V/Å; (c) after heating the emitter at $T = 1750$ K and $F_{tr} = 0.43$ V/Å; and (d) after heating the emitter at $T = 1750$ K and $F_{tr} = 0.65$ V/Å.

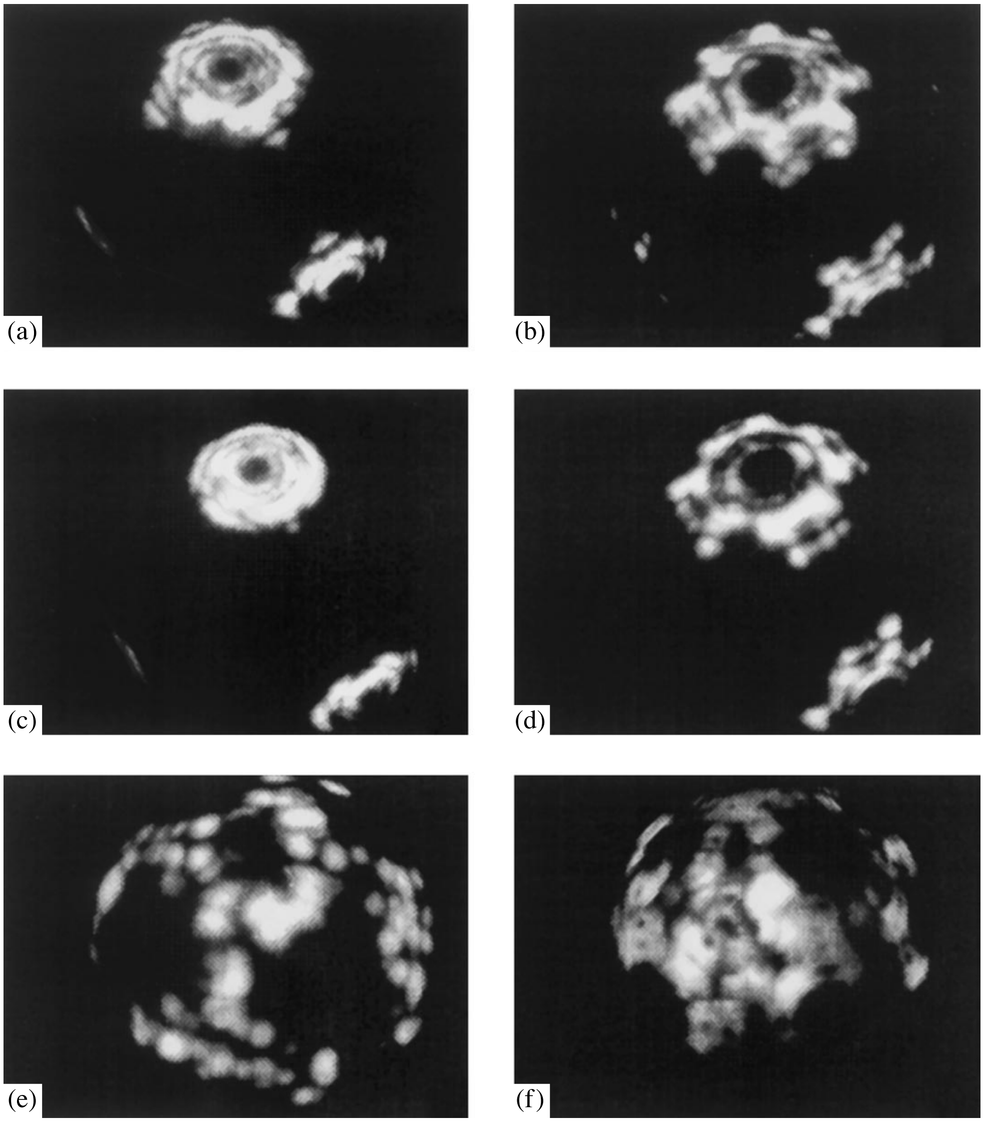

Fig. 2. Field electron images of the surface of the same emitter at the stage of the field-induced crystal growth: (a) after heating the emitter at T = 1800 Kand F_{tr} = 0.58 V/Å; (b) after heating the emitter at T = 1800 K and F_{tr} = 0.65 V/Å; (c) after heating the emitter at T = 1850 K and F_{tr} = 0.38 V/Å; (d) after heating the emitter at T = 1850 K and F_{tr} = 0.58 V/Å; (e) after heating the emitter at T = 1850 K and F_{tr} = 0.65 V/Å; (f) after heating the emitter in state (d) at T = 1600 K in zero external field.

formed into a polyhedron with lobes protruding at angles of approximately 45°; the field factor in this case increased to its maximal value of β = 12 740 cm^{-1}, while the value of F_{fin} attained a value of 1.27 V/Å. It should be noted that only Hf-enriched regions near {001} experienced noticeable changes, while the remaining crystallographic regions of the point do not exhibit any noticeable rearrangement even upon an increase in the applied voltage.

If the treatment temperature T is increased to 1800 K at F_{tr} = 0.58 V/Å, the initial stage of the typical field-induced rearrangement takes place, which is manifested in the formation of a large number of atomic steps around the poles of {001}; this can be seen in Fig. 2a and even better in Fig. 2b at the same temperature T, but at F_{tr} = 0.65 V/Å. The field factor increases insignificantly: β = 7470 cm^{-1} for the structure shown in Fig. 2a and β = 8147 cm^{-1} for the structure shown in Fig. 2d. Such a stage of rearrangement was observed for the first time at high values of F_{tr} and low values of T in W [14]; in our earlier work [15], this type of rearrangement of the point was also observed for Re. A further increase in T to 1850 K leads to F_{tr} = 0.38 V/Å and to the formation of noticeable rings of steps around {001} (Fig. 2c). At F = 0.58 V/Å, four faces of the type of {510} and {310} can be seen on the rearranged faces of the cube in the direction of faces {011}; such faces have never been observed on a rounded point (Fig. 2d), for which the value of β is 8697 cm^{-1}. It is only for F_{tr} = 0.65 V/Å that a large number of microprotrusions is

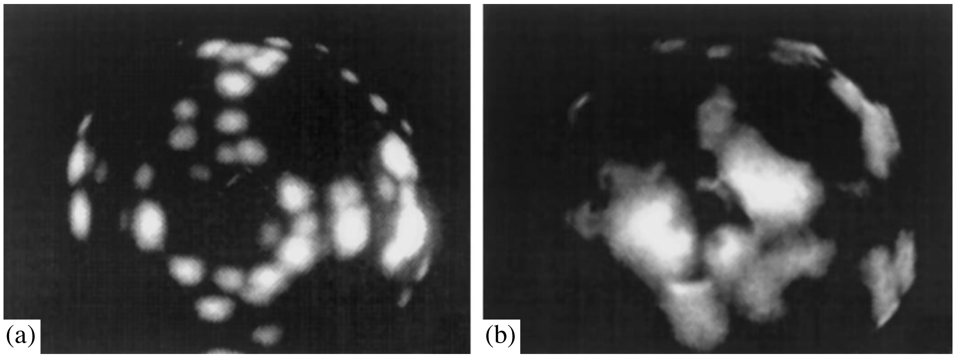

Fig. 3. Field electron images of the same emitter after the ion current takeoff: (a) the state of the surface after takeoff of the ion current i = 2 nA at T = 1930 K. F_{tr} = 0.65 V/Å, and F_{fin} = 1.20 V/Å; microprotrusions can be seen on the surface; (b) after the reduction of the value of F_{tr} to 0.55 V/Å at the same T = 1930 K; microprotrusions and ion current are absent.

observed on the entire surface of the point at a given temperature T (Fig. 2e); however, the value of β in this case decreases to 7434 cm^{-1} and the value of F_{fin} becomes equal to 1.12 V/Å. The heating of the structure shown in Fig. 2e at T = 1600 K in zero external field reveals a large number of macro-outgrowths on various faces of the point (both densely packed and loose); microprotrusions grow just at the vertices and edges of such faces (Fig. 2f).

Such emitters (both initially rounded and modified) may serve as effective sources of electrons as well as ions. Electron currents i on the order of several microamperes can easily be attained for a current density of $j \sim 10^3$–10^4 A/cm^2 for the initial annealing shape and $j \sim 10^6$–10^7 A/cm^2 for modified shapes. Ion currents are produced only in the presence of microprotrusions on the emitter surface. Atoms evaporate in the form of ions from the vertices of such microprotrusions, while modified shapes do not produce ion currents (at least at a level of $i \sim 10^{-11}$ A, which can be reliably detected). At T = 1850 K and F_{tr} = 0.65 V/Å, the values of ion currents were in the range of i = 0.3–0.5 nA and were as high as i = 1–2 nA at T = 1930 K and at the same value of F_{tr}. Emission patterns in Fig. 3 illustrate this situation. Figure 3a shows the state of the emitter surface after takeoff of ion current i = 2 nA at T = 1930 K and F_{tr} = 0.65 V/Å, F_{fin} = 1.20 V/Å, and surface “freezing” by an abrupt stoppage of emitter heating. It can be seen that the surface of the point has a large number of microprotrusions. If the field is reduced to F_{tr} = 0.55 V/Å after attaining this value of the ion current, the current ceases and the microprotrusions also disappear after subsequent “freezing” of the surface (Fig. 3b).

Another property of emitters made of the given alloy is worth noting. The emissive properties of the emitter surface are weakly sensitive to adsorption of residual gases as compared to emitters made of pure metals. Holding of an emitter at room temperature T in a vacuum of $\sim 10^{-10}$ Torr (in the atmosphere of mainly hydrogen and nitrogen) for 1 h virtually does not change the work function: φ = 3.68 ± 0.05 eV vs. initial φ = 3.70 eV, although a monolayer of residual gases is adsorbed over this time interval at the surface. Even after holding for 6 days, when adsorbed gases may even corrode the surface, the work function still changes insignificantly as compared to, for example, pure W (φ = 4.40 ± 0.05 eV). Such a weak variation of φ under the action of residual gases can be explained either by a decrease in the adhesion coefficient of gas molecules, or by the weak effect of these molecules on the surface atoms of this alloy. This phenomenon is typical of emitters with the initial annealing shape as well as emitters subjected to the effect of temperature and field.

DISCUSSION

First of all, we note that the same stages of temperature- and field-induced form changes (rearrangement in the field and field-induced crystal growth with the formation of microprotrusions and macro-outgrowths) are observed for the given strongly enriched alloy (which is no longer a solid solution, but an intermetallide) as for pure metals; i.e., such changes in the shape of crystalline field emitters are universal. On the other hand, typical differences from the case of pure metals are determined by noticeable segregation of Hf at the point surface in crystallographic regions near {001}. Temperature- and field-induced form changes occur when the pressure $P_F = F^2/8\pi$ exerted by ponderomotive forces of electric field exceed the Laplace pressure $P_\gamma = 2\gamma/r$ of surface tension forces (γ is the surface tension). Hafnium segregated at the surface in the vicinity of {001} reduces the values of γ and P_γ and creates conditions for preferential form changes precisely in these regions.

It was noted above that emitters made of the Hf–Mo alloy of the given composition may produce electron currents for values of U noticeably lower than in the case of pure metals due to a lower value of φ as well as ion currents from fractions of a nanoampere to several nanoamperes. Ion currents are mainly formed by Hf ions with different charges. It was shown in [5], where high-temperature field evaporation of precisely this alloy was studied with the help of an atomic probe, that, for example, the mass spectrum recorded at $T = 1400$ K in fields $F = 0.6–0.8$ V/Å revealed only Hf^{3+} and Hf_2^{3+} ions; at a higher temperature $T = 1850$ K, the mass spectra showed, apart from these ions, small amounts of cluster ions of intermetallide Mo_2Hf^{3+} as well. Consequently, using the method of temperature and field action on emitters made of alloys and the effect of high-temperature field evaporation (atomic and cluster) ion currents of various charge and composition can be obtained for elements from which point emitters cannot be made, or can be made but with difficulty.

Another important aspect is also worth noting. The obtaining of point sources of electrons and ions is very important for nanotechnology as well as for other branches of emission electronics. For this purpose, emitters localizing emission in a narrow solid angle are required. A conventional point autoemitter emits electrons in a solid angle α from 1 to 2 sr. Such emitters can be regarded as point emitters in many fields of application, but are not effective in nanotechnology in view of strong beam divergence. It is well known that such adsorbates as Hf and Zr at W localize emission in a small solid angle in the vicinity of {001}, forming small strongly emitting regions even in zero external field; the values of α in this case amount to 0.01–0.03 sr. Thermal and field treatment of such emitters may considerably reduce the values of α; for example, for a Hf–W alloy with a low concentration of Hf (below 3%), extremely small values of $\alpha = 0.001–0.002$ sr were obtained by growing solitary microprotrusions precisely in the regions of small spots of Hf [6]. Experiments with the alloy Mo–15%Hf prove that such a point localization and growth of individual microprotrusions cannot be obtained, although a localization of emission is undoubtedly observed during heating of the emitter in a field and even in zero field. Microprotrusions appear on the entire surface of the point emitter. Although each individual microprotrusion exhibits a pronounced localization with $\alpha = 0.003–0.005$ sr and can produce ion currents on the order of 10^{-11} A (which is quite sufficient for purposes of nanotechnologies) the situation in this case does not differ in principle from the case of pure metals. Thus, the alloys containing emission-active components such as Zr and Hf and strongly enriched with these components are advantageous as regards their long working life, but are apparently less promising for attaining extremely high localization of emission.

CONCLUSIONS

We have studied the temperature and field effect on the emitters made of the Mo–15%Hf alloy in a wide range of values of T and F. It is shown that this alloy, which is strongly enriched with Hf and contains an intermetallide, exhibits the same stages of form modification as pure metals.

Peculiarities of temperature- and field-induced changes in the form are associated with surface segregation of Hf, which is enhanced when high temperatures and fields act simultaneously.

Under the thermal and field effect, high-temperature field evaporation takes place, leading to predominant evaporation of Hf ions (both atomic and cluster-type) with different charges. In this case, ion currents from a solitary microprotrusion may reach values of $i \sim 10^{-11}$ A, while the currents from the entire surface of the emitter can be on the order of $i \sim 10^{-9}$ A.

With the help of thermal action in the field, emission can be localized in a solid angle of $\alpha \sim 0.003–0.005$ sr; however, such Hf-enriched alloys are inferior to alloys in the form of solid solutions with a small Hf concentration as regards the obtaining of extremely strong localization, although the former have much longer working life.

The emissive properties of such emitters with the annealing shape and with the shape resulting from the temperature and field effect are such that they possess a quite low sensitivity to adsorption of residual gases; the work function during adsorption changes insignificantly as compared to that of emitters made of pure metals.

ACKNOWLEDGMENTS

This study was supported by the Russian Foundation for Basic Research (project no. 01-02-17803) and a program of the Ministry of Science and Technology of the Russian Federation (contract no. 40.012.1.1.1152).

REFERENCES

1. V. N. Shrednik, in *Crystal Growth* (Nauka, Moscow, 1980), Vol. 13, pp. 68–79 [in Russian].
2. Yu. A. Vlasov, O. L. Golubev, and V. N. Shrednik, in *Crystal Growth* (Nauka, Moscow, 1991), Vol. 19, pp. 5–21 [in Russian].
3. V. G. Pavlov, A. A. Rabinovich, and V. N. Shrednik, Fiz. Tverd. Tela (Leningrad) **17**, 2045 (1975) [Sov. Phys. Solid State **17**, 1335 (1975)].
4. E. L. Kontorovich, M. V. Loginov, and V. N. Shrednik, J. Vac. Sci. Technol. B **15**, 495 (1997).
5. M. V. Loginov and V. N. Shrednik, Zh. Tekh. Fiz. **68** (3), 69 (1998) [Tech. Phys. **43**, 327 (1998)].
6. O. L. Golubev and V. N. Shrednik, Zh. Tekh. Fiz. **73** (6), 118 (2003) [Tech. Phys. **48**, 776 (2003)].

7. M. Hansen and K. Anderko, *Constitution of Binary Alloys* (McGraw-Hill, New York, 1958; GNTI Chern. Tsvetn. Metall., Moscow, 1962).
8. C. Bill, Trans. Metall. Soc. AIME **224**, 61 (1962).
9. V. N. Shrednik and G. A. Odishariya, Izv. Akad. Nauk SSSR, Ser. Fiz. **33**, 536 (1969).
10. L. W. Swanson and L. C. Crouser, J. Appl. Phys. **40**, 4741 (1969).
11. B. Ch. Dyubua and L. A. Stepanov, Élektron. Tekh. Ser. Élektron. SVCh, No. 7, 70 (1973).
12. V. N. Shrednik, Fiz. Tverd. Tela (Leningrad) **3**, 1750 (1961) [Sov. Phys. Solid State **3**, 1268 (1961)].
13. *Hafnium: Collection of Articles*, Ed. by L. N. Komissarova (Inostrannaya Literatura, Moscow, 1962).
14. D. N. Krotevich, Candidate's Dissertation (Bonch-Bruevich State University of Telecommunications, Leningrad, 1985).
15. O. L. Golubev, E. L. Kontorovich, and V. N. Shrednik, Pis'ma Zh. Tekh. Fiz. **22** (18), 72 (1996) [Tech. Phys. Lett. **22**, 766 (1996)].

Translated by N. Wadhwa

Technical Physics, Vol. 49, No. 8, 2004, pp. 1050–1054. Translated from Zhurnal Tekhnicheskoĭ Fiziki, Vol. 74, No. 8, 2004, pp. 95–99.
Original Russian Text Copyright © 2004 by Davydov, Pavlyk.

SURFACES, ELECTRON AND ION EMISSION

Adsorption of Alkali Metals on the (100) Silicon Surface: Calculation of the Adatom Charge and the Work Function

S. Yu. Davydov* and A. V. Pavlyk**
** Ioffe Physicotechnical Institute, Russian Academy of Sciences, St. Petersburg, 194021 Russia*
*** St. Petersburg State Electrical Engineering University (LÉTI), St. Petersburg, 197376 Russia*
e-mail: apavlyk@rol.ru

Received January 30, 2004

Abstract—The charges of adatoms and the work function variation $\Delta\phi$ caused by the deposition of submonolayer films of alkali metals on the (100) surface of silicon is calculated in the framework of a model that takes into account the dipole–dipole repulsion of adatoms and metallization of the adsorbate layer. Good agreement with the experimental data is achieved. Variation of the model parameters in the sequence Li $\longrightarrow$ Cs is analyzed. *© 2004 MAIK “Nauka/Interperiodica”.*

1. Work function ϕ and desorption energy E_d are the main macroscopic characteristics of the adsorption system [1, 2]. The study of the dependences of these characteristics on the surface coverage by adsorbed atoms $\Theta = N_a/N_{ML}$ (N_a is the actual density of adatoms, N_{ML} is the density of adatoms corresponding to the monolayer) is of the utmost interest, since it enables one to establish the character of adatoms interaction in the adsorption layer by using the corresponding theory [3, 4].

Nowadays, submonolayer metallic films on semiconductor substrates are extensively studied. The model system for such investigations is AM/Si(100), where AM is an alkali metal (which is clear since AM is the simplest metal atom containing only one electron in the outer shell), whereas the silicon (100) surface has been studied most thoroughly [5–7]. Numerous studies have shown that upon a coverage variation from zero to a monolayer in the system AM/Si(100), a number of structural transitions occurs, which are accompanied in addition by metal-semiconductor transitions (see [8] and references therein). So, it is clear that the theoretical description of such a system is an extremely complex problem.

However, the work function variation $\Delta\phi(\Theta)$ is a smooth function of coverage Θ and as a rule does not exhibit noticeable kinks or sudden changes. Moreover, the behavior of work function variation caused by the adsorption of metals on semiconductors is similar to that caused by the adsorption of metals on metals; in particular, a sharp decrease under small coverage is retarded as the coverage Θ increases and sometimes is even accompanied by an increase in ϕ under high coverage that is close to monolayer. Therefore, the theoretical models developed previously to account for the adsorption of metals on metals can in principle be applied for metal–semiconductor systems in spite of the distinction between the electronic structures of the substrates. We undertook the first attempt of this kind [9], where the Anderson–Newns model [10] adopted generally for adsorption on metallic substrates was reformulated for adsorption on semiconductors. The adatom film was considered as structureless, and only the increase of its density with Θ was taken into account. Such a simplification of the actual pattern (i.e., disregard of structural transitions) is possible because the main channel of the interaction of adatoms is the dipole–dipole repulsion [11], which depends primarily on the distance between nearest neighbors rather than on the details of the adsorbed layer geometry (see [12] and references therein). Since in addition to the dipole–dipole interaction the direct and indirect electronic exchange takes place between atoms in the film [11], the broadening of the quasi-level of the adatom Γ was taken into account in the model [9],

$$\Gamma(\Theta) = \Gamma_0(1 + \gamma\Theta), \tag{1}$$

where Γ_0 is the quasi-level halfwidth at zero coverage and γ is the dimensionless coefficient.

It must be emphasized that here Γ_0 accounts for all processes including Auger transitions as opposed to adsorption on a metallic substrate, where Γ_0 describes the probability of electron tunneling from an isolated adatom to the conduction band of the substrate (or back). The density of states at the isolated adatom is equal as before to

$$\rho_0 = \frac{1}{\pi}\frac{\Gamma_0}{(\omega - \Omega)^2 + \Gamma_0^2}, \tag{2}$$

where ω is the energy variable and Ω is the energy of the adatom quasi-level relative to the Fermi level of the substrate.

In this study, we will calculate the variations of charge and work function in the Li, Na, K, Rb,

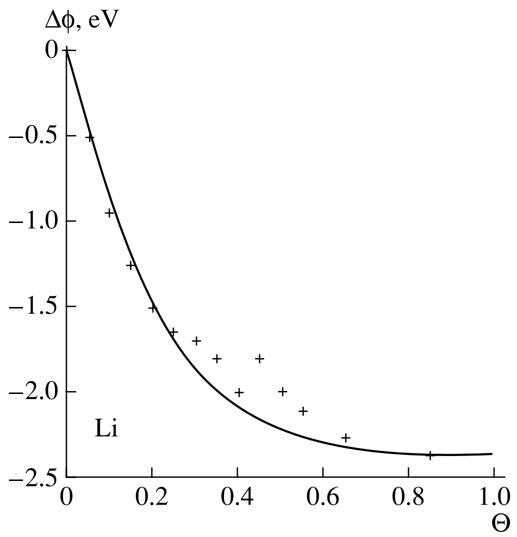

Fig. 1. Work function variation Δφ as a function of coverage Θ of the silicon (100) surface by lithium atoms. Solid curve—theory, +—experiment [14].

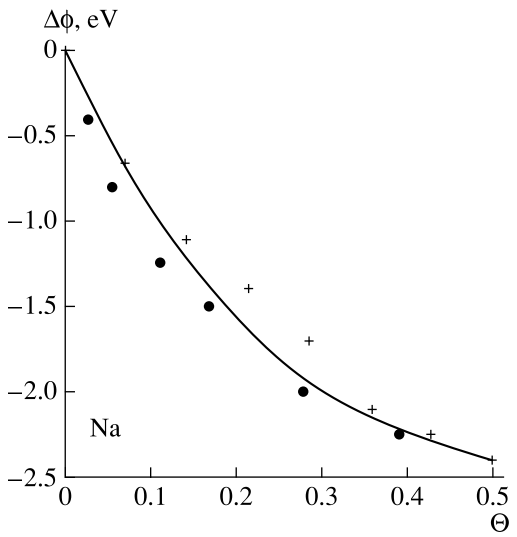

Fig. 2. Same as Fig. 1, but for sodium adatoms. Solid curve—theory; experiment: +—[18], ●—[19].

Cs/Si(100) in the framework of the model [9] and discuss the results of these calculations.

2. Let us present the design equations of the model [9]. The adatom charge $Z = 1 - n$ (n is the occupation number of the s orbital) can be determined from the self-consistent equation

$$\begin{gathered} Z(\Theta) = \frac{2}{\pi}\arctan\frac{\Omega - \xi\theta^{3/2}Z(\Theta)}{\Gamma(\Theta)}, \\ \xi = 2e^2\lambda^2N_{ML}^{3/2}A, \quad \Omega = \phi - I + \Delta, \\ \Delta = e^2/4\lambda. \end{gathered} \tag{3}$$

Here, I is the ionization potential; Δ is the Coulomb shift due to the interaction of the adatom's electron with the electrons in the substrate, which we calculate disregarding the dielectric correction $(\varepsilon_0 - 1)/(\varepsilon_0 + 1)$, where ε_0 is the static dielectric constant; ξ is the constant of the dipole–dipole repulsion of adatoms; 2λ is the shoulder of the surface dipole formed by an adsorbed atom and its image in the substrate; $A \approx 10$ is the dimensionless coefficient weakly dependent on the geometry of the adatom geometry, which has a similar meaning as the Madelung constant for the bulk crystal. Work function variation $\Delta\phi$ is determined as follows:

$$\begin{gathered} \Delta\phi(\Theta) = -\Phi\Theta Z, \\ \Phi = 4\pi e^2N_{ML}\lambda. \end{gathered} \tag{4}$$

The scheme of choice of the model parameters was described in [9] as follows. In all cases, we assume the density of adatoms in the monolayer equal to 1 ML = 6.78×10^{14} cm^{-2} (it is the density of silicon atoms on the nonreconstructed (100) surface) and set the work function ϕ for the clean surface $\phi = 4.9$ eV [13] (for some strange reason, experimentalists in their papers almost never present values for the work function of a clean surface). The λ value is assumed to be equal to half the sum of the ionic r_i and atomic r_a radii (their values, as well as the ionization potential values I, are taken from [13]), since with increasing Θ, depolarization of the adatom takes place and the radius of the adatom shell should increase as a result [4]. The charge value $Z_0 \equiv Z(\Theta \longrightarrow 0)$ we determine by adjusting the theoretical value $(d\phi/d\Theta)_{\Theta \to 0}$ to the slope $\Delta\phi(\Theta)$ determined from the experiment in the limit of zero coverage. Hence it follows that

$$\Gamma_0 = \frac{\Omega}{\tan\left(\frac{\pi}{2}Z_0\right)}. \tag{5}$$

Then we determine the parameter γ using the experimental value of $\Delta\phi_{ML} \equiv \Delta\phi(\Theta = 1)$, or (see below) $\Delta\phi^*_{ML} \equiv \Delta\phi(\Theta = \Theta^*)$. In recent years, it has become customary among experimentalists to present data on the work function variation as a function of exposure time τ (time of deposition of adatoms on the substrate surface) even without attempts to assign a specific value of Θ to the measured value of $\Delta\phi$. From the point of view of the theory, this involves certain difficulties, since a theorist should take some value of τ as τ_{ML}, which corresponds to monolayer coverage.

3. The results of calculations of $\Delta\phi(\Theta)$ in comparison with experimental data are presented in Figs. 1–5, and the calculated function $Z(\Theta)$ is shown in Fig. 6. The values of the parameters calculated and obtained from the fitting to the experimental data are listed in the table.

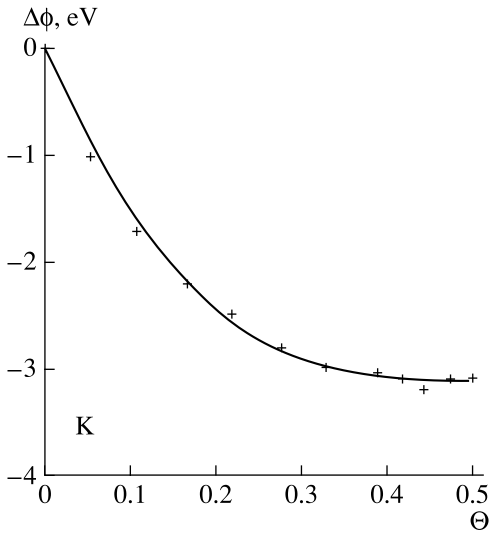

Fig. 3. Same as Fig. 1, but for potassium adatoms. Solid curve—theory, +—experiment [19].

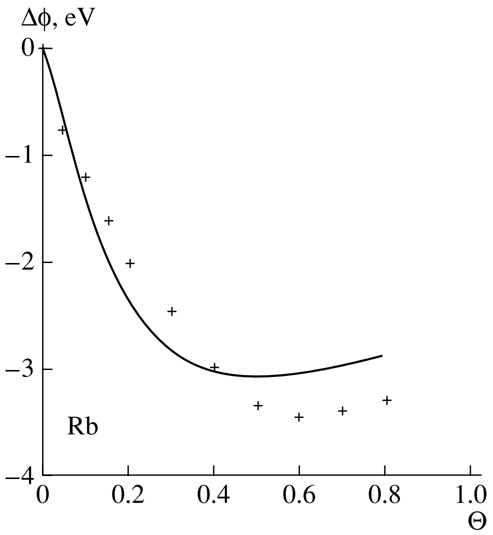

Fig. 4. Same as Fig. 1, but for rubidium adatoms. Solid curve—theory, +—experiment [22].

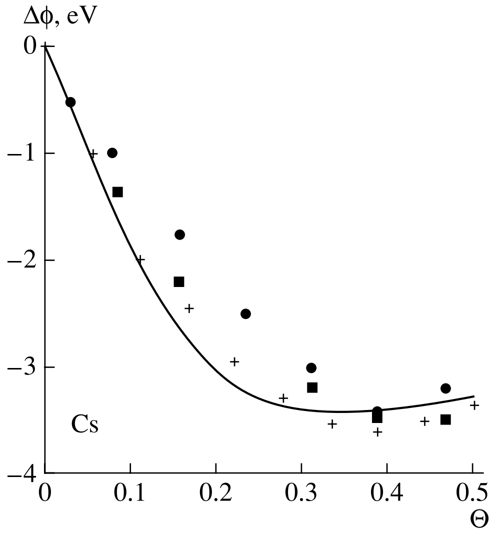

Fig. 5. Same as Fig. 1, but for cesium adatoms. Solid curve—theory; experiment: +— [19], ●—[23], ■—[24].

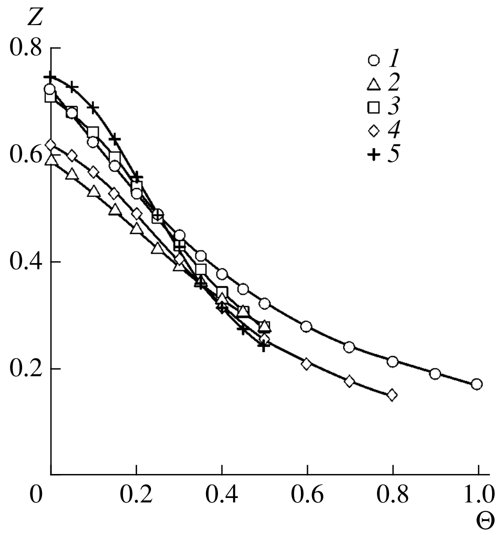

Fig. 6. Variation of the adatom charge Z as a function of coverage Θ of the silicon (100) surface by lithium (*1*), sodium (*2*), potassium (*3*), rubidium (*4*), and cesium (*5*) atoms.

Now we come to the discussion of the results.

Lithium. The work function of the Li/Si(100) system in the range of submonolayer coverages was measured in [14] (see also [15], where the range of small Θ was studied). In our calculations, we assumed τ_{ML} = 10 min. The agreement with experiment can be admitted as quite satisfactory. The sudden changes in Δφ at Θ ≈ 0.3 and 0.45 are related to the structural transitions (2 × 2) to (2 × 1) and to $(3\sqrt{2} \times \sqrt{2})R45°$, respectively. Clearly, our structureless model cannot account for these peculiarities of the dependence Δφ(Θ).

Sodium. The results of ΔΦ(Θ) measurements are presented in [16–19] also as a function of τ and not of Θ. We established the correspondence between the τ and Θ values using [16], where the characteristic drop of the work function was assigned to the coverage Θ = 0.5. The fitting was carried out using the data of [18], the value of Θ = 0.5 was attributed to the exposure time $\tau_{0.5}$ = 7 min. The results are presented in Fig. 2. There is a reasonable agreement between calculated and experimental data.

Potassium. Adsorption of potassium on Si(100) was studied in [19]. Because the data on adsorption of Na (and Cs) are also presented in this paper, relating again the sudden change in the work function in the system Na/Si(100) to the coverage $\Theta = 0.5$ [16], we find that the relative coverage $\theta^* = 0.9$ adopted in [19] corresponds to the half-monolayer coverage of the surface by potassium. Figure 3 demonstrates good agreement between theory and experiment. Note that essentially the same $\Delta\phi(\Theta)$ dependence is typical of the adsorption on the (111) silicon surface [20, 21].

Rubidium. The results of the $\Delta\phi(\Theta)$ calculation are presented in Fig. 4 in comparison with the experimental data of [22], where $\tau_{ML} = 10$ min. Here, the discrepancy between the calculated and experimental data is rather strong under high coverage. Better agreement could be obtained by changing the scenario of parameter fitting. However, we did not do this, assuming that additional experimental data are necessary to make final conclusions.

Cesium. Cesium adsorption on the surface of semiconductors is the most thoroughly studied in the context of the negative electron affinity problem. Fitting of the parameters was performed in [19], assuming again that $\theta^* = 0.9$ corresponds to $\Theta = 0.5$. The results of calculations are compared to the data of experiments [19, 23, 24] in Fig. 5. Here, we also assume that a good agreement with the experiment is achieved.

The charge of adatoms $Z(\Theta)$ is shown in Fig. 6. This is a very important parameter that determines the band bending of the semiconductor and, hence, the height of the Schottky barrier formed at the metal-semiconductor interface [25].

4. Let us now discuss model parameters and consider their variation in the sequence Li ⟶ Cs. In accordance with the increase of the adsorption bond length λ in this sequence, Φ, i.e., the work function variation at $\Theta = Z = 1$, increases linearly, whereas the constant of the dipole–dipole interaction ξ increases quadratically as we pass from lithium to cesium. The position of the adatom quasi-level Ω changes insignificantly (from here on, Na is an exception) in spite of the fact that the ionization energy in the sequence Li ⟶ Cs decreases from 5.39 eV for lithium to 3.89 eV for cesium (see Eqs. (3)). This is because the Coulomb shift Δ of the quasilevel decreases due to an increase in λ. Thus, the two trends balance each other. The charge Z_0 of an isolated adatom also changes insignificantly and the quasi-level width Γ_0 defined by relation (5) remains approximately constant as a result (again with the exception of Na). And finally, the band-broadening parameter γ decays drastically in going from lithium to cesium and the γ value for Li seems to be too high (note that in the case of Rb, we had to set $\gamma = 0$, since our scheme for determining the parameters gave a value of $\gamma < 0$; unfortunately, we have found no experimental data on rubidium adsorption besides [22]).

Model parameters

Parameter	Li	Na	K	Rb	Cs
λ	1.125	1.39	1.845	1.985	2.24
Ω	2.71	2.30	2.51	2.53	2.62
Γ_0	1.25	1.73	1.24	0.96	1.10
ξ	6.44	9.82	17.31	20.03	25.51
Φ	13.80	17.05	22.64	24.36	27.16
γ	3.72	1.26	0.93	0	0.08
Z_0	0.72	0.59	0.71	0.62	0.75
$Z_{0.5}$	0.32	0.28	0.27	0.26	0.24
$\mathrm{Z_{ML}}$	0.17	–	–	0.13	–

Note: λ is given in Å; Ω_0, Δ, ξ, Φ, Γ_0 are in eV.

As shown in [26, 27], the band broadening of the quasi-level can be described by the parameter

$$\eta = \frac{T_{ML}^2 \Gamma_0 \Omega}{(\Omega^2 + \Gamma_0^2)^2}, \tag{6}$$

where T_{ML} is the effective integral of the electron transition between the neighboring adatoms in the monolayer.

Since Ω and Γ_0 change only slightly in going from Li to Cs, it can be assumed that T_{ML} decreases in going from lithium to cesium. If the distance between alkali metal adatoms in the monolayer on the silicon (100) surface were equal to the distances d between the nearest neighbors in bulk crystals (d = 3.02, 3.66, 4.53, 4.84, 5.24 Å [28] for Li, Na, K, Rb, Cs, respectively), assuming that $T_{ML} \sim d^{-2}$ [29], we obtain for $(d/d_{\rm Cs})^{-4}$ the following values in the sequence Li ⟶ Cs: 9 : 4.2 : 1.8 : 1.4 : 1. From the table we have for $(\gamma/\gamma_{\rm Cs})$: 46.5 : 15.8 : 11.6 : 0:1. These series are similar with the exception of the case of Rb adsorption. Here, it should be stressed that parameter γ describes both the direct tunneling of the electrons between neighboring adatoms and their indirect exchange through the substrate, whereas the integral T_{ML} conforms to the direct exchange only [30]. Therefore, the presented estimates for T_{ML} are rather crude.

Thus, in the framework of the simple model, the alkali metal adsorption on the silicon (100) surface has been adequately described using only two fitting parameters (Z_0 and Z_{ML}) determined from experiment. The fact that our results agree with the experimental data during intermediate coverage $0 < \Theta < 1$ indicates the feasibility of the proposed model.

REFERENCES

1. É. Ya. Zandberg and N. I. Ionov, *Surface Ionization* (Nauka, Moscow, 1969) [in Russian].

2. L. A. Bol’shov, A. P. Napartovich, A. G. Naumovets, and A. G. Fedorus, Usp. Fiz. Nauk **122**, 125 (1977) [Sov. Phys. Usp. **20**, 432 (1977)].
3. O. M. Braun, Ukr. Fiz. Zh. **23**, 1234 (1978).
4. O. M. Braun and V. K. Medvedev, Usp. Fiz. Nauk **157**, 631 (1989) [Sov. Phys. Usp. **32**, 328 (1989)].
5. *Physics and Chemistry of Alkali Metal Adsorption*, Ed. by H. P. Bonsel, A. M. Bradshow, and G. Ertl (Elsevier, Amsterdam, 1989).
6. S. Pick, Surf. Sci. Rep. **12** (3), 99 (1990).
7. G. P. Srivastava, Rep. Prog. Phys. **60**, 561 (1997).
8. S. Yu. Davydov, Fiz. Tverd. Tela (St. Petersburg) **42**, 1129 (2000) [Phys. Solid State **42**, 1164 (2000)].
9. S. Yu. Davydov and A. V. Pavlyk, Fiz. Tekh. Poluprovodn. (St. Petersburg) **35**, 831 (2001) [Semiconductors **35**, 796 (2001)].
10. D. M. Newns, Phys. Rev. **178**, 1123 (1969).
11. O. M. Braun and V. K. Medvedev, Usp. Fiz. Nauk **157**, 631 (1989) [Sov. Phys. Usp. **32**, 328 (1989)].
12. J. P. Muscat and D. M. Newns, J. Phys. C **7**, 2630 (1974).
13. *A Handbook of Physical Quantities*, Ed. by I. S. Grigoriev and E. Z. Meilikhov (Énergoatomizdat, Moscow, 1991; CRC, Boca Raton, 1997).
14. C. Y. Kim, K. S. Shin, K. D. Lee, and J. W. Chung, Surf. Sci. **324**, 8 (1995).
15. H. Klein, M. Eckhardt, and D. Fick, Surf. Sci. **329**, 71 (1995).
16. M. Tikhov, G. Boishin, and L. Surnev, Surf. Sci. **241**, 103 (1991).
17. L. S. O. Johanson and B. Reil, Phys. Rev. B **47**, 1401 (1993).
18. Y.-C. Chao, L. S. O. Johanson, and R. I. G. Uhrberg, Phys. Rev. B **55**, 7198 (1997).
19. T. Kan, K. Misukawa, T. Ueyama, *et al.*, Surf. Sci. **460**, 214 (2000).
20. K. Sakamoto, T. Okuda, H. Nashimoto, *et al.*, Phys. Rev. B **50**, 1725 (1994).
21. D. Gorelik, S. Aloni, J. Eitle, *et al.*, J. Chem. Phys. **108**, 9877 (1998).
22. L. S. O. Johansson, T. Duteneyer, L. Duda, and B. Reihl, Phys. Rev. B **58**, 5001 (1998).
23. J. E. Ortega, E. M. Oellig, J. Ferron, and R. Miranda, Phys. Rev. B **36**, 6213 (1987).
24. Y.-C. Chao, L. S. O. Johanson, and R. I. G. Uhrberg, Phys. Rev. B **54**, 5901 (1996).
25. W. Mönch, Rep. Prog. Phys. **53**, 221 (1990).
26. S. Y. Davydov, Surf. Sci. **407**, L652 (1998).
27. S. Y. Davydov, Surf. Sci. **411**, L878 (1998).
28. C. Kittel, *Introduction to Solid State Physics*, 5th ed. (Wiley, New York, 1976; Nauka, Moscow, 1978).
29. W. A. Harrison, *Electronic Structure and the Properties of Solids: The Physics of the Chemical Bond* (Freeman, San Francisco, 1980; Mir, Moscow, 1983), Vol. 1.
30. S. Yu. Davydov, Fiz. Tverd. Tela (Leningrad) **20**, 1752 (1978) [Sov. Phys. Solid State **20**, 1013 (1978)].

Translated by M. Lebedev

Technical Physics, Vol. 49, No. 8, 2004, pp. 1055–1063. Translated from Zhurnal Tekhnicheskoĭ Fiziki, Vol. 74, No. 8, 2004, pp. 100–108.
Original Russian Text Copyright © 2004 by T. Yakhno, V. Yakhno, Sanin, Sanina, Pelyushenko.

Protein and Salt: Spatiotemporal Dynamics of Events in a Drying Drop

T. A. Yakhno, V. G. Yakhno, A. G. Sanin, O. A. Sanina, and A. S. Pelyushenko

Institute of Applied Physics, Russian Academy of Sciences,
Nizhni Novgorod, 603950 Russia
e-mail: tanya@awp.nnov.ru; yakhno@appl.sci-nnov.ru

Received January 12, 2004

Abstract—Self-organization processes in biological fluids and aqueous solutions containing protein and salt in various ratios have been studied in drops drying on the surface of a solid substrate. Morphological and histochemical data show that the salt solution exhibits the phase transition in an organic jelly matrix formed in the system. The physical properties of this matrix influence the kinetics of salt crystallization and the morphological features of the observed salt patterns. Controlled UV-radiation-induced protein damage in protein–salt solutions violates the formation of a regular gel and introduces chaotic features into the salt pattern. A new method of investigation of the self-organization processes in drying drops is developed based on acoustomechanical impedance measurements. It is suggested that the dynamic parameters of salt crystallization in drying drops bear information on the composition of the whole biological fluid. © *2004 MAIK "Nauka/Interperiodica".*

INTRODUCTION

In recent years, there has been increasing interest in the investigation of processes in drying drops of liquids [1–5]. On the one hand, this is related to the development of technologies involving such processes (e.g., spray application of lacquer and paint coatings on various substrates), equipment (e.g., jet printers), and methods of predicting atmospheric phenomena. On the other hand, a drying drop is an interesting object for basic physics: it offers a natural model of self-organizing systems with a rich set of possible scenarios determined by the liquid composition, substrate properties, and ambient conditions [6–8]. The character of salt pattern formation in drying drops of biological fluids is an important auxiliary criterion in medical diagnostics [9]. The knowledge of laws governing the spatiotemporal dynamics of events in drying drops is important in selecting their integral evaluation criteria and in developing methods and techniques for the investigation of such processes.

This paper reports on the results of investigation of the sequence of phase transitions in drying drops of biological fluids and model protein–salt solutions. The obtained data elucidate some causal relations between the solution composition and the character of salt crystallization.

MATERIALS AND METHODS

The experiments were performed with samples of biological fluids taken from ten healthy donors (saliva, urine, and blood serum) and from ten patients suffering from various liver disorders (saliva and blood serum). In each experiment, six to eight 5-μl drops of a given fluid were placed onto a separate glass substrate and allowed to dry for one day at room temperature. In some experiments, the drops on glass slides were dried in a microscope (MBS-10) equipped with a TV camera linked to a computer. By means of the Fly Video program, the process of structure formation was studied using digitized images recorded every minute into the computer's memory.

The spots of drops that dried on a substrate were fixed for 10 min in methanol at 4°C and stained either with cyanine blue to reveal glycosaminoglycans and acid mucopolysacchcarides, or with periodic acid (Schiff's reagent) to reveal glycoproteins (periodic acid–Schiff reaction) [10]. The stained spots were studied in a LUMAM-I3 microscope.

In a separate series of experiments, 5-μl drops of blood serum were sequentially applied onto glass slides with a time interval of 1 min (a total of 40 drops). One minute after application of the last drop, all glasses were simultaneously blotted with one layer of a sterile bandage. As a result, the remaining liquid was absorbed and it was possible to trace the development of processes at the drop–substrate interface.

We have also studied the character of NaCl crystallization in drying drops of a model protein solution (0.5 mg/ml carboanhydraze in physiological solution) before and after exposure to XeCl excimer laser radiation ($\lambda = 308$ nm) [11]. The extent of the UV-radiation-induced protein damage was evaluated by fast protein liquid chromatography (FPLC system, Pharmacia Biotech). The effect of protein concentration on the dynamics of salt crystallization was studied using 7, 8,

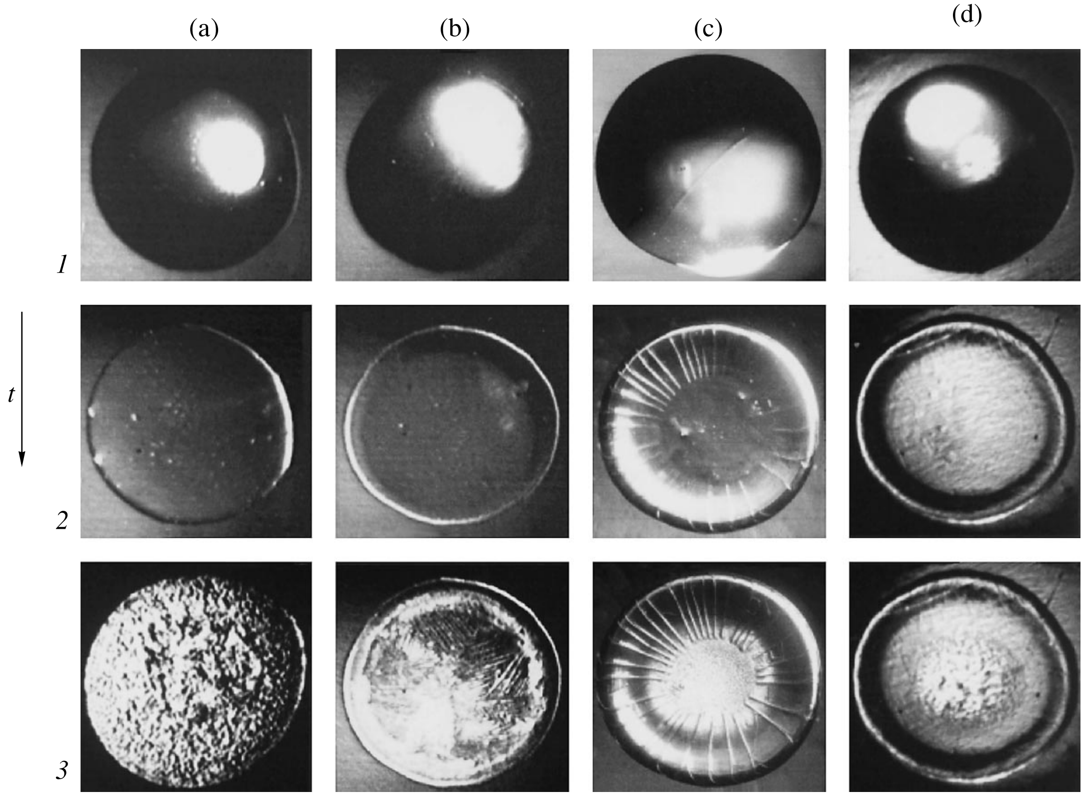

Fig. 1. Phase transitions in drying drops of (a–c) urine, saliva, and blood serum, respectively, of a healthy donor and (d) blood serum of a patient with hepatitis: (*1*) beginning of drying; (*2*) gel matrix formation; (*3*) phase transition in the salt solution (magnification, ×5).

and 9 wt % solutions of dry bovine serum albumin (BSA) in physiological NaCl solution.

The dynamical characteristics of phase transitions in drying drops were determined by measuring the acoustomechanical impedance (AMI) using a computer-controlled setup described elsewhere [12]. The idea of this method is essentially as follows. When a 5-μl liquid drop is drying on the surface of a quartz resonator plate oscillating at a constant frequency (equal to the resonance frequency of the unloaded resonator, 60 kHz), there arises a shear wave highly sensitive to the formation and growth of a new phase at the liquid–quartz interface. The experimental setup measures a change in the complex electric conductivity of the liquid–quartz system, calculates the parameters of the AMI dynamics in the drying drop, and displays their variation on a monitor in the real time scale.

RESULTS AND DISCUSSION

Previously [12, 13], we reported that the first stage of drying in the drops of biological fluids is accompanied by flattening of the initial dome. The mechanism of this flattening is related to the drop attachment to the substrate surface along the boundary of three phases [7, 14]. The process of dome flattening gives rise to centrifugal flows carrying particles of the solid phase to the periphery [7, 8]. A common feature for the drops of all biological fluids studied was the formation of an organic jelly matrix in the initial stage of solution condensation, which is followed by a phase transition in the salt solution in this matrix (Fig. 1). Therefore, the kinetics of salt crystallization may bear information about peculiarities of the gel structure and, hence, on the whole fluid structure. In order to check for this assumption, the first series of experiments was devoted to investigation of the kinetics of a phase transition in the salt solution depending on the protein content in this solution.

Figure 2 shows the AMI curves reflecting the dynamics of structure formation in the drops of 7, 8, and 9 wt % BSA solutions in physiological salt solution (0.9 wt% NaCl). We divide each curve into five regions corresponding to various stages of the process. Let us consider these stages as manifested in curve *3* of Fig. 2. With the onset of drying, a drop adheres to the substrate, which is accompanied by flattening of the dome and the formation of a protein ring (region *ab*). The next stage (region *bc*) corresponds to the gel formation. Region *cd* reflects the phase transition (crystallization) in the salt solution. This stage is followed by evaporation of the remaining free water (region *de*). The final region *ef* corresponds to the weight of a dry residue containing weakly bound and immobilized water. Thus, measurement of the AMI dynamics (Fig. 2) shows various stages in the structure formation and reveals differ-

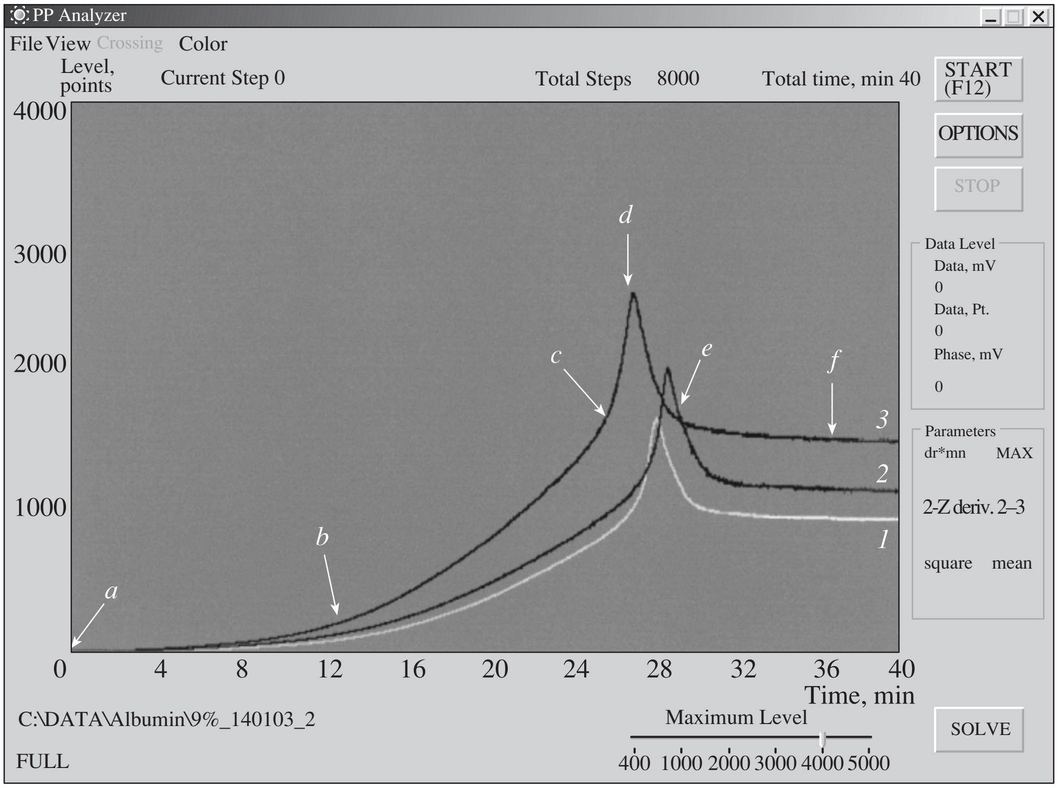

Current Step 0

Total Steps 8000

Total time, min 40

Data, mV
0
Data, Pt.
0
Phase, mV
0

2-Z deriv. 2–3

C:\DATA\Albumin\9%_140103_2

FULL

Fig. 2. The dynamics of AMI signal (*Y* axis, arb. units) variation with time (*X* axis, min) in drying drops of (*1*) 7, (*2*) 8, and (*3*) 9 wt % BSA solutions in 0.9% NaCl (physiological solution): arrows indicate the boundaries *a*–*f* of regions corresponding to different stages of the process (see the text for explanation).

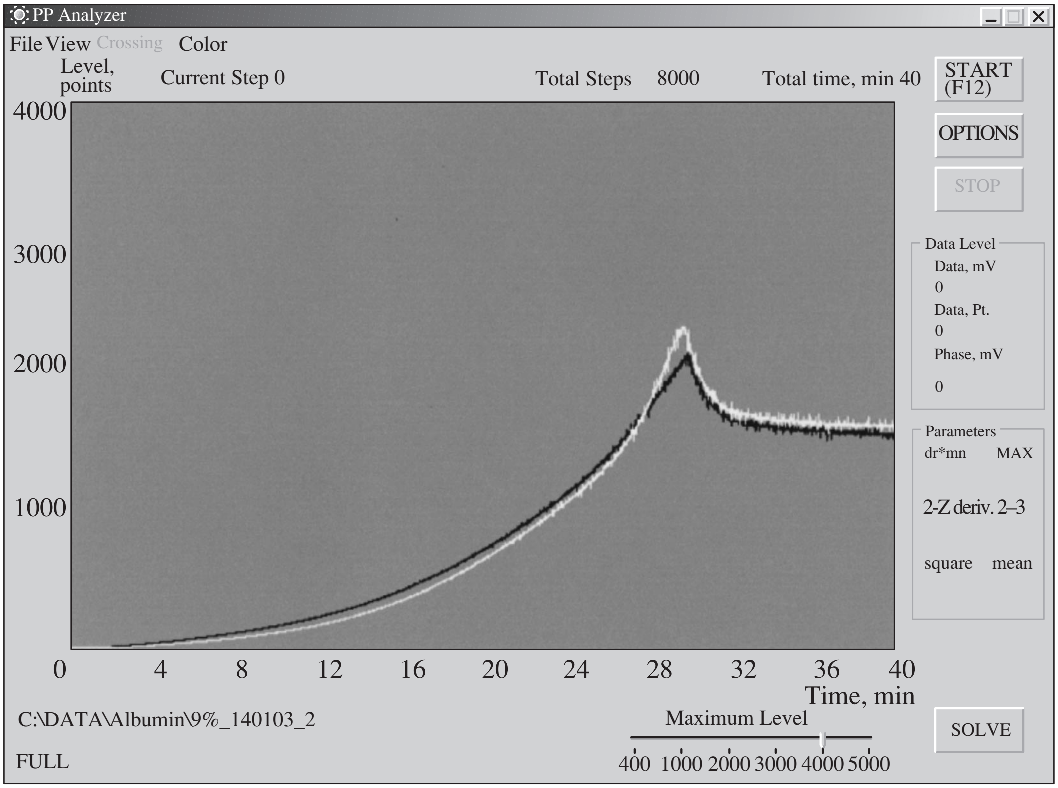

Current Step 0

Total Steps 8000

Total time, min 40

Data, mV
0
Data, Pt.
0
Phase, mV
0

2-Z deriv. 2–3

C:\DATA\Albumin\9%_140103_2

FULL

Fig. 3. The dynamics of AMI signal (*Y* axis, arb. units) variation with time (*X* axis, min) in drying drops of blood plasma (black curve) and serum (bright curve) prepared from the same sample of donor blood.

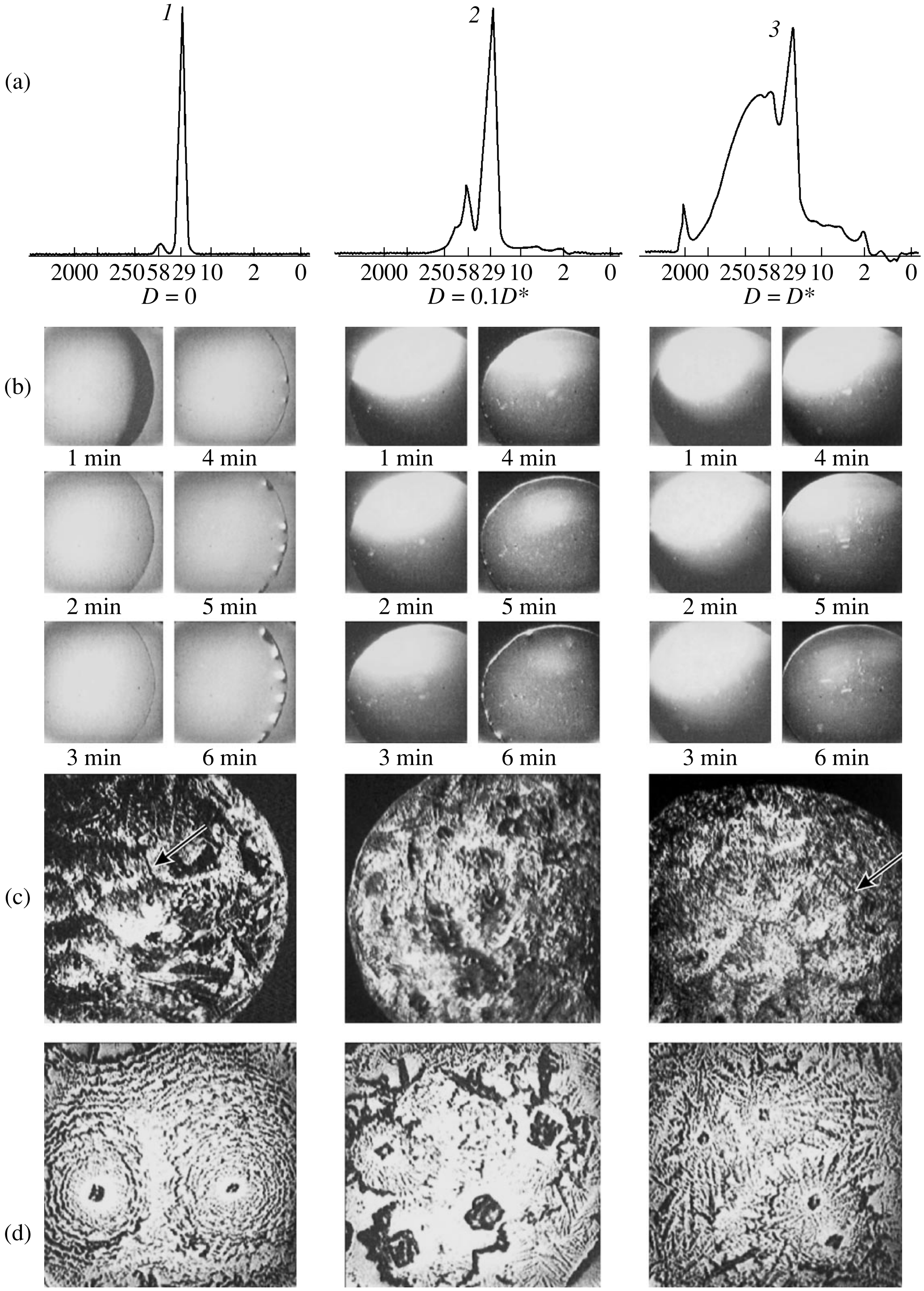

Fig. 4. Structure formation in drying drops of 0.5 mg/ml carboanhydraze solution in physiological solution (*1*) before and (*2*, *3*) after UV irradiation to a dose of 20 and 200 J/m^2, respectively: (a) molecular mass distribution; (b) the pattern of light scattering during the first six minutes of drying; (c) micrographs of the dry spot; (d) micrographs of salt patterns in the central zone indicated by arrows in (c) (magnification, ×140).

ences between solutions with various protein concentrations. The observed distinctions can be related to different densities of the gel: an increase in the protein content leads to slower rate of water evaporation in the salt crystallization stage (region *cd*), which limits the rate of crystallization.

Analogous results were obtained in a comparative study of the dynamics of structure formation in the drying drops of plasma and serum prepared from blood of the same donor. Indeed, the partial removal of protein from the liquid blood fraction accelerated the phase transition in the salt solution (Fig. 3).[1]

The next series of experiments was devoted to the kinetics of structure formation in drying drops of the model protein–salt solutions with different extent of the UV-radiation-induced protein damage.[2] In the intact model protein solution (0.5 mg/ml carboanhydraze in physiological solution), the protein was present in the form of monomers (Fig. 4a, curve *1*). Exposure to XeCl excimer laser radiation to a dose of 20 J/m^2 led to the appearance of dimers and molecular fragments (curve *2*). Upon a tenfold increase in the radiation dose, protein mostly occurred in the form of dimer, trimer, and polymer fractions with a considerable amount of fragments (curve *3*).

A change in the state of protein in solution was indicated by the light-scattering ability of drops within the very first minutes of drying (Fig. 4b). The drops of unirradiated solution retained a homogeneous structure up to the moment of salt crystallization. The relief of dry spots exhibited a central zone of the salt pattern (Fig. 4c), representing a regular NaCl crystal, surrounded by concentric scalloped structures (Fig. 4d).

Irradiation of the protein solution to a dose of 20 J/m^2 led to a significant increase in the light scattering from drying drops as a result of protein aggregation and was accompanied by the formation of a coarse protein matrix with an admixture of protein aggregates (Fig. 4b, series *2*). the central zone of the spot appeared disordered (Fig. 4c, image *2*) and consisted predominantly of coarse salt crystals with distorted shapes and rare patterns with broken symmetry (Fig. 4d, image *2*).

An increase in the radiation dose to 200 J/m^2 was accompanied by very rapid aggregation of the damaged protein: massive aggregates precipitated on the substrate within one minute and did not take part in subsequent events. As a result, the content of protein in the liquid part of the irradiated drop was much lower than in the initial solution. Apparently, the remaining protein formed a more homogeneous medium than that in the drop irradiated to a lower dose. For this reason, the dry spot relief again exhibited a clear central zone with salt patterns. The patterns also represented centrosymmetric figures, but their shapes were different from those observed in the case of unirradiated solutions: each pattern comprised a salt crystal surrounded by radial arrowlike structures (Fig. 4d, image *3*).

Figure 5 shows the AMI signal dynamics reflecting the aforementioned peculiarities in the process of structure formation in drying drops of the model protein solution. Acceleration of the protein aggregation and its precipitation on the quartz crystal surface upon irradiation are manifested in the radiation-dose-dependent leftward shift of the ascending part of the curve. The chaotic structure formation in the drops irradiated to a dose of 20 J/m^2 corresponds to a higher peak, which can be explained by a greater amount of water immobilized in the drying gel. Broadening of the AMI curve and the appearance of secondary peaks upon irradiation to a dose of 200 J/m^2 is evidence of violated spatiotemporal synchronicity of the process of salt crystallization.

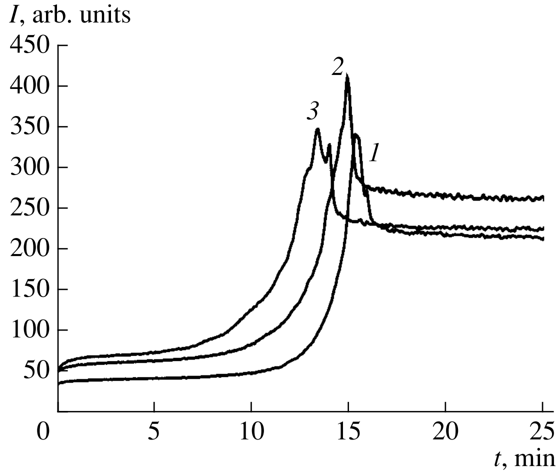

Fig. 5. Dynamics of the AMI signal variation in the drying drops of 0.5 mg/ml carboanhydraze solution in physiological solution measured (*1*) before and (*2*, *3*) after UV irradiation to a dose of 20 and 200 J/m^2, respectively.

Thus, the degree of protein damage influences the kinetic parameters of salt crystallization in protein–salt solutions. The dynamics of AMI signals measured in the drying drops reliably reflects physicochemical features of the structure formation related to both the concentration and qualitative state of the protein.

The events in drying drops of blood plasma and serum are characterized by more complicated patterns. To the best of our knowledge, the first description of the dynamics of structure formation in drying drops of protein solutions was presented by Rapis [15]. According to [15], various protein solutions (including blood serum) exhibit the following sequence of events: (i) the formation of rings at the periphery of drops; (ii) the appearance of radial arclike cracks; (iii) the formation of the central zone free of the rings. The dry spots of various protein solutions exhibited the characteristic “rosette,” formed as a result of the radial cracking, and blocks resembling “cages with balls” formed as a result of the transverse cracking. In [15], the observed phenomena were attributed for the first time to the process of self-organization in a protein solution occurring under nonequilibrium conditions. These investigations were continued in [9], where a considerable body of experimental data was collected for the structure formation in the drops of human biological fluids in application to medical diagnostics. In [9], morphological

---

[1] Blood serum differs from plasma by the absence of protein fibrinogen (which amounts to 4–5 wt % in the blood plasma).

[2] These results were obtained in the joint investigation [11].

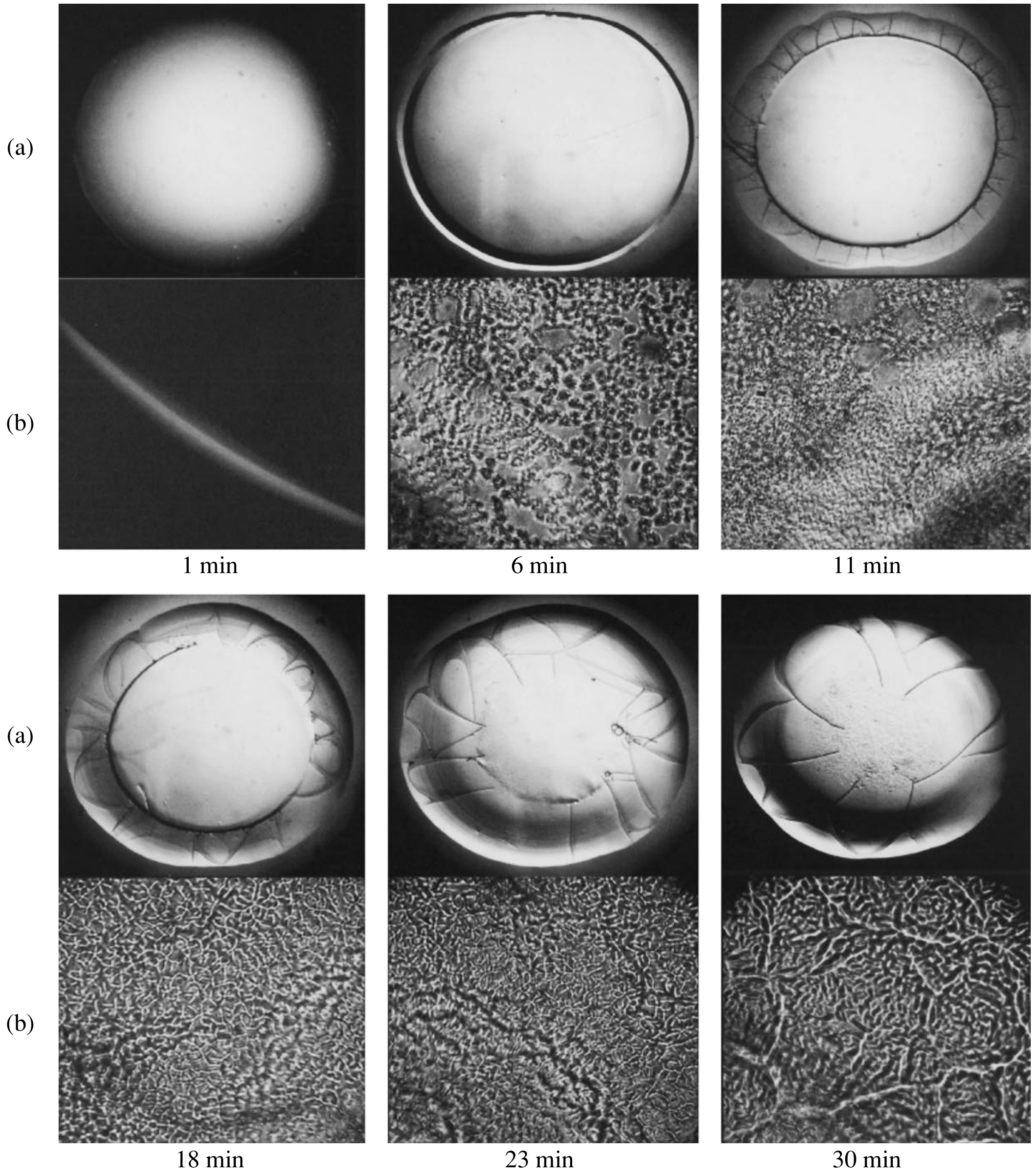

Fig. 6. Sequential stages of structure formation in drying drops of blood serum at the liquid–substrate interface revealed via removal of the liquid part of drops at various moments of time after the beginning of drying: (a) images of the solid phase formed in the drops (magnification, ×5); (b) gel structure (magnification, ×140).

description was provided for the drying drops of blood serum and the morphological features of salt and protein structures were studied depending on the concentrations of these components in biological fluids. Our observations coincide with the previously reported data on the sequence of morphological patterns observed in drying drops of blood serum under a microscope. However, some published data and the new results obtained in our investigations allow the process to be interpreted from a somewhat different standpoint.

We have traced the sequence of structures formed in the drying drops of blood serum by terminating the process via removal of the liquid part of drops at various moments of time after the beginning of drying. The results presented in Fig. 6 illustrate the development of processes at the liquid–substrate interface. Figure 7 shows the dynamics of structure formation as reflected by the AMI data for the drying drop of the same blood serum.

As early as in one minute after placing a drop onto the glass substrate, a solid ring appeared indicating the

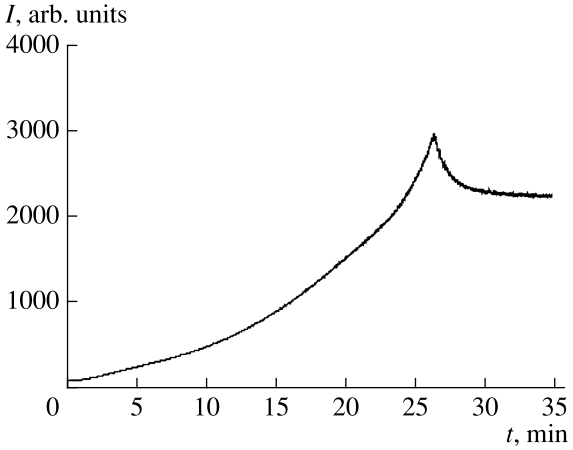

Fig. 7. The AMI signal dynamics in a drying drop of blood serum used in the experiment presented in Fig. 6.

line of drop attachment to the substrate. The same phenomenon was observed in suspensions of polystyrene microspheres in deionized water and related to centrifugal hydrodynamic flows arising in drying drops [7]. For this reason, we believe that a certain role in the process is played by the aggregation of protein, which is manifested by gradually increasing light scattering. A part of protein aggregates are transferred to the periphery to form the attachment line, while the other are precipitated onto the substrate and involved in the gel formation in the course of condensation (Fig. 6).

Thus, the front of structure formation in the liquid part of the drop propagates simultaneously with the gel layer formation at the liquid–substrate interface: the liquid drop “moves” over the gel surface leaving concentric circles behind (Fig. 8a).

The nature of this front motion in drying drops, as described in detail by Geguzin [14], is related to a periodic jumplike restoration of the most equilibrium drop shape corresponding to the minimum ratio of the surface area to volume. As the drop boundary moves toward the center, the ratio of protein to salt changes in favor of the latter component. As is known [16, 17], the presence of salts significantly influences the process of gel formation in solution by modifying both the solution structure and the polymer properties. It was demonstrated [18] that increasing salt concentration in protein–salt solutions inhibits the gel formation. Probably, it is this circumstance that accounts for the typical concave shape of a drying drop of blood serum or plasma. An increase in the concentration of salts leads to a decrease in the coefficient of water diffusion through the gel [19]. For this reason, the front of salt crystallization propagates from the periphery to the center (Figs. 8c and 8d). If the gel is loose, it cannot hold the drop on the surface [20]. The front of structure formation in the gel is difficult to distinguish under an optical microscope (Fig. 1d). In some cases, it is possible to observe the formation and separation of a rather dense gel, with residues of the liquid phase of the blood serum drying on a hydrophobic surface of this gel (Figs. 8e and 8f).

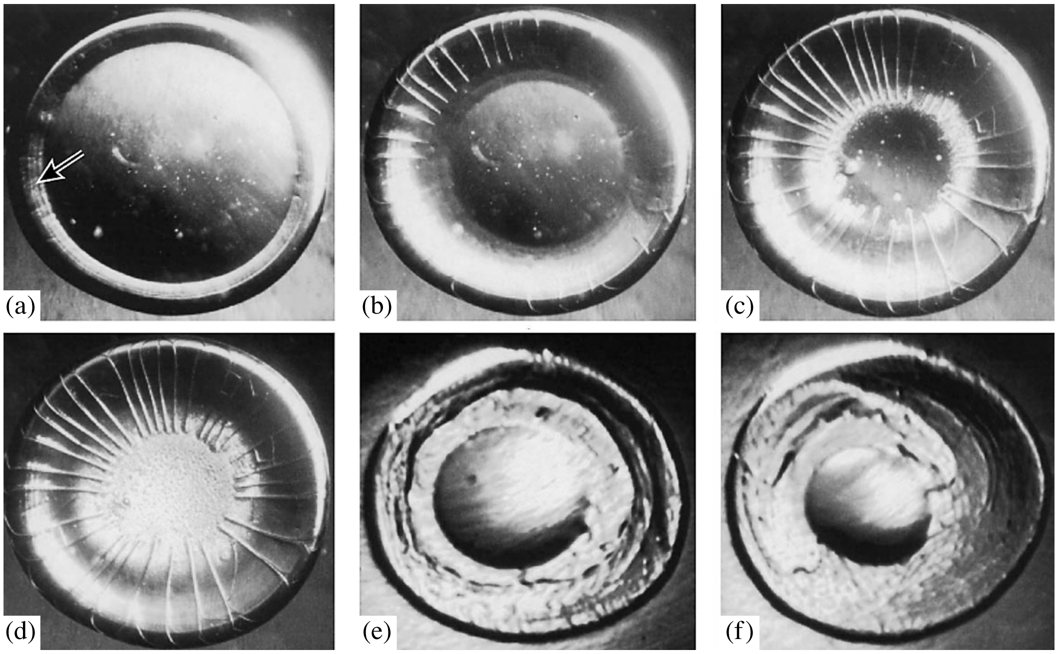

Fig. 8. Propagation of the structure formation front in drying drops: (a–d) the beginning of salt crystallization in a drop of the blood serum of a healthy donor (the arrow indicates traces of the front propagation); (e, f) liquid phase on the surface of a dense gel in a drop of the blood serum of a patient suffering from chronic liver disorder.

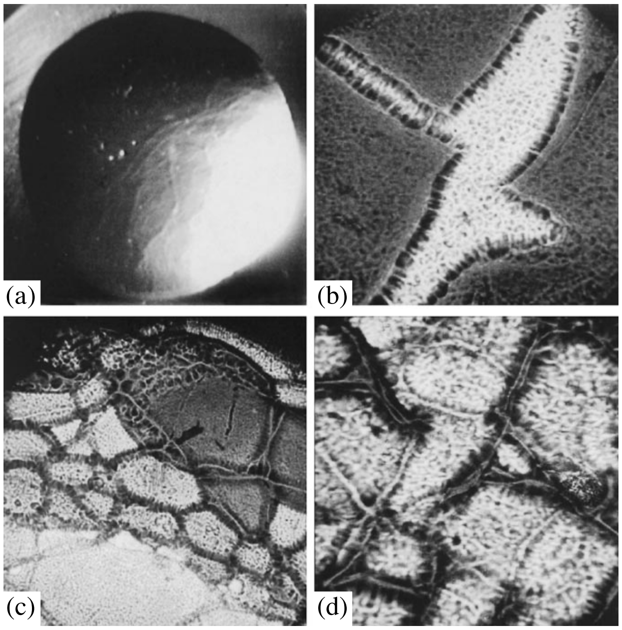

Fig. 9. Micrographs of the surface of a drying drop of blood serum showing the formation of (a) "cords" (magnification, ×10) and (b–d) a multilevel fiber network revealed in the dry spot by a procedure of fixation and staining (magnification, ×140): (b) cracked surface; (c) peripheral region; (d) central region.

Thus, the process of gel formation in a drying drop of blood serum or plasma precedes the phase transition in the salt solution. Some aspects of this process were considered in our previous paper [21]. The cooperative character of processes involved in the structure formation in drying drops is reflected in the dynamics of the AMI signal variation.

In the above considerations, the main attention was devoted to the events at the drop–substrate interface. However, transformations observed at the drop–air interface are sometimes no less interesting. These phenomena, originally described in [9], were repeatedly observed in our experiments. During the first minutes of drying, the surface adsorption layer features the formation of quasi-opposite "cords" capable of moving within the near-surface layer (Fig. 9a) and eventually vanishing from the visual field. We believe this to be a manifestation of the polymerization of macromolecules and the onset of framework formation in the drop from above. This process may involve such macromolecules as glycoproteins, glycolipids, and glycoaminoglycans. Indeed, histochemical staining of the dry spots shows that the protein framework comprises a multilevel network (Figs. 9b–9d). Although the salt components are washed out during this treatment, it is obvious that the framework structure can influence the kinetics of water evaporation and, hence, salt crystallization in this system.

The process of self-organization in drying drops of liquid media having complex compositions is highly rich in events and by no means exhaustively studied so far. Many years of research and great effort of researchers will be required for elucidating this phenomenon step by step in detail. Nevertheless, the known physical phenomena and the results of our investigations allow some key points to be outlined in concluding remarks.

CONCLUSIONS

A liquid drop on a solid substrate acquires the equilibrium shape corresponding to the minimum surface area for a given volume and the degree of substrate wetting. The process of self-organization in drying drops of protein–salt solutions begins with the formation of protein adsorption layers at the phase boundaries. Condensation of the material stimulates the aggregation of protein and the polymerization of macromolecules, thus leading to the development of a multilevel gel structure. The formation of a solid phase ring at the periphery determines the line of attachment to the substrate and forces the drop to flatten so that its shape deviates from equilibrium.

If the surface energy exceeds the force of adhesion at the boundary of three phases, the drop exhibits a jumplike decrease in diameter and acquires the equilibrium shape again. This process can be repeated, leaving concentric circles of solid phase corresponding to the drop attachment lines. As the front approaches the center, the drop mass decreases and the salt concentration increases.

If the gel density is low, the residual liquid phase does not form a drop on the gel surface. In this case, the drying proceeds inside the gel.

The final stage of drying involves the phase transition in the salt solution. Special features of this stage are determined by the gel structure. The kinetics of water evaporation during the phase transition is determined by physical properties of the gel, which depend on the concentration and characteristics of macromolecules and the concentration of low-molecular-weight organic components in the medium. In other words, the kinetics of the final stage of drying (i.e., of the phase transition in the salt solution) contains integral information about the composition and state of the whole liquid.

It was established that the dynamics of AMI signal variation reflects the sequential stages of structure formation in a drying drop and can be used for their characterization.

ACKNOWLEDGMENTS

The authors are grateful to the staff of hospitals and medical research institutions of Nizhni Novgorod for kindly providing the samples of blood serum and plasma for investigation. Special thanks to P.P. Potekhin for consulting on histochemical staining of samples, V.V. Nemov for conducting the liquid chromatog-

raphy measurements, and L.V. Soustov and E.V. Chelnokov for their help in experiments with the Xe–Cl laser.

This study was supported in part by the Russian Foundation for Basic Research (project nos. 01-01-00388 and 02-04-49342), the INTAS Foundation (grant no. 01-06-90), and the US Civilian Research and Development Foundation for Independent States of the former Soviet Union (CRDF Award no. RMO-10214-BNL, 36943).

REFERENCES

1. G. G. Khaidarov, Zh. Fiz. Khim. **57**, 2528 (1983).
2. L. Monchick, J. Chem. Phys. **81**, 2010 (1984).
3. K. S. Birdi, D. T. Vu, and A. Winter, J. Phys. Chem. **93**, 3702 (1989).
4. Y. H. Erbil, J. Phys. Chem. B **102**, 9234 (1998).
5. J. H. Clint, P. D. I. Fletcher, and I. T. Todorov, Phys. Chem. Chem. Phys. **1** (21), 5005 (1999).
6. R. D. Deegan, Phys. Rev. E **61**, 475 (2000).
7. R. D. Deegan, O. Bakajin, T. F. Dupont, *et al.*, Phys. Rev. E **62**, 756 (2000).
8. L. Pauchard, F. Parisse, and C. Allain, Phys. Rev. E **59**, 3737 (1999).
9. V. N. Shabalin and S. N. Shatokhina, *Morphology of Body Liquids* (Khrizostom, Moscow, 2001) [in Russian].
10. *Microscopic Techniques: A Manual for Doctors and Laboratory Workers*, Ed. by D. S. Sarkisov and Yu. L. Petrov (Meditsina, Moscow, 1996), pp. 76–77, 80–81 [in Russian].
11. L. V. Soustov, E. V. Chelnokov, N. M. Bityurin, *et al.*, Preprint No. 599, IPF RAN (Russian Institute of Applied Physics, Russian Academy of Sciences, Nizhni Novgorod, 2002).
12. T. A. Yakhno, V. G. Yakhno, A. G. Sanin, and I. I. Shmelev, Biofizika **47**, 1101 (2002).
13. T. A. Yakhno, V. G. Yakhno, G. Ya. Levin, *et al.*, in *Proceedings of the 4th International Conference on Mathematical Modeling, Moscow, 2001,* Vol. 2, pp. 265–275.
14. Ya. E. Geguzin, *A Drop* (Nauka, Moscow, 1973), pp. 54–56 [in Russian].
15. E. G. Rapis, Pis'ma Zh. Tekh. Fiz. **14**, 1561 (1988) [Sov. Tech. Phys. Lett. **14**, 679 (1988)].
16. E. Chiotelli, G. Pilosio, and M. Le Meste, Biopolymers **63**, 41 (2002).
17. E. Kesselman, O. Ramon, R. Berkovich, and Y. Paz, Polym. Adv. Technol. **13**, 982 (2002).
18. A. C. Palacios, C. Sarnthein-Graf, and C. LaMesa, Colloids Surf., A **228**, 25 (2003).
19. B. C. Anderson, S. M. Cox, A. V. Ambardekar, and S. K. Mallapragada, J. Pharm. Sci. **91**, 180 (2000).
20. V. N. Izmaĭlov, G. P. Yampol'skaya, and B. D. Summ, *Surface Phenomena in Protein Systems* (Khimiya, Moscow, 1988) [in Russian].
21. T. A. Yakhno, O. A. Sedova, A. G. Sanin, and A. S. Pelyushenko, Zh. Tekh. Fiz. **73** (4), 23 (2003) [Tech. Phys. **48**, 399 (2003)].

Translated by P. Pozdeev

Technical Physics, Vol. 49, No. 8, 2004, pp. 1064–1067. Translated from Zhurnal Tekhnicheskoĭ Fiziki, Vol. 74, No. 8, 2004, pp. 109–112.
Original Russian Text Copyright © 2004 by Pogrebnjak, Tyurin.

BRIEF COMMUNICATIONS

The Structure and Properties of Al_2O_3 and Al Coatings Deposited by Microarc Oxidation on Graphite Substrates

A. D. Pogrebnjak* and Yu. N. Tyurin**
** Institute of Surface Modification, Sumy, 40030 Ukraine*
*** Paton Institute of Electric Welding, National Academy of Sciences of Ukraine, Kiev, Ukraine*
e-mail: apogrebnjak@simp.sumy.ua

Received May 8, 2003; in final form, August 12, 2003

Abstract—Protective α-Al_2O_3 coatings on the surface of a graphite article have been obtained by method of electric-arc metallization with aluminum and microarc oxidation (anodic spark process). Investigation of the obtained coating by scanning electron microscopy (SEM), X-ray diffraction (XRD), and proton elastic recoil detection analysis (ERDA) showed good quality of the Al and α-Al_2O_3 coatings on graphite. The proposed technology can be used for obtaining protective coatings in low-accessible sites of graphite articles. *© 2004 MAIK “Nauka/Interperiodica”.*

Articles made of carbon-based composites are widely used in various technologies. However, carbon is subject to oxidation in oxygen-containing media at high temperatures, which decreases the working life of such materials. This paper presents the results of evaluation of a new technology developed for protecting the surface of articles made of carbon-containing materials, which is based on a combination of two methods: electric-arc metallization with aluminum and microarc (anodic spark) oxidation.

The process of electric-arc metallization is one of the most effective coating technologies, characterized by high output and low consumption of energy and materials. This method is based on arc melting of a wire and gas spraying of the melt and allows using both compact and powdered coating materials. The main disadvantage of coatings obtained by this method is porosity of the deposit. Using aluminum wire for the surface metallization provides for the formation of coatings characterized by high plasticity and low porosity. The protection of an aluminum-coated article is provided by a layer of an aluminum oxide, which is formed using the anodic spark process conducted in an aqueous electrolyte [1, 2]. This technology is also characterized by low consumption of energy and materials and by relatively simple equipment. A partly oxidized aluminum layer forms a heat-resistant film of α-Al_2O_3.

In order to protect the surface of graphite-based composite materials from high-temperature oxidation, a complex technology has been developed that includes metallization of the surface of articles with aluminum, followed by partial oxidation of this metal coating. This study was aimed at the development of equipment for the microarc (anodic spark) oxidation of extended articles made of carbon-containing composites, after preliminary metallization by electric arc spraying. The initial metallization was performed using a wire of technical-purity aluminum, which allows subsequent formation of aluminum oxide.

The technology of formation of a protective oxide layer was as follows. First, the article was coated with an aluminum-based alloy by means of electric arc wire spraying. This method ensured a rather dense aluminum coating with porosity not exceeding 4%. The pores are of the closed type and do not influence the subsequent oxidation stage.

A special feature of the anodic spark or microarc oxidation (MAO) process is that this treatment utilizes the energy of electric microarc discharges initiated at the surface of an article immersed in electrolyte. Numerous investigations [1–6] describe the formation of oxides at potentials corresponding to the breakdown of a continuous material. The thickness of the oxide layer formed on the surface of a continuous material depends on the electric field strength and can vary from 5 to 1000 μm [3, 4].

In the course of electrolysis, oxygen that has evolved on the anode and has been activated by electric discharge oxidizes the base metal. In order to maintain the required electrical regime in the course of oxidation (increasing the oxide thickness), it is necessary to increase the applied electric voltage so as to provide stabilization of microarc discharge. The MAO process has a decaying character and the electric field has to be maintained on a level ensuring breakdown of the oxide layer and the formation of arc discharge. The discharge lifetime varies within 0.1–0.001 s. The onset of the oxide breakdown has an avalanche character and is accompanied by a sharp increase in the electric current density up to 10 A/cm^2. Then, the discharge gradually decays with time as the oxide thickness grows and the electric strength of the oxidized layer increases.

Oxidation of the surface layer of a metallized article by means of the MAO process ensures the formation of a uniform oxide film as a result of high-temperature transformations in oxygen-containing electric discharge at the metal surface. Electric discharges occur on the surface areas possessing higher conductivity, thus ensuring the formation of a dense oxide layer with closed porosity. During the working life of an article bearing such a protective coating, pores reduce thermal conductivity of the surface layer and serve as compensators for stress release, which favors the protection of this article against high-temperature oxidation.

We have developed an experimental setup for the MAO processing of extended articles such as tubes (Fig. 1). The experiments were performed with graphite cylinders (tubes) having an external diameter of 5 cm, an internal diameter of 3 cm, and a length of about 65 cm. The setup for MAO processing of extended articles (tubes) comprises base *1*, case *2*, and container *3* with electrolyte *4*. Article *5* is driven by mechanism *6* via closed ring cathodes *7*. The electrolyte, supplied by pump *8* into cathode cavities *9* with holes, fills a ring-shaped gap between the tubular article (anode) and cathodes *10*. The flow of electrolyte prevents the article-anode from overheating and allows the process to be conducted at a high energy density.

The setup operates as follows. The electrolyte is supplied to cathodes *7* and the article *5* is driven by mechanism *6* through the cathodes occurring at a preset electric potential. The applied potential gradually is increased from 150 to 380 V in the course of article propagation, which ensures a smooth increase in the thickness of oxide layer formed on the surface of metallized article (Fig. 2).

The drive mechanism also serves as a current-carrying electrode in contact with the aluminum-coated article. The electric potential is applied by connecting this electrode to a special converter using leads passing through holes in the case.

The experiments were performed with technical graphite of a grade using for manufacturing electrodes. This material has elongated grains and certain porosity. Metallization was provided by method of electric arc spraying of a wire made of technical-purity aluminum. The initial graphite exhibits certain open porosity, with the pore size being comparable to the size of sprayed metal drops. As a result, material deposited on the surface of graphite was partly incorporated into pores of the graphite base. The aluminum layer thickness reached 250–350 μm (Figs. 3a and 3b). Arrows in Fig. 3a indicate the boundary of an Al_2O_3 layer with dopants and inclusions and the boundary of the Al metallization layer.

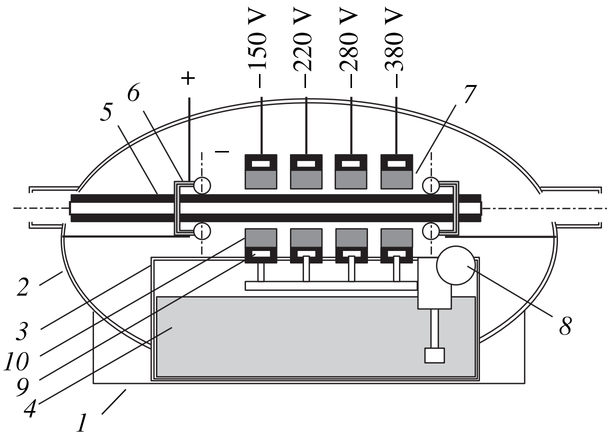

Fig. 1. Schematic diagram of the experimental setup for MAO processing of extended articles made of carbon composites with metallized (Al-coated) surface (see the text for explanations).

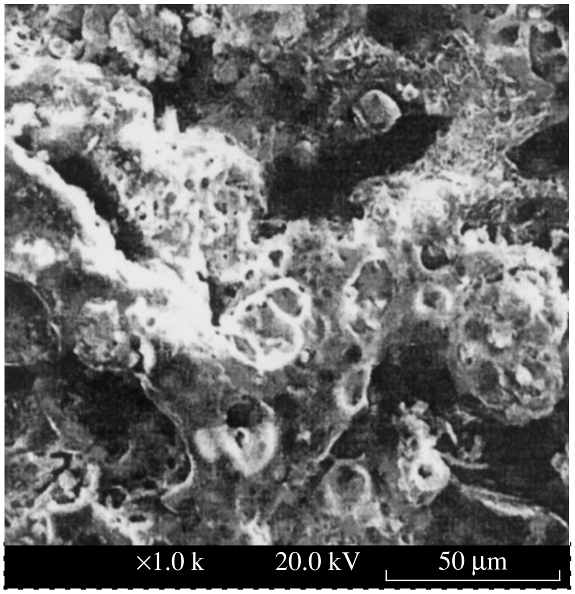

Fig. 2. SEM image of the surface of a metallized graphite article upon MAO processing.

The surface of metallized articles was processed by MAO in the setup schematically depicted in Fig. 1. The process was conducted for 15 min using a KOH solution as electrolyte, with the applied voltage gradually increased from 150 to 380 V. Oxidation takes place only on the surface in contact with electrolyte, which allows the protective coating to be formed on local areas of the article.

The results of metallographic examination showed that the oxide layer has a thickness exceeding 120 μm and possesses a higher density at the boundary with aluminum substrate (Fig. 3b). The oxide surface is highly porous and exhibits numerous fused areas in the form of microcraters and droplets formed as a result of partial melting of the oxide layer. An analysis of the metallographic data showed that MAO process extends inside the pores, where the traces of microarc localization (fused craters) are also present. Thus, it should be noted that the oxide layer grows not only from the outer surface, but from the inner pore surface as well, which

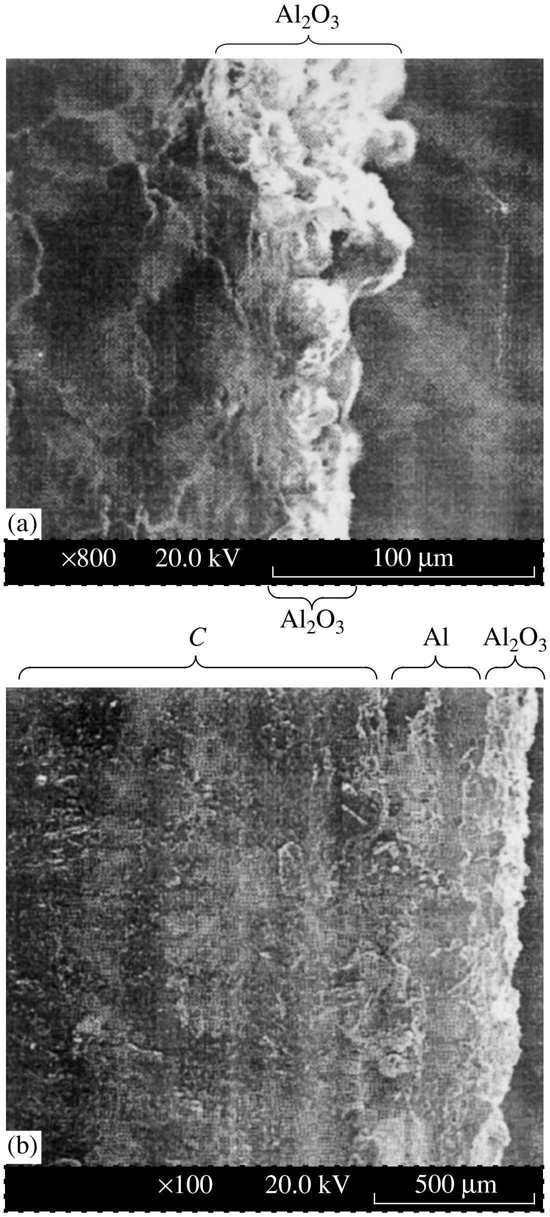

Fig. 3. SEM images showing (a) a general view of the traverse section of a graphite article with (Al, Al_3O_3) coating and (b) the same section at a greater magnification for examination of Al_2O_3 coating.

results in the formation of a developed oxide surface incorporated deep into the metallization layer [7–10].

The proposed setup allows the MAO process to be conducted for an interelectrode gap width of 20–30 mm, which reduces the electric energy losses and ensures the formation of oxide with a thickness of up to 150 µm at an applied voltage of ~340 V. It was found that the optimum electrolyte temperature for the MAO process (50–60°C) is provided by heating due to the electric energy losses in the interelectrode gap filled with electrolyte. Articles can have arbitrary thickness and a length of 1 m or more.

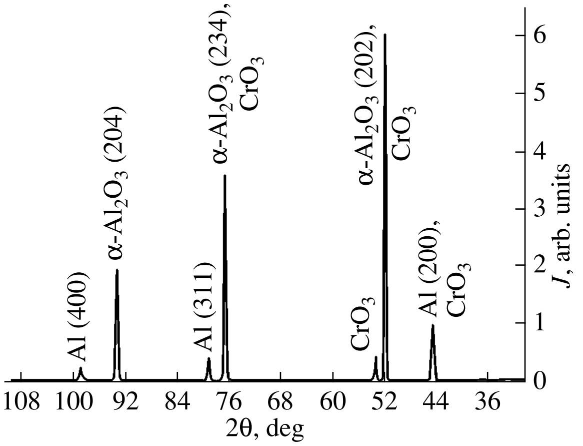

Fig. 4. X-ray diffraction pattern from the surface of aluminum alloy upon MAO processing.

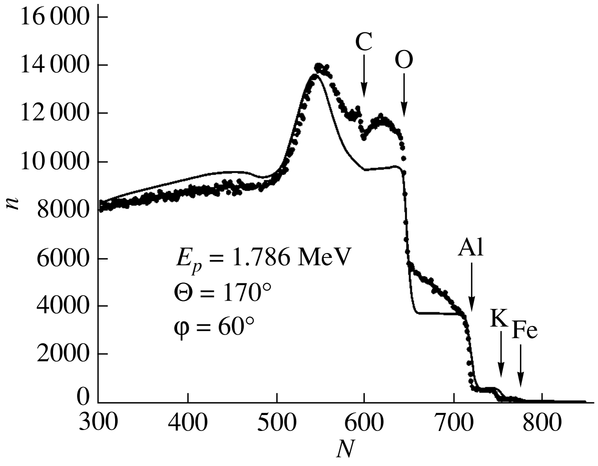

Fig. 5. The energy spectra obtained by ERDA of Al_2O_3 coating obtained by MAO on the metallized (Al-coated) graphite surface. Points show experimental data; the solid curve shows the results of theoretical fitting.

The X-ray diffraction (XRD) analysis of the coating (Fig. 4) showed that the oxide layer consists predominantly of a heat-resistant phase of aluminum oxide (α-Al_2O_3), aluminum, and, probably, about 9% of a chromium oxide phase (CrO_3). Particles of a finely disperse powder (e.g., chromium oxide) introduced into the electrolyte are incorporated into the coating and fused into aluminum oxide. The high-temperature form of the oxide is formed predominantly at the oxide–metal interface. The energy spectra obtained by proton elastic recoil detection analysis (ERDA) of α-Al_2O_3 coating formed on the surface of metallized graphite showed that the oxide film contains the metal component of electrolyte (potassium), the metal of cathode (iron), and, probably chromium (Fe and Cr are difficult to distinguish by this analytical method).

The density of the upper layer of the oxide coating, having the phase composition (Al_2O_3; Al; CrO_3), amounts to 3.74 g/cm^3, which is close to the density of α-Al_2O_3 (ρ = 3.98 g/cm^3) [5]. The adhesion of the oxidized layer formed on the surface of aluminum (determined by scribing with a diamond pyramid) varies within 42–67 MPa on various areas. The surface hardness on some areas of the oxide coating (at the dark spots representing inclusions of the CrO_3 phase) varies from 1.36×10^4 to 1.72×10^4 N/mm^2.

The process of oxidation involves the formation of mixed oxides of aluminum and metals contained in the complex anion of electrolyte. Metal anions can be introduced into electrolyte via dissolution of an electrode (cathode) or the corresponding alloy. In a oxidation steady-state regime, the current density amounts to 0.1–0.5 A/cm^2. The main parameters for controlling the MAO process and the properties of oxide layers are the electrolyte concentration, the applied voltage and current, the process duration, the alloy composition, and the thermal treatment conditions.

Preliminary tests performed for the articles coated by the proposed complex technology (graphite, Al, Al_2O_3) and exposed in atmosphere at high humidity and elevated temperature (600–900°C) showed good resistance and sufficiently high working properties of the articles.

CONCLUSIONS

(1) We have developed experimental equipment for obtaining protective coatings on the surface of articles made of carbon-containing composites (in particular, tubes having an external diameter of 5 cm, an internal diameter of 3 cm, and a length of about 65 cm). The setup ensures high quality of the local oxide coating in low-accessible sites of articles. The articles made of graphite can be protected by oxide coatings containing several components such as Al_2O_3, CrO_3, etc., and doped with elements contained in the electrode (e.g., Fe) and electrolyte (e.g., K).

(2) The obtained coatings can provide protection of articles made of carbon-containing composites, intended for operation under high-temperature oxidation conditions.

ACKNOWLEDGMENTS

The authors are grateful to A.P. Kobzev (JINR, Dubna), O.P. Kul'ment'eva (Institute of Surface Modification and Sumy National University, Sumy), and O.V. Kolisnichenko (Paton Institute of Electric Welding, Kiev) for their help in conducting experiments.

This study was supported in part by the Ministry of Education and Science of Ukraine, project no. 2M/0145-2001.

REFERENCES

1. V. I. Chernenko, L. A. Snezhko, and I. I. Papanova, *Anode-Spark Electrolytic Production of Coatings* (Khimiya, Leningrad, 1991) [in Russian].
2. V. I. Chernenko, L. A. Snezhko, I. I. Papanova, and K. I. Litovchenko, *Theory and Technology of High-Voltage Anode Processes* (Naukova Dumka, Kiev, 1995) [in Russian].
3. P. S. Gordienko, *The Formation of Coatings on Anode-Polarization Electrodes in Water Electrolytes at the Potentials of Sparking and Breakdown* (Dal'nauka, Vladivostok, 1996) [in Russian].
4. E. S. Antroshchenko, I. A. Kazantsev, and A. E. Rozen, Tekh. Prog. At. Prom., Ser. Tekhnol. Montazhnykh Rabot, No. 1, 28 (1996).
5. Yu. B. Shul'gin, in *Collection of Articles of the 22nd Youth Scientific–Technical Conference (Gagarin's Readings), Moscow, 1996*, pp. 80–81.
6. O. V. Titorenko, E. A. Rat'kova, and E. A. Savel'eva, in *Proceedings of the Scientific–Technical Conference on Modern Electrochemical Technologies, Saratov, 1996*, p. 51.
7. G. A. Markov, A. I. Slonova, and O. P. Terleeva, Zashch. Met., No. 3, 289 (1997).
8. A. V. Timoshenko, Yu. V. Magurova, and S. Yu. Artemova, Fiz. Khim. Obrab. Mater., No. 2, 57 (1996).
9. V. N. Kuskov and I. D. Morgun, in *Proceedings of the International Scientific–Technical Conference on Oil and Gas of Western Siberia, Tyumen', 1996*, pp. 21–23.
10. É. S. Antroshchenko, I. A. Kazantsev, A. E. Rozen, and N. V. Golovanova, Fiz. Khim. Obrab. Mater., No. 3, 8 (1996).

Translated by P. Pozdeev

Technical Physics, Vol. 49, No. 8, 2004, pp. 1068–1070. Translated from Zhurnal Tekhnicheskoĭ Fiziki, Vol. 74, No. 8, 2004, pp. 113–115.
Original Russian Text Copyright © 2004 by Gulyaev, A.A. Veselov, A.G. Veselov, Burylin, Dzhumaliev, Zyuryukin, Kiryasova, Ryabushkin.

BRIEF COMMUNICATIONS

Effect of Surface Composition on Melting of Thin InSb Films

Yu. V. Gulyaev, A. A. Veselov, A. G. Veselov, E. I. Burylin, A. S. Dzhumaliev, Yu. A. Zyuryukin, O. A. Kiryasova, and S. L. Ryabushkin

Institute of Radioengineering and Electronics (Saratov Branch), Russian Academy of Sciences, Saratov, 410019 Russia

Received November 3, 2003

Abstract—We demonstrate the possibility of melting thin (0.1–0.5 μm) InSb films directly in atmosphere under the protective layer of native oxides to obtain high mobility of majority carriers (up to 25 000 cm^2/V s). The features of the film synthesis process based on thermal pulsed evaporation of InSb powder in vacuum are studied experimentally. Such a technique makes it possible to provide necessary compositional inhomogeneity of the deposited film for subsequent melting in air. *© 2004 MAIK "Nauka/Interperiodica".*

The increase in the number of problems solved by functional electronics stimulates continuous interest in one of the III–V compounds (semiconductors), indium antimonide, since it has a small band gap (0.165 eV) and an extremely high electron mobility (up to 78 000 cm^2/V s in a single crystal at room temperature) [1]. The effective mass of electrons in InSb is 0.014 of the free electron mass. The outlined properties distinguish this compound from other III–V materials to the extent that just InSb films are appropriate for use in such information processing devices as magnetoresistors, Hall transducers, amplifiers, detectors, and surface-acoustic-wave convolvers [1].

It is well known [1] that fabrication of thin InSb films, which are interesting due to the necessity of increasing the sample impedance without changing the carrier mobility, is an extremely difficult task. Most studies on thermal film deposition pose the problem of obtaining the deposited material with the stoichiometric composition and subsequent deposition of the protective layer to preserve stoichiometry after annealing or remelting. However, these operations are poorly reproducible; in particular, it is difficult to ensure stoichiometry and especially to preserve it when the substrate is heated to its melting temperature because of the high antimony vapor pressure. Nevertheless, this approach has found many technological implementations, although in most cases no reproducibility of the parameters has been achieved so far [1].

We propose a new technique for film deposition that ensures compositional nonuniformity over the film thickness (having the percentage of In and Sb in mind), which makes it possible subsequently to melt the film under the native oxide layer. Thermal evaporation of the InSb powder and film deposition onto the Polikor substrate was carried out using the pulsed method [1, 2] in the quasi-closed tantalum crucible. Preliminary substrate degassing was performed at 500°C for 5 min. Contrary to the discrete technique, in which the InSb powder from a vibrobunker falls onto the preheated crucible, the evaporation from the quasi-closed crucible does not ensure compositional uniformity over the whole area of the substrate [1]. Film stoichiometry is preserved only in the substrate region located against the crucible nozzle, as shown schematically in Fig. 1, and strongly depends on the time of crucible run-up [2, 3]. The method of pulsed evaporation is simple, reproducible, and ensures the constancy of the following two parameters: the mass of the loaded powder (20 mg in our case) and the time of crucible heating to complete evaporation, which determined our choice of film deposition technique. The substrate was positioned at a distance of 40 mm from the crucible nozzle. The nozzle edges were turned through an angle of 20°–30° towards the sample surface. The direction of the flux of the evaporated substance, which results in spatial compositional nonuniformity (Fig. 1), ensured the initial excessive antimony content at the film surface. The cru-

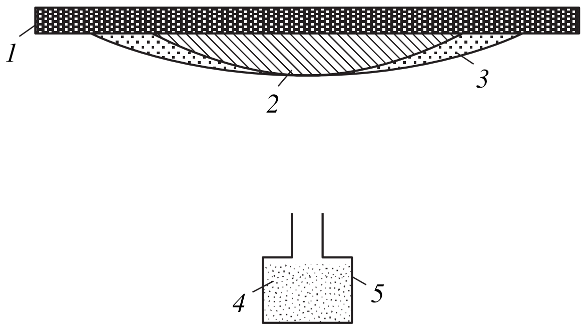

Fig. 1. Schematic representation of the In and Sb distribution over the substrate. (*1*) Polikor substrate; (*2*) In, Sb; (*3*) Sb; (*4*) InSb powder; (*5*) crucible cross section.

cible was heated to 2000°C for 1–2 s using a current pulse with an amplitude of 150 A. The crucible configuration, the distance to the substrate, and the tilt of the nozzle were adjusted empirically via the continuous monitoring of the film composition by Auger spectroscopy. Then the fact was taken into account that, in addition the method of deposition, the substrate temperature also affects the film composition. Figure 2 shows the dependences of In and Sb contents at the film surface (measured by Auger spectroscopy and using Hall mobility measurements before and after melting, respectively) on the substrate temperature at the instant of deposition. The Hall mobility was measured by the van der Pauw four-contact technique [4]. Note that the composition of the film surface became stoichiometric after melting, which explains the drastic increase in mobility.

The dependence of the carrier mobility in a plasma on the substrate temperature at the instant of evaporation gives a clear idea of the character of the processes involved. As the substrate temperature is about 200°C, the surface composition of the film is determined in fact by the crucible geometry and the heating mode. It was impossible to melt films obtained at these temperatures (Fig. 2, zone I). Globulation of In (i.e., the formation of semispherical droplets with base diameter of several micrometers) is observed at the surface. The mobility is several tens of cm^2/V s in this case. These features are observed at temperatures up to 270–280°C. Only in the narrow temperature range (280–290°C, zone II), where the antimony content is four times higher than that of indium, the oxidation of the upper surface of the film is observed with the change of its color and subsequent (at 560–580°C, zone III) formation of the liquid phase. The homogeneous melting itself, as in [1, 5], was observed visually in reflected light due to the difference in reflections from the surfaces of solid and liquid phases, which were diffuselike and mirrorlike, respectively. The melting occurred in air; the substrate with the melt was rapidly removed from the heater so that the film was in the liquid phase for a fraction of a second only. As the residence time of the film in the molten state increased, the oxide layer was destroyed and the film was reevaporated.

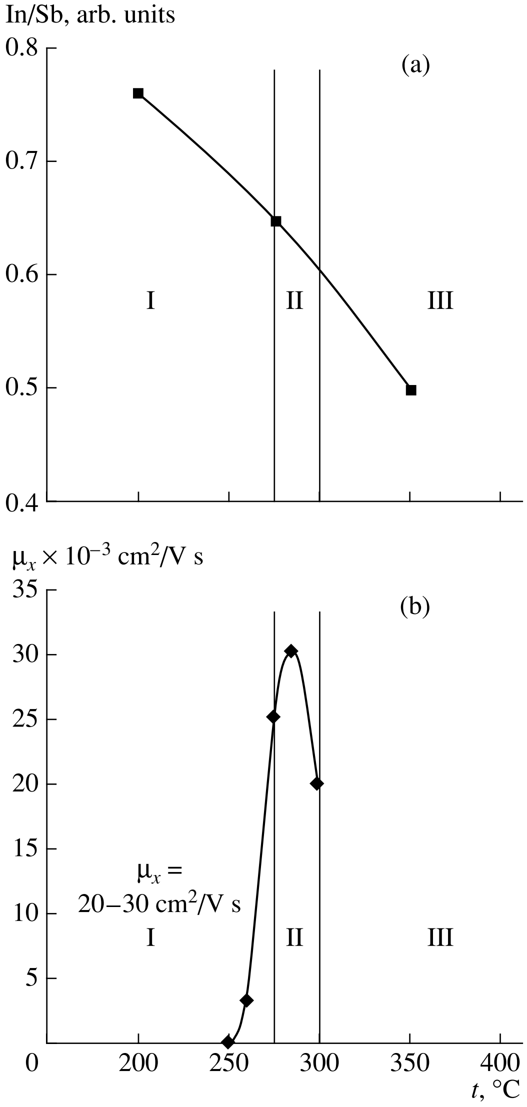

Fig. 2. (a) Dependence of the composition ratio In/Sb at the substrate surface on the substrate temperature; (b) dependence of the Hall mobility on the substrate temperature.

One can assume that the excess antimony at the surface is partially oxidized during the heating, which is manifested as a change in film color at 300–350°C. On further heating, the remaining antimony passes into the melt under the protective layer formed during oxidation; therefore, it is of interest to elucidate how the oxidation of the upper layer affects the film properties, which was actually performed in this study. It was found that this layer is indeed formed from the oxidized antimony, since it is reevaporated at 660°C (the evaporation temperature of indium oxide is about 2000°C), and successfully protects the film during melting. The considerable increase in the mobility (Fig. 2) in relation to the results obtained in [1] can be associated with the elimination of the donor centers formed by the excess antimony [1]. In our case, the excess antimony probably passes into the oxide or melt. Such an interpretation of the processes occurring during melting enables us to explain the high values of the Hall mobility in the formed films as compared to the results obtained by other research groups [1], when special protective layers were used.

This series of experiments on obtaining films using the aforesaid technique showed a high extent of reproducibility (more than 90%) of the Hall mobility values.

Such technology makes it possible to synthesize with high reproducibility films 0.1–0.5 μm in thickness with a mobility of 25000–30000 cm^2/V s.

It is the authors' opinion that the results may form the basis for developing technologies for the synthesis of thin films with reproducible electrophysical parameters.

The results on the Hall mobility values at such small film thicknesses (down to 0.1 μm) can become a basis for experiments on quantum size effects as well as radio- and acoustoelectric effects.

ACKNOWLEDGMENTS

This work was supported by the Russian Foundation for Basic Research, project no. 01-02-16317.

REFERENCES

1. V. A. Kas'yan, P. I. Kutrush, Yu. A. Nikol'skiĭ, and F. I. Pasechnik, *Indium Antimonide Thin Films* (Shtinitsa, Kishinau, 1989) [in Russian].
2. V. I. Petrosyan, A. G. Veselov, N. I. Sinitsin, *et al.*, Mikroélektronika **8** (6) (1979).
3. A. G. Veselov, S. L. Ryabushkin, and I. Ya. Shuler, Pis'ma Zh. Tekh. Fiz. **18** (11), 63 (1992) [Sov. Tech. Phys. Lett. **18**, 361 (1992)].
4. E. V. Kuchis, *Hall Effect Research Methods* (Sov. Radio, Moscow, 1974) [in Russian].
5. A. G. Veselov, I. M. Kotelyanskiĭ, A. I. Krikunov, *et al.*, USSR Patent No. 713179 (1979).

Translated by M. Lebedev

Technical Physics, Vol. 49, No. 8, 2004, pp. 1071–1074. Translated from Zhurnal Tekhnicheskoĭ Fiziki, Vol. 74, No. 8, 2004, pp. 116–119.
Original Russian Text Copyright © 2004 by Zharov, Shiryaeva, Grigor'ev.

BRIEF COMMUNICATIONS

On Nonlinear Corrections to Oscillations Frequencies of a Charged Drop in an Incompressible Ambient Medium

A. N. Zharov, S. O. Shiryaeva, and A. I. Grigor'ev
Yaroslavl State University, ul. Sovetskaya 14, Yaroslavl, 150000 Russia
e-mail: grig@uniyar.ac.ru

Received November 4, 2003

Abstract—An analytic expression in the third order of smallness in the amplitude of the initial deformation of an equilibrium, spherical, charged, ideally conducting drop in an incompressible dielectric medium is derived for its generatrix and for nonlinear corrections to oscillation frequencies. It is shown that the presence of the ambient liquid reduces the absolute values of the corrections to frequency and of the self-charge critical for the realization of drop instability. *© 2004 MAIK "Nauka/Interperiodica".*

1. The problem of nonlinear oscillations of a charged drop in a dielectric medium is of interest in connection with numerous academic, technical, and technological applications [1, 2]. For this reason, this problem has been analyzed in the second order of smallness in the case of both an incompressible [3] and a compressible ambient medium [4]. However, nonlinear corrections to oscillation frequencies appearing only in the third order of smallness have not been studied [5–7]. This stimulated the present study.

2. Let us suppose that we have a spherical drop (having a radius R and bearing a charge Q) of an ideal, incompressible, perfectly conducting liquid of density $\rho_{(i)}$, which is placed in an ideal incompressible liquid of density $\rho_{(e)}$ with permittivity ε_d and interface surface tension σ. A complete mathematical formulation of the problem on nonlinear capillary oscillations of a drop in a medium can be found in [3, 8]; for this reason, we will not consider this problem here for lack of space.

Solving the problem of the shape of a nonlinearly oscillating drop by a multiscale method (as was done in [3, 5–7]), we can find an analytic expression for the generatrix of the axisymmetric drop at any instant to within third-order terms. In dimensionless variables, in which $\rho_{(i)} = R = \sigma = 1$, this expression has the form

$$r(\vartheta, t) = 1 + \varepsilon \sum_{n \in \Omega} M_n^{(1)}(t) P_n(\cos\vartheta)$$

$$+ \varepsilon^2 \sum_{n=0}^{\infty} (M_n^{(2)}(t) + \varepsilon M_n^{(3)}(t)) P_n(\cos\vartheta),$$

$$M_n^{(1)}(t) = h_n \cos(\omega_n t + \varepsilon^2 b_n t);$$

$$M_0^{(2)}(t) = -\sum_{m \in \Omega} \frac{h_m^2}{2m+1} \cos^2(\omega_m t);$$

$$b_n = \frac{1}{2\omega_n}\left\{\frac{h_n^2(\Xi_n^2 + 2\omega_n^2(\Xi_n^1 - 2\Xi_n^2))}{4(2n+1)} + \sum_{k \in \Omega} \frac{h_k^2 \Xi_n^0}{2(2k+1)}\right.$$

$$- \sum_{k \in \Omega} \frac{h_k^2}{4} [H_{nkkn}^{1(-)(+)} + H_{knkn}^{2(+)(+)} + H_{knkn}^{2(-)(-)} + (1 - \delta_{kn})$$

$$\left. \times (H_{kknn}^{1(-)(+)} + H_{kknn}^{2(+)(+)} + H_{nkkn}^{2(-)(-)})]\right\};$$

$$M_n^{(2)}(t) = \sum_{l, m \in \Omega} \frac{h_l h_m}{2} (\lambda_{lmn}^{(+)}(\cos((\omega_l + \omega_m)t) - \cos(\omega_n t))$$

$$+ \lambda_{lmn}^{(-)}(\cos((\omega_l - \omega_m)t) - \cos(\omega_n t)));$$

$$M_0^{(3)}(t) = -\sum_{k \in \Omega} \frac{2h_k}{2k+1} M_k^{(2)}(t) \cos(\omega_k t)$$

$$- \sum_{k, m, l \in \Omega} \frac{K_{kml} h_k h_m h_l}{3(2l+1)} \cos(\omega_k t) \cos(\omega_m t) \cos(\omega_l t); \tag{1}$$

$$M_n^{(3)}(t) = -\sum_{k \in \Omega} \frac{h_n h_k^2 (\Xi_n^0 - 2\Xi_n^1 \omega_n \omega_k - 4\Xi_n^2 \omega_k^2)}{8(2k+1)\omega_k(\omega_n + \omega_k)}$$

$$\times \sin((\omega_n + \omega_k)t) \sin(\omega_k t)$$

$$- \sum_{k \in \Omega} \frac{h_n h_k^2 (1 - \delta_{nk})(\Xi_n^0 + 2\Xi_n^1 \omega_n \omega_k - 4\Xi_n^2 \omega_k^2)}{8(2k+1)\omega_k(\omega_n - \omega_k)}$$

$$\times \sin((\omega_n - \omega_k)t) \sin(\omega_k t)$$

$$- \sum_{g=1}^{\infty} \sum_{k, m, l \in \Omega} \frac{h_k h_m h_l (\lambda_{lmg}^{(+)} + \lambda_{lmg}^{(-)})}{4}$$

1063-7842/04/4908-1071$26.00 © 2004 MAIK "Nauka/Interperiodica"

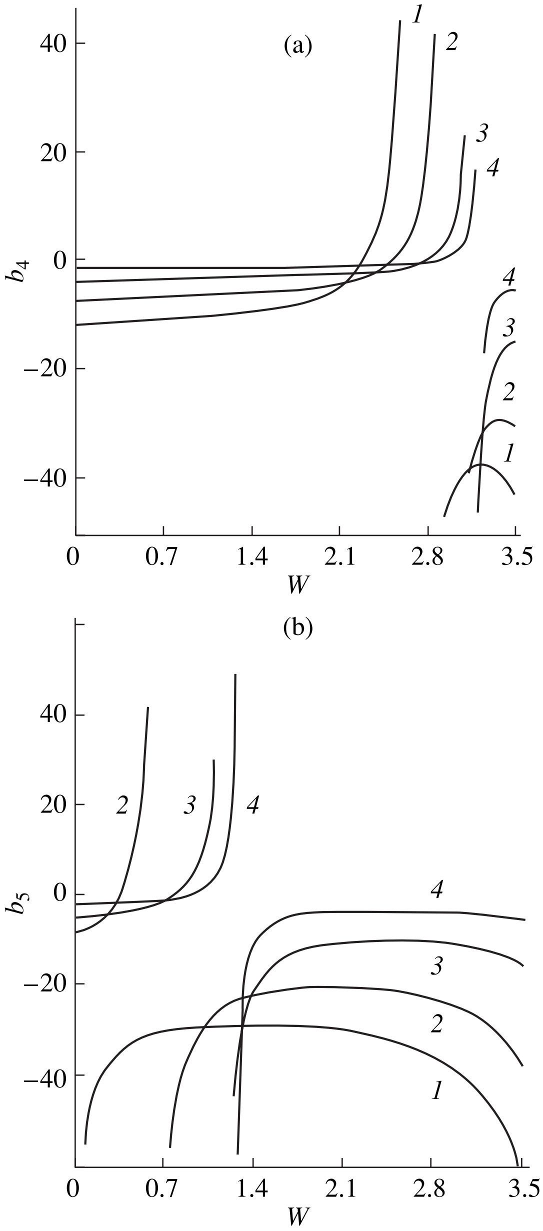

Fig. 1. Dependence of coefficient b_n characterizing the frequency shift of the *n*th mode on the Rayleigh parameter *W* for the initial excitation of the *n*th mode for various values of density $\rho_{(e)}$ of the surrounding medium: 0 (*1*), 1 (*2*), 10 (*3*), and 100 (*4*); *n* = 4 (a) and 5 (b).

$$\times\left\{\frac{H^{0(+)}_{kgn}(\cos((\omega_k+\omega_g)t)-\cos(\omega_n t))}{\omega_n^2-(\omega_k+\omega_g)^2}+\frac{H^{0(-)}_{kgn}(\cos((\omega_k-\omega_g)t)-\cos(\omega_n t))}{\omega_n^2-(\omega_k-\omega_g)^2}\right\}$$

$$\begin{aligned}&+\sum_{k,\,m,\,l\,\in\,\Omega}\frac{h_kh_mh_l}{4}\left\{\frac{H^{1(+)(-)}_{kmln}(\cos(\psi^{(+)(+)}_{klm}t)-\cos(\omega_n t))}{\omega_n^2-(\omega_k+\omega_l+\omega_m)^2}\right.\\&+\frac{H^{1(-)(+)}_{kmln}D^{kn}_{lm}D^{ln}_{km}(\cos(\psi^{(+)(-)}_{klm}t)-\cos(\omega_n t))}{\omega_n^2-(\omega_k+\omega_l-\omega_m)^2}\\&+\frac{H^{2(+)(+)}_{kmln}D^{mn}_{kl}D^{ln}_{km}(\cos(\psi^{(-)(-)}_{klm}t)-\cos(\omega_n t))}{\omega_n^2-(\omega_k-\omega_l-\omega_m)^2}\\&\left.+\frac{H^{2(-)(-)}_{kmln}D^{mn}_{kl}D^{kn}_{ml}(\cos(\psi^{(+)(-)}_{klm}t)-\cos(\omega_n t))}{\omega_n^2-(\omega_k-\omega_l+\omega_m)^2}\right\},\end{aligned}$$

where ε is a small parameter defining the amplitude of the initial deformation; $P_n(\cos\vartheta)$ is the *n*th order Legendre polynomial; ϑ is the polar angle of the spherical system of coordinates; *t* is the time; Ω is the set of indices of initially excited modes; h_m are constants taking into account the contribution of the *m*th mode to the formation of the initial shape of the drop ($\sum_{m\in\Omega}h_m = 1$); $\omega_n = (\chi_n(n-1)n(n+1)(n+2-W))^{1/2}$ is the frequency of capillary oscillations of the drop; $W = Q^2/(4\pi)\varepsilon_d$ is the Rayleigh parameter; δ_{kn} is the Kroneker delta; and $\chi_n\lambda^{(+)}_{lmn}$, $\lambda^{(-)}_{bmn}K_{lmn}$, Ξ^0_n, Ξ^1_n, Ξ^2_n, $H^{0(\pm)}_{kgn}$, $H^{1(\pm)(\pm)}_{kmln}$, $H^{2(\pm)(\pm)}_{kmln}$, $\psi^{(\pm)(\pm)}_{kml}$, and D^{kn}_{lm} are the coefficients defined in the Appendix.

3. It can be seen from relations (1) that the frequency corrections proportional to b_n have the second order of smallness in ε and contain in their denominators factors vanishing for certain relations between the frequencies of different modes (in this case, we are talking about the resonance nature of the corresponding corrections [9]). If the fourth mode is excited at the initial instant, the frequency correction has a resonance at $\omega_6^2-4\omega_4^2 = 0$; if the fifth mode is excited, the resonance takes place for $\omega_8^2-4\omega_5^2 = 0$. Away from resonance positions, corrections to frequencies $b_n\varepsilon^2$ decrease in absolute value with increasing density $\rho_{(e)}$ of the ambient medium (Fig. 1).

The allowance for nonlinear corrections to the frequencies of capillary oscillations of a drop leads to a change in the critical value $W_{\rm cr}$ of the Rayleigh parameter at which instability of the *n*th mode to self-charge takes place [6]. The condition for the emergence of instability of the *n*th mode with allowance for a nonlinear correction to frequency can be written in the form

$$(\omega_n+\varepsilon^2b_n)^2 = \omega_n^2+2\varepsilon^2\omega_nb_n+O(\varepsilon^4) = 0.$$

The effect of the ambient medium on the critical conditions of instability boils down to an insignificant increase in the critical value of the Rayleigh parameter

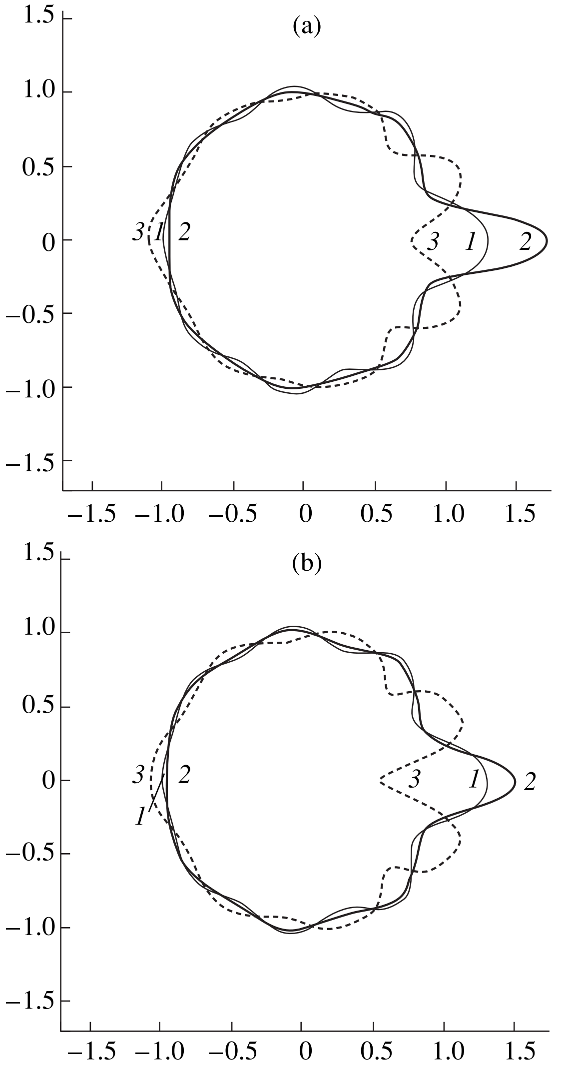

Fig. 2. Contour of the generatrix of a drop in the case of initial excitation of the seventh and eighth modes for $h_7 = h_8 = 0.5$, $W = 3$, and $\varepsilon = 0.3$. (a) $\rho_{(e)} = 0$, t = (*1*) 0.01, (*2*) 0.075, and (*3*) 0.22; (b) $\rho_{(e)} = 5$, t = (*1*) 0.02, (*2*) 0.14, and (*3*) 0.525.

upon an increase in the density $\rho_{(e)}$ of the ambient medium (due to a decrease in the absolute value of coefficient b_b) [7] and to a substantial decrease in the interface surface tension coefficient as compared to the surface tension coefficient for a drop in vacuum [10]. As a result, the value of self-charge critical for realization of instability in the presence of the ambient medium decreases.

The amplitudes of the second- and third-order modes $M_n^{(2)}$ and $M_n^{(3)}$ also depend on the density of the ambient liquid, which leads to a certain change in the shape of the surface of the drop (a local decrease in the curvature of the drop's surface) in a medium as compared to a drop in vacuum (Fig. 2). The presence of an external medium produces the most noticeable effect on the shape of the drop's surface in the vicinity of points with the highest velocity.

CONCLUSIONS

The values of nonlinear corrections to the oscillation frequencies of a charged drop of an ideal incompressible conducting liquid in a dielectric incompressible external medium substantially depend on the ratio of the densities of the media and become smaller with increasing density of the surrounding medium. The effect of the ambient medium simulated by an incompressible liquid on the stability of the drop to the self-charge is a combination of the following two factors: on the one hand, a nonlinear shift in the frequency of oscillations slightly increases the critical charge; on the other hand, a substantial decrease in the interface surface tension coefficient (as compared to that for a drop in vacuum) leads to a noticeable decrease in the critical charge.

APPENDIX

Expressions for Coefficients

$$\gamma_{mln} = (n+1)\chi_n K_{mln}(\omega_m^2(n-m+1 - \rho_{(e)}n(n-m-1)/(n+1)) + 2n(l(l+1)-1) + (l(m+1)-m(2m-2n+7)+3)nW/2) + (n+1) \times \chi_n \alpha_{mln}((1/m - n\rho_{(e)}/((n+1)(m+1)))\omega_m^2 + nW/2);$$

$$\lambda_{mln}^{(\pm)} = \frac{\gamma_{mln} \pm \omega_m\omega_l\eta_{mln}}{\omega_n^2 - (\omega_m \pm \omega_l)^2};$$

$$\eta_{mln} = (n+1)\chi_n K_{mln}(n/2 - m + 1 + \rho_{(e)}n(2m+3-n)/(2(n+1))) + (n+1)\chi_n\alpha_{mln}((1+n/(2l))/m - n\rho_{(e)}(n+2l+3)/(2(m+1)(l+1)(n+1)));$$

$$H_{kmln}^{1(\pm)(\mp)} = \sum_{g=1}^{\infty}(\beta_{kmgln}^{1(\pm)}\lambda_{lmg}^{(\pm)} + \mu_{kmgln}^{1(\mp)}) + \sum_{g=0}^{\infty}\mu_{kmgln}^{0(\mp)};$$

$$\chi_n = (1+n(1+\rho_{(e)}))^{-1}; \quad K_{mln} = (C_{m0l0}^{n0})^2;$$

$$H_{kmln}^{2(\pm)(\pm)} = \sum_{g=1}^{\infty}(\beta_{kmgln}^{2(\pm)}\lambda_{lmg}^{(\pm)} + \mu_{kmgln}^{1(\pm)}) + \sum_{g=0}^{\infty}\mu_{kmgln}^{0(\pm)};$$

$$\alpha_{mln} = -C_{m0l0}^{n0}C_{m(-1)l1}^{n0}\sqrt{m(m+1)l(l+1)};$$

$$H_{mgn}^{0(\pm)} = (\Pi_{mgn}^0 \mp \Pi_{mgn}^1\omega_m\omega_g - \Pi_{mgn}^2\omega_g^2)(\lambda_{mmg}^{(+)} + \lambda_{mmg}^{(-)});$$

$$\psi_{kml}^{(\pm)(\pm)} = \omega_k \pm \omega_m \pm \omega_l;$$

$$\Xi_n^0 = \omega_n^2 + n(n+1)\chi_n(n-1)(4+2n-5W);$$

$$\psi_{kml}^{(+)(-)} = \omega_k + \omega_m - \omega_l;$$

$$\beta^{1(\pm)}_{kmgln} = \Pi^0_{kgn} + -\Pi^1_{kgn}\omega_k(\omega_l \pm \omega_m) - \Pi^2_{kgn}(\omega_l \pm \omega_m)^2;$$

$$\Xi^1_n = ((n+1)(n-1) - 3n\rho_{(e)})\chi_n;$$

$$\beta^{2(\pm)}_{kmgln} = \Pi^0_{kgn} + \Pi^1_{kgn}\omega_k(\omega_l \pm \omega_m) - \Pi^2_{kgn}(\omega_l \pm \omega_m)^2;$$

$$\Xi^2_n = \rho_{(e)}n(n-1)\chi_n;$$

$$\mu^{1(\pm)}_{kmgln} = \Lambda^1_{kmgln} \pm \Gamma^1_{kmgln}\omega_m\omega_k;$$

$$\mu^{0(\pm)}_{kmgln} = \Lambda^0_{kmgln} \pm \Gamma^0_{kmgln}\omega_m\omega_k; \quad D^{kn}_{lm} = 1 - \delta_{lm}\delta_{kn};$$

$$\begin{gathered}
\Lambda^0_{kmgln} = (n+1)\chi_n\omega_k^2 K_{gln} \\
\times(\alpha_{kmg}(k-2)/k + (k-1)(n-k+2)K_{kmg}/2) \\
+ \rho_{(e)}n\chi_n\omega_k^2\Big(((g+1-n)K_{gln} - \alpha_{gln}/(g+1)) \\
\times((k+2)K_{kmg} - \alpha_{kmg}/(k+1)) + ((k+3)\alpha_{kmg}/(k+1) \\
+ (k+2)(n-2-k)K_{kmg}/2)K_{gln}) \\
+ n(n+1)\chi_n(WK_{gln}((k^3 - 2(m+1)(m+2) - k^2(n-9) \\
- k(2m(m+3) + 3n - 22))K_{kmg} - 2(k+2)\alpha_{kmg})/2 \\
- ((3k(k+1) - 2)K_{kmg} - l(l+1)\alpha_{kmg}/2)K_{gln} \\
+ \alpha_{kmg}\left(l^2 K_{lgn} - \sum_{\nu=1}^{[l/2]}(2l - 4\nu + 1)K_{l-2\nu,g,n}\right)\Big);
\end{gathered}$$

$$\begin{gathered}
\Lambda^1_{kmgln} = n(n+1)\chi_n WkK_{kmg} \\
\times((g+1)(l-2-g+n)K_{lgn} + \alpha_{lgn}) + (n+1)\chi_n \\
\times((\alpha_{lgn}/g + (n+1-g)K_{lgn}) \\
\times(\alpha_{kmg}/m + (1-m)K_{kmg}))\omega_m^2;
\end{gathered}$$

$$\begin{gathered}
\Gamma^0_{kmgln} = (n+1)\chi_n((k-2)(K_{gln}((k-1)K_{kmg}/2 - \alpha_{kmg}/k) \\
+ K_{mgn}((k-1)K_{klg}/2 - \alpha_{klg}/k)) \\
- n(k-1)K_{gln}(\alpha_{kmg}/(mk) + K_{kmg})) \\
- \rho_{(e)}n\chi_n(((g+2)K_{mgn} - \alpha_{mgn}/(g+1)) \\
\times((k+2)K_{klg} - \alpha_{klg}/(k+1)) + (k+3)K_{mgn} \\
\times(\alpha_{klg}/(k+1) - (k+2)K_{klg}/2) \\
+ ((g+2)K_{gln} - \alpha_{gln}/(g+1))((k+2)K_{kmg} \\
- \alpha_{kmg}/(k+1)) + (k+3)K_{gln}(\alpha_{kmg}/(k+1) \\
- (k+2)K_{kmg}/2) - (n+1) \\
\times((\alpha_{mgn}/((m+1)(g+1)) + K_{mgn})((k+2)K_{klg} \\
- \alpha_{klg}/(k+1)) + K_{gln}((k+2)K_{kmg} - \alpha_{kmg}/(k+1)) \\
- (\alpha_{kmg}/((k+1)(m+1)) + K_{kmg})(k+2)K_{gln}));
\end{gathered}$$

$$\begin{gathered}
\Gamma^1_{kmgln} = (n+1)\chi_n((\alpha_{lgn}/g + (n+1-g)K_{lgn}) \\
\times((m-1)K_{kmg} - \alpha_{kmg}/m) + ((k+n)\alpha_{kgn}/(gk) \\
+ (n+1-g)K_{kgn})((m-1)K_{mlg} - \alpha_{mlg}/m));
\end{gathered}$$

$$\begin{gathered}
\Pi^0_{kmn} = (n+1)\chi_n(nK_{kmn}(2((k-1)(k+2) + m(m+1)) \\
+ W(k-1)(n-5-k)) + (\alpha_{kmn}/k + (n+1-k)K_{kmn})\omega_k^2) \\
- \rho_{(e)}n\chi_n\omega_k^2((n-1-k)K_{kmn} + \alpha_{kmn}/(k+1)) \\
+ n(n+1)\chi_n W((m+1)(k+n-m-2)K_{kmn} + \alpha_{kmn});
\end{gathered}$$

$$\begin{gathered}
\Pi^1_{kmn} = (n+1)\chi_n((k+m-n-2)K_{kmn} \\
- (n+k+m)\alpha_{kmn}/(mk)) + n\rho_{(e)}\chi_n((n-k-m-3)K_{kmn} \\
+ (k+m+n+3)\alpha_{kmn}/((m+1)(k+1)));
\end{gathered}$$

$$\begin{gathered}
\Pi^2_{kmn} = (n+1)\chi_n((m-n-1)K_{kmn} - \alpha_{kmn}/m) \\
+ n\rho_{(e)}\chi_n((n-m-1)K_{kmn} + \alpha_{kmn}/(m+1)),
\end{gathered}$$

C^{n0}_{m0l0} and $C^{n0}_{m(-1)l1}$ being the Clebsch–Gordan coefficients.

ACKNOWLEDGMENTS

This study was supported by the Russian Foundation for Basic Research (project no. 03-01-00760).

REFERENCES

1. A. I. Grigor'ev, Zh. Tekh. Fiz. **70** (5), 22 (2000) [Tech. Phys. **45**, 543 (2000)].
2. A. I. Grigor'ev and S. O. Shiryaeva, Izv. Ross. Akad. Nauk, Mekh. Zhidk. Gaza, No. 3, 3 (1994).
3. V. A. Koromyslov, S. O. Shiryaeva, and A. I. Grigor'ev, Zh. Tekh. Fiz. **73** (9), 44 (2003) [Tech. Phys. **48**, 1124 (2003)].
4. A. R. Gaibov and A. I. Grigor'ev, Zh. Tekh. Fiz. **73** (7), 13 (2003) [Tech. Phys. **48**, 813 (2003)].
5. A. N. Zharov, A. I. Grigor'ev, and S. O. Shiryaeva, Pis'ma Zh. Tekh. Fiz. **29** (9), 75 (2003) [Tech. Phys. Lett. **29**, 388 (2003)].
6. A. N. Zharov, S. O. Shiryaeva, and A. I. Grigor'ev, Zh. Tekh. Fiz. **73** (6), 36 (2003) [Tech. Phys. **48**, 697 (2003)].
7. A. N. Zharov, S. O. Shiryaeva, and A. I. Grigor'ev, Zh. Tekh. Fiz. **73** (12), 9 (2003) [Tech. Phys. **48**, 1511 (2003)].
8. S. O. Shiryaeva, A. I. Grigor'ev, V. A. Koromyslov, and A. N. Zharov, Zh. Tekh. Fiz. **73** (9), 60 (2003) [Tech. Phys. **48**, 1141 (2003)].
9. A.-H. Nayfeh, *Perturbation Methods* (Wiley, New York, 1973; Mir, Moscow, 1976).
10. R. C. Reid and T. K. Sherwood, *The Properties of Glasses and Liquids* (McGraw-Hill, New York, 1966; Khimiya, Leningrad, 1971).

Translated by N. Wadhwa

Technical Physics, Vol. 49, No. 8, 2004, pp. 1075–1078. Translated from Zhurnal Tekhnicheskoĭ Fiziki, Vol. 74, No. 8, 2004, pp. 120–123.
Original Russian Text Copyright © 2004 by Buyanov, Stishkov.

BRIEF COMMUNICATIONS

Peculiarities in the Structure of Electrohydrodynamic Through Flow in a Symmetric Electrode System

A. V. Buyanov and Yu. K. Stishkov
Research Institute of Physics, St. Petersburg State University, St. Petersburg, 198504 Russia
e-mail: stishkov@paloma.spbu.ru

Received November 25, 2003

Abstract—The patterns of velocity and acceleration distribution in an electrohydrodynamic through flow in a symmetric system of electrodes have been experimentally studied. Analysis of the main features in the kinematic and dynamic flow structures provides information on the distribution of space charge and the course of events in the recombination zone. It is established that the recombination zone extends beyond the interelectrode space. *© 2004 MAIK “Nauka/Interperiodica”.*

INTRODUCTION

Previously [1, 2] we described the zone structure of electrodynamic through flows in an asymmetric (wire–plane, sheet–plane) electrode system and performed a comparative analysis of such flows and counterflows in symmetric (wire–wire) electrode systems. One distinguishing feature of the flows in symmetric electrode systems is the presence of long lateral streams featuring charge recombination [3]. As is known, the structure of electrodynamic flows in symmetric electrode systems is determined by the ratio of the rates of ion formation at the cathode and anode. If these rates are equal, the flow has the form of two streams of equal intensity. In the lateral streams, the fluid moves perpendicularly to the line connecting the centers of electrodes. If the ion formation rates are different, the flow structure is distorted and the flow from a more “active” electrode (characterized by a higher rate of charge production) dominates over the counterflow and the boundary between these flows shifts toward the “passive” electrode (characterized by a lower rate of charge production). The case of a through flow is essentially a limiting case of counterflow, whereby the flow from the active electrode is much more intense than that from the passive one. The angle of lateral streams relative to the initial direction is very small, and the streams go far beyond the interelectrode space [1]. For this reason, such electrodynamic through flows in electrode systems are most promising for practical applications.

This paper addresses the kinematic and dynamic structures of an electrohydrodynamic through flow in a symmetric system of electrodes. The flows were imaged using fine (several dozen microns) air bubbles and the images were recorded with a TV camera. The recorded data were processes on a computer using a special program package described elsewhere [2, 5]. The results provide data on the fields of electrohydrodynamic flow velocity and acceleration vectors, surface diagrams, and maps of the velocity and acceleration isolines.

KINEMATIC STRUCTURE OF ELECTRODYNAMIC FLOW

Figure 1 shows a map of velocity isolines for an electrohydrodynamic through flow in a symmetric system of electrodes. The lengths are measured in units of the interelectrode distance. The maps are normalized to the maximum velocity. A stream from the active electgrode (cathode) is indicated by arrow *1*, while streams going beyond the passive electrode (anode) are indicated by arrow *2*. The centers of electrodes occur at the points with the coordinates (0, 0) for the cathode and (0, 1) for the anode. As can be seen, the velocity field structure in the electrohydrodynamic flow significantly differs from that in a system of the “wire over plane” type [2]. The main distinctions (similar to the case of counterflows) refer to the zones where the fluid flow exhibits drag (deceleration). In a through flow, the zone of

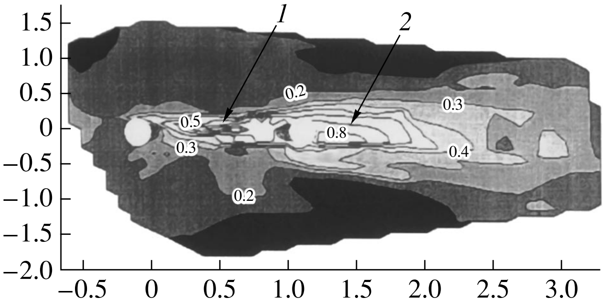

Fig. 1. A map of velocity isolines in an electrohydrodynamic through flow in a symmetric electrode system. Arrows indicate (*1*) a stream behind the active electrode (cathode) and (*2*) a stream protruding behind the passive electrode (anode).

1063-7842/04/4908-1075$26.00 © 2004 MAIK “Nauka/Interperiodica”

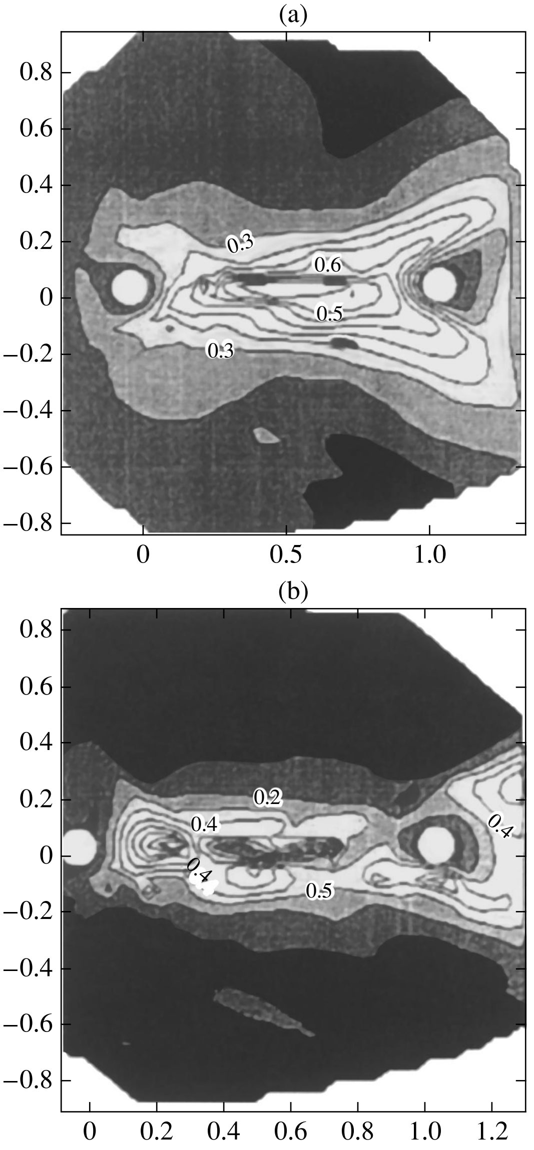

Fig. 2. Maps of (a) velocity isolines and (b) acceleration isolines in an electrohydrodynamic flow within the interelectrode space.

deceleration protrudes beyond the interelectrode space: in the region behind the passive electrode, the fluid velocity decreases by half at a distance equal to the electrode spacing *L*. In this region, the field direction is opposite to the direction of fluid motion. However, the deceleration effect is quite small. This feature makes the electrohydrodynamic through flow in the electrodes especially attractive from a practical standpoint. However, these prospects require thorough investigation on the flow structure.

Figure 2 shows the maps of velocity (a) and force (b) isolines for a through flow in the region between electrodes. The front edges of the active and passive electrode occur at (0, 0) and (0, 1), respectively. As can be seen, the zone structure characteristic of the flows in asymmetric electrode systems (wire–plane, sheet–plane) is retained on the whole, except for the deceleration zone. Longitudinal dimensions of the acceleration zone amount to 0.3–0.4*L*, while the analogous zones for counterflows and flows in the wire–plane system do not exceed 0.2*L*. The maps clearly reveal the zone of uniform flow, which begins at a distance of 0.3*L* from the active electrode and terminates at 0.8*L*, thus covering most of the interelectrode space. The zone of deceleration of the through flow begins at 0.8*L* and extends far beyond the interelectrode space.

THE STRUCTURE OF ACCELERATION AND DECELERATION ZONES

In order to study the acceleration zone structure in the through flow regime in more detail, we have processed the video recordings of the electrohydrodynamic flow in this zone near the passive electrode. The recordings were made at large magnification, which allowed the zone of interest to be studied with significantly higher resolution. The results of such data processing are presented in Fig. 3. As can be seen, the current lines of the electrohydrodynamic flow exhibit significant concentration at the active electrode and form a narrow central stream. The acceleration zone has a funnel-like shape with relatively small dimensions (2–4*D* in length and about 2*D* in the cross section, where *D* is the electrode diameter). This zone is localized immediately at the surface of the active electrode (cathode). In the acceleration zone, the electrohydrodynamic flow velocity significantly increases. Similar to the case of flows in an asymmetric electrode system, the kinetic energy of the flow is accumulated due to the energy supplied by electric current. As can be seen in Fig. 3b, a strong volume electric force is operative near the active electrode. At a distance of 1–2*D* from the electrode, the acceleration acquires a component directed at a sharp angle relative to the central axis. This effect is probably related to the electric charge present in the central stream of the electrohydrodynamic flow.

The magnitude of acceleration before the electrode edge (0, 0) is significantly smaller than in the interelectrode space, whereas in an asymmetric electrode system and in counterflows [3] the fluid is noticeably accelerated even in the region in front of the active electrode. Another peculiarity of the electrohydrodynamic through flow in the symmetric electrode system is a relatively small width (1–2*D*) of the central stream (Fig. 3).

Figures 4 and 5 show the results of high-resolution investigation of a zone near the passive electrode. The front edge of the passive has the coordinates (0, 1). In the case of the usual streamlining of a cylinder by a fluid under such conditions, the current lines go around the surface in the so-called creeping flow regime and the current line configuration is symmetric with respect to the system axis [6]. An increase in the flow velocity leads to the appearance of flow detachment behind the

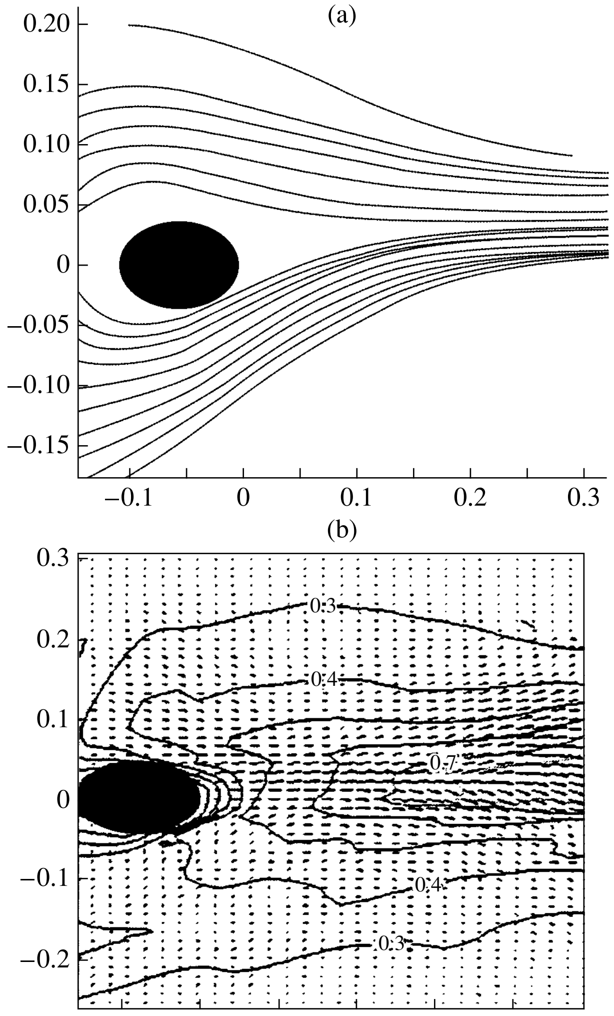

Fig. 3. Maps of (a) current lines and (b) velocity isolines near the active electrode. Arrows show the acceleration vector field.

cylinder. An analysis of the electrohydrodynamic through flow in the electrode system under consideration showed that detachment of the flow behind the electrode takes place at lower velocities. Moreover, the flow structure in this system exhibits a characteristic feature: the flow separates into two streams not connecting over a large distance downstream from the electrode (Fig. 4). Thus, the flow exhibits a "loop" inside which the hydrodynamioc stability of the electrohydrodynamic flow is broken: the current lines change their direction, the flow exhibits the first signs of turbulization, and the line trajectories change with time.

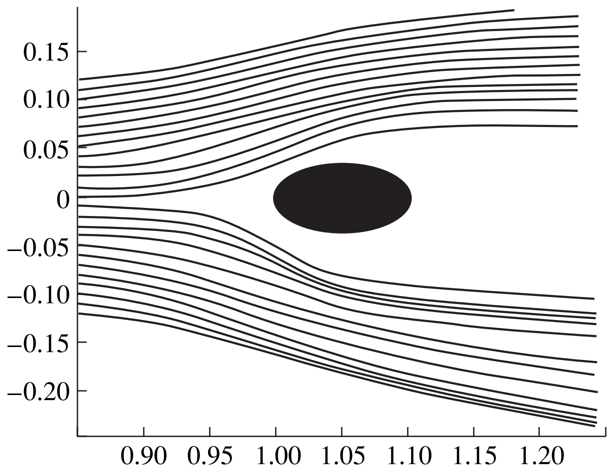

Fig. 4. A map of current lines near the passive electrode.

As can be seen from Fig. 2, the rate of acceleration (deceleration) in the drag zone is significantly lower than that in the acceleration zone and only slightly higher than in the zone of uniform flow. Figure 5 shows that most pronounced changes in the flow velocity occur in the vicinity of the passive electrode. This region contains a small wedge-shaped stagnation zone in front of the electrode. As can be seen from the image of the acceleration vector field (Fig. 5b), the region in front of the passive electrode features rather large drag forces. The presence of this zone is related to the injection of charge from the passive electrode, which is carried away by the main flow to the region behind the electrode. In this case, the injection is much less intense than in the case of counterflows and is incapable of forming an opposite stream. Nevertheless, a bipolar structure of the recombination zone is retained, although the zone is displaced to the region behind the electrode. In this region, the inner layers of the stream are charged so that the sign of this charge is the same as that of the passive electrode, while the outer layers carry the opposite charge.

This bipolar structure is precisely what accounts for the hydrodynamic structure observed in the region behind the passive electrode, comprising two streams resembling the structure of lateral streams characteristic of the electrohydrodynamic counterflows [7]. In the case of counterflow, the streams bearing opposite charges separate at the point of merging to form lateral streams in which the fluid is moving in parallel jets without intermixing. Since the bipolar structure of the lateral streams in counterflows is evident, it is reasonable to assume that this bipolar structure is retained on the passage from counterflow to through flow. By the same token, the region of active charge recombination is also retained but displaced beyond the intgerelectrode space. Under this assumption, the flow structure observed behind the electrode can be explained. The charge supplied from the active electrode is equilibtrated on the whole in the region behind the passive electrode by the charge injected from the latter electrode. Behind this electrode, the stream (possessing a bipolar structure) as a whole is not subjected to the action of electric forces and the flow velocity decreases predominantly under the action of viscous forces. As the flow propagates, the opposite charges attract and recombine. This process is hindered by the molecular surrounding of ions. Because of the mutual attraction of ions and rather slow recombination process, the transverse dimensions of the flow behind the electrode remain almost constant, as can be clearly seen in Fig. 1.

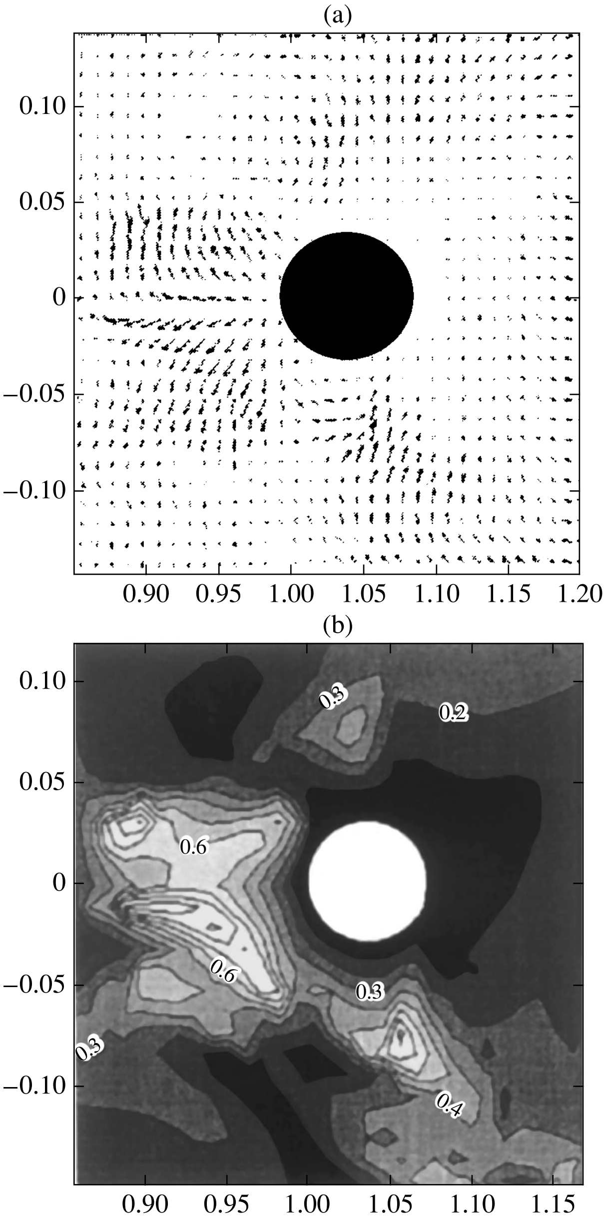

Fig. 5. (a) Structure of the acceleration vector field and (b) map of the acceleration isolines near the passive electrode.

CONCLUSIONS

The properties of the electrohydrodynamic through flow in the symmetric electrode system are highly attractive from the standpoint of various electrohydrodynamic devices. Such a flow provides optimum conditions for the conversion of electric energy into hydrodynamic energy, which can be of considerable practical value, opening a new direction in the design of electrohydrodynamic systems. The new approach is characterized by rational selection of the properties of the electrode–fluid interface and by making allowance for a particular zone structure of the electrohydrodynamic flow.

REFERENCES

1. Yu. K. Stishkov and A. A. Ostapenko, *Electrohydrodynamic Flows in Liquid Dielectrics* (Leningr. Gos. Univ, Leningrad, 1989) [in Russian].
2. Yu. K. Stishkov and M. A. Pavleĭno, Élektrokhim. Obrab. Met., No. 1, 14 (2000).
3. Yu. K. Stishkov and A. Buyanov, Zh. Tekh. Fiz. **73** (8), 34 (2003) [Tech. Phys. **48**, 972 (2003)].
4. Yu. K. Stishkov, Dokl. Akad. Nauk SSSR **288**, 861 (1986) [Sov. Phys. Dokl. **31**, 500 (1986)].
5. Yu. K. Stishkov and M. A. Pavleĭno, in *Proceedings of the 6th International Scientific Conference on Modern Problems of Electrophysics and Electrohydrodynamics of Fluids, St. Petersburg, 2000*, pp. 4–9.
6. Van Dyke, *Album of Fluid Motion* (Parabolic, Stanford, 1982; Mir, Moscow, 1986).
7. A. V. Buyanov, M. A. Pavleĭno, and Yu. K. Stishkov, Vestn. S-Peterb. Univ., Ser. 4: Fiz., Khim., No. 2 (12), 109 (2001).

Translated by P. Pozdeev

Technical Physics, Vol. 49, No. 8, 2004, pp. 1079–1080. Translated from Zhurnal Tekhnicheskoĭ Fiziki, Vol. 74, No. 8, 2004, pp. 124–125.
Original Russian Text Copyright © 2004 by Protasevich.

BRIEF COMMUNICATIONS

Prospects of the Combined Use of Laser and Microwave Radiation for Increasing the Efficiency of Interaction with Metal Targets

E. T. Protasevich

Tomsk Polytechnic University, Tomsk, 6334050 Russia

e-mail: lev@tpu.ru

Received November 28, 2003

Abstract—It is proposed to use centimeter microwaves to enhance the interaction of laser radiation with metal targets. *© 2004 MAIK “Nauka/Interperiodica”.*

It is well known [1] that high-power laser radiation can produce high-density heat fluxes through a small area of the target surface and, thus, makes it possible to heat, melt down, and evaporate almost all the materials. All the above processes are governed by the thermal effect of radiation absorption by solids. However, when a target is made of metal, optical radiation is well reflected from its surface. In particular, for tungsten, the reflection coefficient for a CO_2 laser is about 0.9; i.e., the absorption coefficient of a cold target is no higher than 10% [1].

When the radiation intensity is $\sim 10^{10}$ W/cm^2, an optical breakdown of air occurs over the target surface and a plasma is produced with a temperature of a few tens of thousands of kelvins [2]. Depending on the experimental conditions, the generation of a plasma near the target can significantly change the character of the interaction of laser radiation with the target: this interaction can either be weakened or enhanced.

For short ($\tau \sim 1$ μs) pulses, the interaction is enhanced when the plasma has no time to move away from the target during the laser pulse. In this case, the efficiency of energy transfer increases due to the increase in radiation absorption with a subsequent heat transfer to the target by either heat conduction or short-wavelength (optical or UV) radiation that is emitted by the plasma and is absorbed by the target more efficiently than the original long-wavelength CO_2 laser radiation.

The effective absorption coefficient of the target α is maximum when the radiation intensity reaches the breakdown intensity. As the radiation intensity increases further, the value of α decreases rapidly, because the plasma propagation velocity increases and the plasma has time to move away from the target during the laser pulse. There is an obvious contradiction: on the one hand, the initial breakdown requires a high intensity of optical radiation; on the other hand, the energy deposition is more efficient at a lower radiation intensity. This contradiction is usually eliminated by specially shaping the laser pulse. For this purpose, a laser pulse is formed that consists of a narrow peak with a duration of ~200 ns (which is intended for breakdown) and a long tail comprising most energy of the pulse (which is intended for energy deposition in a plasma).

In this paper, we point out to the fact that the above problem can also be solved by simultaneously applying laser and microwave radiation to the target. In this case, laser radiation produces an air breakdown over the target surface, whereas microwave radiation provides efficient energy deposition. Let us consider both these processes in more detail.

The reflection of microwaves from the conducting surface of the target is accompanied by the formation of a standing wave. According to the boundary conditions, the tangential component of the electric field of the incident wave vanishes at the conductor surface. The first maximum of the standing wave is located at a distance of about $l = \lambda/4$ from the target surface (here, λ is the microwave wavelength). Obviously, to achieve the maximum energy deposition in the plasma, it is necessary that $l \longrightarrow 0$. In practice, the centimeter wavelength range is optimal from the standpoint of energy deposition, because the power of the generated microwave radiation decreases sharply when passing to shorter (millimeter) microwaves [3]. For $\lambda = 3$ cm, we find that $l \approx 0.75$ cm.

Our measurements show [4] that, for a relative air humidity of ~70% and a temperature of $T = 292.5$ K, the velocity of the front of an expanding plasma produced by a CO_2 laser ($\lambda = 10.6$ μm, $I = 10^8$–10^{10} W/cm^2, and $\tau = 100$ ns) depends on the time passed from the instant of breakdown. In the initial stage, the plasma velocity decreases linearly over time. However, 3.5 μs after the breakdown, the time dependence of the veloc-

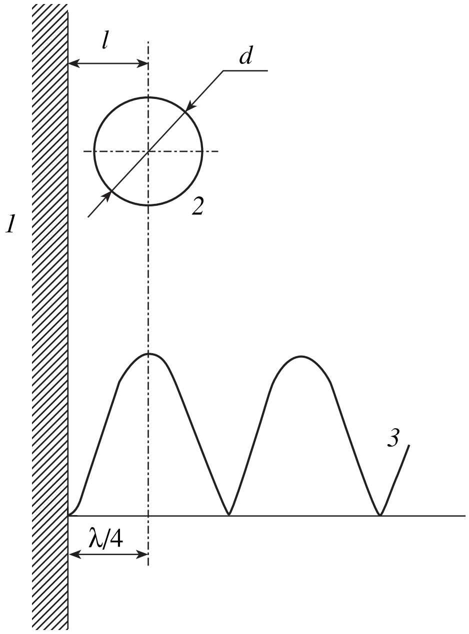

Schematic diagram of the combined action of laser and microwave radiation: (*1*) target, (*2*) laser plasma, and (*3*) standing wave.

ity shows a steep inflection and the plasma velocity becomes lower than (or comparable to) the speed of sound. The average velocity at the descending segment of the curve $V = f(t)$ is about 3×10^3 m/s. Assuming 3.5 μs to be the time the laser plasma takes to move away from the target, it is easy to calculate that, at this time, the plasma is located a distance of ~1 cm from the target surface; i.e., it is at a distance nearly equal to λ/4 for the microwave radiation that provides the necessary energy deposition in the plasma. Therefore, the plasma bunch falls into the first (counted from the target) maximum of the electric field of the standing wave, as is seen in the figure.

To provide the maximum energy deposition in the plasma, it is necessary that the condition [5]

$$\lambda = 3.65d \qquad (1)$$

be satisfied (here, d is the plasma diameter).

In our case, this condition means that $d \sim 0.8$ cm; i.e., the plasma radius $d/2$ turns out to be smaller than the distance to the target l. Since the microwave energy absorption is resonant in character, the plasma size becomes stabilized. As a result, the efficiency with which the plasma acts on the target in the course of microwave absorption increases. Since $\lambda > 1$ cm, the structure of the standing wave is only slightly distorted throughout the microwave pulse. Model experiments performed in a standing wave with a probing body whose dimensions are close to the plasma diameter also showed that the field structure is distorted only slightly.

Hence, it follows from the above consideration that the combined action of laser and microwave radiation provides a new method for making holes in metal targets.

REFERENCES

1. A. A. Vedenev and G. G. Gladush, *Physical Processes in Laser Treatment of Materials* (Énergoatomizdat, Moscow, 1985) [in Russian].
2. Yu. D. Kopytin, E. T. Protasevich, L. K. Chistyakova, and V. I. Shishkovskiĭ, *The Effect of Laser and Microwave Radiation on Air* (Nauka, Novosibirsk, 1992) [in Russian].
3. D. A. Swegle and J. N. Benford, in *Proceedings of the 12th International Conference on High-Power Particle Beams, Haifa, 1998*, Vol. 1, pp. 149–152.
4. E. T. Protasevich and V. A. Khan, *Propagation of Electromagnetic Wave Beams through the Atmosphere* (Izd. Tomsk. Univ., Tomsk, 1994) [in Russian].
5. P. L. Kapitsa, Dokl. Akad. Nauk **101**, 245 (1995).

Translated by N. Larionova

Technical Physics, Vol. 49, No. 8, 2004, pp. 1081–1083. Translated from Zhurnal Tekhnicheskoĭ Fiziki, Vol. 74, No. 8, 2004, pp. 126–127.
Original Russian Text Copyright © 2004 by Baranov.

BRIEF COMMUNICATIONS

Proof of Expansion of the Reciprocal Distance in Spheroidal Coordinates

A. S. Baranov

Pulkovo Observatory, Russian Academy of Sciences,
Pulkovskoe shosse 65, St. Petersburg, 196140 Russia

Received December 1, 2003

Abstract—A concise proof is given for the expansion of the reciprocal distance between two points in spheroidal harmonics. The proof is given for an oblate and a prolate spheroid. *© 2004 MAIK “Nauka/Interperiodica”.*

INTRODUCTION

The expansion of the reciprocal distance D^{-1} between two arbitrary points in spheroidal harmonics plays the decisive role in the representation of solutions to the Laplace and Poisson equations in spheroidal coordinates. The corresponding general formula is derived in [1], but the proof is rather cumbersome. An analogous derivation was later given in the handbook [2]. Another proof was given in [3], but it is still indirect and based on surface integrals.

Here, we show how at least the axisymmetric part of the expansion of D^{-1} can be obtained in a concise and direct manner. In all probability, the asymmetric part can also be obtained in a similar way using the derivation proposed here as an example. This will facilitate the construction of a more elegant theory of potential in spheroidal coordinates (apart from the aforementioned handbooks, a concise description of this theory can be found in [4]).

COORDINATES OF AN OBLATE SPHEROID

We will use the Cartesian coordinates x_1, x_2, x_3 and spheroidal coordinates t, τ, φ connected via the well-known relations

$$x_1 = R\cos\varphi, \quad x_2 = R\sin\varphi,$$

$$R = c\sqrt{(1+\lambda^2)(1-\mu^2)}, \tag{1}$$

$$x_3 = c\lambda\mu, \quad \varphi = \arctan\left(\frac{x_2}{x_1}\right)$$

(the x_3 axis is the polar axis).

We presume the existence of a certain reference spheroid with semiaxes $a_1(=a_2)$ and a_3, where $a_1 > a_3$ (i.e., we consider an oblate spheroid for the time being). The parameter c introduced in relations (1) is defined as the focal length $c = \sqrt{a_1^2 - a_3^2}$. We proceed from the well-known identity [5]

$$\frac{1}{h-t} = \frac{1}{c}\sum_{n=0}^{\infty}(2n+1)P_n\left(\frac{t}{c}\right)Q_n\left(\frac{h}{c}\right) \tag{2}$$

$$(-c < t < c, \quad h > c)$$

(P_n and Q_n are the standard notation for associated Legendre functions of the first and second kind, respectively).

Substituting $-ic$ for c in relation (2), we obtain

$$\frac{1}{h-t} = \frac{i}{c}\sum_{n=0}^{\infty}(2n+1)P_n\left(\frac{it}{c}\right)Q_n\left(\frac{ih}{c}\right). \tag{3}$$

To apply the theorem of addition of spherical functions ([6], vol. II), we will use the representation $t = -ic(\cos\theta\cos\psi + \sin\theta\sin\psi\cos\varphi)$ (angles θ, ψ, and φ vary from 0 to 2π). This gives

$$P_n\left(\frac{it}{c}\right) = P_n(\cos\theta)P_n(\cos\psi)$$

$$+ 2\sum_{m=1}^{n}\frac{(n-m)!}{(n+m)!}P_n^m(\cos\theta)P_n^m(\cos\psi)\cos n\varphi.$$

Integration with respect to φ from 0 to 2π gives

$$\frac{2\pi}{\sqrt{(h+ic\cos\theta\cos\psi)^2 + c^2\sin^2\theta\sin^2\psi}}$$

$$= \frac{2\pi i}{c}\sum_{n=0}^{\infty}(2n+1)Q_n\left(\frac{ih}{c}\right)P_n(\cos\theta)P_n(\cos\psi). \tag{4}$$

We assume that $\cos\psi$ is purely imaginary ($\cos\psi = i\eta$); then $\sin\psi > 1$). Canceling out 2π in relation (4), we obtain on the left-hand side

$1/\sqrt{(h - c\eta\cos\theta)^2 + c^2\sin^2\theta\sin^2\psi}$ (i.e., the reciprocal distance between the test point with coordinate $z = h$ on the one hand and the attracting point with the cylindrical coordinates $R = c\sin\theta\sin\psi$, $z = c\eta\cos\theta$ on the other hand). A comparison of these relations with (1) gives

$$\sqrt{(1 + \lambda^2)(1 - \mu^2)} = \sin\theta\sin\psi, \quad \lambda\mu = \eta\cos\theta. \tag{5}$$

The real-valued solution of Eqs. (5) has the form

$$\lambda = \eta, \quad \mu = \cos\theta. \tag{6}$$

To unify notation, we denote the spheroidal coordinates of the test point by λ and μ, but with prime. As long as we consider the position of this point on the axis, the following conditions must be satisfied: $\mu' = 1$ and $\lambda' = h/c$.

With allowance for these remarks and the definition of function q adopted in [6], we obtain from expression (4)

$$\begin{aligned} \frac{1}{D} &= \frac{i}{c}\sum_{n=0}^{\infty}(2n+1)Q_n(i\lambda')P_n(\mu)P_n(i\lambda) \\ &= \frac{1}{c}\sum_{n=0}^{\infty}(2n+1)q_n(\lambda')P_n(\mu)p_n(\lambda). \end{aligned} \tag{7}$$

This relation was obtained for the test point on the axis. In the remaining space, if we take the rotationally symmetric part and mark it by angle brackets, we must replace, in accordance with the general rule, $q_n(\lambda')$ by the harmonic function $P_n(\mu')q_n(\lambda')$; this leads to the sought formula

$$\left\langle\frac{1}{D}\right\rangle = \frac{1}{c}\sum_{n=0}^{\infty}(2n+1)P_n(\mu')q_n(\lambda')P_n(\mu)p_n(\lambda). \tag{8}$$

Naturally, this formula coincides with those given in [1–3].

COORDINATES OF PROLATE SPHEROID

In some physical problems, the coordinate system is based on a prolate spheroid. Instead of relations (1) slightly different relationships operate:

$$R = c\lambda\mu, \quad z = c\sqrt{(1 + \lambda^2)(1 - \mu^2)}. \tag{9}$$

In this case, we substitute $t = c(\cos\theta\cos\psi + \sin\theta\sin\psi\cos\varphi)$ into relation (2), which gives

$$P_n\left(\frac{t}{c}\right) = P_n(\cos\theta)P_n(\cos\psi) + 2\sum_{m=1}^{n}\frac{(n-m)!}{(n+m)!}P_n^m(\cos\theta)P_n^m(\cos\psi)\cos n\varphi.$$

Integration of Eq. (2) with respect to φ gives

$$\begin{aligned} &\frac{2\pi}{\sqrt{(h - c\cos\theta\cos\psi)^2 - c^2\sin^2\theta\sin^2\psi}} \\ &= \frac{2\pi}{c}\sum_{n=0}^{\infty}(2n+1)Q_n\left(\frac{h}{c}\right)P_n(\cos\theta)P_n(\cos\psi). \end{aligned} \tag{10}$$

A comparison with relationships (9) leads to

$$\begin{aligned} R = ic\sin\theta\sin\psi, \quad h = c\sqrt{\lambda'^2 + 1}, \\ z = c\cos\theta\cos\psi. \end{aligned} \tag{11}$$

After simple transformations, we obtain

$$\lambda = i\sin\psi, \quad \mu = \sin\theta, \tag{12}$$

i.e., $\sin\psi$ must be purely imaginary and $\cos\psi > 1$ must be greater than unity.

As a result, we obtain the relation

$$\begin{aligned} \frac{1}{\sqrt{(h - z)^2 + R^2}} &= \frac{1}{c}\sum_{n=0}^{\infty}(2n+1)Q_n\left(\frac{h}{c}\right) \\ &\times P_n(\sqrt{1 - \mu^2})P_n(\sqrt{1 + \lambda^2}) \end{aligned} \tag{13}$$

with its sought generalization to an arbitrary point

$$\begin{aligned} \left\langle\frac{1}{D}\right\rangle &= \frac{1}{c}\sum_{n=0}^{\infty}(2n+1)Q_n(\sqrt{1 + \lambda'^2})P_n(\sqrt{1 - \mu'^2}) \\ &\times P_n(\sqrt{1 - \mu^2})P_n(\sqrt{1 + \lambda^2}). \end{aligned} \tag{14}$$

This formula is also known from the literature (to within the notation).

CONCLUSIONS

Most of the problems associated with separation of variables in the theory of potential were solved by the beginning of the 20th century. However, various details and the structure of the theory itself continue to be improved [7]. We hope that our approach will be helpful since it reveals a logical relationship between various formulas and can hence facilitate the derivation of new relation of practical interest for problems in astronomy, electrostatics, theory of elasticity, and other aspects of mathematical physics.

ACKNOWLEDGMENTS

I am sincerely grateful to V.A. Antonov for his persistent interest and attention to this research.

REFERENCES

1. E. W. Hobson, *The Theory of Spherical and Ellipsoidal Harmonics* (Cambridge University Press, Cambridge, 1931; Inostrannaya Literatura, Moscow, 1952).
2. L. Robin, *Fonctions spheriques de Legendre et fonctions spheroidales* (Gauthie-Villars, Paris, 1958), Vols. 2–3.
3. A. S. Baranov, Zh. Tekh. Fiz. **72** (2), 36 (2002) [Tech. Phys. **47**, 177 (2002)].
4. V. A. Antonov, E. I. Timoshkova, and K. V. Kholshevnikov, *Introduction to the Newtonian Potential* (Nauka, Moscow, 1988) [in Russian].
5. M. Abramovitz and I. A. Stegun, *Handbook of Mathematical Functions* (Dover, New York, 1971; Nauka, Moscow, 1979).
6. *Higher Transcendental Functions*, Ed. by A. Erdelyi (McGraw-Hill, New York, 1955; Nauka, Moscow, 1979), Vol. 2.
7. B. P. Kondrat'ev, *Theory of Potential and Figures of Equilibrium* (Inst. Komp'yut. Issled., Moscow, 2003) [in Russian].

Translated by N. Wadhwa

Technical Physics, Vol. 49, No. 8, 2004, pp. 1084–1085. Translated from Zhurnal Tekhnicheskoĭ Fiziki, Vol. 74, No. 8, 2004, pp. 128–129.
Original Russian Text Copyright © 2004 by Anashko, Semirov, Gavrilyuk, Dushutin.

BRIEF COMMUNICATIONS

Influence of Annealing on the Magnetoimpedance Effect in Amorphous FeCoMoSiB Ribbons

A. A. Anashko, A. V. Semirov, A. A. Gavrilyuk, and K. V. Dushutin
Irkutsk State Teachers Training University, Irkutsk, 664011 Russia
e-mail: semirov@isttu.irk.ru

Received December 4, 2003

Abstract—The effect of annealing by electric current passing through a sample prepared from the amorphous metallic alloy Vitrovac 6025 Z of the composition $Fe_4Co_{67}Mo_{1.5}Si_{165}B_{11}$ on the form of the dependence of the sample impedance on the external magnetic field is investigated. The results are explained on the basis of the concepts concerning the change in the preferred direction of the sample magnetization. © *2004 MAIK “Nauka/Interperiodica”.*

This communication is devoted to the analysis of the effect of annealing by an electric current passing through the sample on the form of the dependence of the sample impedance on a constant external magnetic field. The experiments were made on the samples prepared from the ribbons of amorphous metallic alloy Vitrovac 6025 Z of the composition $Fe_4Co_{67}Mo_{1.5}Si_{165}B_{11}$ in the form of 20-mm-long strips 1mm in width and 25 μm in thickness. The saturation magnetostriction of the alloy was $\lambda_s \approx -3 \times 10^{-7}$, while the saturation induction was $B_s \approx 0.55$ T. The samples for studying the influence of annealing on the magnetoimpedance effect were cut along the initial ribbon.

Annealing was carried out by an ac current of f = 50 Hz passing through the sample by gradually increasing the current from 0.5 to 1.3 A with a step of 0.1 A for 20 s.

The magnetoimpedance effect was studied in magnetic fields of up to 9600 A/m with an ac current frequency varying from 0.1 to 10 MHz. During all measurements, the external magnetic field was oriented along the sample.

The magnetoimpedance effect was measured using a circuit consisting of a series-connected high-resistance resistor and the sample. The magnetoimpedance effect $\Delta Z/Z$ was determined using the expression

$$\frac{\Delta Z}{Z} = \frac{Z_H - Z_0}{Z_0} = \frac{U_H - U_0}{U_0},$$

where Z_0 is the sample impedance for $H = 0$, Z_H is the sample impedance in a magnetic field H, U_0 is the voltage across the sample at $H = 0$, and U_H is the voltage across the sample in field H.

The $Z(H)$ dependence obtained in the initial sample has two characteristic segments. The first is observed in weak magnetic fields and impedance Z on this segment is independent of the value of field H. The second segment corresponds to a monotonic decrease in Z with increasing H and the attainment of saturation in the $Z(H)$ dependence (curve *1* in Fig. 1). The maximal value of the negative magnetoimpedance effect in this case amounts to 62%.

During annealing at the first stage, the sample impedance Z_0 in field $H = 0$ increases, but the form of the $Z(H)$ dependence is preserved (curve *2*). In the course of further annealing by increasing current, the value of Z_0 decreases, but the $Z(H)$ dependence acquires a segment on which $Z > Z_0$ (curves *2*–*9*). Initially, upon an increase in the annealing current, the positive magnetoimpedance effect increases (curves *3* and *4*), its maximum observed value being 59%. Subsequent annealing at higher values of the current leads to a decrease in the sample impedance Z_+, corresponding

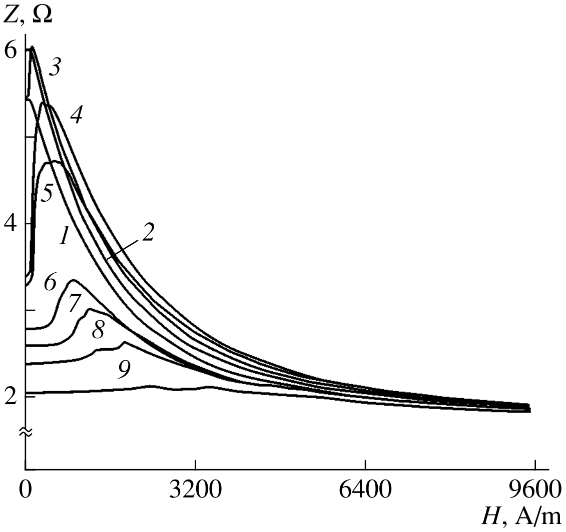

Fig. 1. Dependence of impedance Z of the sample on the external magnetic field H at various annealing stages.

1063-7842/04/4908-1084$26.00 © 2004 MAIK “Nauka/Interperiodica”

to the maximum positive effect (curves *6–9*) and reduces the value of the maximal positive and negative magnetoimpedance effect.

It should also be noted that the widths of the peaks on the *Z*(*H*) curves increase in the course of annealing and the peaks are shifted towards stronger magnetic fields.

The dependence of the sample impedance on the constant magnetic field *Z*(*H*) is determined by the mutual orientation of the easy magnetization axis on the sample surface, the direction of the constant applied magnetic field *H*, and the direction of the rf current *I* and is determined by various mechanisms of magnetization reversal process [1, 2]. It should be noted that in Co-based amorphous metallic alloys obtained by fast quenching (e.g., in Vitrovac 6025 Z), the easy magnetization axis on the sample surface coincides with the rolling axis of the ribbon [3]. This is confirmed by the results of investigation of magnetic hysteretic properties.

If the easy magnetization axis of the sample is parallel to the direction in which the constant external magnetic field *H* and high-frequency current *I* are applied, processes of domain wall displacement predominantly occur in the samples with increasing *H*. In relatively weak magnetic fields, sample impedance *Z* remains unchanged. With a further increase in *H*, sample impedance *Z* decreases monotonically until the *Z*(*H*) dependence attains saturation (curve *1* in Fig. 2).

If the easy magnetization axis of the sample is perpendicular to the direction in which the constant external magnetic field *H* is applied, magnetization reversal takes place in the samples upon an increase in *H* so that the magnetization rotates in the direction of magnetic field *H*. The sample impedance *Z* in this case first increases, attains its maximal value Z_+, and then monotonically decreases until the *Z*(*H*) dependence attains saturation (curve *2* in Fig. 2).

It follows hence that the change in the *Z*(*H*) dependence during annealing can be caused by the following factors. During annealing by a current passing through the sample, the sample is heated by the current and the sample experiences the action of the magnetic field induced by the current passing through it. Under the action of this magnetic field, a domain structure is formed with a preferred direction of magnetization (and, hence, the direction of the easy magnetization axis) lying in the plane of the sample perpendicular to its length. This is confirmed by the matching forms of the *Z*(*H*) dependences in Fig. 1 (curves *3–8*) and Fig. 2 (curve *2*). The increase in the peak widths on the *Z*(*H*) curves observed as a result of sample annealing and the displacement of the peaks towards stronger magnetic fields may stem from an increase in the coercive force and the anisotropy field during sample crystallization.

Thus, the following facts were established as a result of our experiments.

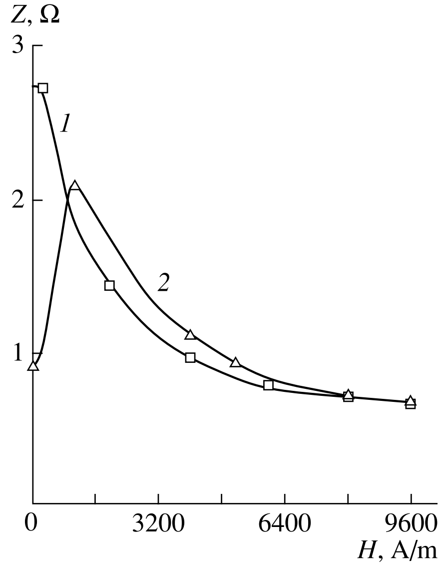

Fig. 2. Dependence of sample impedance *Z* on external magnetic field *H*, obtained on samples of composition $Fe_4Co_{67}Mo_{1.5}Si_{165}B_{11}$, which were cut in the form of 10-mm-long ribbons 1mm in width and 25 μm in thickness along (*1*) and across (*2*) the rolling axis of the amorphous ribbon. The directions of application of the constant external magnetic field and the rf current coincide with the long side of the sample.

(1) As a result of annealing by a current passing through the sample, the form of the dependence *Z*(*H*) of the sample impedance on the external constant magnetic field changes, which can be due to the formation of a domains structure during annealing with the preferred direction of magnetization in the plane of the sample perpendicular to its length.

(2) During annealing, the widths of the peaks on the curves describing the dependence of the sample impedance on the external magnetic field increase and the peaks are displaced towards stronger magnetic fields, which may be due to an increase in the coercive force and the anisotropy field during the sample crystallization.

(3) Annealing is completed by a gradual decrease in the sample impedance to its value in the saturating magnetic field; i.e., the sample impedance becomes independent of the external magnetic field and, accordingly, the magnetoimpedance effect becomes equal to zero.

REFERENCES

1. A. A. Anashko, A. V. Semirov, and A. A. Gavrilyuk, Zh. Tekh. Fiz. **73** (4), 49 (2003) [Tech. Phys. **48**, 427 (2003)].
2. M. Vazquez, J. Magn. Magn. Mater. **226–230**, 693 (2001).
3. K. Suzuki, H. Fujimori, and K. Hasimoto, *Amorphous Metals* (Metallurgiya, Moscow, 1987) [translated from Japanese].

Translated by N. Wadhwa

Technical Physics, Vol. 49, No. 8, 2004, pp. 1086–1088. Translated from Zhurnal Tekhnicheskoĭ Fiziki, Vol. 74, No. 8, 2004, pp. 130–132.
Original Russian Text Copyright © 2004 by Brazhe, Shustov.

BRIEF COMMUNICATIONS

Resonant Absorption of Shear Instabilities in Flow Systems with Energy Dissipation

R. A. Brazhe and M. I. Shustov
Ul'yanovsk State Technical University, Ul'yanovsk, 432027 Russia
e-mail: brazhe@ulstu.ru

Received December 23, 2003

Abstract—It is shown that hydrodynamic and electrohydrodynamic waves excited in two-layer dissipative systems due to shear instabilities experience resonant absorption of two types: at the rotational frequency of particles of the medium and the frequency of their collision with the lattice. *© 2004 MAIK "Nauka/Interperiodica".*

INTRODUCTION

It was proved long ago by Helmholtz and Kelvin that the interface between two different liquids flowing with different velocities is unstable. Vortices formed in the vicinity of the velocity discontinuity surface propagate in the form of two hydrodynamic waves. One of these waves is directed along the vector of the relative velocity of the liquids, while the other propagates in the opposite direction in the case of long-wave perturbations, but can be reversed by the flow if the wavelength does not exceed a certain critical value for which the real part of the perturbation frequency Reω is equal to zero. It was shown in [1] that in the presence of viscosity, the region of such instability (convective instability or the Kelvin–Helmholtz instability) is observed in the entire range of wave numbers k; the hydrodynamic wave reversed by the flow carries a negative energy and is enhanced at the expense of the flow energy.

One of the authors (R.A.B.) took part in investigations of an electrohydrodynamic analogue of such instability [2, 3] in semiconducting n–n^+ and p–p^+ junctions with a longitudinal drift current in one of the layers. The dispersion equation describing the evolution of instabilities in question has the universal form [1–3]

$$a(\omega - Uk)^2 + \omega^2 - (1-a)kw = -4i\nu_2\omega k^2. \qquad (1)$$

Here, $a = \rho/\rho_2$ is the ratio of the densities of the upper and lower liquids in the case of the hydrodynamic problem or the ratio of the free charge carrier concentrations in the high- and low-resistivity layers of the junction in the case of the electrohydrodynamic problem and U is the velocity of the upper liquid relative to the stationary lower liquid or the drift velocity of charge carriers in the high-resistivity layer; w denotes the acceleration due to gravity or the mean value of acceleration of charge carriers in the contact electric field of the junction, respectively. The kinematic viscosity of the conventional or electron (hole) liquid is taken into account only in the lower (low-resistivity) layer and is denoted by ν_2.

The problem considered here can be extended to the case of collisional flow of the corresponding liquids. Let us imagine a situation when small spheres playing the role of atoms or ions in the crystal lattice of a semiconductor are arranged periodically in the lower layer (including the interface). On account of this circumstance, the equation of motion of the lower (low-resistivity) liquid acquires a term directly proportional to the velocity of particles and inversely proportional to the time of particle momentum relaxation [4, 5], while dispersion equation (1), as was shown by the authors, assumes the form

$$\begin{aligned} & a(\omega - Uk)^2 + \omega^2 - (1-a)kw \\ & = -4i\nu_2\omega k^2 - 2\nu_2\frac{k^2}{\tau_2} - i\frac{\omega}{\tau_2}. \end{aligned} \qquad (2)$$

We will study below the dispersion characteristics derived from this equation and above all the possibility of resonant absorption and amplification of waves with positive and negative energy, which was disregarded earlier.

RESONANCES ON DISPERSION CHARACTERISTICS

The solution of dispersion equation (2) has the form

$$\omega_{1,2} = \omega^*\frac{k}{k^*}\left(1 - i\nu_{2r}\frac{k}{k^*} - i\frac{1}{\tau_{2r}}\frac{k^*}{k} \pm \sqrt{D}\right),$$

$$\begin{aligned} D = {} & \frac{1}{a}\left(\frac{k^*}{k} - 1\right) - \nu_{2r}^2\left(\frac{k}{k^*}\right)^2 - 2i\nu_{2r}\frac{k}{k^*} \\ & - \frac{1}{\tau_{2r}^2}\left(\frac{k^*}{k}\right)^2 - 2i\frac{1}{\tau_{2r}}\frac{k^*}{k} + 2a\nu_{2r}\frac{1}{\tau_{2r}}. \end{aligned} \qquad (3)$$

Here, as in [3], the following notation has been

1063-7842/04/4908-1086$26.00 © 2004 MAIK "Nauka/Interperiodica"

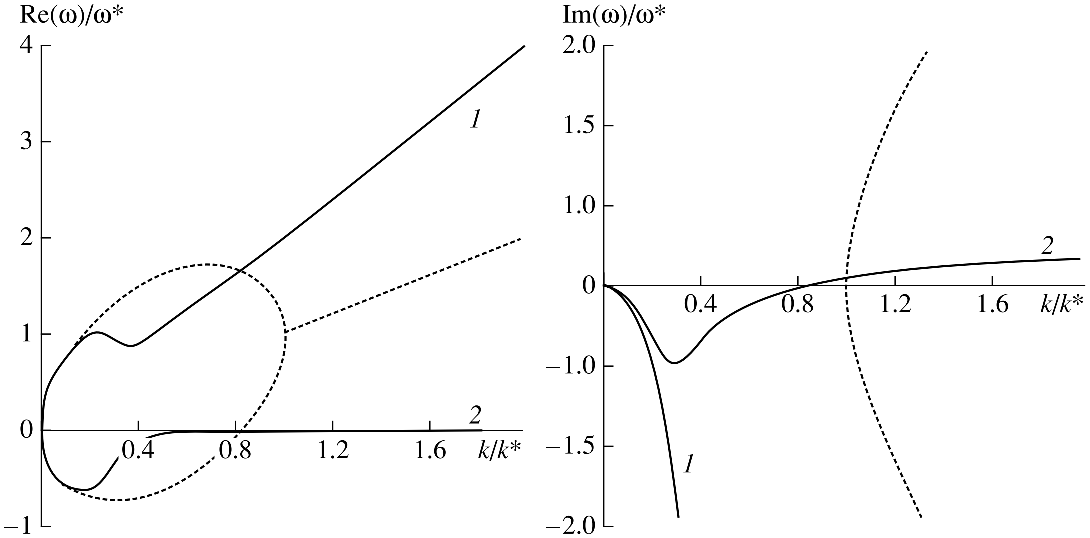

Fig. 1. Dispersion characteristics for waves with positive (*1*) and negative (*2*) energy in a flow system in the presence of viscosity and in the absence of collisions with the lattice ($a = 0.2$, $\nu_{2r} = 10$, $\tau_{2r} \longrightarrow \infty$). Dashed curves correspond to $\nu_{2r} = 0$.

introduced:

$$k^* = \frac{1-a^2}{aU^2}\omega, \quad \omega^* = \frac{aU}{1+a}k^*,$$

and the dimensionless viscosity and relaxation time are given by

$$\nu_{2r} = \frac{2\nu_2}{aU}k^*, \quad \tau_{2r} = 2\tau_2 aUk^*.$$

The dispersion characteristics defined by expression (3) are shown in Figs. 1 and 2. Branches *1* correspond to hydrodynamic (electrohydrodynamic) waves directed along the flow, while branches *2* correspond to waves counterpropagating relative to the flow for $\mathrm{Re}\omega < 0$ and reversed by the flow for $\mathrm{Re}\omega > 0$. Positive values of the imaginary part of frequency ($\mathrm{Im}\omega > 0$) correspond to amplification of negative-energy waves which attenuate with increasing dissipation [3], while its negative values indicate the absorption of positive-energy waves, which is the stronger, the higher the dissipation.

However, on the long-wave segments of the dispersion characteristics, we can see the segments corresponding to strong absorption of the waves counterpropagating relative to the flow (Fig. 1) and to attenuation of absorption (which is equivalent to amplification) of the waves directed along the flow (Fig. 2). In our opinion, these segments indicate the presence of two types of resonances for the waves considered here: at the frequency of rotation of hydrodynamic particles and at the frequency of their collisions with the lattice.

Let us begin with the first resonance, taking into account the model assumptions concerning hydrodynamic particles as spheres of radius r touching one another. In the wave processes analyzed here, the trajectories of these particles are circles of radius $R = \eta_0/2$, where η_0 is the wave amplitude. Rotation in a circle occurs at a velocity $v = R\omega$, where ω is the wave frequency. In the case of synchronism with the phase velocity v_{ph} of the wave, its resonant absorption takes place.

The torque M that should be applied to a sphere to set it in rotation in a viscous medium in a circle of radius $R \gg r$ is given by [6]

$$M = 8\pi\eta r^3\omega, \tag{4}$$

and the power spent for this is

$$P = M\omega. \tag{5}$$

This power can be equated to the expenditures of the kinetic energy of the sphere during the energy relaxation time τ_E,

$$\frac{mv^2}{2\tau_E} = \frac{mR^2\omega^2}{2\tau_E} = P. \tag{6}$$

From relations (4)–(6), we obtain

$$\tau_E = \frac{mR^2}{16\pi\eta r^3},$$

which leads to the resonance frequency for a “rotational resonance”

$$\omega_{0\mathrm{rot}} = \frac{1}{\tau_E} = \frac{16\pi\eta r^3 k^2}{m}, \tag{7}$$

where $k = \omega/v_{\mathrm{ph}}$ is the wave number.

The mass of the sphere is

$$m = \frac{4}{3}\pi r^3\rho_s,$$

where the density ρ_s of the sphere is equal to 12 times the value of the density ρ of the liquid since the critical

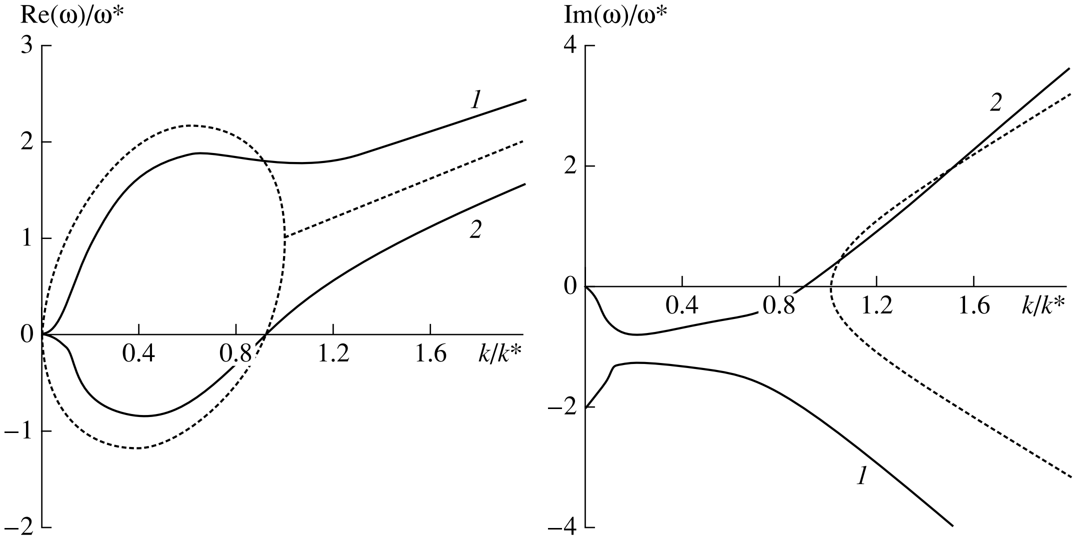

Fig. 2. Dispersion characteristics for waves with positive (*1*) and negative (*2*) energy in the collisional regime; $a = 0.1$, $\nu_{2r} = 0$, and $\tau_{2r} = 1.0$.

volume for which the gas becomes indistinguishable from the liquid is $V_c = 3b$ and the van der Waals constant b is equal to four time the volume of all molecules in the gas [7]. In this case, we have

$$\omega_{0\text{rot}} = \frac{\eta k_0}{\rho} = \nu_2 k_0^2, \qquad (8)$$

and in dimensionless variables,

$$\frac{\omega_{0\text{rot}}}{\omega^*} = \nu_{2r}\frac{1+a}{2}\left(\frac{k_0}{k_0^*}\right)^2. \qquad (9)$$

The second (collisional) resonance is shifted relative to the collision frequency $1/\tau_2$ due to the Doppler effect and is observed at a frequency

$$\omega_{0\text{col}} = \frac{1}{\tau_2} - Uk_0 \qquad (10)$$

or, in the dimensionless form,

$$\frac{\omega_{0\text{col}}}{\omega^*} = \frac{1+a}{2}\left(\frac{2a}{\tau_{2r}} - \frac{k_0}{k_0^*}\right). \qquad (11)$$

A distinguishing feature of the dispersion characteristics in the collisional regime is the attenuation of wave propagating along the drift flow in the long-wave limit ($k = 0$). This is due to the fact that the waves of this type “surge” towards the crystal lattice together with the flow and give away their total energy to the lattice at any frequency. At the resonance frequency, this attenuation is suppressed.

QUANTITATIVE RELATIONS AND CONCLUSIONS.

In the case represented in Fig. 1, rotational resonance occurs at $k_0/k_0^* = 0.3$, The value of the relative resonant frequency calculated by formula (9) is $\omega_{0\text{rot}}/\omega^* = 0.5$, This correlates well with the value obtained from the curve for $\mathrm{Re}\,\omega/\omega^*$.

Collisional resonance for the case represented in Fig. 2 occurs at $k_0/k_0^* = 0.15$. The expected relative resonant frequency calculated by formula (11) is $\omega_{0\text{col}}/\omega^* = 0.6$, which is also very close to the value obtained from the graph.

Thus, the hydrodynamic and electrohydrodynamic waves excited in two-layer dissipative systems due to shear instabilities experience resonant absorption of two types: at the rotational frequency of the particles of the medium and at the frequency of their collisions with the lattice.

REFERENCES

1. L. A. Ostrovskiĭ, S. A. Rybak, and L. Sh. Tsymring, Usp. Fiz. Nauk **150**, 417 (1986) [Sov. Phys. Usp. **29**, 1040 (1986)].
2. R. A. Brazhe and T. A. Novikova, Zh. Tekh. Fiz. **69** (8), 1 (1999) [Tech. Phys. **44**, 869 (1999)].
3. R. A. Brazhe, R. M. Meftakhutdinov, and T. A. Novikova, Izv. Vyssh. Uchebn. Zaved. Radiofiz. **42**, 1105 (1999).
4. E. M. Lifshitz and L. P. Pitaevskiĭ, *Physical Kinetics* (Nauka, Moscow, 1979; Pergamon, Oxford, 1981).
5. A. M. Anile, V. Romano, and G. Russo, Appl. Math., April (12), (1999).
6. I. Fabelinskiĭ, Usp. Fiz. Nauk **167**, 721 (1997) [Phys. Usp. **40**, 689 (1997)].
7. D. V. Sivukhin, *General Course of Physics* (Nauka, Moscow, 1975), Vol. 2 [in Russian].

Translated by N. Wadhwa

Technical Physics, Vol. 49, No. 8, 2004, pp. 1089–1092. Translated from Zhurnal Tekhnicheskoĭ Fiziki, Vol. 74, No. 8, 2004, pp. 133–135.
Original Russian Text Copyright © 2004 by Romashin, Sedov, Kasatkin, Kharlamov.

BRIEF COMMUNICATIONS

Self-Organization during Deposition of Semiconductor Films in the Atmosphere of Atomic Hydrogen

S. N. Romashin*, A. V. Sedov*, É. V. Kasatkin, and V. F. Kharlamov***
** Orel State Technical University, Orel, 302020 Russia*
e-mail: kharl@ostu.ru
*** Karpov Research Institute of Physical Chemistry, ul. Vorontsovo pole 10, Moscow, 103064 Russia*
e-mail: elchem@cc.nifhi.ac.ru

Received November 10, 2003

Abstract—A scanning tunneling microscope is used to establish that nanostructures with characteristic dimension 30–40 nm are contained in germanium films deposited on copper substrates in an atmosphere of atomic hydrogen. Local conductance, photoconductivity, and nonequilibrium chemiconduction of the films are studied. Etching of germanium and silicon films and also of fullerene soot by atomic hydrogen is observed. © *2004 MAIK “Nauka/Interperiodica”.*

In planning this research, we hypothesized that atoms bonded weakly to the surface would be driven off in the form of volatile hydrides in the course of deposition of carbon, germanium, or silicon atoms onto the substrate in an atmosphere of atomic hydrogen; this circumstance would set the stage for formation of stable carbon, germanium, or silicon nanoparticles or nanostructures that do not contain amorphous inclusions.

Undoped germanium or silicon crystals or graphite were milled; the powder was then put into a current-heated boat that was installed in a flow-through reactor through which an atomic–molecular hydrogen mixture ($P_{H_2} = 50$ Pa, $n_H = 10^{14}$ cm^{-3}) was pumped through continuously. The impurity content in hydrogen amounted to 5×10^{-3}%. Hydrogen atoms were obtained using a radio-frequency discharge in molecular hydrogen. The boat temperature was measured using a thermocouple and was equal to 800 K. A polished copper substrate, a glass substrate, and a sensor for the piezoresonance quartz balances with a sensitivity of 4.4×10^{-9} g were mounted near the boat. Two aluminum contacts spaced 5 mm apart were preliminarily deposited onto the glass substrate. Electrical conductance of the film during its deposition onto the glass substrate and the mass of deposited material were monitored in the course of experiments. All substrates were at a temperature of 295 K during deposition of the films. It is established that, under the same conditions, the rate of deposition of atoms onto the glass substrate and a silver strain gage decreases rapidly in the following sequence of sputtered targets: germanium, silicon, graphite.

The surface structure of germanium films that had various values of thickness and were deposited on copper substrates was studied using a scanning tunneling microscope (STM) in the mode I_0 = const (where I_0 is the specified and stabilized tunneling current); we performed the STM measurements in atmospheric air and used discrete measurement steps that ranged from 0.036 to 7 nm (over the scanned area with sizes from 5 nm to ~1 μm). We also studied electrical properties of the films. We found that the surface profile of the films replicated the surface profile of the copper substrate; in a number of sites where the germanium coating was not continuous, we observed properties that corresponded to those of the oxidized copper surface. If magnification was high, we observed almost smooth regions with the least pronounced nanoprofile. In Figs. 1 and 2, we show typical results for two samples with the smallest (sample 1) and largest (sample 2) thickness of germanium film.

The STM image of sample 1 (Fig. 1a) over the scanned area of 109.90×111.32 nm^2 has the largest height of 8.75 nm; a clearly pronounced nanoprofile is not observed (the average height difference is 1 nm). Nanodefects of the type of scratches can be recognized on the right-hand side of the STM image. Local measurements of the dependences of the tunneling current I_t on tunneling voltage U_t indicate multiple distortions in the curves $I_t(U_t)$; namely, electrical breakdown and temporary suppression of conduction are observed and are attributed to blocking properties of the surface copper oxide. This anomalous shape of the $I_t(U_t)$ curves is also observed for the reference copper sample; the appearance of this anomaly depends on the sweep swing of the tunneling voltage. The $I_t(U_t)$ curves have a normal shape in other (“not anomalous”) surface areas as can be seen from Fig. 1b, where the results of measuring the local current–voltage characteristics for a fragment of the above STM image obtained with the highest resolution are shown. The STM tip was moved over the sample along a line that contained 18 sites with

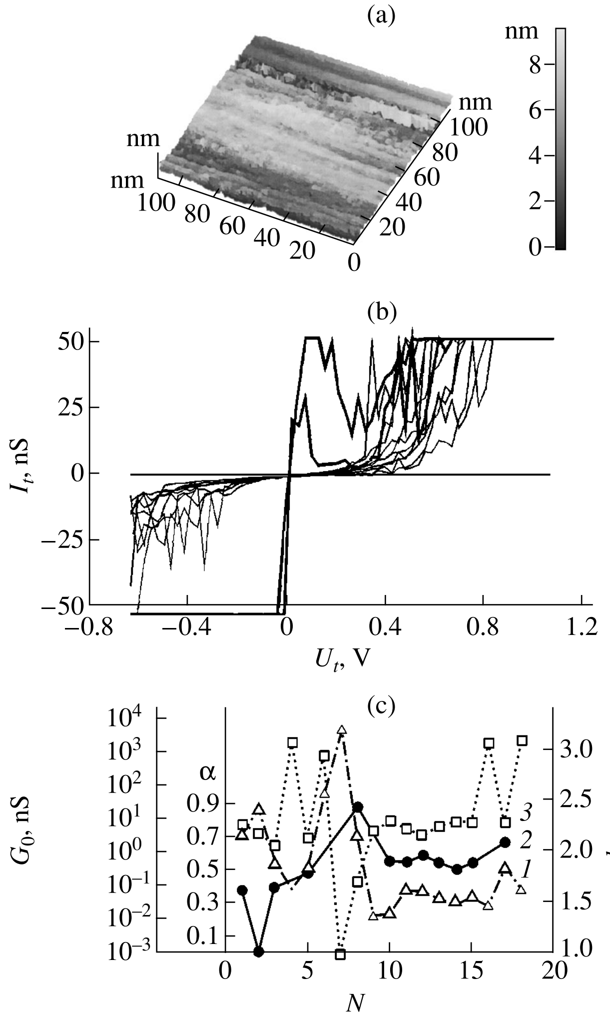

Fig. 1. The results of studying a germanium film that was deposited on the substrate in the atmosphere of atomic hydrogen and had the smallest thickness; the results were obtained using a scanning tunneling microscope.

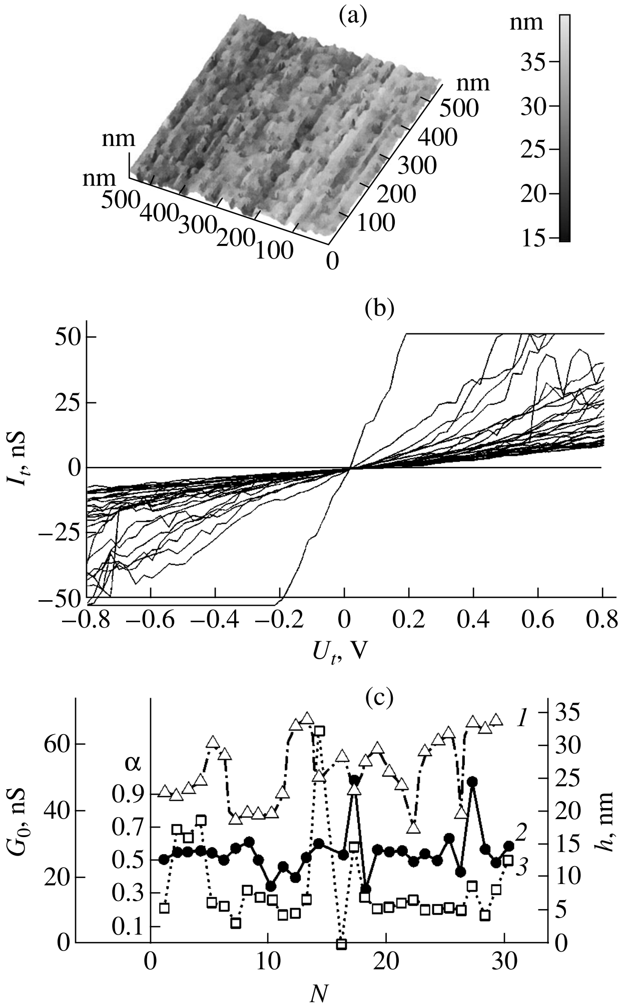

Fig. 2. The results of studying a germanium film that was deposited on the substrate in the atmosphere of atomic hydrogen and had the largest thickness.

a step of 0.0044 nm. Processing of the corresponding spectra made it possible to recognize that the local (unperturbed by electric field) tunneling conductance G_0 for four sites with anomalous conductance was as high as 1–3 μS, whereas this conductance was equal to 7.3 ± 1.6 nS for other sites. Taking into account that initial STM-supporting conductance was equal to G_1 = 8.42 nS, we find that the ratio G_0/G_1 is close to unity. In Fig. 1c, we show the values of G_0 and the *z* coordinates of corresponding points measured by STM. The total spread in the heights in this image did not exceed 3.5 nm. The coefficient α that accounts for an asymmetry in the electron transport through the tunneling gap was equal to 0.42 ± 0.03 for the experiment under consideration; this finding indicates that donor properties of the surface are enhanced owing apparently to a heavy doping of germanium with copper in the course of forming the coating.

The STM image of sample 2 a fragment of which is shown in Fig. 2a exhibits the largest height of 40 nm over an area of 552 × 550 nm^2; an irregular profile that corresponds to hills with a height of about 5 nm and an average diameter of 30–40 nm is observed. Local measurements of the tunneling current–voltage characteristics for this sample using a linear scanning with the points spaced by 5.817 nm indicate that the shape of the $I_t(U_t)$ curves is fairly regular; some of these curves (a quarter of the total number) exhibit a noticeably increased slope, which indicates that the tunneling conductance at the corresponding sites is increased. In contrast, the conductance at the site that neighbors the site with the highest conductance is almost unobserved (G_0 = 0.001 nS, points 15 and 16). Processing of these 31 spectra made it possible to find that the local tunneling conductance was G_0 = 12.605 ± 2.748 nS with the STM-supporting conductance G_1 = 8.42 nS (the same as in Fig. 1); i.e., the value of G_0 is larger than that for sample 1 by a factor of 1.5 (if the sites with anomalously high conductance are disregarded). In Fig. 2c, we show both the z coordinates of all relevant sites (curve *1*) and the values of G_0 (curve *3*); it can be seen which sites exhibit an increased local conductance. The total spread in the heights for this spectrum did not exceed 15 nm with the difference in heights in the STM image equal to that mentioned above. The average value of the coefficient α was equal to 0.530 ± 0.018 (curve *2*) for the experiment under consideration, which indicates that donor properties of the surface were enhanced (probably owing to a lowered concentration of free charges in Ge).

Thus, the results of measurements in the scanning tunneling microscope show that there are significant differences between the samples with different thickness of deposited germanium. These differences indicate that a nanostructure appears on the thicker film (sample 2) and that the copper substrate is completely isolated by this film; this behavior is not observed in the case of sample 1 with thinner germanium coating. The tunneling conductance and donor–acceptor properties of the surface depend on the germanium film thickness.

We studied the nonequilibrium electrical conductance observed in the deposited germanium films and caused by formation of electron–hole pairs as a result of interaction between atomic hydrogen and the film surface. Relatively slow variations in electrical conductance are observed after switching on and switching off of the source of H atoms. The nonequilibrium electrical conductance increases with increasing temperature that is varied by heating the reactor walls (Fig. 3). Similar data were obtained in the studies of the film photoconductivity. These results are indicative of the hopping mechanism of the film conductivity caused by tunneling of charge carriers between inhomogeneities in the film.

We also studied sputtering of the germanium and silicon films by atomic hydrogen. To this end, we used the piezoresonance quartz balances to monitor the mass of the film that was deposited preliminarily onto one or both surfaces of the strain gage. We observed etching of the germanium and silicon films by hydrogen atoms; the etching rate increased with increasing temperature (Fig. 4).

We observed an intense etching of fullerene soot by atomic hydrogen; this soot is a product of condensation of graphite vapors and represents an amorphous residue that does not contain fullerenes. In Fig. 5, we show the kinetic curve for a decrease in the mass of fullerene soot placed in the atmosphere of atomic hydrogen and also the simultaneously measured temperature dependence of the dynamic effect of the reaction $H + H \longrightarrow H_2$; this reaction proceeds at the surface of fullerene soot $F(t) = GJ(t)$, where J is the rate of this reaction and G is a coef-

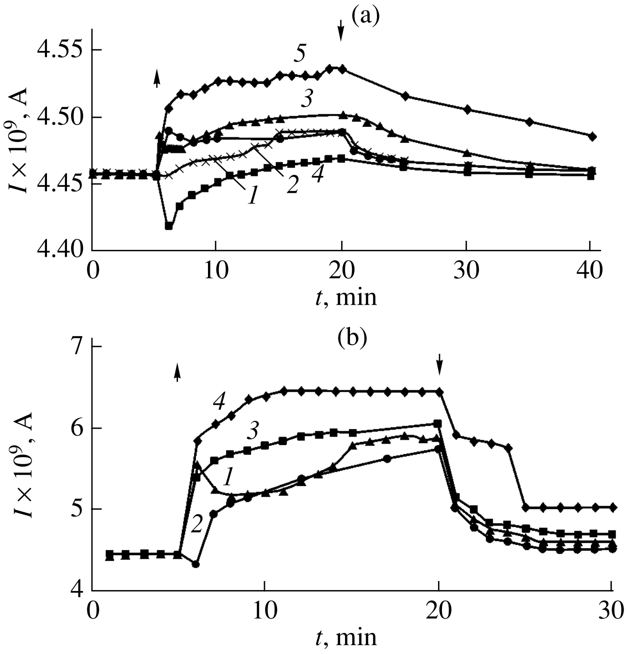

Fig. 3. The time dependences of the current flowing through the germanium film after switching on (↑) and switching off (↓) of the hydrogen atom source. T = (a) 295 and (b) 315 K. The numbers at the curves correspond to the numbers of measurements of experimental curves.

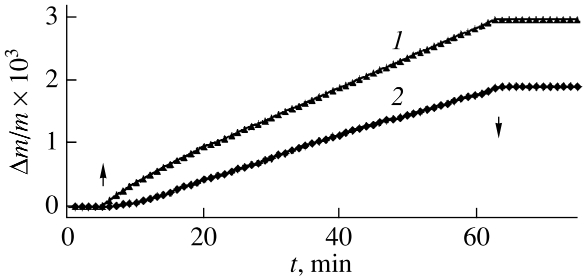

Fig. 4. The time dependnences of a decrease in the mass of a germanium film as a result of etching of this film by atomic hydrogen (↑) after switching on and (↓) switching off of the source of hydrogen atoms at the temperatures T = (*1*) 315 and (*2*) 295 K. $\Delta m = m_0 - m$, where m_0 is the initial mass of the film and m is the film mass at the instant t.

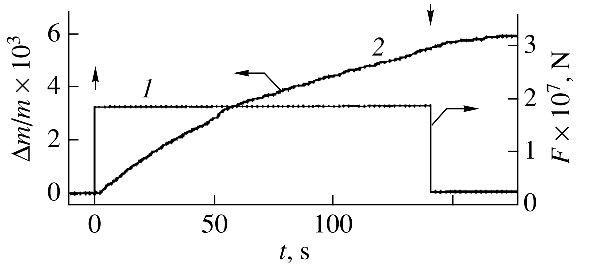

Fig. 5. Time dependences of (*1*) the dynamic effect of recombination reaction for hydrogen atoms at the surface of fullerene soot and (*2*) a decrease in the mass of fullerene soot as a result of etching by atomic hydrogen after (↑) switching on and (↓) switching off of the source of atomic hydrogen. T = 295 K.

ficient that depends on the momentum distribution of the gas particles in the surface plane.

Thus, we established that germanium films deposited on the substrate in the atmosphere of atomic hydrogen are inhomogeneous and contain nanostructures with a characteristic dimension of 30–40 nm. We found that the films of germanium, silicon, and fullerene soot are sputtered by the flux of atomic hydrogen. Apparently, by choosing the appropriate technological parameters, one can enhance the self-organization processes in the germanium, silicon, or graphite layers deposited in the atmosphere of atomic hydrogen.

We thank A.V. Kulikov (Institute of Problems of Chemical Physics, Russian Academy of Sciences) for his kindly providing us with fullerene soot for our studies.

Translated by A. Spitsyn

Technical Physics, Vol. 49, No. 8, 2004, pp. 1093–1097. Translated from Zhurnal Tekhnicheskoĭ Fiziki, Vol. 74, No. 8, 2004, pp. 136–139.
Original Russian Text Copyright © 2004 by Naydenov.

BRIEF COMMUNICATIONS

The Effect of Determined Chaos on Light Collection in Optical Systems

S. V. Naydenov
Institute of Single Crystals, National Academy of Sciences of Ukraine, Kharkov, 61001 Ukraine
e-mail: naydenov@isc.kharkov.com

Received January 13, 2004

Abstract—In terms of the dynamic approach, the collection of light in optical systems and the influence of determined chaos on the photometry and fluctuations of regular and chaotic collection are considered. The photometric relationships generalizing the formula of the integrating sphere as applied to chaotic collection are obtained. A universal law for noise in the regular light collection is predicted and found to be in good agreement with the available experimental data. The relationships studied can find use in the elaboration of a new-design detectors, light guides, light-emitting diodes, etc., for the enhancement of their efficiency and the reduction of noise. *© 2004 MAIK “Nauka/Interperiodica”.*

The physical phenomenon of light collection plays an important role for many optical systems [1–4]. The elimination of light trapping (which stems, for example, from total internal reflection) and the related increase in light output allows one to enhance significantly the efficiency of light-emitting diodes and laser resonators, to enlarge the light guide apertures, and to increase the efficiency of scintillation detectors. The suppression of collection fluctuations (noise) enhances the intrinsic energy resolution of detectors, increases the threshold sensitivity of photoelectron multipliers, improves the contrast–frequency characteristic of the fiber-optic elements, etc.

Optimization of light collection implies the establishment of the general laws of this process. This will make the choice of the required design of optical systems more expedient. In our opinion, the key role here is played by the prevalence of either chaotic or regular dynamics of light beams. For this purpose, it is convenient to use the dynamic approach. However, the propagation of light beams should be considered not in the common (configuration) space but in the phase space of one-valued states of the corresponding dynamic system, which is described by billiards [5–7]. As the phase coordinates of beams, it is possible to take, for example, the canonically conjugate variables, i.e., the spatial coordinate and the momentum (direction) of the beam. Then, the characteristics of collection are determined by the summation of light fluxes in the phase space. Note that this approach provides the most complete spatial–angular description of the light field in an optical system.

Let us derive the general expression for the coefficient of light collection τ (the ratio of the output light flux to the initial one). In contrast to the techniques developed previously for numerical simulations, computer codes, etc. (see, e. g., [8–12]), our method is based on the calculations in the phase space rather than in the configuration space. Each particular beam is represented as a point in the phase space Φ. It is essential to note that not every beam emerges from the system. Therefore, one can separate from the entire space Φ a set Φ_L of initial beams that ever reach the output window. The “light collection” Φ_L depends on the “input” Φ_{in} and the “output” Φ_{out}, where Φ_{in} corresponds to scintillations (detector, optical cavity, light emitting diode) or input light (optical fiber) and Φ_{out} accounts for the beams incident on the output window. The beams are absorbed as they propagate through the system. The intensity loss depends exponentially on the (discrete) number of the reflection events. For this reason, it is convenient to turn to discrete summation of light fluxes (thus, ensuring a rapid convergence of the appearing analytical expansions). To do this, one should separate from Φ_{in} the beams that reach the output window immediately after one, two, or more reflections, i.e., to divide the total flux into the fluxes corresponding to multiple reflections. As a result, we have

$$\tau = \tau_0 + (1-q_0)T_0\sum_{m=1}^{+\infty} T^n S_n; \quad S_n = q_n\prod_{m=1}^{n-1}(1-q_m), \quad (1)$$

where $\tau_0 = q_0 T_0$ defines direct light and T_0 and T are the respective mean losses for direct and multiply reflected light (between two successive reflections) under the assumption of insignificant loss, $1 - T \ll 1$.

The amplitude of multiple scattering $S = S[q] = \sum_n S_n$ depends on the sequence $\{q_m\}$ of the partial output apertures in the phase space. Each value q_m represents the fraction of light (in the phase space) that outcomes at the mth step of multiple reflections with respect to that at the previous step. In other words, q_m defines the rate of the light outcome, with m playing the part of discrete time. The straight-propagating light permits an independent control: for example, it can be completely eliminated, as in the case of the Ulbricht sphere. This is the distinction of factor q_0 from the others. Replacing the summation of fluxes by their multiplication and regrouping the terms of the series leads one to the expression

$$S = 1 - \Pi, \quad \Pi = \prod_{m=1}^{+\infty}(1 - q_m). \qquad (2)$$

In the absence of absorption ($T \equiv 1$), the collection of light depends only on S, $\tau = S + \tau_0(1 - S)$.

In the general case, the phase space of billiards contains a regular (single or several) and a chaotic component [5–7]. Accordingly, one can distinguish the regular, chaotic, and the mixed types of the light collection. By controlling the chaos, it is also possible to control the light collection. Its dynamic characteristics are best pronounced in the absence of loss. Using representation (2), one can easily decide which distribution of fluxes yields the maximal collection. The ultimate $\tau_{\max} = 1$ corresponds to $\Pi = 0$. An infinitely large product Π is zero when the series $\sum_m q_m = \infty$ diverges. In the opposite case, it its multipliable. Product $\Pi \neq 0$ if this series converges and its common term tends to zero, $q_m \longrightarrow 0$ at $m \longrightarrow \infty$. The latter condition can be satisfied only at a sufficiently rapid decrease in the partial contributions of the multiply reflected fluxes. Then, $\tau < 1$ (the contribution of direct light, $\tau_0 < 1$, is always incomplete unless the entire surface is radiating). The first case takes place for a chaotic collection. The second is typical of a collection in the presence of the regular component of light beams. The related examples indicate that, here, the rate of the light outcome usually decreases as a power function, $q_m \propto m^{-\gamma}$ ($\gamma > 1$).

Chaotic dynamics involves the mixing of phase trajectories [5, 6]. A chaotic collection takes place in mirror-reflecting systems with the geometry of chaotic billiards: "stadium," "dumb-bell," "star," etc. The chaotic billiards also describe the collection in diffuse systems with the scattering indicatrix close to the cosine. From outside, such diffusivity can be provided by the production of a special dull finishing, grooving, or painting of the reflecting surface. From inside, such scattering results from the presence of inhomogeneities, impurities, and structural defects or can be attained by the deliberate introduction of light-scattering centers in the initial optical material. Mixing is related to the following property:

$$q_1 \approx q_2 \approx \ldots \approx q_\infty = q;$$
$$q = \lim_{N \to \infty}\left[(1/N)\sum_{m=1}^{N} q_m\right]. \qquad (3)$$

This means that the multiply reflected fluxes are almost uniformly distributed (mixed) in the phase space and the correlation (difference between q_m) is retained only for a number of first orders. It follows from condition (3) that $\sum_m q_m = \infty$; i. e., the chaotic collection is complete, $\tau_{\max} = 1$. Taking into account absorption, the summation of the geometrical progression in formula (1) yields a collection in the form

$$\tau = q_0 T_0 + (1 - q_0)[1 + (1 - T)/qT]^{-1}. \qquad (4)$$

This is a generalization of the well-known formula of an Ulbricht sphere (FUS) [1]. It is of principal importance that the mean aperture q (probability of outcome after one reflection) is defined here in the phase space rather than in the configuration space. This improves the accuracy of the formula and extends the range of its applicability. Aperture q can be determined either numerically or analytically from a given scattering indicatrix of the reflecting surface. Thus, for the azimuth-symmetrical indicatrix

$$f(\theta) = (2\pi)^{-1}\sum_{k=0}^{+\infty}(k+1) f_k \cos^k\theta$$

(f_k are the amplitudes normalized so that $\sum_k f_k = 1$ and θ is the polar angle), the calculation yields

$$q = fg, \quad f = \sum_{k=0}^{+\infty} f_k\{1 - [1 - n^{-2}]^{(k+1)/2}\},$$
$$g = S_{\text{out}}/S, \qquad (5)$$

where n is the relative refractive index and S_{out} and S are the areas of the output window and the entire surface, respectively.

The product of the angular f and the geometrical g apertures defines the total output aperture q. In the absence of total internal reflection, when $n = 1$, the aperture becomes purely geometrical, $f = 1$ and $q = g$. Note that in the previous applications of FUS, either solely f (the mean spatial angle, at which the output window is seen from an arbitrary point inside the optical system) or solely g was considered as the aperture, but not their total product.

For systems with comparable sizes, $q_0 \approx q$ and $T_0 \approx T$ and formula (4) is reduced to

$$\tau = \tau_{\text{chaos}} = qT/[1 - (1 - q)T]. \qquad (6)$$

This is a universal dependence, since the light outcome is defined by one and the same expression for systems with different geometry, but only under the condition of their highly chaotic character; i.e., the chaotic collection features photometrical generality. The "transparency" $T = \exp(-l_{BIL}/l_{BAL})$ depends on the mean length l_{BIL} of the beam path between two reflections (in the billiards theory, $l_{BIL} = 4V/S$, where V is the volume of system) and the length of the bulk absorption of photon, l_{BAL}. In the first order of the expansion in terms of $l_{BIL}/l_{BAL} \ll 1$, formulas (5) and (6) lead to the light outcome for the cosine indicatrix $f(\theta) = \pi^{-1}\cos\theta$

$$\tau = [1 + n^2(l_{\mathrm{eff}}/l_{BAL})]^{-1}, \quad (7)$$

where $l_{\mathrm{eff}} = l_{BIL}/g$ is the effective length of the path.

The formula obtained can be used, for example, to estimate the efficiency of light emitting devices depending on light collection. In these devices, the radiation brightness is almost uniform over the layer surrounding the semiconductor element ($g = 1$). As the refractive index n grows, the light outcome abruptly drops. To compensate for this loss, one should either increase the transparency of the system or decrease its size. Both ways lead to an increase in ratio l_{BAL}/l_{BIL}. As a result, a sort of a highly rarified “gas of light beams” is formed. The outcome of radiation from such a gas is maximal. For example, at $n \simeq 2$ and $l_{BAL}/l_{BIL} \simeq 16$, the light outcome attains 80%.

The presence of beam chaos in a system is a necessary condition for the FUS to be applicable. Any loss of stochastic character, for example, deterioration of the diffusivity of the scattering surface of the Ulbricht sphere, considerably lowers the accuracy of the FUS-based measurements. In approximation (3), this accuracy is defined by the dispersion

$$Dq = \lim_{N \to \infty}\left[(1/N)\sum_{m=1}^{N}(q_m - q)^2\right].$$

The closer the mean aperture to zero, $q \ll 1$ (the output window is small as compared to the size of the system or the total internal absorption is pronounced), or to unity, $1 - q \ll 1$ (in the optical contact, the entire surface of the system is emitting), the better the accuracy, $Dq \ll 1$. Using formulas (1) and (6), one can readily estimate the relative (root-mean-square) fluctuations of the chaotic collection,

$$\delta\tau = T\delta q, \quad \delta\tau = (D\tau)^{1/2}/\tau, \quad \delta q = (Dq)^{1/2}/q, \quad (8)$$

where $D\tau$ is the dispersion of the light collection coefficient.

These fluctuations (noise) of light collection are caused by the dependence of the collection coefficient on the position of the initial light sources (scintillations). At the same time, the chaotic trajectories appear indistinguishable only within one and the same system whereas the trajectories of different systems have a number of essentially different characteristics (for example, the Lyapunov index). This is due to the exponential sensitivity of chaotic systems to a change in the initial or external conditions. As a result of variations (inhomogeneity) of the output apertures, the values of δq are substantially dependent on the type and geometry of a system, as well as on the reflection character. Therefore, no universal relation (similar to that existing for, say, the statistical Poisson noise) between fluctuations and the light outcome can exist in this case.

Regular light collection is possible only in systems with mirror light fluxes. As a rule, these are systems of regular geometry: rectangular, cylindrical, spherical, or polyhedral (polyhedrons with rationally commensurable angles). Mixed collection occurs in the systems characterized by billiard geometry with mixed dynamics (both the chaotic and the regular components are present) or in diffusive systems with an appreciable contribution of the regular component of mirror-reflected light (for example, in a colored cylindrical fiber). For the regular or mixed collection, the terms q_m decrease fairly fast. For example, in a long cylinder with an axis-positioned light source, the output window at its end, and mirror reflection from its boundaries, $q_m \propto m^{-2}$. The convergence of the sum $\sum_m q_m < \infty$ leads to $\tau_{\max} < 1$. From the physical point of view, this occurs because of the partial “light trapping” of beams that belong to the regular component of the motion. For the chaotic component, such trapping is absent since it is hindered by the mixing of beams. Due to the mixing, any “unfavorable” beam sooner or later gets into the region of the light outcome Φ_{out}, whereas a large number of regular beams can always remain beyond this region.

When light is trapped, the mean aperture is necessarily zero:

$$q_{\mathrm{reg}} = \lim_{N \to \infty}\left[(1/N)\sum_{m=1}^{N} q_m\right] = 0.$$

The light output is sensitive to the distribution of multiply reflected fluxes. Therefore, in this case there is no universal dependence similar to that described by formula (4). For comparison, Fig. 1 shows the plots for the chaotic and the regular light outcomes. The regular collection is considered only for systems of regular geometry, in optical contact with the receiver. As the aperture, we take the geometrical aperture; i.e., $q = g = S_{\mathrm{out}}/S$. Let us omit here the calculations for q_m. Figure 1 indicates not only the qualitative but also the quantitative difference between the regular and the chaotic collections. It is seen that, at high transparency, the chaotic collection dominates over the regular one. As the absorption grows, they exchange their parts (the chaotic collection becomes lower than the regular one). This behavior can be attributed to the diffusive slowing-down of the chaotic beam (note for comparison that, in the case of a Brownian particle, only the squared displacement of the particle is proportional to the time of its motion). As a result, the chaotic beam appreciably attenuates before the moment when it is expected to leave the system.

Concerning the fluctuations of the regular collection, in contrast to those of the chaotic collection, they do obey the general law. This fact reflects the similarity

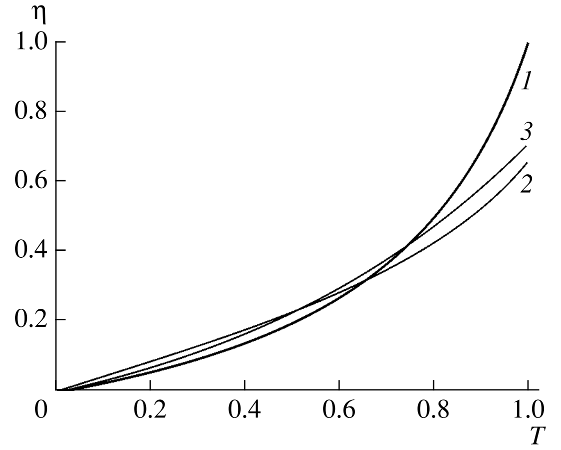

Fig. 1. Theoretical light outcome coefficient η in an optical system with (*1*) chaotic and (*2*) regular collection ((*2*) cylinder and (*3*) hemisphere) vs. optical transparency *T*. The cylinder base or the diameter section of the sphere serves as the output window. In all cases, the output aperture is the same; $q = 1/4$ (the diameter of the output window is equal to the cylinder height and is smaller than the hemisphere diameter by a factor of $\sqrt{1.5} \approx 1.2$).

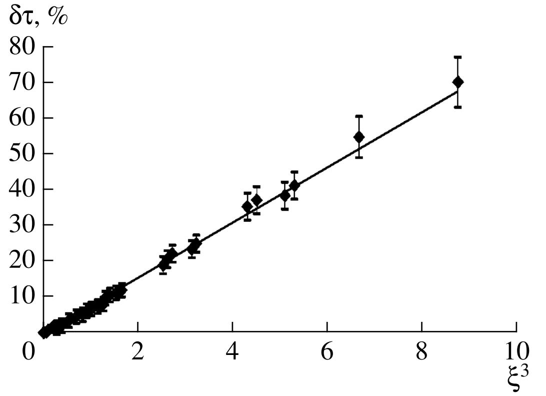

Fig. 2. Universal dependence of the relative fluctuations of the light outcome (δτ) on the dissipative factor (ξ) for various detectors with regular collection. The solid line is the theory and the symbols represent the data of real and numerical experiments. Possible spread of values within 10% is also shown.

of the phase portraits of the regular collection in systems with different geometry. It is known that regular trajectories are characterized by zero Lyapunov indices. In appropriate coordinates, the phase portrait of the regular collection appears as a set of parallel hypersurfaces. Analytically, using the expansion in terms of a small parameter $\alpha \ll 1$ in the phase space, where $T = \exp(-\alpha)$, one can deduce the fluctuations of the regular collection in the form

$$\delta\tau = \alpha[\delta N + \ldots], \tag{9}$$

where the dots denote the higher corrections and δN is the relative (root-mean-square) variance of the number of reflections before the beam emerges from the system.

Changing the variables yields

$$\delta\tau_{\text{reg}} \propto \xi^3; \quad \xi = (1 - \tau/\tau_{\max})^{1/2}, \tag{10}$$

where parameter ξ is the dissipative factor indicating the extent to which the light loss reduces the collection coefficient relative its peak value $\tau_{\max} = \tau\ (\alpha = 0)$.

The latter relation has a regular character. To confirm this, we compared this dependence to the experimental and analytical data for fluctuations of light collection in scintillation detectors [4]. We considered various scintillators (NaI(Tl), CsI(Tl), BWO, and CWO), different geometries (a cylinder and a right prism), a wide range of volumes (from 1 to 1000 cm^3) and size ratios, as well as the presence or absence of optical contact. A total of 200 points were involved in the calculation, the results of which are presented in Fig. 2. With an accuracy of no worse than 10% (which is typical of such a type of measurements), all of them fall on a theoretical straight line. The constant in the dependence $\delta\tau = C_{\text{reg}}\xi^3$ appears to be ≈ 7.77.

Thus, using the dynamical approach, we have elaborated a unified description of light collection in optical systems. Special features of the collection are closely related to the type (regular or chaotic) of the dynamics inherent to the corresponding billiard. The chaotic collection obeys a universal photometrical law described by formulas (4), (5) or (6), (7). This universal character can be of use, for example, for designing the white light emitting diodes, since it ensures independent control over the proportion in which the colors from various light sources should be mixed. The light outcome of the regular collection (with the characteristic light localization) strongly depends on the system geometry and does not feature the universal character. A rapid decrease in its partial output apertures q_m with increasing multipolarity m signifies that the main fraction of the light energy is carried here by beams that experience only a few reflections before the outcome from the system. Therefore, the regular light collection is useful for systems where a high-speed transmittance of optical signals is required. The universal law (10) has been established for the fluctuations (noise) of the regular collection. In contrast, the chaotic collection is devoid of such generality. The photometric and fluctuation behavior of the regular and chaotic collections can be considered as counterparts in some sense. The noise universality of the regular collection is important for applications. For example, it allows one to predict the detector noise (energy resolution) from the measurements of the light outcome alone. Further advances in this approach imply deeper analysis of the results obtained, as well as the study of other special features related to the dynamics of light beams. This way is likely promising for the elaboration of new highly efficient detectors, optical fibers, light emitting diodes, laser cavities, etc.

REFERENCES

1. Yu. A. Tsirlin, *Light Collection in Scintillation Counters* (Atomizdat, Moscow, 1975) [in Russian].
2. V. B. Veĭnberg and D. K. Sattarov, *Optics of Light Waveguides* (Mashinostroenie, Leningrad, 1977) [in Russian].
3. J. U. Nocel and A. D. Stone, Nature **385**, 45 (1997).
4. M. E. Globus and B. V. Grinev, *Inorganic Scintillators* (Akta, Kharkov, 2000) [in Russian].
5. I. Cornfeld, S. Fomin, and Ya. G. Sinai, *Ergodic Theory* (Nauka, Moscow, 1980; Springer-Verlag, New York, 1982) [in Russian].
6. G. M. Zaslavskiĭ and R. Z. Sagdeev, *Introduction to Nonlinear Physics* (Nauka, Moscow, 1988); R. Z. Sagdeev, D. A. Usikov, and G. M. Zaslavsky, *Nonlinear Physics: From the Pendulum to Turbulence and Chaos* (Harwood Academic, New York, 1988).
7. S. V. Naydenov, V. V. Yanovsky, and A. V. Tur, Pis'ma Zh. Éksp. Teor. Fiz. **75**, 499 (2002) [JETP Lett. **75**, 426 (2002)].
8. L. S. Kukushkin and A. M. Ratner, Zh. Tekh. Fiz. **28**, 345 (1958) [Sov. Phys. Tech. Phys. **3**, 318 (1958)].
9. S. E. Derenzo and J. K. Rilers, IEEE Trans. Nucl. Sci. **29**, 191 (1982).
10. C. Carrier and R. Lecomte, Nucl. Instrum. Methods Phys. Res. A **294**, 355 (1990).
11. Ya. A. Berdnikov, V. V. Grebenshchikov, V. F. Kosmach, *et al.*, Prib. Tekh. Éksp., No. 4, 49 (2002).
12. F.-X. Gentit, Nucl. Instrum. Methods Phys. Res. A **486**, 35 (2002).

Translated by A. Sidorova

Technical Physics, Vol. 49, No. 8, 2004, pp. 1098–1100. Translated from Zhurnal Tekhnicheskoĭ Fiziki, Vol. 74, No. 8, 2004, pp. 140–142.
Original Russian Text Copyright © 2004 by Belomestnykh, Tesleva.

BRIEF COMMUNICATIONS

Interrelation between Anharmonicity and Lateral Strain in Quasi-Isotropic Polycrystalline Solids

V. N. Belomestnykh and E. P. Tesleva
Yurga Technological Institute (Branch of the Tomsk Polytechnical University),
Yurga, Kemerovo oblast, 652050 Russia
e-mail: adm@ud.tpu.edu.ru; belka150@yandex.ru

Received January 13, 2004

Abstract—A new formula that relates the acoustic Grüneisen parameter to the Poisson ratio is suggested on the basis of the previously derived expression for this parameter. *© 2004 MAIK "Nauka/Interperiodica".*

Belomestnykh [1] suggested a relation between the average value of the Grüneisen parameter γ that characterizes the degree of anharmonicity of interatomic forces and the velocities of sound (longitudinal v_L and transverse v_t) in an isotropic, spatially unbounded elastic medium; i.e.,

$$\gamma_1 = \frac{9}{2}\left(\frac{v_L^2 - 4v_t^2/3}{v_L^2 + 2v_t^2}\right). \quad (1)$$

The Grüneisen parameter γ_1 defined by (1) was referred to as the corresponding acoustic parameter. In this study, the above approach was developed and led to a new and very important relation between the Grüneisen parameter and the Poisson ratio σ (the lateral strain coefficient) that characterizes the tendency of material towards retaining its initial volume in the course of elastic deformation and is defined as

$$\sigma = -\frac{\varepsilon'}{\varepsilon} = -\frac{(\Delta d/d)}{(\Delta l/l)}, \quad (2)$$

where $\varepsilon' = (\Delta d/d)$ is the lateral contraction ratio of the sample with transverse size d and $\varepsilon = (\Delta l/l)$ is the relative longitudinal extension of the sample that has length l and is subjected to loading.

We use the well-known formulas that relate the quantities v_L and v_t to Young's modulus E, the density of the material ρ, and the Poisson ratio σ [2]; i.e.,

$$v_\mathrm{L} = \sqrt{\frac{E(1-\sigma)}{\rho(1+\sigma)(1-2\sigma)}}, \quad v_\mathrm{t} = \sqrt{\frac{E}{2\rho(1+\sigma)}}. \quad (3)$$

We now modify formulas (1) and (3) and express γ and σ in terms of the quantity $x^2 (x = v_\mathrm{L}/v_\mathrm{t})$; as a result, we obtain

$$\gamma = \frac{9x^2 - 12}{2x^2 + 4}, \quad \sigma = \frac{x^2 - 2}{2x^2 - 2}. \quad (4)$$

We then derive a simple expression that relates the Grüneisen parameter γ to the Poisson ratio (in this case, we refer to the Grüneisen parameter as the corresponding elastic parameter and denote it by γ_2); i.e.,

$$\gamma_2 = \frac{3}{2}\left(\frac{1+\sigma}{2-3\sigma}\right). \quad (5)$$

A formal analysis of expression (5) shows that (i) at values of the Poisson ratio of $\sigma = 0.05$–0.46 for actual polycrystalline materials [3], the Grüneisen parameter γ_2 is in the range from 0.85 to 3.53, which is consistent with experimental data (see table); (ii) if the Cauchy relation is valid (central forces act between homogeneously deformed regions of a cubic lattice), i.e., if $c_{12} = c_{44}$ and $\sigma = 0.25$, we have $\gamma_2 = 1.5$; (iii) the lower limit of the values of the Poisson ratio ($\sigma = -1$) corresponds to a "harmonic" solid ($\gamma_2 = 0$); (iv) the largest possible positive value of the Poisson ratio σ tends to 0.67, so that the anharmonicity would be infinitely large in a material with this σ; (v) the case of interest $\sigma = 0$ (a change in the transverse size of the sample is not accompanied with lateral deformation) corresponds to $\gamma_2 = 0.75$; and (vi) in the case of $\sigma = 0.5$ (the volume of the solid remains unchanged in the course of elastic deformation), we have $\gamma_2 = 4.5$, and this value can be treated as the actual limiting value of the Grüneisen parameter.

We test the practical validity of formula (5) by comparing γ_2 with thermodynamic (Debye) value γ_D of the Grüneisen parameter considered as experimental [4] (this comparison was also performed previously [1]); we have

$$\gamma_\mathrm{D} = \frac{\beta B^s \mu}{C_p \rho}, \quad (6)$$

where β is the temperature coefficient of the volume expansion, B^S is the adiabatic modulus of uniform compression (of volume elasticity), μ is the molar mass, and C_p is the molar heat capacity at constant pressure.

The results of this comparison for metals and for binary, ternary, and quaternary compounds are listed in the table. The values of the Poisson ratio are taken from available publications (books and original reports) [4–11]; in some cases, we used the limiting values of σ according to different publications. The values of the thermodynamic parameter γ_D (except for those with an asterisk) can be found in numerous publications [12–18].

For the majority of materials listed in the table, there is good agreement between γ_2 and γ_D, which indicates that the formula (5) is valid in practice. Since the Poisson ratio can be determined both directly from measurements of the longitudinal and lateral strains and indirectly [not using formula (3)] from elastic moduli (for example, in terms of the Young and shear moduli [2]), the range of applicability of new expression (5) can be much wider than that of previous formula (1). Evidently, if formula (5) is valid, the Poisson ratio σ can be determined in terms of the presumably known Grüneisen parameter of the material as

$$\sigma = \frac{4/3\gamma - 1}{2\gamma + 1}. \tag{7}$$

The domain of applicability of formula (5) requires additional investigation. Still, we may already state that a calculation using formula (5) (for example, for lanthanides, or rare-earth metals) without corrections yields values of γ_2 that differ considerably from those of the thermodynamic Grüneisen parameters γ_D. It is conceivable that the causes of this discrepancy are related to a mismatch between the true values of the Poisson ratio and the values obtained from indirect measurements (according to Ivanov and Lebedev [19], the discrepancies can amount to as large as one hundred percent). It is also not inconceivable that the determining role in this discrepancy can be played by the extent to which the relation between the Poisson ratio and the exponents m and n is clarified; these exponents specify the attraction and repulsion potentials for atoms in the Mie equation for the dependence of the potential energy U of particles in a solid on the distance r; i.e.,

$$U = -Ar^{-m} + Br^{-n}.$$

Since original Grüneisen's studies (1910s), the relation between the bulk modulus (compressibility), atomic volume, and the energy U expressed using the exponents m and n has been analyzed repeatedly [5, 13, 20]; a relation between the shear modulus and the Poisson ratio was analyzed by Nemilov [21]. As a result of this analysis, it was suggested that the Mie equation is invalid for materials with an anomalously large ratio of lattice constants c/a. However, Oshcherin [22] used the kinetic theory to account for the multiplicity of empirically determined coefficients in the above relations for crystals with different structures.

Comparison of the elastic and thermodynamic Grüneisen parameters (standard conditions: $T = 298.15$ K and $p = 1.013 \times 10^5$ Pa)

Elements and compounds	Poisson ratio	Grüneisen parameters		γ_2/γ_D
		γ_2	γ_D	
Ag	0.379	2.40	2.4	1.00
Al	0.340	2.01	2.11	0.95
Au	0.420	2.88	2.8	1.03
Cu	0.350	2.13	2.06	1.03
Ni	0.277	1.64	1.73	0.95
	0.33	1.98	2.2	0.90
Pd	0.374	2.35	2.4	0.98
Pb	0.405	2.68	2.92	0.92
W	0.283	1.67	1.7	0.98
Be	0.034	0.82	0.83	0.99
Co	0.357	2.16	2.1	1.03
Mg	0.270	1.60	1.41	1.13
Fe	0.292	1.72	1.68	1.02
Pt	0.390	2.51	2.54	0.99
Ta	0.337	2.03	1.73*	1.17
Th	0.254	1.52	1.40*	1.09
Y	0.245	1.48	1.25*	1.18
U	0.230	1.41	1.62*	0.87
LiF	0.214	1.35	1.34	1.01
LiCl	0.245	1.48	1.52	0.97
LiBr	0.256	1.53	1.70	0.90
LiI	0.265	1.81	2.22	0.82
NaF	0.240	1.45	1.72	0.84
	0.234	1.43	1.57	0.91
NaCl	0.243	1.47	1.46	1.01
NaBr	0.270	1.60	1.56	1.03
NaI	0.274	1.62	1.90	0.85
	0.250	1.50	1.59	0.94
KF	0.274	1.62	1.73	0.94
KCl	0.259	1.54	1.60	0.96
KBr	0.283	1.67	1.68	0.99
KI	0.265	1.57	1.63	0.96
RbF	0.276	1.63	1.41	1.16
RbCl	0.268	1.59	1.53	1.04
RbBr	0.267	1.59	1.50	1.06
RbI	0.309	1.83	1.73	1.06
CsF	0.318**	1.89	1.49	1.27
CsCl	0.264	1.57	1.98	0.80
CsBr	0.270	1.60	1.93	0.83
CsI	0.265	1.57	2.00	0.79
AgCl	0.409	2.73	2.02*	1.35
AgBr	0.396	2.56	2.33*	1.10
NH_4ClO_4	0.271	1.54	1.81*	0.85
$NaClO_3$	0.270	1.60	1.37*	1.17
$NaClO_4$	0.278	1.64	1.56*	1.05
$KClO_4$	0.296	1.75	1.64*	1.07
$NaNO_3$	0.257	1.53	1.31*	1.17
KNO_3	0.331	1.98	1.95*	1.02
CaF_2	0.224	1.38	1.55*	0.89
	0.301	1.78	1.63*	1.09
Al_2O_3	0.223	1.38	1.34*	1.03

Note: We calculated the Grüneisen parameters with an asterisk γ_D^* using formula (6). We determined the Poisson ratio for CsF (σ**) from the elastic constants of a CsF single-crystal (measured by Haussühl [18]) using the Voigt–Reuss–Hill method [5].

We now summarize the results. The simple formula that unambiguously relates two important characteristics of solids was derived. Good agreement between elastic (according to our terminology) and thermodynamic Grüneisen parameters is generally observed. Formula (5) yields realistic limiting values of γ and σ. Additional studies of the domain of applicability of formula (5) are needed.

REFERENCES

1. V. N. Belomestnykh, Pis'ma Zh. Tekh. Fiz. **30** (3), 14 (2004) [Tech. Phys. Lett. **30**, 91 (2004)].
2. L. D. Landau and E. M. Lifshitz, *Course of Theoretical Physics*, Vol. 7: *Theory of Elasticity* (Pergamon, New York, 1986; Nauka, Moscow, 1987).
3. S. Ya. Mikitishin, Fiz.-Khim. Mekh. Mater. **18** (3), 84 (1982).
4. I. N. Frantsevich, F. F. Voronov, and S. A. Bakuta, *A Handbook of the Elastic Constants and Elastic Modulus of Metals and Nonmetals* (Naukova Dumka, Kiev, 1982) [in Russian].
5. *Physical Acoustics*, Ed. by W. P. Mason (Academic, New York, 1968; Mir, Moscow, 1970), Vol. 3, Part B.
6. V. N. Belomestnykh, *Physicochemical Acoustics of Crystals* (TROTs, Tomsk, 1998) [in Russian].
7. V. N. Belomestnykh, Yu. P. Pokholkov, V. L. Ul'yanov, and O. L. Khasanov, *Elastic and Acoustical Properties of Ionic, Ceramic Insulators and Hight-Temperature Superconductors* (STT, Tomsk, 2001) [in Russian].
8. V. N. Belomestnykh and L. A. Belomestnykh, in *Proceedings of the International Conference "All-Siberian Lectures on Mathematics and Mechanics,"* Vol. 2: *Mechanics* (Izd. Tomsk. Univ., Tomsk, 1997), pp. 189–190.
9. V. N. Belomestnykh and V. L. Ul'yanov, in *Proceedings of the 3rd International Conference "Crystals: Growth, Properties, Real Structure, and Applications"* (VNIISIMS, Aleksandrov, 1997), Vol. 2, pp. 22–34.
10. V. N. Belomestnykh, E. M. Karpova, E. P. Khrolenko, *et al.*, in *Proceedings of the 5th International Conference "Crystals: Growth, Properties, Real Structure, and Applications"* (VNIISIMS, Aleksandrov, 2001), pp. 145–147.
11. V. N. Belomestnykh, E. M. Efimova, and E. P. Tesleva, in *Proceedings of the 4th International Scientific–Engineering Conference "Dynamics of Systems, Mechanisms, and Machines"* (Omsk. Gos. Tekh. Univ., Omsk, 2002), Vol. 1, pp. 350–353.
12. L. Girifalco, *Statistical Physics of Materials* (Wiley, New York, 1973; Mir, Moscow, 1975).
13. C. Kittel, *Introduction to Solid State Physics*, 5th ed. (Wiley, New York, 1976; Nauka, Moscow, 1978).
14. K. P. Rodionov, Fiz. Met. Metalloved. **26**, 1120 (1969).
15. S. R. Urzendowski and A. H. Guenther, Int. Symp. Therm. Expansion Solids, 256 (1974).
16. K. G. Bansigir, J. Appl. Phys. **39**, 4024 (1968).
17. A. A. Vorob'ev, *Mechanical and Thermal Properties of Alkali-Halide Single Crystals* (Vysshaya Shkola, Moscow, 1968) [in Russian].
18. S. Haussühl, Z. Kristallogr. **138**, 177 (1973).
19. G. N. Ivanov and T. A. Lebedev, Tr. Leningr. Politekh. Inst. im. M.I. Kalinina, No. 236, 38 (1964).
20. S. S. Batsanov, Neorg. Mater. **35**, 1144 (1999).
21. S. V. Nemilov, Dokl. Akad. Nauk SSSR **181**, 1427 (1968) [Sov. Phys. Dokl. (1968)].
22. B. N. Oshcherin, Zh. Fiz. Khim. **45**, 2622 (1971).

Translated by A. Spitsyn

Technical Physics, Vol. 49, No. 8, 2004, pp. 951–956. Translated from Zhurnal Tekhnicheskoĭ Fiziki, Vol. 74, No. 8, 2004, pp. 1–5.
Original Russian Text Copyright © 2004 by Volov.

GASES AND LIQUIDS

A Nonisentropic Compression Heater

D. B. Volov
Samara State Academy of Road Machinery, Samara, 443066 Russia

Received May 5, 2003

Abstract—Mathematical and mechanical models of a heating device based on periodic nonisentropic compression are constructed; the fields of application of these models are outlined. An expression for the minimal period of eigenmodes is deduced and special features of the behavior of such a nonlinear system are revealed. The phenomenon of self-organization leading to the definite quasi-linear behavior of the system is considered. © *2004 MAIK "Nauka/Interperiodica".*

INTRODUCTION

The general principle of operation of the so-called HS systems is the nonisentropic heating of gas upon its periodical to-and-fro forcing between the two volumes. This phenomenon is employed, in particular, by ballistic heating devices, such as multistage plasmatrons [1]. Ballistic plasmatrons are of great importance for various applications, such as the quenching and thermal hardening of tools, the pumping of solid-state lasers [2, 3], and plasma- and photochemistry [4].

A nonisentropic periodic heater can either be applied as a separate unit or be incorporated into a laser pump system. Elaboration of such a system opens wide possibilities for the application of inexpensive, serviceable lasers in processing technologies (cutting, welding, thermal hardening of parts, etc.). It is well known that the laser-treated surfaces feature a number of unique advantageous properties, which ensures high quality of the final product.

The simplest and most evident application of the HS systems is air-heating systems. The heat sources presently available are based on either heating elements with a high working temperature (which leads to the burning of oxygen and gives rise to the fumes smell in the air) or low-temperature heat-transfer media (in oil heaters), which fail to rapidly drive the device to its rating duty. In the system proposed here, the heating of air is effected via the direct transfer of thermal energy to the gas, without resorting to a heat-transfer agent.

The basic element of such systems is a cylinder and a piston with a nozzle. In one way or another, reciprocating motion is imparted to the piston. Gas is warmed as it flows through the nozzle [5].

The principle of operation of an open system is as follows. An external gas comes into the cylinder, where its temperature increases due to the periodic motion of the piston. Then, the gas partially leaves the cylinder (a new portion comes in) and further heating occurs (Fig. 1).

Let the notation HS-1 refer to HS systems with a fixed amplitude of the piston motion, while the devices of HS-2 type are HS systems where periodic excitation is imparted to a free piston capable of vibrations with a varying amplitude.

MATHEMATICAL MODEL

By making use of the polysectional theory [6], it is feasible to construct a mathematical model of device operation and to integrate the obtained system of nonlinear differential equations by numerical methods. However, taking into account some special features of the HS system operation, one can also apply the analytical approach. Let us split the system into three sections: the volumes to the left and right from the piston comprise sections *I* and *II*, respectively; the external volume is referred to as section *III*. The initial system of equation has the form

$$\frac{d\rho_1}{dt} = \frac{1}{V_1}(G_{12} + G_{13}) - \frac{\rho_1}{V_1}\frac{dV_1}{dt}, \qquad (1)$$

$$\frac{d\rho_2}{dt} = \frac{1}{V_2}(G_{21} + G_{23}) - \frac{\rho_2}{V_2}\frac{dV_2}{dt}, \qquad (2)$$

$$\rho_3 = \frac{1}{V_3}(m_{01} + m_{02} + m_{03} - \rho_2 V_2 - \rho_1 V_1), \qquad (3)$$

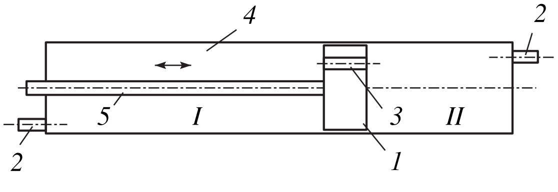

Fig. 1. Scheme of the device: (*1*) piston, (*2*) outlet, (*3*) nozzle, (*4*) cylinder, and (*5*) rod.

1063-7842/04/4908-0951$26.00 © 2004 MAIK "Nauka/Interperiodica"

$$\frac{dT_1}{dt} = \frac{1}{V_1}\left(\frac{1}{\rho_1}\begin{cases}(\gamma T_1 - T_1)G_{12}, & p_1 > p_2\\ (\gamma T_2 - T_1)G_{21}, & p_1 \le p_2\end{cases} + \frac{1}{\rho_1}\begin{cases}(\gamma T_1 - T_1)G_{13}, & p_1 > p_3\\ (\gamma T_3 - T_1)G_{31}, & p_1 \le p_3\end{cases}\right) - (\gamma - 1)\frac{T_1}{V_1}\frac{dV_1}{dt}, \tag{4}$$

$$\frac{dT_2}{dt} = \frac{1}{V_2}\left(\frac{1}{\rho_2}\begin{cases}(\gamma T_2 - T_2)G_{21}, & p_2 > p_1\\ (\gamma T_1 - T_2)G_{12}, & p_2 \le p_1\end{cases} + \frac{1}{\rho_2}\begin{cases}(\gamma T_2 - T_2)G_{23}, & p_2 > p_3\\ (\gamma T_3 - T_2)G_{32}, & p_2 \le p_3\end{cases}\right) - (\gamma - 1)\frac{T_2}{V_2}\frac{dV_2}{dt}, \tag{5}$$

$$\frac{dT_3}{dt} = \frac{1}{V_3}\left(\frac{1}{\rho_3}\begin{cases}(\gamma T_3 - T_3)G_{31}, & p_3 > p_1\\ (\gamma T_1 - T_3)G_{13}, & p_3 \le p_1\end{cases} + \frac{1}{\rho_3}\begin{cases}(\gamma T_3 - T_3)G_{32}, & p_3 > p_2\\ (\gamma T_2 - T_3)G_{23}, & p_3 \le p_2\end{cases}\right) - \frac{\alpha_3(T_3 - T_0)S'_3}{c_v\rho_3 V_3}, \tag{6}$$

$$G_{ml} = -S_{ml}\rho_m a_{ml} \times \begin{cases}\left(\dfrac{2}{\gamma_m + 1}\right)^{\frac{\gamma_m + 1}{2(\gamma_m - 1)}}, & p_l < p_m k_m,\\ \sqrt{\dfrac{2}{\gamma_m - 1}\left(1 - \left(\dfrac{p_l}{p_m}\right)^{\frac{\gamma_m - 1}{\gamma_m}}\right)}\left(\dfrac{p_l}{p_m}\right)^{\frac{1}{\gamma_m}}, & p_m k_m \le p_l < p_m,\end{cases} \tag{7}$$

$$k_m = \left(1 - \frac{\gamma_m - 1}{\gamma_m + 1}\right)^{\frac{\gamma_m}{\gamma_m - 1}}, \quad a_{ml} = \frac{p_m - p_l}{|p_m - p_l|}\sqrt{\gamma_m \frac{R_0}{\mu_m}T_m},$$

$$m, l = \begin{cases} i, j, & p_i > p_j\\ j, i, & p_i \le p_j,\end{cases}$$

where t is time; a is the velocity of sound; γ is the adiabatic exponent; S is the area of the opening; ρ, p, T, and m are the density, the pressure, the temperature, and the mass of the gas, respectively; R_0 is the universe gas constant; μ is the molar mass; α' is the heat-transfer coefficient; S' is the heat-transfer surface; V is the volume of a section; subscript 0 relates to the initial values of the parameters; and subscripts 1–3 indicate the section number. In Eqs. (4) and (5), one should also take into consideration the heat removal through the cylinder walls.

For a sufficiently high-power engine, one can assume a harmonic change in the coordinate of the piston center of mass. Otherwise, the periodic motion of the center-of-mass coordinate can be represented as a Fourier series.

Immediately after the switching on the system, one observes a transient regime in which the position of the point at which the gas flow changes its direction migrates from the middle of the piston to a certain stable value, which is characteristic of the steady operation of the device. An advance with respect to switching to the reverse direction of the flow and, accordingly, to the other branch of Eqs. (1)–(7) is formed. After the completion of the transient stage, two stable positions appear, in which of the reversal of velocity u takes place. These positions are spaced by the distance ψ to the left and right from $L_0/2$ (L_0 is the cylinder length) and correspond to the equality of pressure in the sections, $p_1 = p_2$. This phenomenon takes place because the moving piston heats up the gas behind it and, during the reverse motion, has to compress the previously heated gas. This gas is characterized by a higher pressure; hence, the condition $p_1 = p_2$ is met before the piston passes through the point $L_0/2$. Since the gas heating within one passage is not large, the displacement of the reversal point from the equilibrium position is insignificant and its coordinate can be taken at $x = L_0/2$ in the calculations of temperature.

MECHANICAL MODEL OF THE GAS HEATER OPERATION

A mechanical analogy is considerably helpful in the case under study. The periodic compression of gas during operation can be represented by the action of two springs with variable rigidity (*1* and *2* in Fig. 2). The presence of a nozzle with the diameter d_n in the piston results in the gas heating, i.e., in the energy scattering. At $d_\text{n} = 0$, no temperature growth occurs (the loss by friction between the parts of the system is negligibly small as compared to the effect considered). This makes convenient the introduction of a nonconservative force of quasifriction that accounts for the effect of d_n and causes the energy dissipation. Thus, the mechanical model of the device appears as a body of mass m_p (the piston mass) with two springs of variable rigidity fixed to it at the distance L_0 from each other. In addition, the body experiences the action of the friction force R (Fig. 2).

Assume that the eigenfrequency of oscillation is independent of the nozzle diameter. This assumption is valid for narrow nozzles ($d_\text{n} < D$). Then, the eigenmodes of the mechanical system are described by the equation

$$m_\text{p}\frac{d^2x}{dt^2} + F(x) = 0, \quad F(x) = p_2\sigma - p_1\sigma, \tag{8}$$

where x is the coordinate of the piston center of mass and σ is the cylinder cross-sectional area.

Let us set $x = 0$ in the equilibrium position. In this case, the gas pressure can be calculated from the adiabat equation

$$\frac{p_1}{p_0} = \left(\frac{V_{01}}{V_1}\right)^{\gamma} = \left(\frac{L_0/2 - l_p/2}{L_0/2 + x - l_p/2}\right)^{\gamma},$$

$$\frac{p_2}{p_0} = \left(\frac{L_0/2 - l_p/2}{L_0/2 - x - l_p/2}\right)^{\gamma},$$

where l_p is the piston length; subscript 0 on the gasdynamic parameters corresponds to the equilibrium position; and subscripts 1 and 2 point to the section number (Fig. 1).

The reduced length of the system is $L = L_0 - l_p$. Then, the function $F(x)$ in Eq. (8) can be expressed as

$$F(x) = k((L/2 - x)^{-\gamma} - (L/2 + x)^{-\gamma}), \quad k = p_0\sigma(L/2)^{\gamma}.$$

Integrating Eq. (8) yields the law of the piston motion in the form

$$t = \int \frac{dx}{\pm\sqrt{\frac{2}{m_p}\left(C - \int\limits_0^x F(\zeta)d\zeta\right)}}, \quad C = \text{const}.$$

Taking into consideration the symmetry of the problem (A is the oscillation amplitude), we obtain for the oscillation period

$$T_p = 4\int\limits_0^A \frac{dx}{\sqrt{\frac{2}{m_p}\int\limits_x^A F(\zeta)d\zeta}}. \tag{9}$$

Let us introduce three dimensionless parameters: the relative coordinate $l = x/A$, the outflow factor λ_1, and the geometrical factor λ_2, such that

$$\lambda_1 = \frac{uS}{\sigma A\omega}, \quad \lambda_2 = \frac{L}{2A},$$

where ω is the stimulated oscillation frequency.

Then, the free oscillation period appears in the form

$$T_p = 4A^{\frac{1+\gamma}{2}}\sqrt{\frac{m_p(\gamma - 1)}{2k}}$$

$$\times\int\limits_0^1 \frac{dl}{\sqrt{(\lambda_2 + 1)^{1-\gamma} + (\lambda_2 - 1)^{1-\gamma} - (\lambda_2 + l)^{1-\gamma} - (\lambda_2 - l)^{1-\gamma}}}. \tag{10}$$

Thus, the oscillation period turns out to be amplitude-dependent and attains its maximum at $A \longrightarrow 0$. In order to find the peak value, we expand function $F(x)$ into a power series in terms of x and, bearing in mind that $x \longrightarrow 0$ at $A \longrightarrow 0$, retain the first term of the series. Substituting it to Eq. (9) and integrating, we obtain the maximal period of free oscillations:

$$(T_p)_{\max} = \pi\sqrt{\frac{m_p L}{k\gamma}\left(\frac{L}{2}\right)^{\gamma}}. \tag{11}$$

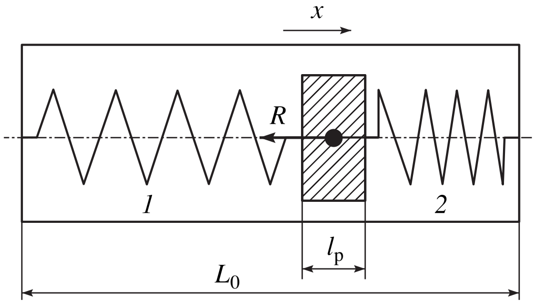

Fig. 2. Mechanical model.

We now consider the periodic motion of the system under the external action. Assuming the harmonic perturbing force, we employ the harmonic balance method [7]. At a sufficiently high power of the engine, the piston center-of-mass coordinate x is also described by a harmonic function. Any other periodic motion of the piston can be described with the help of a Fourier series.

The equation of motion has the form

$$m_p\frac{d^2x}{dt^2} + F(x) + R\left(x, \frac{dx}{dt}\right) + N = P_0\cos(\omega t + \phi), \tag{12}$$

where R is the pseudoforce of friction; N is the reaction of the support; and P_0 and φ are the stimulating force amplitude and phase, respectively.

For an HS system of the second type, $N = 0$, while for the first type, the reaction of the support compensates the forces defined by the properties of the system $N = -F(x) - R(x, dx/dt)$.

We seek the solution to Eq. (12) in the form $x = A\cos\omega t$.

Equation (12) includes the nonconservative forces $R(x, dx/dt)$; the work done by these forces increases the temperature of the system. The mechanical analogy is insufficient to elucidate the dependence of these forces on the parameters of the system. For this purpose, the thermodynamic approach based on the mathematical model (1)–(7) is required. This system of nonlinear differential equations was numerically integrated, and the temperature and pressure in sections were calculated. The character of friction is determined by the shape of the hysteresis curve [7]. The effect of the drag forces is defined by the value $\sigma(p_2 - p_1) = R(x, dx/dt) + F(x)$.

As is seen from Fig. 3, the behavior of pseudofriction has a complex character. When the nozzle diameter is much smaller than the piston diameter D (Fig. 3a), the work done by these forces per period is not large and the curve repeats the contour of the $F(x)$ curve.

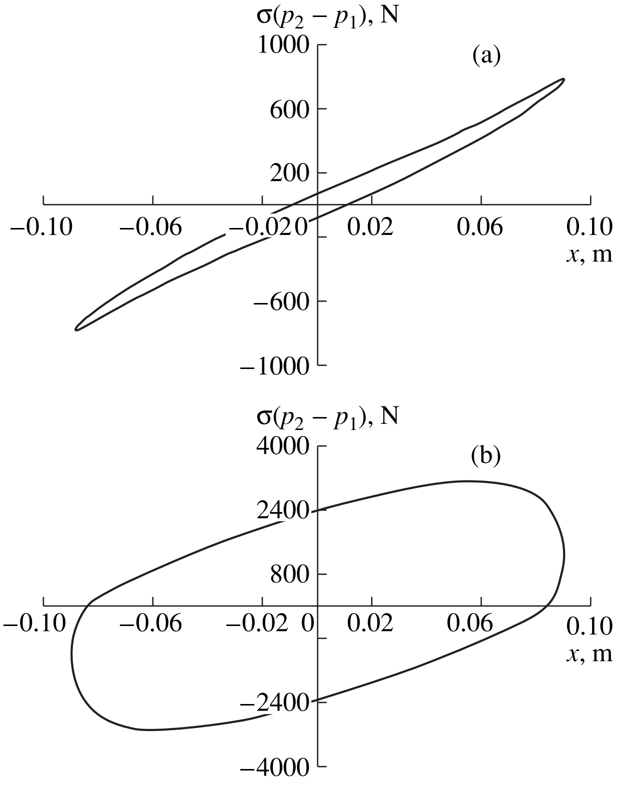

Fig. 3. Hysteresis loops in the steady-state mode for different nozzle diameters: (a) $d_n \ll D$ and (b) d_n is close to the optimal one.

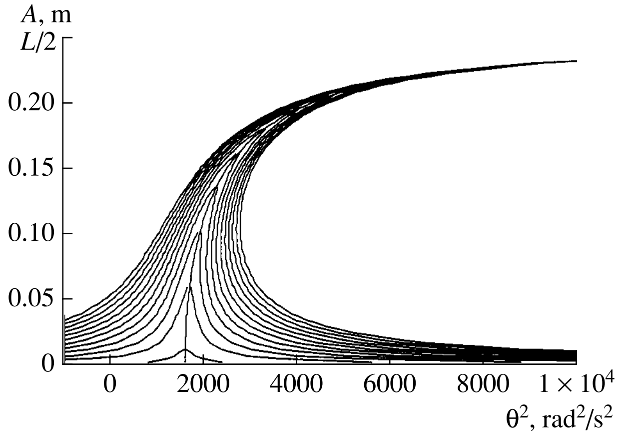

Fig. 4. The amplitude–frequency characteristic of a nonlinear system of the HS-2 type.

With the nozzle diameter providing for the maximal heating (as before, $d_n \ll D$) (Fig. 3b), the loop shape is close to elliptical.

According to [7], the liquid friction in a linear system ($F(x) \sim x$) corresponds to an elliptical hysteresis loop.

It follows from the energy estimation of the drag forces [7] that, despite the completely different shape of the hysteresis loop, the general character of attenuation is often similar. The friction emerging during oscillations is mainly governed by the absorption factor [7], while the shape of the hysteresis loop plays only a minor part. This is the first remark on the character of pseudofriction. The second is that, in the most important case of the optimal nozzle diameter, the operation mode corresponds to the motion in the presence of liquid friction (Fig. 3b). Third, from the aspect of calculations, an arbitrary friction function $R(x, dx/dt)$ can be approximated by an equivalent viscous friction with the same absorption factor. This is due to the fact that, in terms of the harmonic balance method, any periodic function $R(x, dx/dt)$ can be represented in the form of a Fourier expansion. Retaining only the first term $R_1(A, \omega)\sin(\omega t)$ leads to the case of the liquid friction [7].

These three arguments allow us to confine our analysis to the case of liquid friction $R = \alpha(dx/dt)$, $\alpha = \text{const}$ (coefficient α depends on the parameters λ_1 and λ_2). Then, taking the solution to Eq. (12) in the form $x = A\cos(\omega t)$ and using the harmonic balance method, for the second-type systems, we obtain [7]

$$[\omega_0^2(A) - \omega^2]A = \frac{P_0}{m_p}\cos\phi, \quad 2n\omega A = \frac{P_0}{m_p}\sin\phi,$$

where $\alpha/m_p = 2n$ and $\omega_0(A) = 2\pi/T_p$ is the eigenfrequency of oscillations.

Eliminating the phase shift from the above expressions, we arrive at the following relationship between the frequency of the perturbing force and the amplitude of the stimulated oscillations in an HS-2 system:

$$\omega^2 = \omega_0^2(A) - 2n^2 \pm \sqrt{\left(\frac{P_0}{m_p A}\right)^2 - 4n^2\omega_0^2(A) + 4n^4}. \quad (13)$$

Figure 4 shows the amplitude–frequency characteristic $A(\omega^2)$ calculated from formula (13). Here, the skeleton curve $\omega_0^2(A)$ is plotted by using the exact solution (10). The system is seen to be highly nonlinear: the resonance frequency depends on the oscillation amplitude. Note the existence of the minimal resonance frequency whose value corresponds to the period (11).

In HS-2-type systems, one can also consider such nonlinear effects as the free piston “drift,” the spontaneous transition upon an increase in frequency from low-amplitude oscillations to oscillations with $A \approx L/2$ and attainment of resonance, and the appearance of subharmonic oscillations.

Thus, the mechanical model of a heat-energy device enables one to determine the resonance modes and to reveal special features in the operation of the nonlinear system. This approach makes it possible to omit the integration of the polysectional system and to pass directly to the engineering calculation of the energy parameters.

NUMERICAL CALCULATION: ATTRACTORS IN THE NONISENTROPIC-COMPRESSION HEATING SYSTEMS

In the absence of heat removal, the system of equations (1)–(7) permits an analytical solution under the condition that the function of the piston periodic motion is known. In the approximation of a constant velocity of sound, this solution has already been found. In this case, a change in the gas temperature in sections is described by the geometrical progression

$$\begin{cases} T_1^{\langle m+1\rangle} = T_1^m((c_4+c_5)(c_4'+c_5')+c_3c_6') \\ +\,T_2^m(c_4'+c_5')c_6, \\ T_2^{\langle m+1\rangle} = T_1^m(c_4+c_5)c_3+T_2^mc_6c_3, \end{cases} \qquad (14)$$

where the coefficients c_i = const in the given geometry and operation mode and m is the period number.

However, when carrying out the numerical integration of the system, it turned out that the solution to system (14) is valid in a limited region. The nonlinear segment determined by this formula is followed by a linear temperature rise in the system (Fig. 5). At first glance, this result may seem unexpected; the more so as the system is initially nonlinear (see Eqs. (1)–(7)). The geometrical progression, which describes the initial temperature growth, gives way to the arithmetical progression.

On closer examination, it was found that a change in the character of the solution should be attributed to the temperature dependence of the velocity of sound. When searching for (14), this fact can be disregarded within only a certain temperature range. In reality, the velocity of sound slowly grows with temperature (as the square root of the temperature). It is precisely this dependence that forms the feedback responsible for the self-organization of the system.

In a more general case, the feedback can be established from the dependences of the dimensionless complexes λ_1 and λ_2 on the thermodynamic parameters of the system rather than from the temperature dependence of the sound velocity. This circumstance shows up in numerical solution of system (1)–(7). If any quantity entering these complexes depends on the thermodynamic functions of state (temperature, pressure, etc.), the system is “tuned” to the external action and passes to the mode of a linear temperature growth. According to numerical results, the particular form of the dependence of values in complexes λ_1 and λ_2 on the function of state is of no importance (at least, in the case of a monotonic continuous function). In any case, self-organization occurs and the distribution of the parameters of the system in space and time is attracted to a certain stable solution (attractor). The shape of the attractor is governed by the geometrical and thermodynamic parameters of system (Figs. 6 and 7). In the absence of feedback, no attraction occurs.

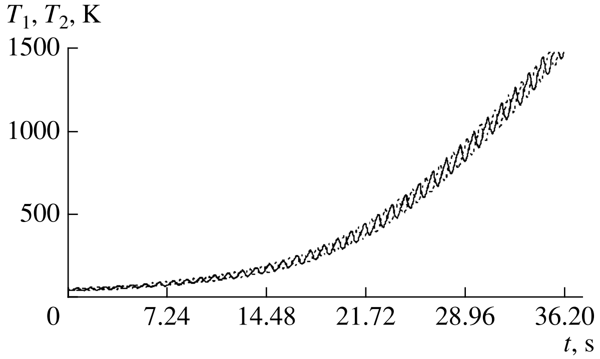

Fig. 5. Variation of temperature in the first (T_1, solid curve) and second (T_2, dot-and-dash curve) sections in the absence of heat removal.

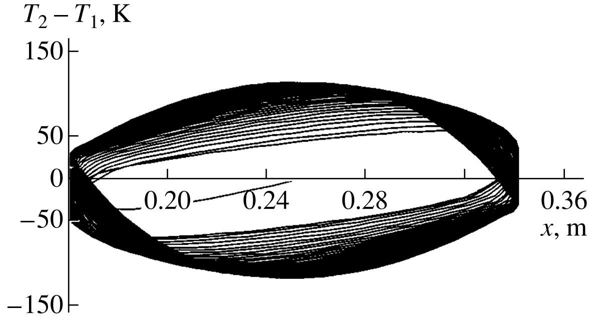

Fig. 6. Temperature difference vs. the piston coordinate x.

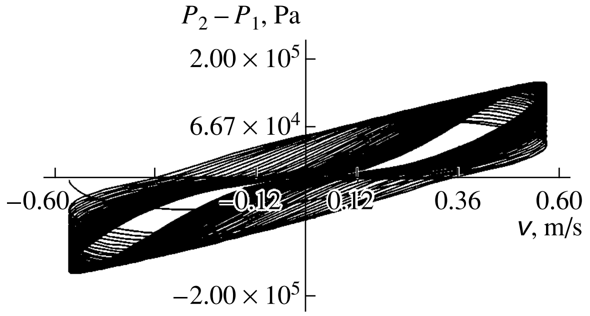

Fig. 7. Pressure difference vs. the piston velocity.

In actual conditions of operation, this effect is less pronounced because of the influence of the heat loss. Its presence gives rise to the energy balance, and the system passes to a stationary mode with a constant mean temperature. This is true for both linear and nonlinear temperature growth. For this reason, we disregarded the heat loss when considering the special features of these modes.

It has been demonstrated that, irrespective of the particular form of feedback, its presence gives rise to stable solutions. The fact of the presence of feedback is decisive. In this case, we are dealing with the phenomenon of self-organization, which leads to a definite quasilinear behavior of a nonlinear system.

By using various approaches complementing each other, one can obtain a detailed insight into the process and reveal a great number of special features in the behavior of the system.

REFERENCES

1. V. M. Shmelev, V. T. Volov, and D. B. Volov, Zh. Tekh. Fiz. **70** (5), 17 (2000) [Tech. Phys. **45**, 538 (2000)].
2. J. A. Dowling, J. Shumsky, J. Echerman, and R. E. Schelier, Appl. Phys. Lett. **12**, 184 (1968).
3. V. M. Shmelev, V. T. Volov, D. B. Volov, *et al.*, Zh. Tekh. Fiz. **68** (9), 67 (1998) [Tech. Phys. **43**, 1069 (1998)].
4. A. D. Margolin, N. Ya. Vasilik, V. M. Shmelev, *et al.*, in *Proceedings of the 1st All-Union Symposium on Radiation Plasmadynamics, Moscow, 1989*, p. 33.
5. D. B. Volov, V. M. Shmelev, and V. T. Volov, Teplofiz. Vys. Temp. **38**, 188 (2000).
6. D. B. Volov, in *Interinstitute Collection of Scientific Works with International Participations, 2002*, No. 23, pp. 477–480 [in Russian].
7. V. L. Biderman, *Applied Theory of Mechanical Vibrations* (Vysshaya Shkola, Moscow, 1972) [in Russian].

Translated by A. Sidorova

Technical Physics, Vol. 49, No. 8, 2004, pp. 957–966. Translated from Zhurnal Tekhnicheskoĭ Fiziki, Vol. 74, No. 8, 2004, pp. 6–14.
Original Russian Text Copyright © 2004 by Shiryaeva, Grigor'ev, Levchuk.

Nonlinear Analytical Asymptotic Investigation of Oscillations of Nonaxisymmetric Modes of a Charged Jet of an Ideal Liquid

S. O. Shiryaeva, A. I. Grigor'ev, and T. V. Levchuk
Yaroslavl State University, Yaroslavl, 150000 Russia
e-mail: shir@uniyar.ac.ru

Received October 27, 2003; in final form, January 13, 2004

Abstract—A jet of an ideal incompressible conducting liquid with a uniformly charged surface is considered. The jet moves at a constant velocity along the symmetry axis of its unperturbed cylindrical surface. An analytical expression for the jet shape is derived as a function of time for the excitation of nonaxisymmetric modes at the initial instant. The solution is found in the second order of smallness with respect to the amplitude of capillary oscillations of the jet. In the same approximation, the liquid velocity field in the jet and the distribution of the electric field in the jet region are determined. Second-order corrections to the analytical expressions for the jet shape and potentials of the liquid velocity field in the jet and the electrostatic field around the jet have resonant forms determined by the conditions of their interaction with the solutions of the first order of smallness. *© 2004 MAIK "Nauka/Interperiodica".*

1. Investigations of capillary oscillations and stability of a charged cylindrical jet is of interest in connection with numerous scientific, technical and technological applications of this phenomenon (see, for example, monograph [1], which includes a detailed review of publications concerning the issue discussed up to the 1990s). In view of the problem's relevance, this issue has repeatedly become a subject of theoretical studies in linear and nonlinear formulations in recent years [2–9]. However, in all of the works devoted to nonlinear oscillations, only axisymmetric jet oscillations were considered because researchers were mainly interested in the mechanisms of disintegration of a jet into drops inasmuch as in due time Rayleigh showed that disintegration of an uncharged jet into separate drops occurs due to excitation of an axisymmetric wave [10]. At the same time, it is shown [11,12] that for highly charged jets (with a surface or volume charge), the instability growth rates of nonaxisymmetric waves may exceed that of an axisymmetric wave. Therefore, in the present paper, we conduct an analytical asymptotic investigation of nonlinear oscillations in nonaxisymmetric waves at the surface of a charged ideally conducting jet in the frame of a method of many scales. This method was earlier employed in [13] to study nonlinear oscillations of an uncharged jet.

2. Let us consider an infinite jet of an ideal incompressible ideally conducting liquid with a density ρ and a surface tension coefficient σ. The jet has a constant radius R and moves at a constant velocity $\overline{\mathbf{U}_0}$. Assume that the ambient medium is absent; however, in the ambient space, an electrostatic field directed normally to the jet axis is produced. For this reason, a charge is distributed over the jet surface with the surface density χ in the equilibrium state (that is, in the absence of any perturbations of the cylindrical jet shape).

We conduct the analysis in a cylindrical coordinate system with the origin moving at velocity $\overline{\mathbf{U}_0}$ and with the z axis codirectional with the jet so that $\mathbf{n}_z \parallel \mathbf{U}_0$. It is obvious that in such a system the liquid velocity field in the jet is entirely governed by capillary oscillations of the jet surface.

Let us track the evolution with time of a nonaxisymmetric wave with the wave number k, propagating over the jet surface in the positive direction of z axis. The wave amplitude is assumed to be small as compared with the jet radius.

The analysis will be conducted in dimensionless variables with basic units of R, ρ, and σ (that is, we assume that $R = \rho = \sigma = 1$). In this case, the equation of the free jet surface perturbed by a capillary wave motion is written in the form

$$r = 1 + \xi(\varphi, z, t); \quad |\xi| \ll 1, \tag{1}$$

where r, φ, and z are the cylindrical coordinates; t is time; and ξ is a function describing the perturbation of the equilibrium cylindrical jet shape.

In the frame of the model of a potential flow, the mathematical statement of the problem on calculating of the time evolution of a virtual wave perturbation of the jet surface includes the following equations and conditions the Laplace equations for potential Ψ of the liquid velocity field in the jet and electrostatic potential Φ around the jet,

$$\Delta\Psi = 0, \quad \Delta\Phi = 0; \tag{2}$$

the conditions of boundedness of the solutions at the jet axis and at infinity,

$$r \longrightarrow 0\colon |\nabla\Psi| \longrightarrow 0; \quad r \longrightarrow \infty\colon |\nabla\Phi| \longrightarrow 0; \tag{3}$$

the boundary conditions at the free jet surface (1), namely, kinematic condition

$$\begin{gathered} r = 1 + \xi\colon \frac{\partial F}{\partial t} + \nabla\Psi \cdot \nabla F = 0; \\ F(r, \varphi, z, t) \equiv r - [1 + \xi(\varphi, z, t)]; \end{gathered} \tag{4}$$

and the dynamic condition

$$\begin{gathered} r = 1 + \xi\colon \Delta P - \frac{\partial\Psi}{\partial t} - \frac{1}{2}(\nabla\Psi)^2 \\ + \frac{1}{8\pi}(\nabla\Phi)^2 - \nabla \cdot \mathbf{n} = 0 \end{gathered} \tag{5}$$

and the condition of equipotentiality of the jet surface,

$$r = 1 + \xi\colon \Phi = \Phi_S(t). \tag{6}$$

In expression (5), ΔP is the difference between the pressures inside and outside the jet in equilibrium ($\xi = 0$, $\Psi = 0$); the next to last and last terms are the pressures of the electric field and the forces of surface tension, respectively; $\mathbf{n}$ is a vector normal to the jet surface (1); $\mathbf{n} = \nabla F/|\nabla F|$.

Boundary value problem (1)–(6) should be supplemented with the conditions of conservation of the charge and volume of a jet segment with a length equal to the wavelength $\lambda = 2\pi/k$,

$$-\frac{1}{4\pi}\oint_S (\mathbf{n} \cdot \nabla\Phi) r d\varphi dz = 2\pi\chi\lambda;$$

$$S = \begin{cases} r = 1 + \xi(\varphi, z, t) \\ 0 \le \varphi \le 2\pi \\ z_0 \le z \le z_0 + \lambda; \end{cases} \tag{7}$$

$$\int_V r dr d\varphi dz = \pi\lambda; \quad V = \begin{cases} 0 \le r \le 1 + \xi(\varphi, z, t) \\ 0 \le \varphi \le 2\pi \\ z_0 \le z \le z_0 + \lambda. \end{cases} \tag{8}$$

For complete closure of the set of equations (2)–(8), it is also necessary to formulate the initial conditions. However, the initial conditions of an arbitrary form may lead to an extremely cumbersome solution; therefore, in nonlinear problems of determining periodic wave profiles of the surface of an ideal liquid, the initial conditions are usually formulated in such a way that the solution would take the simplest form [14, 15]. Precisely this approach will be employed in the following analysis.

We shall seek the solution of problem (2)–(8) in the form of an expansion in a small parameter ε equal to the ratio of the wave amplitude to the jet radius. Using a method of many scales and confining ourselves to an accuracy up to and including the second order of smallness, we represent the sought functions ξ, Ψ, and Φ in the form of power series in ε. Simultaneously, we assume that variation of these functions with time is determined by two time scales: the main scale $T_0 = t$ and a slower one $T_1 = \varepsilon t$,

$$\begin{gathered} \xi(\varphi, z, t) = \varepsilon\xi^{(1)}(\varphi, z, T_0, T_1) + \varepsilon^2\xi^{(2)}(\varphi, z, T_0) + O(\varepsilon^3); \\ \Psi(r, \varphi, z, t) \\ = \varepsilon\Psi^{(1)}(\varphi, z, T_0, T_1) + \varepsilon^2\Psi^{(2)}(\varphi, z, T_0) + O(\varepsilon^3); \\ \Phi(r, \varphi, z, t) = \Phi^{(0)}(r) + \varepsilon\Phi^{(1)}(r, \varphi, z, T_0, T_1) \\ + \varepsilon^2\Phi^{(2)}(r, \varphi, z, T_0) + O(\varepsilon^3). \end{gathered} \tag{9}$$

Inasmuch as we assume that the wave propagates over the jet surface in the positive direction of the z axis, the shape of the free liquid surface can be represented in the form

$$r = 1 + \varepsilon f(\varphi)(A(T_1)\exp(i\theta) + \overline{A(T_1)\exp(i\theta)}) + O(\varepsilon^2),$$

where $\theta \equiv kz - \omega_m(k)T_0$, where $\omega_m(k)$ is the frequency of a wave with the wave number k and azimuthal number m; $f(\varphi)$ is a real function describing the jet cross section; $A(T_1)$ is an as yet unknown function that depends on slow time T_1; and the vinculum means complex conjugation.

It is obvious that $f(\varphi)$ is a periodic function with period 2π and, consequently, it can be expanded into a Fourier series:

$$f(\varphi) = \sum_{m=0}^{\infty} (C_m \exp(im\varphi) + \overline{C_m}\exp(-im\varphi));$$

$$C_m = \frac{1}{2\pi(1 + \delta_{m,0})}\int_{-\pi}^{\pi} f(\varphi)\exp(-im\varphi)d\varphi.$$

To simplify the following calculations, we confine ourselves to the case when the jet cross section shape is determined by a single harmonic; that is, we assume that

$$f(\varphi) = C_m\exp(im\varphi) + \overline{C_m}\exp(im\varphi).$$

Now, changing the notation of coefficients ($\zeta^{(+)}(T_1) = C_m A(T_1)$, $\zeta^{(-)}(T_1) = \overline{C_m} A(T_1)$) in the proper way allows us to write the expression for the free jet surface in the form

$$r = 1 + \varepsilon[(\zeta^{(+)}(T_1)\exp(im\varphi) + \zeta^{(-)}(T_1)\exp(-im\varphi))\exp(i\theta) + (\text{c.c.})] + O(\varepsilon^2). \tag{10}$$

Here and below, abbreviation (c.c.) means terms that are complex conjugate to the preceding ones. We shall consider expression (10) as the initial condition which is necessary for closure of the boundary value problem (2)–(8).

3. The substitution of expansions (9) into Eqs. (2)–(8), the calculation of the derivative with the help of the operator

$$\frac{\partial}{\partial t} = \frac{\partial}{\partial T_0} + \varepsilon\frac{\partial}{\partial T_1},$$

and the expansion of conditions (4)–(8) into Taylor series in the vicinity of the equilibrium cylindrical surface $r = 1$ allow us to find and sum the terms with the same powers of ε. Equating the factors multiplying various powers of ε to zeros leads to problems of various orders of smallness instead of the initial boundary value problem.

(a) In the zeroth approximation, an equilibrium state takes place which corresponds to an immovable (in the moving coordinate system) cylindrical liquid column with a constant surface charge density χ. The electric field in the vicinity of a charged unperturbed homogeneous cylindrical column is determined by the potential

$$\Phi^{(0)}(r) = -4\pi\chi\ln(r). \tag{11}$$

When writing (11), we assume that the surface potential of a cylindrical jet unperturbed by the wave motion is equal to zero ($\Phi_S^{(0)} = 0$). The dynamic boundary condition in the zeroth approximation allows one to determine the equilibrium pressure differential at the jet surface

$$\Delta p = 1 - 2\pi\chi^2.$$

(b) Due to the linearity of Eqs. (2), boundedness conditions (3), and expansions (9), functions $\Psi^{(j)}$ and $\Phi^{(j)}$ ($j = 1, 2$) in the first approximation are solutions to the equations for them that are entirely analogous to (2) and (3).

The set of boundary and additional conditions (4)–(8) in the first order of smallness takes the form

$$r = 1\colon \frac{\partial\Psi^{(1)}}{\partial r} - \frac{\partial\xi^{(1)}}{\partial T_0} = 0; \tag{12}$$

$$-\frac{\partial\Psi^{(1)}}{\partial T_0} + \frac{1}{8\pi}\left\{2\frac{\partial\Phi^{(0)}}{\partial r}\frac{\partial\Phi^{(1)}}{\partial r} + \frac{\partial}{\partial r}\left[\left(\frac{\partial\Phi^{(0)}}{\partial r}\right)^2\right]\xi^{(1)}\right\} + \xi^{(1)} + \frac{\partial^2\xi^{(1)}}{\partial\varphi^2} + \frac{\partial^2\xi^{(1)}}{\partial z^2} = 0; \tag{13}$$

$$\Phi^{(1)} + \frac{d\Phi^{(0)}}{dr}\xi^{(1)} = \Phi_S^{(1)}(t); \tag{14}$$

$$\int_{z_0}^{z_0+\lambda}\int_0^{2\pi}\left[\frac{\partial\Phi^{(1)}}{\partial r} + \frac{\partial}{\partial r}\left(r\frac{\partial\Phi^{(0)}}{\partial r}\right)\xi^{(1)}\right]\bigg|_{r=1} d\varphi dz = 0; \tag{15}$$

$$\int_{z_0}^{z_0+\lambda}\int_0^{2\pi}\xi^{(1)} d\varphi dz = 0. \tag{16}$$

On the basis of Eqs. (1), (9), and (10), we can obtain the following expression for the function of correction $\xi^{(1)}$ of the first order of smallness to the wave profile:

$$\xi^{(1)}(\varphi, z, T_0, T_1) = [\zeta^{(+)}(T_1)\exp(im\varphi) + \zeta^{(-)}(T_1)\exp(-im\varphi)]\exp(i\theta) + (\text{c.c.}). \tag{17}$$

The explicit form of functions $\zeta^{(+)}(T_1)$ and $\zeta^{(-)}(T_1)$ can be revealed only when analyzing the problem of the next order of smallness. It can readily be verified that function $\xi^{(1)}$ in the form (17) meets the condition of invariability of the jet volume (16).

Taking into account the fact that corrections of the first order of smallness to the potential of the velocity field $\Psi^{(1)}$ and electrostatic potential $\Phi^{(1)}$ are related to function $\xi^{(1)}$ by kinematic boundary condition (12) and condition of equipotentiality (14), we shall seek expressions for $\Psi^{(1)}$ and $\Phi^{(1)}$ by a method of separation of variables, taking them in the form

$$\Psi^{(1)}(r, \varphi, z, T_0, T_1) = A(T_1)B(r)D(\varphi)\exp(i\theta) + (\text{c.c.});$$

$$\Phi^{(1)}(r, \varphi, z, T_0, T_1) = [S(T_1)C(r)W(\varphi)\exp(i\theta) + (\text{c.c.})] + \Phi_S^{(1)}(t). \tag{18}$$

Substituting Eqs. (18), as well as (17) and (11), into Eqs. (12) and (14) and equating the coefficients of the exponents with the same powers, we obtain

$$A(T_1)D(\varphi) = \frac{-i\omega}{B'(1)}[\zeta^{(+)}(T_1)\exp(im\varphi) + \zeta^{(-)}(T_1)\exp(-im\varphi)];$$

$$S(T_1)W(\varphi) = \frac{4\pi\chi}{C(1)}[\zeta^{(+)}(T_1)\exp(im\varphi) + \zeta^{(-)}(T_1)\exp(-im\varphi)]. \tag{19}$$

Here and below, the prime denotes a derivative with respect to the argument calculated at the unperturbed jet surface.

Corrections to potentials $\Psi^{(1)}$ and $\Phi^{(1)}$ as functions of coordinate r are determined from Laplace equations (2) that, after substitution into them of Eqs. (18) and (19), are easily reduced to the ordinary differential equations for functions $B(r)$ and $C(r)$ of the same form:

$$\frac{d^2G(r)}{dr^2} + \frac{1}{r}\frac{dG(r)}{dr} - \left(k^2 + \frac{m^2}{r^2}\right)G(r) = 0.$$

Here, $G(r) \equiv B(r)$ or $G(r) \equiv C(r)$. Solutions to this equation are modified Bessel functions $I_m(kr)$ and $K_m(kr)$. Taking into account the fact that corrections to potentials $\Psi^{(1)}$ and $\Phi^{(1)}$ must meet boundedness conditions (3), we can write $B(r) = I_m(kr)$ and $C(r) = K_m(kr)$. Eventually, the expressions for corrections to potential $\Psi^{(1)}$ of the velocity field and electrostatic potential $\Phi^{(1)}$ take the final form

$$\begin{gathered}\Psi^{(1)}(r, \varphi, z, T_0, T_1) = -i\omega\frac{I_m(kr)}{kI'_m(k)}[\zeta^{(+)}(T_1)\exp(im\varphi) \\ + \zeta^{(-)}(T_1)\exp(-im\varphi)]\exp(i\theta) + (\text{c.c.}); \\ \Phi^{(1)}(r, \varphi, z, T_0, T_1) = 4\pi\chi\frac{K_m(kr)}{K_m(k)}[\zeta^{(+)}(T_1)\exp(im\varphi) \\ + \zeta^{(-)}(T_1)\exp(-im\varphi)]\exp(i\theta) + (\text{c.c.}).\end{gathered} \tag{20}$$

When deriving the expression for $\Phi^{(1)}$, we took into account the fact that the condition of conservation of the charge implies that the first-order correction to the electrostatic potential at the jet surface is equal to zero ($\Phi_S^{(1)}(t) = 0$).

Note that dynamic boundary condition (13) entering into the set of boundary and additional conditions (12)–(16) has remained unemployed. Substituting into it solutions (11), (17), and (20) gives the dispersion equation relating wave number k and azimuthal number m to oscillation frequency ω,

$$\begin{gathered}\omega_m^2(k) = G_m(k)[k^2 + m^2 - 1 + W(1 + H_m(k))]; \\ G_m(k) \equiv \frac{kI'_m(k)}{I_m(k)}; \quad H_m(k) \equiv \frac{kK'_m(k)}{K_m(k)}; \quad W \equiv 4\pi\chi^2.\end{gathered} \tag{21}$$

(c) In the second order of smallness, using set (4)–(8), we obtain an inhomogeneous equation for second-order corrections $\xi^{(2)}$, $\Psi^{(2)}$, and $\Phi^{(2)}$ (see Appendix A). The right-hand sides of these equations play the role of inhomogeneity functions and can be expressed in terms of solutions of the zeroth (11) and first order of smallness (17) and (20). After substitution of these solutions, boundary and additional conditions (A.1)–(A.5) take the form

$$\begin{gathered}r = 1: \frac{\partial\Psi^{(2)}}{\partial r} - \frac{\partial\xi^{(2)}}{\partial T_0} = \left[\frac{\partial\zeta^{(+)}}{\partial T_1}\exp(im\varphi) \right. \\ \left. + \frac{\partial\zeta^{(-)}}{\partial T_1}\exp(-im\varphi)\right]\exp(i\theta) + i[X_1((\zeta^{(+)})^2\exp(i2m\varphi) \\ + (\zeta^{(-)})^2\exp(-i2m\varphi)) + X_2 2\zeta^{(+)}\zeta^{(-)}]\exp(i2\theta) + (\text{c.c.});\end{gathered} \tag{22}$$

$$\begin{gathered}-\frac{\partial\Psi^{(2)}}{\partial T_0} - \chi\left[\frac{\partial\Phi^{(2)}}{\partial r} + 4\pi\chi\xi^{(2)}\right] + \xi^{(2)} + \frac{\partial^2\xi^{(2)}}{\partial\varphi^2} + \frac{\partial^2\xi^{(2)}}{\partial z^2} \\ = -i\omega\frac{1}{G_m(k)}\left[\frac{\partial\zeta^{(+)}}{\partial T_1}\exp(im\varphi) + \frac{\partial\zeta^{(-)}}{\partial T_1}\exp(-im\varphi)\right] \\ \times\exp(i\theta) + [Y_1((\zeta^{(+)})^2\exp(i2m\varphi) + (\zeta^{(-)})^2\exp(-i2m\varphi)) \\ + Y_2 2\zeta^{(+)}\zeta^{(-)}]\exp(i2\theta) + Y_3 2\zeta^{(+)}\overline{\zeta^{(-)}}\exp(i2m\varphi) \\ + Y_4(|\zeta^{(+)}|^2 + |\zeta^{(-)}|^2) + (\text{c.c.});\end{gathered} \tag{23}$$

$$\begin{gathered}\Phi^{(2)} - 4\pi\chi\xi^{(2)} = \Phi_S^{(2)} + L\{[(\zeta^{(+)})^2\exp(i2m\varphi) \\ + (\zeta^{(-)})^2\exp(-i2m\varphi) + 2\zeta^{(+)}\zeta^{(-)}]\exp(i2\theta) \\ + 2\zeta^{(+)}\overline{\zeta^{(-)}}\exp(i2m\varphi) + (|\zeta^{(+)}|^2 + |\zeta^{(-)}|^2) + (\text{c.c.})\};\end{gathered} \tag{24}$$

$$\begin{gathered}\int_{z_0}^{z_0+\lambda}\int_0^{2\pi}\frac{\partial\Phi^{(2)}}{\partial r}d\varphi dz \\ = -4\pi^2\lambda\chi[k^2 + m^2 - 4H_m(k)](|\zeta^{(+)}|^2 + |\zeta^{(-)}|^2);\end{gathered} \tag{25}$$

$$\int_{z_0}^{z_0+\lambda}\int_0^{2\pi}\xi^{(2)}d\varphi dz = -\pi\lambda(|\zeta^{(+)}|^2 + |\zeta^{(-)}|^2). \tag{26}$$

All missing notation is given in Appendix B. When deriving Eq. (25), we used the recurrent relation

$$K''_m(k) = \left(1 + \frac{m^2}{k^2}\right)K_m(k) - \frac{1}{k}K'_m(k).$$

Let us obtain a second-order partial solution of the problem satisfying Eqs. (2) and (3) for functions $\Psi^{(2)}$ and $\Phi^{(2)}$, as well as the set of equations (22)–(26). The form of inhomogeneity functions in Eqs. (22)–(24) determines the character of dependence of the sought solution on coordinate φ and argument θ. On this basis, we assume that

$$\begin{gathered}\xi^{(2)}(\varphi, z, T_0) = A_0 + [A_1^{(+)}\exp(im\varphi) + A_1^{(-)}\exp(-im\varphi)] \\ \times\exp(i\theta) + [A_2 + A_2^{(+)}\exp(i2m\varphi) + A_2^{(-)}\exp(-i2m\varphi)] \\ \times\exp(i2\theta) + A_3\exp(i2m\varphi) + (\text{c.c.});\end{gathered} \tag{27}$$

$$\begin{gathered}\Psi^{(2)}(r, \varphi, z, T_0) = B_0F_0(r) + [B_1^{(+)}F_1^{(+)}(r)\exp(im\varphi) \\ + B_1^{(-)}F_1^{(-)}(r)\exp(-im\varphi)]\exp(i\theta) + [B_2F_2(r) \\ + B_2^{(+)}F_2^{(+)}(r)\exp(i2m\varphi) + B_2^{(-)}F_2^{(-)}(r)\exp(-i2m\varphi)] \\ \times\exp(i2\theta) + B_3F_3(r)\exp(i2m\varphi) + (\text{c.c.});\end{gathered} \tag{28}$$

$$\begin{aligned}\Phi^{(2)}(r, \varphi, z, T_0) &= D_0C_0(r) + [D_1^{(+)}C_1^{(+)}(r)\exp(im\varphi)\\ &+ D_1^{(-)}C_1^{(-)}(r)\exp(-im\varphi)]\exp(i\theta) + [D_2C_2(r)\\ &+ D_2^{(+)}C_2^{(+)}(r)\exp(i2m\varphi) + D_2^{(-)}C_2^{(-)}(r)\exp(-i2m\varphi)]\\ &\times\exp(i2\theta) + D_3C_3(r)\exp(i2m\varphi) + (\text{c.c.}).\end{aligned} \tag{29}$$

The form of functions $\Psi^{(2)}$ and $\Phi^{(2)}$ of coordinate r we find from the Laplace equations. Substituting Eqs. (28) and (29) into relations (2) and equating the sums of coefficients of exponents with various powers to zero, we obtain ordinary differential equations for each of functions $F_j^{(\pm)}(r)$ and $C_j^{(\pm)}(r)$; $j = 0, 1, 2, 3$. Solutions to these equations, subject to conditions of boundedness (3), allows one to render expressions (28) and (29) for the potentials in the form

$$\begin{aligned}\Psi^{(2)}(r, \varphi, z, T_0) &= B_0 + [B_1^{(+)}\exp(im\varphi) + B_1^{(-)}\exp(-im\varphi)]\\ &\times I_m(kr)\exp(i\theta) + [B_2I_0(2kr) + (B_2^{(+)}\exp(i2m\varphi)\\ &+ B_2^{(-)}\exp(-i2m\varphi))I_{2m}(2kr)]\exp(i2\theta)\\ &+ B_3r^{2m}\exp(i2m\varphi) + (\text{c.c.});\end{aligned} \tag{30}$$

$$\begin{aligned}\Phi^{(2)}(r, \varphi, z, T_0) &= D_0\ln r + [D_1^{(+)}\exp(im\varphi)\\ &+ D_1^{(-)}\exp(-im\varphi)]K_m(kr)\exp(i\theta)\\ &+ [D_2K_0(2kr) + (D_2^{(+)}\exp(i2m\varphi)\\ &+ D_2^{(-)}\exp(-i2m\varphi))K_{2m}(2kr)]\exp(i2\theta)\\ &+ D_3r^{-2m}\exp(i2m\varphi) + (\text{c.c.}).\end{aligned} \tag{31}$$

Coefficients $A_j^{(\pm)}$, $B_j^{(\pm)}$, and $D_j^{(\pm)}$ are determined from the set of equations (22)–(26). Note that B_0 may be a function of time chosen in a convenient form for writing the solution since this function has no physical meaning. From the condition of conservation of the volume (26) and charge (25), it is not difficult to find

$$\begin{aligned}A_0 &= -\frac{1}{2}(|\zeta^{(+)}|^2 + |\zeta^{(-)}|^2);\\ D_0 &= -2\pi\chi(k^2 + m^2)(|\zeta^{(+)}|^2 + |\zeta^{(-)}|^2).\end{aligned} \tag{32}$$

Substituting (27) and (30) into kinematic boundary condition (22) and equating the coefficients of the same exponents on the left- and right-hand sides of the equality to each other, we obtain

$$\begin{aligned}kI'_m(k)B_1^{(\pm)} + i\omega_m(k)A_1^{(\pm)} &= \frac{\partial\zeta^{(\pm)}}{\partial T_1};\\ 2kI'_m(2k)B_2^{(\pm)} + i2\omega_m(k)A_2^{(\pm)} &= iX_1(\zeta^{(\pm)})^2;\\ 2kI'_0(2k)B_2 + i2\omega_m(k)A_2 &= iX_22\zeta^{(+)}\zeta^{(-)};\\ B_3 &= 0.\end{aligned} \tag{33}$$

Analogously to the above, employing Eqs. (27) and (31), from condition (24) of equipotentiality of the jet surface, we obtain the following set of equalities:

$$\begin{aligned}K_m(k)D_1^{(\pm)} - 4\pi\chi A_1^{(\pm)} &= 0;\\ K_{2m}(2k)D_2^{(\pm)} - 4\pi\chi A_2^{(\pm)} &= L(\zeta^{(\pm)})^2;\\ K_0(2k)D_2 - 4\pi\chi A_2 &= L2\zeta^{(+)}\zeta^{(-)};\\ D_3 - 4\pi\chi A_3 &= L2\zeta_+\overline{\zeta_-};\\ \Phi_S^{(2)} &= 4\pi\chi(1 + H_m(k))(|\zeta^{(+)}|^2 + |\zeta^{(-)}|^2).\end{aligned} \tag{34}$$

Let us note that when deriving the expression for the second-order correction to surface potential $\Phi_S^{(2)}$, we used expressions (32).

Lastly, substituting Eqs. (27), (30), and (31) into dynamic boundary condition (23) subject to (32) gives

$$\begin{aligned}&(1 - k^2 - m^2 - 4\pi\chi^2)A_1^{(\pm)} + i\omega_m(k)I_m(k)B_1^{(\pm)}\\ &\quad - \chi kK'_m(k)D_1^{(\pm)} = -i\frac{\omega_m(k)}{G_m(k)}\frac{\partial\zeta^{(\pm)}}{\partial T_1};\\ &(1 - 4k^2 - 4m^2 - 4\pi\chi^2)A_2^{(\pm)} + i2\omega_m(k)I_{2m}(2k)B_2^{(\pm)}\\ &\quad - \chi 2kK'_{2m}(2k)D_2 = Y_1(\zeta^{(\pm)})^2;\\ &(1 - 4k^2 - 4\pi\chi^2)A_2 + i2\omega_m(k)I_0(2k)B_2\\ &\quad - \chi 2kK'_0(2k)D_2^{(\pm)} = Y_22\zeta_+\zeta_-;\\ &(1 - 4m^2 - 4\pi\chi^2)A_3 + 2m\chi D_3 = Y_32\zeta^{(+)}\overline{\zeta^{(-)}};\\ &\frac{\partial B_0}{\partial T_0} = -\left[Y_4 + \frac{1}{2} - 2\pi\chi^2(k^2 + m^2 + 1)\right](|\zeta^{(+)}|^2 + |\zeta^{(-)}|^2).\end{aligned} \tag{35}$$

Finding the form of function B_0 (see the last equality (35)) is only of theoretical importance because the potential is determined to an accuracy of an arbitrary additive function depending only on time [17].

Solving the set of equations (33)–(35) simultaneously allows one to determine the sought coefficients. Consider the first equalities in the sets written. Expressing coefficients $B_1^{(\pm)}$ using (33) and coefficients $D_1^{(\pm)}$ using (34), and substituting the result into (35), we obtain

$$\begin{aligned}&\left[1 - k^2 - m^2 - 4\pi\chi^2(1 + H_m(k)) + \frac{\omega_m^2(k)}{G_m(k)}\right]A_1^{(\pm)}\\ &\quad = -i2\frac{\omega_m(k)}{G_m(k)}\frac{\partial\zeta^{(\pm)}}{\partial T_1}.\end{aligned}$$

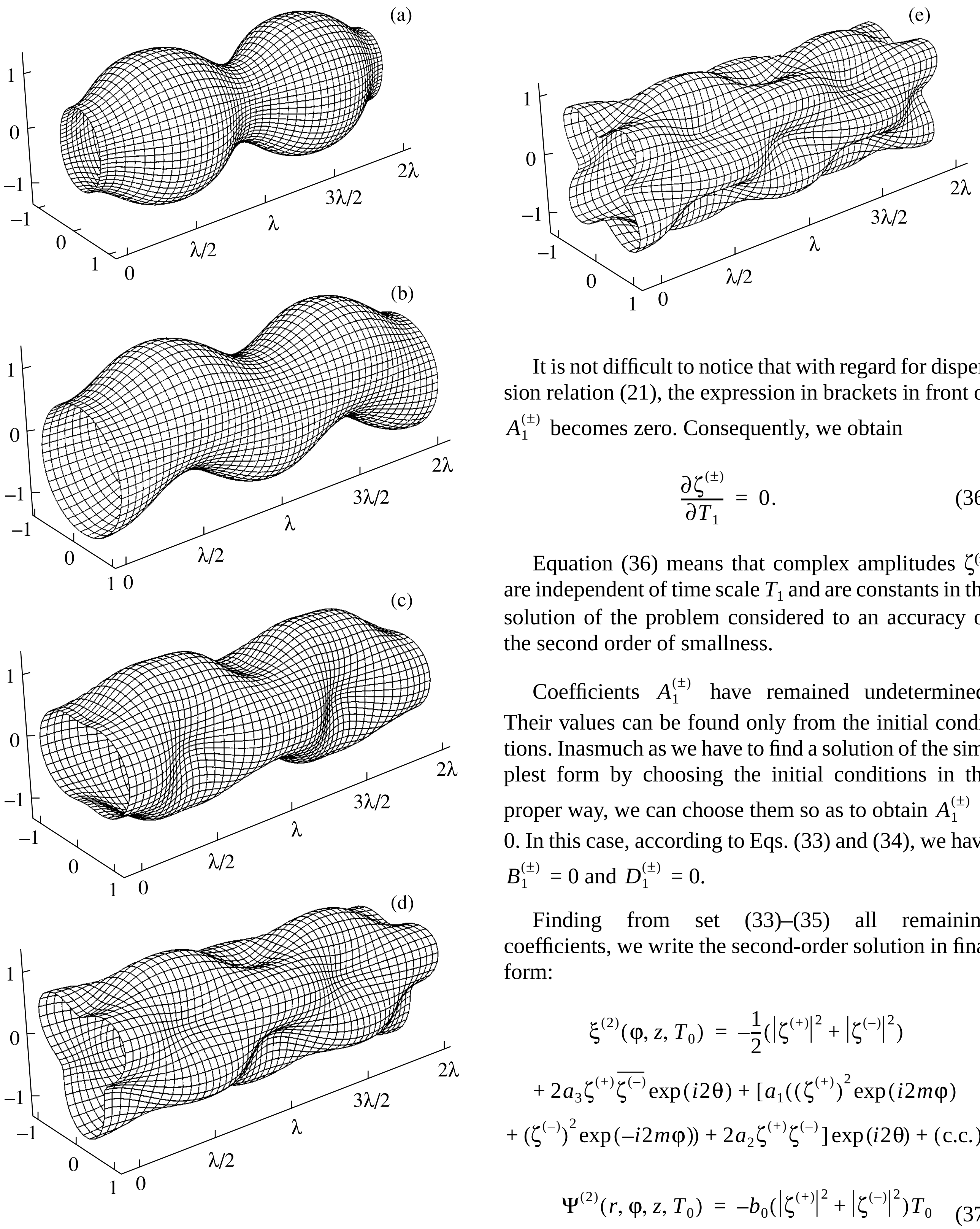

Fig. 1. Surface shape of nonlinearly oscillating jets at subcritical magnitudes of the surface density of the self-charge in the sense of jet stability. The calculations are conducted at $\varepsilon = 0.3$, $k = 2$; (a) $W = 0.5$, $m = 0$; (b) $W = 1$, $m = 1$; (c) $W = 1$, $m = 2$; (d) $W = 1$, $m = 3$; (e) $W = 1$, $m = 4$.

It is not difficult to notice that with regard for dispersion relation (21), the expression in brackets in front of $A_1^{(\pm)}$ becomes zero. Consequently, we obtain

$$\frac{\partial \zeta^{(\pm)}}{\partial T_1} = 0. \tag{36}$$

Equation (36) means that complex amplitudes $\zeta^{(\pm)}$ are independent of time scale T_1 and are constants in the solution of the problem considered to an accuracy of the second order of smallness.

Coefficients $A_1^{(\pm)}$ have remained undetermined. Their values can be found only from the initial conditions. Inasmuch as we have to find a solution of the simplest form by choosing the initial conditions in the proper way, we can choose them so as to obtain $A_1^{(\pm)} = 0$. In this case, according to Eqs. (33) and (34), we have $B_1^{(\pm)} = 0$ and $D_1^{(\pm)} = 0$.

Finding from set (33)–(35) all remaining coefficients, we write the second-order solution in final form:

$$\begin{aligned}
\xi^{(2)}(\varphi, z, T_0) &= -\frac{1}{2}(|\zeta^{(+)}|^2 + |\zeta^{(-)}|^2) \\
&+ 2a_3\zeta^{(+)}\overline{\zeta^{(-)}}\exp(i2\theta) + [a_1((\zeta^{(+)})^2\exp(i2m\varphi) \\
&+ (\zeta^{(-)})^2\exp(-i2m\varphi)) + 2a_2\zeta^{(+)}\zeta^{(-)}]\exp(i2\theta) + (\text{c.c.});
\end{aligned}$$

$$\begin{aligned}
\Psi^{(2)}(r, \varphi, z, T_0) &= -b_0(|\zeta^{(+)}|^2 + |\zeta^{(-)}|^2)T_0 \\
&- i[b_1((\zeta^{(+)})^2\exp(i2m\varphi) + (\zeta^{(-)})^2\exp(-i2m\varphi)) \\
&\times I_{2m}(2kr) + 2b_2\zeta^{(+)}\zeta^{(-)}I_0(2kr)]\exp(i2\theta) + (\text{c.c.}); \\
\Phi^{(2)}(r, \varphi, z, T_0) &= -2\pi\chi(k^2 + m^2)(|\zeta^{(+)}|^2 + |\zeta^{(-)}|^2)\ln r
\end{aligned} \tag{37}$$

$$+[d_1((\zeta^{(+)})^2\exp(i2m\varphi)+(\zeta^{(-)})^2\exp(-i2m\varphi))$$
$$\times K_{2m}(2kr)+2d_2\zeta^{(+)}\zeta^{(-)}K_0(2kr)]\exp(i2\theta)$$
$$+2d_3\zeta^{(+)}\overline{\zeta^{(-)}}\exp(i2\varphi)+(\text{c.c.});$$

all newly introduced notation is given in Appendix C.

Thus, the solutions of the problem considered to the second order of accuracy are defined by expressions (1), (9), (11), (17), (20), (21), (36), and (37).

4. According to the above arguments, the jet shape as a function of time is defined by the expression

$$r(z,\varphi,t) = 1+\varepsilon\cos(m\varphi)\cos(\theta)$$
$$-\frac{\varepsilon^2}{4}\left[\frac{1}{2}-(a_1\cos(2m\varphi)+a_2)\cos(2\theta)-a_3\cos(2\varphi)\right].$$

Calculations with the help of Matematica program package for analytical calculations with the use of the above equation at $\varepsilon = 0.3$ and subcritical values of parameter $W \equiv 4\pi\chi^2$ in terms of development of instability with respect to the surface charge is illustrated by Fig. 1. For the first five modes ($m = 0, 1, 2, 3, 4$), three-dimensional images of the surfaces of nonlinearly oscillating jets are presented for $t = 0.5T$, where T is the period of waves (the critical magnitude of W for a fixed m is found from the requirement of vanishing of the square of the frequency in dispersion equation (21) [11, 12]). In Fig. 1, it is seen that monodisperse disintegration of jets is the most probable for axisymmetric jets ($m = 0$). As for excitation of the whip-shaped motion of jets [11, 12], the odds are that it is associated with instability of the mode with $m = 1$. When instability of nonsymmetrical waves with $m \geq 2$ develops, the probability of polydisperse disintegration of a jet increases precisely as it is observed in natural conditions upon spontaneous disintegration of strongly charged jets (the latter is a necessary condition for ensuring the instability of nonaxisymmetric modes) [11, 12]. How an increase in the surface charge density in a jet influences its shape is illustrated in Fig. 2, where the shapes of the surfaces of nonaxisymmetric jets with $m = 1, 2, 3, 4$ are shown for $t = 0.5T$ at $\varepsilon = 0.3$ when the surface charge density is close to the critical value for the mode considered. It is seen that the wave amplitudes grow with increasing surface density of electric charge, and the probability of precisely polydisperse disintegration at $m \geq 2$ becomes more obvious. A large magnitude of small parameter $\varepsilon = 0.3$ employed in the calculations for plotting Figs. 1 and 2 is chosen for better visualization.

From the above equation for the jet shape, it is readily seen that, in addition to a wave with wave number k existing at the initial instant, a wave with the double wave number $2k$ is also excited. Between these two waves resonance interaction takes place, which is determined by the denominators of coefficients a_1 and a_2 that vanish under certain conditions [18–20]. Studying the

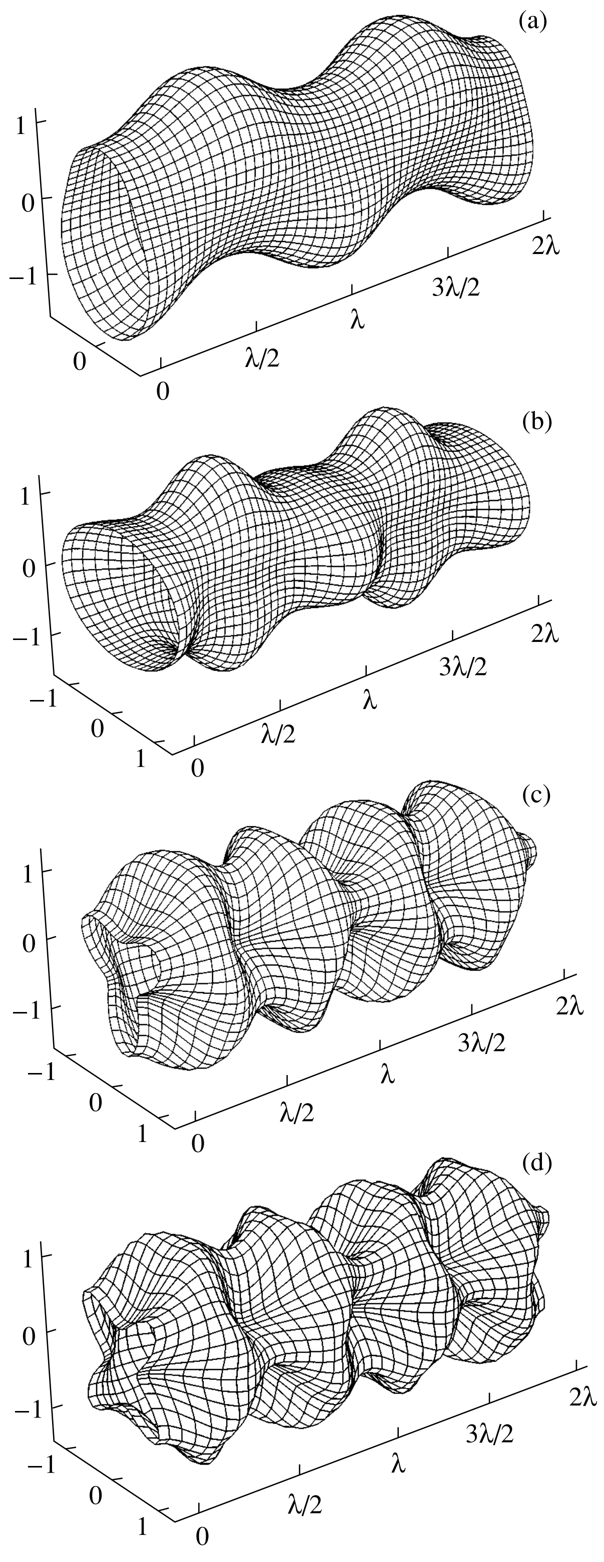

Fig. 2. Surface shape of nonlinearly oscillating jets at $\varepsilon = 0.3$ and $k = 2$ in the case when the surface density of the jet self-charge is close to critical for a given mode: (a) $W = 2.456$, $m = 1$; (b) $W = 3.329$, $m = 2$; (c) $W = 4$, $m = 3$; (d) $W = 5.25$, $m = 4$.

resonant interaction of cylindrical waves is a subject of a separate investigation; here, it is interesting to note that under the resonant interaction of nonlinear oscillations and waves, the total energy exchange between them is possible [20, 21].In addition, it is remarkable that the resonant interaction occurs between waves with different wave and azimuthal numbers (that is, with different symmetries) as is seen from the expression for coefficients a_1 and a_2. How surface density χ of the electric charge at a jet affects the mechanism of development of resonant interaction is reduced to variation of the resonance position (to changes in the wave numbers and azimuthal parameters of the interacting waves with variation of χ). Away from the resonant positions, the influence of the electric charge at the jet surface is reduced to a possibility of development of instability of nonaxisymmetric modes at sufficiently high charge densities (at $4\pi\chi^2 \geq 1$) [11, 12]. It should be recalled that with zero charge (at $\chi = 0$), all nonaxisymmetric modes are stable [1]; this follows from dispersion equation (21). The influence of the (surface or volume) charge on the jet shape is manifested in dependences of coefficients a_j on charge density χ. These coefficients determine the second-order deviation of the jet shape from a cylindrical one.

There are no corrections to the frequencies in the second approximations with respect to the wave frequency analyzed above; these corrections may appear only in the next, third approximation [20, 22, 23]. Therefore, in the present analysis, the critical conditions of instability development of a nonaxisymmetric jet in the sense of its disintegration into separate drops are determined in the frame of a linear approximation by the condition of the square of frequency (21) passing through zero into the region of negative values, as described in [11, 12]. However, it should be noted that corrections to the critical conditions of instability development associated with nonlinear interaction of waves cannot be important and cannot lead to a noticeable change in the existing concepts on the development of instability of the jet surface because these corrections are of the second order of smallness (see, for example, nonlinear analyses of the third order of smallness conducted earlier for charged spherical drops and a charged plane liquid surface [22, 24, 25]).

CONCLUSIONS

The solution of the problem on calculating nonlinear oscillations of a charged jet even in the second order of smallness with respect to the amplitude of deformation of an unperturbed cylindrical jet reveals the resonant interaction between the wave determining the initial virtual deformation and the wave with the double wave number, which emerges as a result of nonlinearity of equations of hydrodynamics. Conditions for the emergence of the resonant situations are dependent on the surface density of the electric charge of a jet.

APPENDIX A

The set of boundary and additional conditions of the second order of smallness

$$\begin{aligned} r = 1:\ & \frac{\partial \Psi^{(2)}}{\partial r} - \frac{\partial \xi^{(2)}}{\partial T_0} = \frac{\partial \xi^{(1)}}{\partial T_1} - \frac{\partial^2 \Psi^{(1)}}{\partial r^2}\xi^{(1)} \\ & + \frac{\partial \Psi^{(1)}}{\partial \varphi}\frac{\partial \xi^{(1)}}{\partial \varphi} + \frac{\partial \Psi^{(1)}}{\partial z}\frac{\partial \xi^{(1)}}{\partial z}; \end{aligned} \tag{A.1}$$

$$\begin{aligned} & -\frac{\partial \Psi^{(2)}}{\partial T_0} + \frac{1}{8\pi}\left\{2\frac{\partial \Phi^{(0)}}{\partial r}\frac{\partial \Phi^{(2)}}{\partial r} + \frac{\partial}{\partial r}\left[\left(\frac{\partial \Phi^{(0)}}{\partial r}\right)^2\right]\xi^{(2)}\right\} \\ & + \xi^{(2)} + \frac{\partial^2 \xi^{(2)}}{\partial \varphi^2} + \frac{\partial^2 \xi^{(2)}}{\partial z^2} = \frac{\partial \Psi^{(1)}}{\partial T_1} + \frac{\partial^2 \Psi^{(1)}}{\partial r \partial T_0}\xi^{(1)} \\ & + \frac{1}{2}\left[\left(\frac{\partial \Psi^{(1)}}{\partial r}\right)^2 + \left(\frac{\partial \Psi^{(1)}}{\partial \varphi}\right)^2 + \left(\frac{\partial \Psi^{(1)}}{\partial z}\right)^2\right] \\ & - \frac{1}{8\pi}\left\{2\frac{\partial}{\partial r}\left[\frac{\partial \Phi^{(0)}}{\partial r}\frac{\partial \Phi^{(1)}}{\partial r}\right]\xi^{(1)} + \frac{1}{2}\frac{\partial^2}{\partial r^2}\left[\left(\frac{\partial \Phi^{(0)}}{\partial r}\right)^2\right](\xi^{(1)})^2 \right. \\ & \left. + \left(\frac{\partial \Phi^{(1)}}{\partial r}\right)^2 + \left(\frac{\partial \Phi^{(1)}}{\partial \varphi}\right)^2 + \left(\frac{\partial \Phi^{(1)}}{\partial z}\right)^2\right\} + (\xi^{(1)})^2 \\ & + \frac{1}{2}\left[\left(\frac{\partial \xi^{(1)}}{\partial \varphi}\right)^2 - \left(\frac{\partial \xi^{(1)}}{\partial z}\right)^2 + 2\xi^{(1)}\frac{\partial^2 \xi^{(1)}}{\partial \varphi^2}\right]; \end{aligned} \tag{A.2}$$

$$\begin{aligned} & \Phi^{(2)} - \frac{\partial \Phi^{(0)}}{\partial r}\xi^{(2)} \\ & = \Phi_S^{(2)}(t) - \frac{\partial \Phi^{(1)}}{\partial r}\xi^{(1)} - \frac{1}{2}\frac{\partial^2 \Phi^{(0)}}{\partial r^2}(\xi^{(1)})^2; \end{aligned} \tag{A.3}$$

$$\begin{aligned} & \int_{z_0}^{z_0+\lambda}\int_0^{2\pi}\left[\frac{\partial \Phi^{(2)}}{\partial r} + \frac{\partial}{\partial r}\left(r\frac{\partial \Phi^{(0)}}{\partial r}\right)\xi^{(2)}\right]d\varphi dz \\ & = -\int_{z_0}^{z_0+\lambda}\int_0^{2\pi}\left[\frac{\partial}{\partial r}\left(r\frac{\partial \Phi^{(1)}}{\partial r}\right)\xi^{(1)} - \frac{\partial \Phi^{(1)}}{\partial \varphi}\frac{\partial \xi^{(1)}}{\partial \varphi}\right. \\ & - \frac{\partial \Phi^{(1)}}{\partial z}\frac{\partial \xi^{(1)}}{\partial z} + \frac{1}{2}\left[\frac{\partial^2}{\partial r^2}\left(r\frac{\partial \Phi^{(0)}}{\partial r}\right)(\xi^{(1)})^2\right. \\ & \left.\left. - \frac{\partial \Phi^{(0)}}{\partial r}\left(\frac{\partial \xi^{(1)}}{\partial \varphi}\right)^2 - \frac{\partial \Phi^{(0)}}{\partial r}\left(\frac{\partial \xi^{(1)}}{\partial z}\right)^2\right]\right]d\varphi dz; \end{aligned} \tag{A.4}$$

$$\int_{z_0}^{z_0+\lambda}\int_0^{2\pi}\xi^{(2)}d\varphi dz = -\frac{1}{2}\int_{z_0}^{z_0+\lambda}\int_0^{2\pi}(\xi^{(1)})^2 d\varphi dz. \tag{A.5}$$

APPENDIX B

Expressions for the coefficients in boundary and additional conditions (22)–(26)

$$X_1 = \frac{\omega_m(k)}{G_m(k)}[2(k^2+m^2) - G_m(k)];$$

$$X_2 = \frac{\omega_m(k)}{G_m(k)}[2k^2 - G_m(k)];$$

$$Y_1 = 1 + \frac{1}{2}(k^2 - 5m^2) + \frac{\omega_m^2(k)}{2(G_m(k))^2}[k^2 + m^2 - 3(G_m(k))^2]$$

$$+ 2\pi\chi^2[3k^2 + 3m^2 - 3 - 4H_m(k) - (H_m(k))^2];$$

$$Y_2 = 1 + \frac{1}{2}(k^2 - 3m^2) + \frac{\omega_m^2(k)}{2(G_m(k))^2}[k^2 - m^2 - 3(G_m(k))^2]$$

$$+ 2\pi\chi^2[3k^2 + m^2 - 3 - 4H_m(k) - (H_m(k))^2];$$

$$Y_3 = 1 - \frac{1}{2}(k^2 + 5m^2) + \frac{\omega_m^2(k)}{2(G_m(k))^2}[k^2 - m^2 - (G_m(k))^2]$$

$$+ 2\pi\chi^2[k^2 + 3m^2 - 3 - 4H_m(k) - (H_m(k))^2];$$

$$Y_4 = 1 - \frac{1}{2}(k^2 + 3m^2) + \frac{\omega_m^2(k)}{2(G_m(k))^2}[k^2 + m^2 - (G_m(k))^2]$$

$$+ 2\pi\chi^2[k^2 + m^2 - 3 - 4H_0(k) - (H_m(k))^2];$$

$$L = -2\pi\chi[1 + 2H_m(k)].$$

APPENDIX C

Notations used when deriving the solution of the second order of smallness

$$a_1 \equiv \frac{G_{2m}(2k)[Y_1 + \chi L H_{2m}(2k)] + 2\omega_m(k)X_1}{4\omega_m^2(k) - \omega_{2m}^2(2k)};$$

$$a_2 \equiv \frac{G_0(2k)[Y_2 + \chi L H_0(2k)] + 2\omega_m(k)X_2}{4\omega_m^2(k) - \omega_0^2(2k)};$$

$$a_3 \equiv \frac{Y_3 - 2m\chi L}{(1-2m)(1+2m-4\pi\chi)^2};$$

$$b_0 \equiv Y_4 + \frac{1}{2} - 2\pi\chi^2(k^2 + m^2 + 1);$$

$$b_1 \equiv \frac{2\omega_m(k)[Y_1 + \chi L H_{2m}(2k)] + [4k^2 + 4m^2 - 1 + 4\pi\chi^2(1 + H_{2m}(2k))]X_1}{I_{2m}(2k)[4\omega_m^2(k) - \omega_{2m}^2(2k)]};$$

$$b_2 \equiv \frac{2\omega_m(k)[Y_2 + \chi L H_0(2k)] + [4k^2 - 1 + 4\pi\chi^2(1 + H_0(2k))]X_2}{I_0(2k)[4\omega_m^2(k) - \omega_0^2(2k)]};$$

$$d_1 \equiv \frac{G_{2m}(2k)[4\pi\chi Y_1 - (4k^2 + 4m^2 - 1 + 4\pi\chi^2)L] + 2\omega_m(k)[4\pi\chi X_1 + 2\omega_m(k)L]}{K_{2m}(2k)[4\omega_m^2(k) - \omega_{2m}^2(2k)]};$$

$$d_2 \equiv \frac{G_0(2k)[4\pi\chi Y_2 - (4k^2 - 1 + 4\pi\chi^2)L] + 2\omega_m(k)[4\pi\chi X_2 + 2\omega_m(k)L]}{K_0(2k)[4\omega_m^2(k) - \omega_0^2(2k)]};$$

$$d_3 \equiv \frac{4\pi\chi Y_3 - (4m^2 - 1 + 4\pi\chi^2)L}{(1-2m)(1+2m-4\pi\chi^2)}.$$

ACKNOWLEDGMENTS

This study was supported by the Russian Foundation for Basic Research, project no. 03-01-00760.

REFERENCES

1. *Monodispersion of Substances: Principles and Application*, Ed. by E. V. Ametistov, V. V. Blazhenkov, A. K. Gorodov, *et al.* (Énergoatomizdat, Moscow, 1991) [in Russian].
2. V. M. Entov and L. E. Shmar'yan, Izv. Ross. Akad. Nauk, Mekh. Zhidk. Gaza, No. 5, 97 (1997).
3. A. A. Shutov and A. A. Zakhar'yan, Prikl. Mekh. Tekh. Fiz. **39** (4), 12 (1998).
4. N. A. Razumovskiĭ and Yu. G. Chesnokov, Izv. Ross. Akad. Nauk, Mekh. Zhidk. Gaza, No. 6, 97 (1999).
5. V. N. Gorshkov and M. G. Chaban, Zh. Tekh. Fiz. **69** (11), 1 (1999) [Tech. Phys. **44**, 1259 (1999)].
6. N. M. Zubarev, Zh. Éksp. Teor. Fiz. **116**, 1990 (1999) [JETP **89**, 1078 (1999)].
7. Yu. G. Chesnokov, Zh. Tekh. Fiz. **70** (8), 31 (2000) [Tech. Phys. **45**, 987 (2000)].
8. Yu. G. Chesnokov, Prikl. Mekh. Tekh. Fiz. **42** (3), 56 (2001).
9. M. N. Hohman, M. Shin, G. Rutledge, and M. P. Brenner, Phys. Fluids **13**, 2201 (2001).
10. J. W. Strutt (Lord Rayleigh), *The Theory of Sound*, 2nd ed. (Macmillan, London, 1896; Gostekhizdat, Moscow, 1955).

11. S. O. Shiryaeva, A. I. Grigor'ev, T. V. Levchuk, and M. V. Rybakova, Zh. Tekh. Fiz. **73** (5), 5 (2003) [Tech. Phys. **48**, 527 (2003)].
12. S. O. Shiryaeva, A. I. Grigor'ev, and T. V. Levchuk, Zh. Tekh. Fiz. **73** (11), 22 (2003) [Tech. Phys. **48**, 1380 (2003)].
13. F. H. Nayfeh, Phys. Fluids **4**, 841 (1970).
14. D. F. Belonozhko and A. I. Grigor'ev, Zh. Tekh. Fiz. **73** (11), 37 (2003) [Tech. Phys. **48**, 1396 (2003)].
15. F. H. Nayfeh, J. Fluid Mech. **48**, 385 (1971).
16. M. Abramovitz and I. A. Stegun, *Handbook of Mathematical Functions* (Dover, New York, 1971; Nauka, Moscow, 1979).
17. L. D. Landau and E. M. Lifshitz, *Course of Theoretical Physics*, Vol. 6: *Fluid Mechanics* (Nauka, Moscow, 1986; Pergamon, New York, 1987).
18. S. O. Shiryaeva, Zh. Tekh. Fiz. **73** (2), 19 (2003) [Tech. Phys. **48**, 152 (2003)].
19. D. F. Belonozhko and A. I. Grigor'ev, Pis'ma Zh. Tekh. Fiz. **29** (8), 1 (2003) [Tech. Phys. Lett. **29**, 309 (2003)].
20. A. N. Zharov, A. I. Grigor'ev, and S. O. Shiryaeva, Pis'ma Zh. Tekh. Fiz. **29** (9), 75 (2003) [Tech. Phys. Lett. **29**, 388 (2003)].
21. S. O. Shiryaeva, Pis'ma Zh. Tekh. Fiz. **29** (17), 28 (2003) [Tech. Phys. Lett. **29**, 714 (2003)].
22. A. N. Zharov, S. O. Shiryaeva, and A. I. Grigor'ev, Zh. Tekh. Fiz. **73** (6), 36 (2003) [Tech. Phys. **48**, 697 (2003)].
23. A. N. Zharov, S. O. Shiryaeva, and A. I. Grigor'ev, Zh. Tekh. Fiz. **73** (12), 9 (2003) [Tech. Phys. **48**, 1511 (2003)].
24. J. A. Tsamopoulos and R. A. Brown, J. Fluid Mech. **147**, 373 (1984).
25. D. F. Belonozhko, A. V. Klimov, and A. I. Grigor'ev, Pis'ma Zh. Tekh. Fiz. **29** (24), 41 (2003) [Tech. Phys. Lett. **29**, 1031 (2003)].

Translated by N. Mende

Technical Physics, Vol. 49, No. 8, 2004, pp. 967–972. Translated from Zhurnal Tekhnicheskoĭ Fiziki, Vol. 74, No. 8, 2004, pp. 15–20.
Original Russian Text Copyright © 2004 by Buryakov.

GASES
AND LIQUIDS

Determination of Kinetic Transport Coefficients for Ions in Air as Functions of Electric Field and Temperature

I. A. Buryakov

Design and Technology Institute of Instrument Engineering for Geophysics and Ecology,
Siberian Division, Russian Academy of Sciences, Novosibirsk, 630090 Russia
e-mail: buryakov@uiggm.nsc.ru

Received September 15, 2003; in final form, January 23, 2004

Abstract—A method for determining the kinetic coefficients of ion transfer in gases, viz., mobility K and longitudinal (D_L) and transverse (D_T) diffusion coefficients, as functions of the electric field E and gas temperature T is described. The method is based on the measurement of the increments to the ion mobility coefficients as functions of the electric field at a parametrically specified temperature. The kinetic transport coefficients $K(E, T)$ and $D_{L,\,T}(E, T)$ are determined for positive ions of aniline, pyridine, benzene, orthotoluidine, dimethyl methyl phosphonate, N-methyl aniline, N,N-dimethyl aniline, N,N-diethyl aniline, and diphenyl amine (DPA) formed as a result of β-ionization in air. *© 2004 MAIK "Nauka/Interperiodica".*

INTRODUCTION

The main kinetic transport coefficients for ions in a gas in an electric field are the coefficients of mobility K and diffusion D for ions, which depend on the effective temperature, the increment of the coefficient of mobility, and the collision integral. The experimental values of these quantities, especially their dependence on the gas temperature T and on the electric field reduced to the number density of particles (E/N) may provide information on the potential of interaction between an ion and a gas particle as well as on the cross sections of elastic, inelastic, and reaction-induced collisions of particles. Information about the mobility and diffusion of ion is essential for a qualitative description of electric gas discharges, for calculating the ion–ion recombination coefficients, and for analyzing the results of experiments on plasma chemical reactions [1, 2]. In addition, information on the dependences $K(E/N, T)$ and $D(E/N, T)$ is required for solving applied problems (e.g., for determining analytic characteristics and fields of application of ion mobility increment spectrometers [3]). In the latter devices, ions are separated according to the dependence of the mobility coefficients on the electric field strength at the temperature and pressure of ambient air.

To calculate the kinetic transport coefficients for ions, the moments method is used, in which these coefficients are determined in terms of the expansion coefficients and the moments of the ion distribution function as well as the integrated scattering cross sections for particles. As a test function, the Maxwell distribution function shifted by the ion drift velocity in the direction of the electric field is used; in this case, the longitudinal and transverse temperatures of ions are variable parameters. This approach is known as the three-temperature theory of ion mobility.

This research is aimed at analysis of the increment of the mobility coefficients as a function of the gas temperature and the electric field reduced to the number density of particles, $\alpha(E/N, T)$, for positive ions of aniline, pyridine, benzene, orthotoluidine (o-TLD), dimethyl methyl phosphonate (DMMP), N-methyl aniline (MA), N,N-dimethyl aniline (DMA), N,N-diethyl aniline (DEA), and diphenyl amine (DPA) formed as a result of β-ionization in air. These dependences are used to determine the collision integrals, mobility coefficients, and longitudinal and transverse diffusion coefficients of ions as a function of the electric field and gas temperature.

EQUATIONS AND PARAMETRIC COEFFICIENTS FOR CALCULATING THE KINETIC TRANSPORT COEFFICIENTS FOR IONS

The equations for calculating the mobility coefficients as functions of parameters E, N, and T [1] have the form

$$K(E/N) \equiv V/E = K(0)(1+\alpha(E/N)), \qquad (1)$$

$$K(0) = \frac{3e}{16N}(2\pi/\mu k T_{\mathrm{eff}})^{1/2}\frac{1}{\bar{\Omega}^{(1,1)}(T_{\mathrm{eff}})}, \qquad (2)$$

$$3/2kT_{\mathrm{eff}} \approx 3/2kT + 1/2M(KE)^2, \qquad (3)$$

$$K_0 = K\frac{p}{760}\frac{273.15}{T} + K\frac{N}{N_0}, \qquad (4)$$

$$\alpha = \sum_{n=1}^{\infty} \alpha_{2n}(E/N)^{2n}, \tag{5}$$

where V is the drift velocity of ions, associated with the action of the electric field; $K(0)$ is the coefficient of ion mobility in a "weak" field ($E/N < 6$ Td is the "townsend," 1 Td = 10^{-17} V cm^2); $\alpha(E/N)$ is the increment of the mobility as a function of parameter E/N; e is the ion charge; N is the number density of neutrals in the gas; $\mu = mM/(m + M)$ is the reduced mass; m is the ion mass; M is the mass of a neutral gas particle; k is the Boltzmann constant; T_{eff} is the effective temperature; $\bar{\Omega}^{(1,1)}(T_{\mathrm{eff}})$ is the collision integral in the transport theory [1]; T is the gas temperature; p is the pressure; K_0 is the coefficient of mobility reduced to normal conditions (T = 273.15 K, p = 760 mmHg, and the Loschmidt number $N_0 = 2.687 \times 10^{19}$ cm^{-3}); and α_{2n} are the expansion coefficients in the power series.

The equations for calculating the longitudinal and transverse diffusion coefficients D_L and D_T as functions of parameters E, N, and T were derived using the generalized Einstein equations [1]. Since the ion diffusion coefficients depend on the number density of gas particles via the ratio $1/N$, it is more convenient to use the product $ND_{L,T}$. In practical units, these expressions have the form [1]

$$\begin{gathered} ND_L \approx 2.32 \times 10^{15} K_0 T_L(1 + (1 + \Delta_L)K'), \\ ND_T \approx 2.32 \times 10^{15} K_0 T_T(1 + \Delta_T K'/(1 + K')), \end{gathered} \tag{6}$$

$$K' = \frac{d\ln K}{d\ln(E/N)}, \tag{7}$$

$$kT_{L,T} \approx kT + \gamma_{L,T} M(KE)^2(1 + \beta_{L,T}K'), \quad \beta_T = 0,$$

$$\gamma_L = \frac{4m - (2m - M)A^*}{4m + 3MA^*}, \tag{8}$$

$$\gamma_T = \frac{(m + M)A^*}{4m + 3MA^*}, \quad A^* \approx 0.9.$$

TYPES OF IONS

When the substances being studied are ionized under atmospheric pressure, a protonated molecule $(m + \mathrm{H})^+$ (H is the hydrogen atom) formed in the proton-transfer reaction [4, 5]

$$(\mathrm{H_2O})_n\mathrm{H}^+ + m \longrightarrow (m + \mathrm{H})^+ + n\mathrm{H_2O}$$

is the main type of ions.

Table 1 contains the molecular mass of these substances, the coefficients of mobility $K_0(0)$ in a weak field [4, 6–8]; the collision integrals calculated with the help of Eq. (2) at T = 294 K; and the values of parametric coefficients Δ_L, Δ_T, β_L, depending on the relation between masses m and M and determined in terms of the collision integrals of the kinetic theory [1].

METHOD FOR DETERMINING DEPENDENCES $K(E/N, T)$ AND $D(E/N, T)$

To find the dependences $K(E/N, T)$ and $D(E/N, T)$, we must have information on the behavior of functions $\bar{\Omega}^{(1,1)}(T_{\mathrm{eff}})$ and $\alpha(E/N)$. Combining Eqs. (1)–(4), we obtain

$$\frac{1}{\bar{\Omega}^{(1,1)}(T_{\mathrm{eff}})} = \frac{1}{\bar{\Omega}^{(1,1)}(T)} \times \sqrt{1 + \frac{M}{3T}\left(N_0 K_0(0)(1 + \alpha)\frac{E}{N}\right)^2}. \tag{9}$$

Table 1. Molecular mass, reduced coefficients of mobility $K_0(0)$ in a weak field, collision integrals $\bar{\Omega}^{(1,1)}$, and dimensionless parametric coefficients Δ_L, Δ_T, and β_L

Substance	m, amu	$K_0(0)$, cm^2/Vs	$\bar{\Omega}^{(1,1)}(T)$, 10^{-14}, cm^2	Δ_L	Δ_T	β_L
Benzene	78.11	1.94	1.235*	0.088	0.098	0.92
DMMP	124.08	1.95	1.14	0.056	0.064	0.964
o-TLD	107.15	1.75	1.315*	0.065	0.076	0.954
MA	107.15	1.74	1.3	0.065	0.076	0.954
Pyridine	79.1	1.7	1.376	0.087	0.096	0.922
Aniline	93.13	1.81	1.232	0.074	0.086	0.941
DMA	121.18	1.81	1.23	0.057	0.065	0.963
DEA	149.23	1.7	1.287	0.045	0.043	0.972
DPA	169.22	1.54	1.407	0.04	0.031	0.979

* T_g = 283 K.

The only unknown in this equation is function $\alpha(E/N, T)$.

The method for determining the increment of the mobility coefficient $\alpha(E/N)$ with the help of a varying periodic solution that is asymmetric in the electric field polarity is described in detail in [9]. Under the action of such a field $E_d(t) = E_d f(t)$ (E_d is the field amplitude and $f(t)$ is the form of the field) described by the conditions

$$\int_{t}^{t+P} f(t)dt = 0, \quad \frac{1}{P}\int_{t}^{1+P} f^{2n+1}(t)dt \equiv \langle f^{2n+1}\rangle \neq 0 \quad (10)$$

($n \geq 1$ is an integer), ions of a definite type in the gas, which perform rapid vibrations with period P, drift along the field lines with the characteristic velocity $\langle V\rangle$ proportional to $\alpha(E/N)$. This velocity can be compensated ($\langle V\rangle = 0$) by a constant electric field E_c; in this case, the expression for the compensating field with allowance for expansion (5) has the form [10]

$$E_c \approx \left(E_d \sum_{n=1}^{\infty} \alpha_{2n}\left(\frac{E_d}{N}\right)^{2n} \langle f^{2n+1}\rangle\right) \Big/ \left(1 + \sum_{n=1}^{\infty} (2n+1)\alpha_{2n}\left(\frac{E_d}{N}\right)^{2n} \langle f^{2n}\rangle\right). \quad (11)$$

Having obtained the dependences $E_c(E_d/N)$ from experiments with various values of T and solving the inverse problem of Eq. (11), we obtain expansion coefficients α_{2n} and dependences $\alpha(E/N, T)$ from Eq. (5). Using $\alpha(E/N, T)$, we find $\overline{\Omega}^{(1,1)}(T_{\text{eff}})$ and determine dependences $K(E/N, T)$ and $ND_{L,T}(E/N, T)$ using Eqs. (1) and (6) and the data compiled in Table 1.

EXPERIMENTAL

The block diagram of the experimental setup shown in Fig. 1 contains heated ionization chamber *1* (β-source was ^{63}Ni, $T_i = 80$°C); drift chamber *3* formed between two coaxial cylindrical electrodes and ventilated with a carrier gas (purified dry air with a water vapor concentration of less than 100 ppm, a flow rate of $Q_g = 30$ cm^3/s, a temperature of $T = 21 \pm 1$°C, and a number density of $N = (2.5 \pm 0.1) \times 10^{19}$ cm^{-3}); system of electrodes *2* ensuring the transport of ions from the ionization chamber to the drift chamber; compensating voltage source *4*; generator *5* of periodic ac voltage asymmetric in polarity, connected to the coaxial electrodes; collector *6*; and electrometric amplifier *7* (with a noise amplitude of 2×10^{-14} A).

The generator parameters were as follows: the form of voltage is given by function $f(t)$ (Fig. 1),

$$f(t) = (\sin[\pi(t-bP)/\tau] - 2\tau/\pi P)/(1-2\tau/\pi P)$$
$$\text{for} \quad bP \leq t \leq (bP+\tau),$$

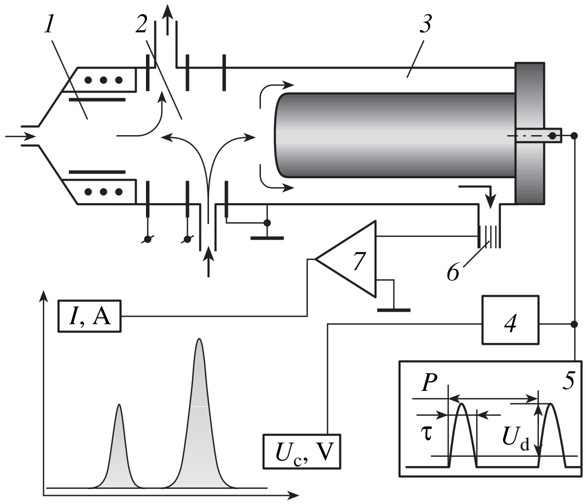

Fig. 1. Block diagram of experimental setup.

$$f(t) = -(2\tau/\pi P)/(1-2\tau/\pi P) \quad (12)$$
$$\text{for} \quad (bP+\tau) \leq t \leq (b+1)P$$

($b \geq 0$ is an integer); the range of voltage amplitude variation was $U_d = \pm(1000\text{–}4000)$ V; period $P = 6$ μs; and pulse duration $\tau = 2$ μs. The margins of permissible errors of measurements were $\delta U_c = \pm 2\%$ for the compensating voltage, $\delta U_d = \pm 10\%$ for the amplitude of ac voltage asymmetric in polarity, and $\delta t = \pm 7\%$ for time intervals.

The samples of the above-mentioned substances were prepared at the Institute of Organic Chemistry, Siberian Division, Russian Academy of Sciences (Novosibirsk). The sample composition was determined using an HP5890 gas-liquid chromatograph; the concentration of the main component was at least 98.5%. Vapor–air mixtures of the studied substances were obtained by passing purified air through a cell in which diffusion tubes containing the samples of the substances were placed. Then the mixture was fed to the ionization chamber.

DETERMINATION OF DEPENDENCES $A(E/N)$ AND $\overline{\Omega}^{(1,1)}(T_{\text{eff}})$

The signal detected in the experimental setup is a spectrum representing the dependence of the ion current on the compensating voltage ($I(U_c)$). Each type of ions is detected as an ion peak on the spectrum. The values of U_c corresponding to the tops of the peaks are observed when relation (11) holds for each *i*th type of ions; the relation between the electric field strength and the applied voltage is defined by the equation

$$U = Er\ln(r_2/r_1), \quad r \approx (r_1+r_2)/2. \quad (13)$$

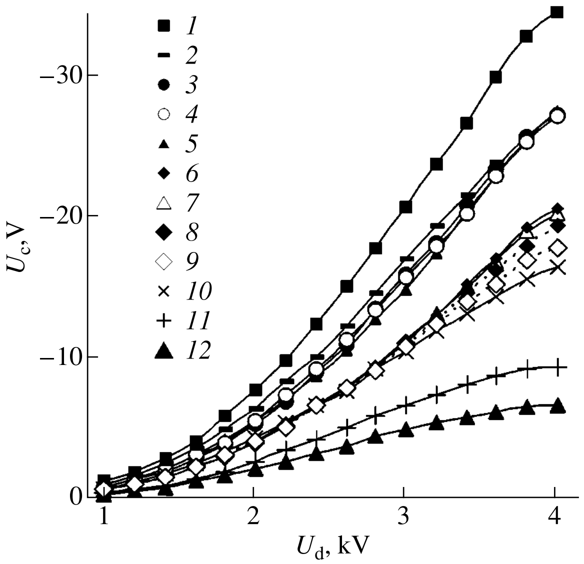

Fig. 2. Experimental dependences $U_c(U_d)$ (symbols) for ions of pyridine (*1*), benzene (*2*), DMMP (*3*), MA (*4*), anidine (*5*), o-TLD at $T = 10$, 20, 30, and 40°C, respectively (*6–9*), DMA (*10*), DPA (*11*), and DEA (*12*).

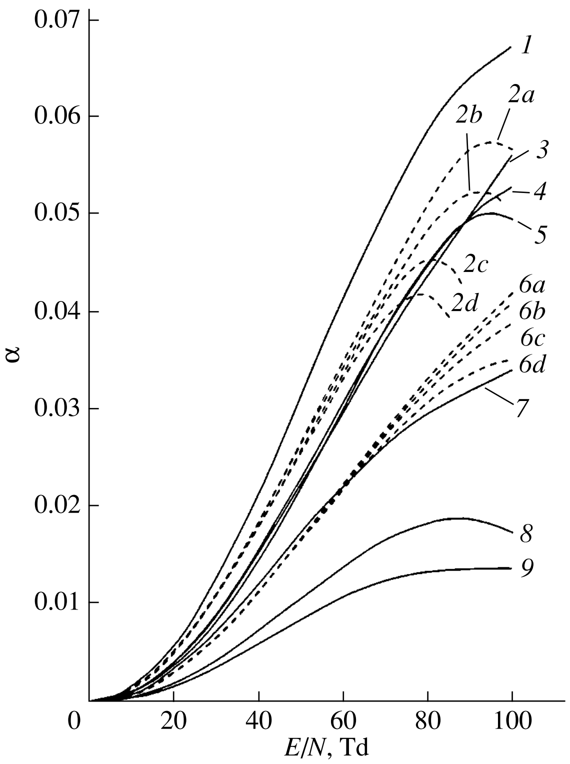

Fig. 3. Dependences $\alpha(E/N)$ for ions of the substances being studied: pyridine (*1*), benzene at $T = 10$, 20, 30, and 40°C, respectively (*2a–2d*), aniline (*3*), MA (*4*), DMMP (*5*), o-TLD at $T = 10$, 20, 30, and 40°C, respectively (*6a–6d*), DMA (*7*), DPA (*8*), and DEA (*9*).

Figure 2 shows experimental dependences $U_c(U_d)$ for ions of the substances being studied. A negative value of U_c for positive ions indicates that $\alpha(E/N) > 0$ and the coefficient of mobility K increases with U_d. For ions of o-TLD, the curves $U_c(U_d)$ were obtained for various temperatures of the carrier gas ($T = 10$, 20, 30, and 40°C). It can be seen from the figure that the dependence $U_c(U_d)$ decreases with increasing temperature of the carrier gas. Similar dependences were also obtained for benzene ions at $T = 10$, 20, 30, and 40°C (not shown in the figure).

Table 2. Values of coefficients α_{2n} for ions of the substances studied

Substance	α_2, 10^{-6}, Td^{-2}	α_4, 10^{-10}, Td^{-4}	α_6, 10^{-14}, Td^{-6}
Benzene, *a*	12.9	−9.36	2.22
Benzene, *b*	13.4	−12.4	4.86
Benzene, *c*	13.4	−13.4	5.74
Benzene, *d*	13.8	−16.2	9.13
DMMP	9.6	−2.58	2.26
o-TLD, *a*	7.94	−5.38	1.61
o-TLD, *b*	7.91	−5.36	1.53
o-TLD, *c*	7.96	−5.67	1.59
o-TLD, *d*	8	−5.93	1.44
MA	10.9	−6.87	1.29
Pyridine	15.1	−11.1	2.65
Aniline	10.8	−8.19	3
DMA	9.05	−9.25	3.6
DEA	4.51	−4.9	1.76
DPA	5.22	−3.96	4.76

Coefficients α_{2n} given in Table 2 were calculated by solving the inverse problem of Eq. (11) and using the experimental data (Fig. 2) expressed in units of field strength with the help of Eq. (13). Coefficients $\langle f^{2n} \rangle$ = 0.23, 0.13, 0.1 and $\langle f^{2n+1} \rangle$ = 0.12, 0.11, 0.1 were determined earlier for $n = 1$, 2, 3, respectively [9]. The values of α_{2n} were calculated using a polynomial approximation by the least squares method (polynomial regression). Notation *a*, *b*, *c*, and *d* in Table 2 for benzene and o-TLD ions corresponds to $T = 10$, 20, 30, and 40°.

Figure 3 shows the dependences $\alpha(E/N)$ calculated using relation (5) and coefficients from Table 2. It can be seen that, at the initial stage, the increment of α increases in proportion to the square of parameter E/N, the rate of this increase decreasing in accordance with the sequence pyridine > benzene > MA = aniline = DMMP > DMA ≈ o-TLD > DPA > DEA. With increasing E/N, the power of the α dependence decreases and the dependence is transformed to a linear dependence. As parameter E/N increases further, the curve for α becomes even more gently sloping and decreases after attaining a peak value for benzene, DMMP, and DPA. For ions of benzene and o-TLD, the dependences

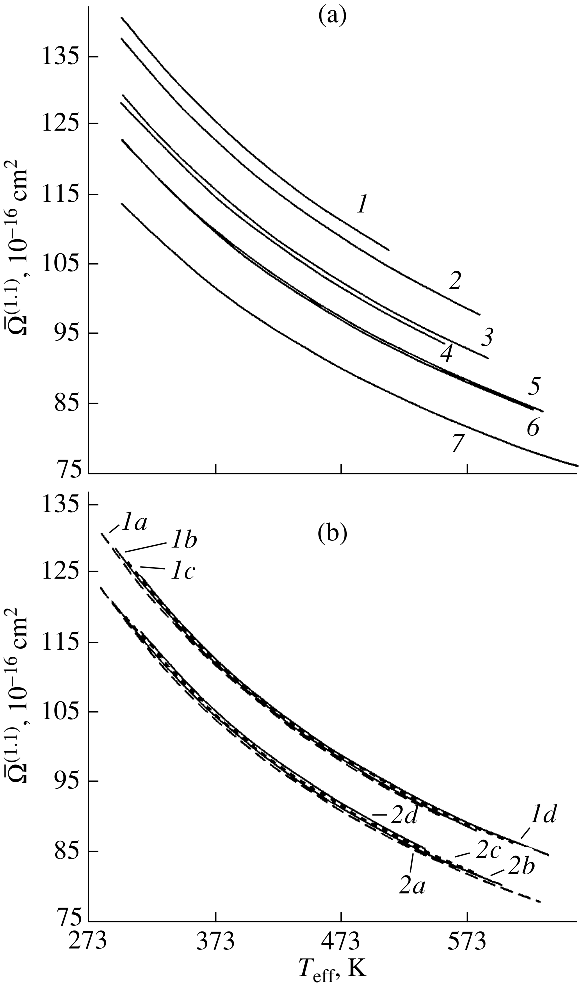

Fig. 4. Dependences $\bar{\Omega}^{(1,1)}(T_{\mathrm{eff}})$ for ions of the substances being studied: (a) DPA (*1*), pyridine (*2*), MA (*3*), DEA (*4*), aniline (*5*), DMA (*6*), DMMP (*7*); (b) o-TLD (*1a–1d*), benzene at $T = 10$, 20, 30, and 40°C, respectively (*2a–2d*).

$\alpha(E/N)$ obtained at different temperatures of the carrier gas ($T = 10$, 20, 30, and 40°C) decrease upon an increase in the temperature, and the positions of the peaks of ion mobility are displaced towards smaller values of parameter E/N.

Figure 4a shows the dependences $\bar{\Omega}^{(1,1)}(T_{\mathrm{eff}})$ calculated using Eq. (9) as well as the dependences $\alpha(E/N)$ for ions of pyridine, aniline, MA, DMMP, DMA, DPA, and DEA obtained at $T = 20$°C, while Fig. 4b shows the same dependences of ions of benzene and o-TLD obtained at $T = 10$, 20, 30, and 40°C. In can be seen that the value of parameter $\bar{\Omega}^{(1,1)}$ decreases with increasing effective temperature T_{eff}, while an increase in the gas temperature T from 283 to 313 K shifts the dependence $\bar{\Omega}^{(1,1)}(T_{\mathrm{eff}})$ as a single entity towards higher values of T_{eff} by less than 0.8% (see Fig. 4b).

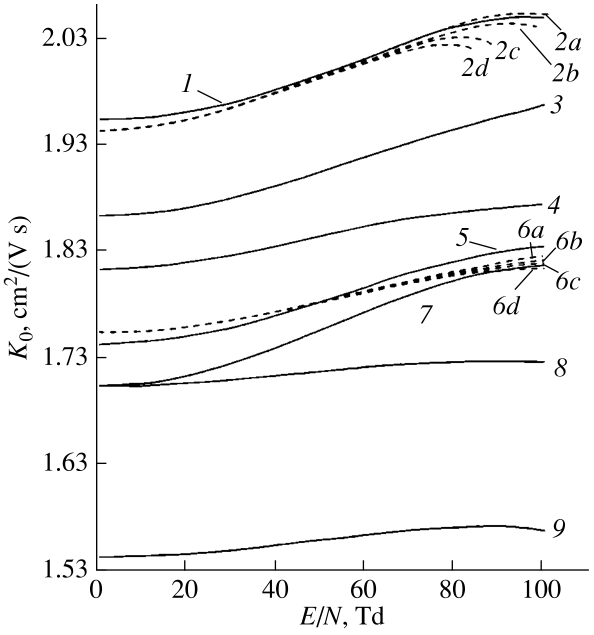

Fig. 5. Dependences $K_0(E/N, T)$ for ions of DMMP (*1*); benzene at $T = 10$, 20, 30, and 40°C, respectively (*2a–2d*); aniline (*3*), DMA (*4*); MA (*5*); o-TLD at $T = 10$, 20, 30, and 40°C, respectively (*6a–6d*); pyridine (*7*), DEA (*8*), and DPA (*9*).

DETERMINATION OF REDUCED KINETIC TRANSPORT COEFFICIENTS AS FUNCTIONS OF ELECTRIC FIELD AND TEMPERATURE $K_0(E/N, T)$, $ND(E/N, T)$

Figure 5 shows the dependences $K_0(E/N, T)$ calculated using Eqs. (1), (2) and Table 1. These dependences were calculated for $T = 10$, 20, 30, and 40°C for ions of benzene and o-TLD and for $T = 20$°C for ions of the remaining substances. The form of the dependences $K_0(E/N)$ is determined by the potential of the ion–neutral gas particle interaction. If the thermal energy of particles in the gas is much smaller than the depth of the well in the ion–neutral particle interaction potential, the ion mobility will increase with the field strength until the mean energy becomes on the order of the depth of the well. After this, the mobility must decrease in an increasing field since it is now determined by the short-range repulsive part of the interaction potential. In this case, the peak of the mobility as a function of the field is displaced upon an increase in the gas temperature towards lower values of the field strength.

Figures 6 and 7 show the dependences of longitudinal and transverse reduced diffusion coefficients $ND_L(E/N, T)$ and $ND_T(E/N, T)$, respectively. It is interesting to note some features in the behavior of these curves. It can be seen from the figures that the diffusion coefficient increase with the field; it is shown using benzene ions as an example that an increase in the gas temperature leads to an increase in the absolute value of

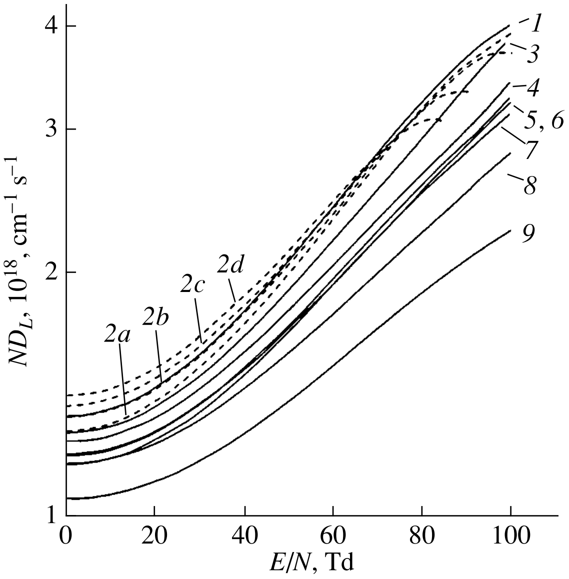

Fig. 6. Dependences of longitudinal reduced diffusion coefficients $ND_L(E/N, T)$ for ions of DMMP (*1*); benzene at T = 10, 20, 30, and 40°C, respectively (*2a*–*2d*); aniline (*3*); DMA (*4*); MA (*5*); o-TLD (*6*); pyridine (*7*), DEA (*8*), and DPA (*9*).

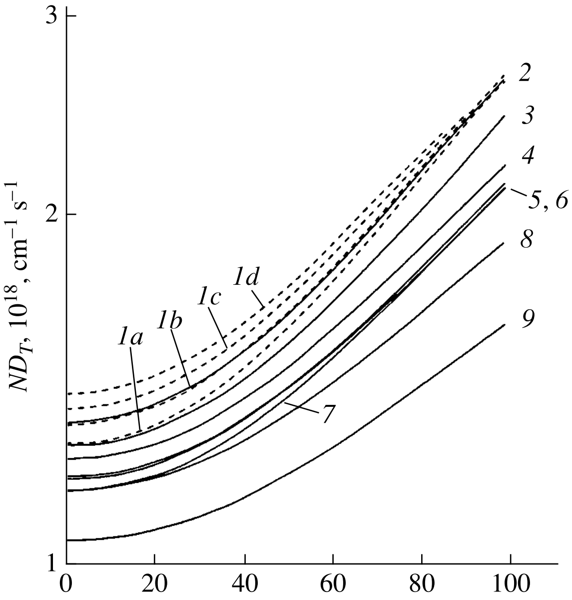

Fig. 7. Dependences of transverse reduced diffusion coefficients $ND_T(E/N, T)$ for ions of benzene at T = 10, 20, 30, and 40°C, respectively (*1a*–*1d*); DMMP (*2*); aniline (*3*); DMA (*4*); MA (*5*); o-TLD (*6*); pyridine (*7*), DEA (*8*), and DPA (*9*).

coefficients ND_L and ND_T for small values of E/N; the rate of increase in these coefficients decreases substantially upon an increase in parameter E/N. As expected, a decrease in the mobility coefficient K_0 produces a stronger effect on the decrease in the dependence of ND_L for large values of E/N (see Fig. 5). The numerical values of the growth rate for the coefficients are as follows: the rate of growth of D_L with parameter E/N in the range of values 0–100 Td increases in the following sequence: DPA (by a factor of 2.13), DEA (by a factor of 2.41), MA (by a factor of 2.71), o-TLD (by a factor of 2.72), DMA (by a factor of (2.76), pyridine (by a factor of 2.79), benzene (by a factor of 2.82), DMMP (by a factor of 3), and aniline (by a factor of 3.07). The growth rate of D_T increases with parameter E/N in the following sequence: DPA (by a factor of 1.54), DEA (by a factor of 1.65), o-TLD (by a factor of 1.78), MA and DMA (by a factor of 1.81), pyridine (by a factor of 1.84), aniline (by a factor of 1.93), benzene (by a factor of 1.97), and DMMP (by a factor of 2).

CONCLUSIONS

It is shown that the kinetic transport coefficients for ions can be determined as function of electric field and temperature using a periodic ac electric field of asymmetric polarity. For ions of the substances studied here, an increase in parameter E/N from 0 to 100 Td leads to an increase in the mobility coefficients K by 1.4–6.7%; the longitudinal and transverse diffusion coefficients D_L and D_T increase thereby by a factor of 2–3 and 1.5–2, respectively.

REFERENCES

1. E. A. Mason and E. W. McDaniel, *Transport Properties of Ions in Gas* (Wiley, New York, 1988).
2. A. A. Radtsig and B. M. Smirnov, *Chemistry of Plasma*, Ed. by B. M. Smirnov (Énergoatomizdat, Moscow, 1984), No. 11, pp. 170–200 [in Russian].
3. I. A. Buryakov, E. V. Krylov, A. L. Makas’, *et al.*, Zh. Anal. Khim. **48**, 156 (1993).
4. Z. Karpas, Anal. Chem. **61**, 684 (1989).
5. S. N. Ketkar, J. G. Dulak, W. L. Fite, *et al.*, Anal. Chem. **61**, 260 (1989).
6. H. Borsdorf and M. Rudolph, Int. J. Mass. Spectrom. 3, No. 1, 1 (2001).
7. V. T. Matsaev, N. N. Kozlov, M. F. Gumerov, *et al.*, Int. J. IMS (2003) (in press).
8. H. Borsdorf, H. Schelhorn, J. Flachowsky, *et al.*, Anal. Chim. Acta **403**, 235 (2000).
9. I. A. Buryakov, Zh. Tekh. Fiz. **72** (11), 109 (2002) [Tech. Phys. **47**, 1453 (2002)].
10. I. A. Buryakov, E. V. Krylov, E. G. Nazarov, *et al.*, Int. J. Mass Spectrom. Ion Processes **128**, 143 (1993).

Translated by N. Wadhwa

Technical Physics, Vol. 49, No. 8, 2004, pp. 973–981. Translated from Zhurnal Tekhnicheskoĭ Fiziki, Vol. 74, No. 8, 2004, pp. 21–29.
Original Russian Text Copyright © 2004 by Korobeĭshchikov, Zarvin, Madirbaev.

GASES AND LIQUIDS

Hydrodynamics of Pulsed Supersonic Underexpanded Jets: Spatiotemporal Characteristics

N. G. Korobeĭshchikov*, A. E. Zarvin, and V. Zh. Madirbaev**
Novosibirsk State University, Novosibirsk, 630090 Russia
*e-mail: * korobei@ci.nsu.ru; ** zarvin@phys.nsu.ru*

Received December 25, 2003

Abstract—The gasdynamic parameters of nonsteady expansion of He, Ar, N_2, and SiH_4 from a sonic nozzle into a space with reduced background gas pressure were experimentally studied for moderate values of n (10^3–10^6) and the Reynolds number ($Re_L \sim 10^0$–10^2). The jet set times necessary for the formation of pulsed jets of a given finite duration are determined. The results are generalized in terms of dimensionless similarity parameters. The laws of motion of the leading and trailing fronts in pulsed jets of various gases are established. The leading front of a pulsed jet propagates at a velocity significantly smaller than the limiting steady value. The jet expansion dynamics is determined by the ratio of the momentum of the expanding gas to that of the background gas displaced from the flow region. The length of the steady flow region in a pulsed jet monotonically decreases downstream from the source and drops with increasing background gas pressure because of the loss of jet particles in the trailing rarefaction wave; this length increases with the initial momentum because the background gas is more intensively displaced from the flow region. *© 2004 MAIK "Nauka/Interperiodica".*

INTRODUCTION

Pulsed jet sources (nozzles) are successfully used in experiments with colliding beams [1, 2], in investigations of relaxation processes in free jets [3, 4], in molecular spectroscopy and photochemistry [5–8], for pulsed gas admission into high-vacuum nuclear setups [9, 10], for semiconductor film deposition in modern electronic device technologies [11, 12], and for solving many other basic and applied problems [13]. The main advantage of pulsed jet nozzles for continuous flow devices is the high economic efficiency of the former's sources, explained by their relatively smaller dimensions, less stringent requirements on pumping systems, and lower consumption of high-cost materials. With pulsed sources, it is possible to obtain gas jets with parameters (gas flow rate, local beam density, etc,) hardly achievable in steady flows.

The main spatiotemporal characteristics of a pulsed jet are the set time and the duration (length) of a steady flow region. The set time of a nonsteady jet is defined as the time interval from the moment of opening of the source to the moment of establishment of steady flow parameters at a given distance from the nozzle. Within this steady flow region, the jet parameters remain unchanged during a certain finite period of time and are determined by the adiabatic exponent γ of the expanding gas and the gasdynamic parameters in the source, including the stagnation pressure P_0 and the stagnation temperature T_0. The total set time of a nonsteady jet includes the time required for the gas flow to establish itself at the nozzle exit (nozzle set time) and the time required for the flow to reach a steady state in the free jet.

The problem of determining the minimum time $\Delta t_{\min}$ for which the pulsed nozzle valve must be open in order to provide for the steady flow parameters at the nozzle output was considered by Saenger [14]. It was found that $\Delta t_{\min}$ is proportional to the square root of the molecular mass and increases linearly with the nozzle diameter d, provided that the product P_0d is fixed. For example, the minimum pulse duration necessary for obtaining steady flow jet parameters at the nozzle output for $P_0d = 1.33$ kPa mm according to [14] is ~4 μs for helium, ~15 μs for argon, and ~18 μs for nitrogen.

The set time of a free jet is determined by motion of the front part of the nonsteady flow, which depends on the interaction of the expanding gas with the background gas. We may distinguish three principal expansion regimes, whereby the gas leaving a nozzle enters (i) a region of very low background pressure (with the theoretical limit of expansion into vacuum), (ii) a continuous medium (flooded space), and (iii) a region with reduced background gas pressure (intermediate case). The diagram in Fig. 1 shows conditional boundaries between these regimes in coordinates of P_0/P_b versus P_b, where P_b is the residual (background) gas pressure.

When a supersonic jet expands into the space with low background gas pressure (Fig. 1, region *A*), the leading front of the expanding gas (left-hand inset to Fig. 1, curve *1*) is followed by a primary (initial) rarefaction wave, the rear boundary of which (curve *2*) coincides with the leading front of a steady flow region. In practice, this regime is observed for very large n

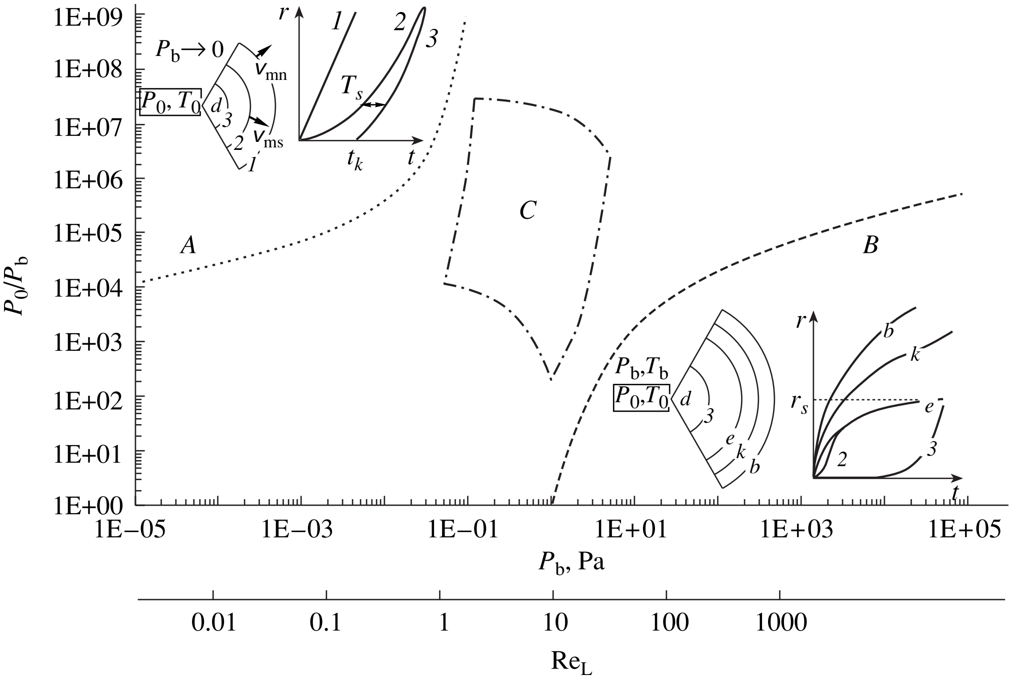

Fig. 1. Supersonic expansion regimes and jet structure for the gas expansion into (*A*) vacuum, (*B*) flooded space, and (*C*) a space with reduced background pressure (see the text for explanations).

($>10^6$) and small background gas pressures $P_b < 10^{-3}$ Pa. It was shown theoretically [15–17] and confirmed by experiments [18, 19] and model calculations [20] that the motion of the leading front of the expanding gas jet is independent of the background gas pressure and is determined by the limiting velocity v_{mn} of the nonsteady flow,

$$v_{mn} = \frac{\gamma + 1}{\gamma - 1} a_*, \tag{1}$$

where a_* is sound velocity in the critical cross section of the nozzle. The velocity of motion of the leading front of the steady flow region is determined by the maximum velocity v_{ms} of the steady flow of the given gas, which is determined by the total enthalpy h_0 of this gas:

$$v_{ms} = \sqrt{2h_0} = \sqrt{\frac{\gamma + 1}{\gamma - 1}} a_*. \tag{2}$$

Thus, the jet set time for a gas expanding into the space with very low background gas pressure is determined by the v_{ms} value. As the gas jet propagates downstream from the source, the length of the primary rarefaction wave increases.

Another limiting case is nonsteady expansion into a flooded space with high background gas pressure ($P_b \sim$ 10 Pa and above) at small n ($\sim 10^0$–10^2), illustrated by region *B* in Fig. 1. A typical example is offered by expansion of a shock-wave-heated gas from sonic and supersonic nozzles. In this case, the drag in the background gas is so large that a shock wave structure is virtually immediately formed at the leading front of the expanding gas jet. This structure consists of compressed layers of the expanding gas (right-hand inset to Fig. 1, curve *e*) and the background gas (curve *b*) displaced from the flow region, separated by the contact interface (curve *k*). Here, the leading front of the steady flow region is the secondary shock wave (*e*) whose propagation determines the jet set time. Velocities of the characteristic surfaces, fine vortex structures of the flow, and gas density distributions at various moments of time and various distances from the source were studied in [21–23]. It was found that the motion of characteristic discontinuities could be described in terms of the radial instantaneous steady-flow source (RISS) model [15].

For practical applications, the most important conditions correspond to region *C* intermediate between *A* and *B*, where the working gas expands into the space with reduced background gas pressure ($P_b \sim 10^{-2}$–10^{-0} Pa) at moderate $n \sim 10^3$–10^6). Such conditions are most frequently encountered in experiments with nonsteady gas jets and molecular beams. The relatively high background gas pressure level allows the nozzle to operate at a sufficiently large gas flow rate and form supersonic jets featuring developed relaxation processes. However, no detailed experimental investigations under such, or close to such, experimental conditions have been reported so far.

Most of the published data refer to processes at the leading front of a nonsteady flow, that is, to the jet set regime of a steady source. However, the notion of a pulsed jet implies that the source operates for a finite time and then is switched off (in the ideal case, instantaneously). Under real conditions, the gas expansion is significantly complicated by transient phenomena involved in the process of source switching on and off. At the switch on moment, there arises a trailing (secondary) rarefaction wave characterized by nonsteady flow. Propagation of this secondary rarefaction wave downstream from the nozzle determines the trailing front of the steady flow region (Fig. 1, curve *3*). Therefore, a question naturally arises as to what is the time of existence (or the spatial length) of the steady flow at a given distance from a pulsed jet source.

According to the theoretical RISS model [15], the time of existence of the steady state in a pulsed gas jet expanding into vacuum (Fig. 1, region A) decreases downstream from the nozzle. The gas pulse exhibits dissipation caused by the loss of particles in the leading and trailing rarefaction waves. As a result, a situation is possible where the flow at a finite distance from the source does not attain a steady state even despite the fact that the necessary nozzle set conditions are satisfied. It was shown [15] that the length of the steady flow region for a gas expanding into vacuum depends on the adiabatic exponent γ of the gas. We may suggest that the presence of a residual (background) gas will significantly influence the steady flow duration, but the corresponding experimental data are unavailable.

In this context, we have studied the gasdynamics of pulsed jets formed upon expansion of a gas for moderate values of n (10^3–10^6) and the Reynolds number ($\mathrm{Re}_L \sim 10^0$–10^2) and determined the laws of motion of the leading and trailing fronts and the formation of a quasi-steady region in the pulsed jet. The region corresponding to the conditions of our experimental measurements is depicted by the dash-dot line in Fig. 1.

EXPERIMENTAL

The investigation was performed on the LEMPUS complex gasdynamic setup created at Novosibirsk State University [24], in which the gas jet is produced by a special electromagnetic valve. The source design and the valve control system allow pulsed supersonic jets to be generated with a pulse duration of 0.3–3 ms and a repetition rate of up to 10 Hz [25]. The valve and the nozzle are mounted in the expansion chamber on a positioning mechanism, which allowed the distance from the source to the point of measurement to be controlled.

The measurements were performed for the most part by method of molecular beam mass spectrometry using an MS 7303 quadrupole mass spectrometer with electron impact ionization. The gasdynamic molecular beam was formed from a pulsed jet using a skimmer ($d_S = 0.53$ mm) and a collimator ($d_C = 6$ mm). The distance from the skimmer to the ionization site (i.e., the time-of-flight base of the molecular beam) was 690 mm. Source operation and data acquisition and processing were performed using a computer-controlled system of pulsed signal registration and display [26]. In some experiments, the pulsed jet was studied by method of electron-beam diagnostics with response signal recording in the visible spectral range [27], which allowed measurements to be performed at small distances from the source.

We have studied the expansion of helium (He), argon (Ar), nitrogen (N_2), and monosilane (SiH_4) from sonic nozzles with a diameter of $d = 1$ and 0.55 mm. The stagnation pressure was controlled within $P_0 = 10^0$–10^3 kPa and the distance from the pulsed nozzle was varied within 10–225d. The background gas pressure in the expansion chamber was maintained at a level of $P_b = 0.1$–1 Pa. We determined the following characteristics of pulsed gas jets: the time of arrival of the leading (T_{i1}) and trailing (T_{i2}) fronts (measured at half the height of a gas pulse) and the full width at half-maximum (FWHM) $D_i = T_{i1} - T_{i2}$ of the pulse. The methods of measurements and experimental data processing are described in detail elsewhere [24].

RESULTS

The main dimensionless parameters characterizing the gas expansion regimes studied are presented in Table 1. The values of n show that the jets were strongly underexpanded ($n \gg 1$) for all gases in the entire range of stagnation pressures P_0. The Reynolds numbers at the nozzle exit aperture ($\mathrm{Re}_a > 10^2$) corresponded to the continuous expansion regime. According to estimates, Re values in the jet in all experimental regimes were $\mathrm{Re}_L < 10^2$. Under these conditions, the gasdynamic structure and the steady flow parameters are affected by the rarefaction, whereby the characteristic barrel-shaped shock wave structure is smeared and the background gas diffusion into the jet core becomes possible [28]. Thus, all the experimentally studied regimes are of the intermediate type with significant influence of the background gas. The pulsed jets are additionally characterized by homochronicity expressed in terms of the Struchal number. Under the conditions of our experiments with an initial gas pulse duration of ~1.5 ms, this value was $\mathrm{Sh} > 10^2$, which corresponds to the regime of long pulses.

Figures 2 and 3 show the typical gas density profiles measured at the jet axis in the course of the gas pulse propagation. These data were obtained by means of molecular beam mass spectrometry in a helium jet behind the nozzle with $d = 0.55$ mm. The measurements were performed at a fixed distance from the nozzle to skimmer ($x/d = 100$) under the conditions of variable stagnation pressure (Fig. 2) or at a fixed P_0 and variable distance from the source (Fig. 3). The signal amplitude is normalized to maximum, while the abscissa axis shows the time measured from the moment of nozzle

Table 1. Calculated dimensionless parameters of pulsed jets expanding from a nozzle with a diameter of $d = 1$ mm

P_0, Pa	P_b, Pa	n		$\mathrm{Re_a} = \rho_a v_a d/\mu_a$		
		He, Ar	N_2	He	Ar	N_2
1.0E+03	5.0E–02	9.4E+03	1.1E+02	5.2E+02	1.5E+02	1.4E+02
1.0E+04	8.0E–02	5.9E+04	6.3E+04	5.2E+02	1.5E+03	1.4E+03
1.0E+05	1.3E–01	3.6E+05	3.9E+05	5.2E+03	1.5E+04	1.4E+04
1.0E+06	3.0E–01	1.6E+06	1.7E+06	5.2E+04	1.5E+05	1.4E+05

P_0, Pa	P_b, Pa	$\mathrm{Re_L} = \mathrm{Re_a}/N^{0.5}$			$\mathrm{Sh} = Dv_a/d$		
		He	Ar	N_2	He	Ar	N_2
1.0E+03	5.0E–02	6.0E–01	1.7E+00	1.6E+00	8.8E+02	2.8E+02	2.4E+02
1.0E+04	8.0E–02	1.9E+00	5.3E+00	5.0E+00			
1.0E+05	1.3E–01	6.0E+00	1.7E+01	1.6E+01			
1.0E+06	3.0E–01	1.9E+01	5.3E+01	5.0E+01			

valve opening. As can be seen, the gas pulse has a leading front width of about ~180–200 μs, a flat region on the top with a duration of ~500 μs, and a trailing front with a long slowly decaying "tail" whose length is determined by the instrumental function of the ionizing source of the mass spectrometer.

At a fixed distance from the source, the leading fronts of gas pulses shift toward shorter times with increasing P_0 (Fig. 2), while the position of the trailing front remains virtually unchanged. As the source–skimmer distance is increased, both the leading and trailing fronts shift toward longer times. The shape of the gas pulse always remains the same, being determined by the time at which the valve opens. Similar behavior was also observed for other gases, provided that cluster formation in the jet could be ignored.

Figure 4 shows the effect of variation of the stagnation pressure P_0 on the time of arrival of the leading (T_{i1}) and trailing (T_{i2}) pulse fronts. The measurements were performed for various distances from the source to the skimmer in a jet of helium expanding from a 1-mm nozzle. As can be seen, the character of variation

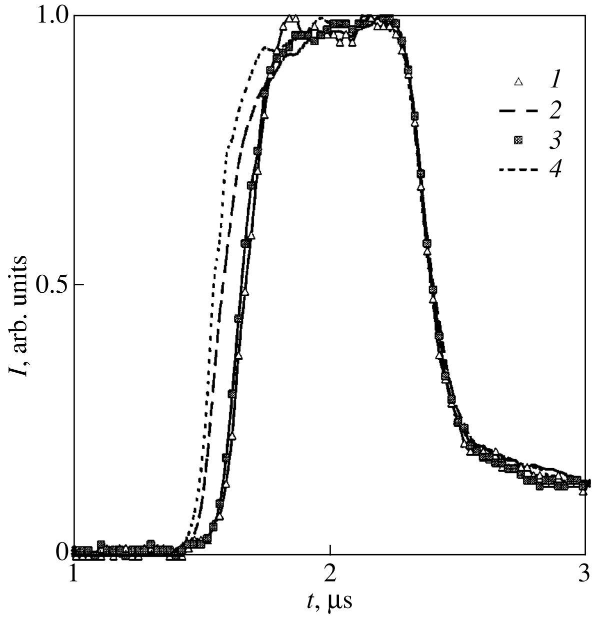

Fig. 2. Gas density profiles for a pulsed molecular beam of helium formed using a sonic nozzle with $d = 0.55$ mm and measured at a nozzle–skimmer distance of $x/d = 100$ for various stagnation pressures P_0 = 80 (*1*), 250 (*2*), 140 (*3*), and 300 kPa (*4*).

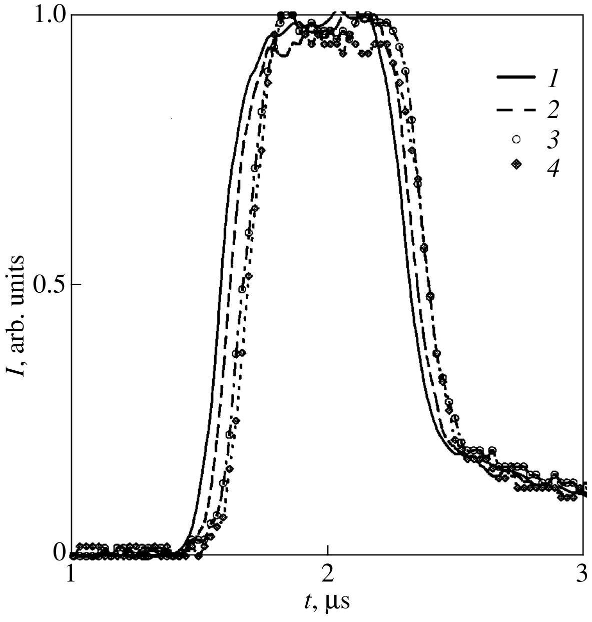

Fig. 3. Gas density profiles for a pulsed molecular beam of helium formed using a sonic nozzle with $d = 0.55$ mm and measured at a stagnation pressure of 100 kPa for a nozzle–skimmer distance of x/d = 40 (*1*), 80 (*2*), 100 (*3*), and 150 (*4*).

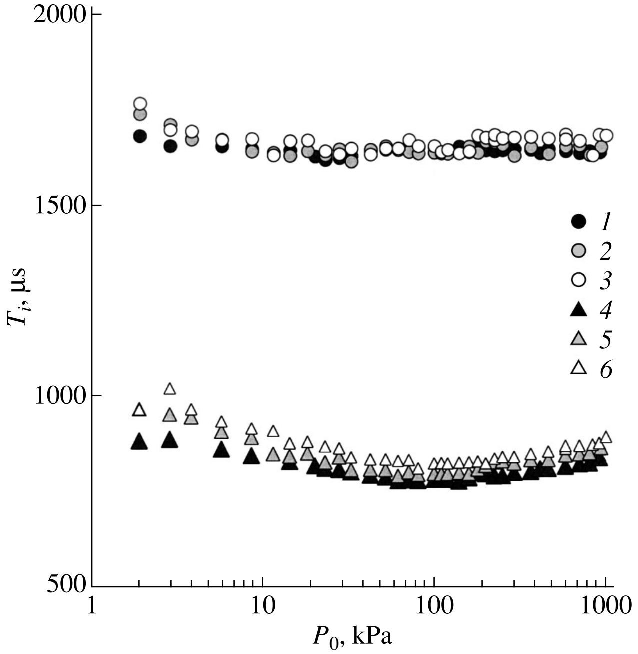

Fig. 4. Effects of the stagnation pressure P_0 on the times of arrival of the (*1*–*3*) leading pulse front (T_{i1}) and (*4*–*6*) trailing pulse front (T_{i2}) in a molecular beam of helium formed using a sonic nozzle with $d = 1$ mm and measured at various source–skimmer distances $x/d = 125$ (*1*, *4*), 150 (*2*, *5*), and 175 (*3*, *6*).

in the front arrival times is the same for all distances: when P_0 grows up to 150 kPa, T_{i1} monotonically decreases and T_{i2} remains virtually unchanged. Accordingly, the pulse halfwidth D_i monotonically increases. As the P_0 value (and, hence, the gas flow rate through the nozzle) is increased further, the leading front exhibits retardation and the pulse halfwidth begins to decrease.

Figure 5 presents data on the halfwidth D_i of pulsed helium, nitrogen, and argon jets for the same initial pulse duration and several fixed stagnation pressures. The measurements were performed by molecular beam mass spectrometry at various distances from the nozzle output to the skimmer. These data are supplemented by the results of electron-beam diagnostics for relatively small source–skimmer distances within $x/d = 14$–100. As can be seen, the pulsed jet halfwidth (and, hence, the length of the steady region) decreases downstream the flow for all gases. Since the pulsed jet halfwidth measured by the electron-beam technique at the skimmer entrance is close to the value measured by the molecular beam mass spectrometry, we may conclude that the main changes in the pulse halfwidth take place in the region between the nozzle exit and the skimmer.

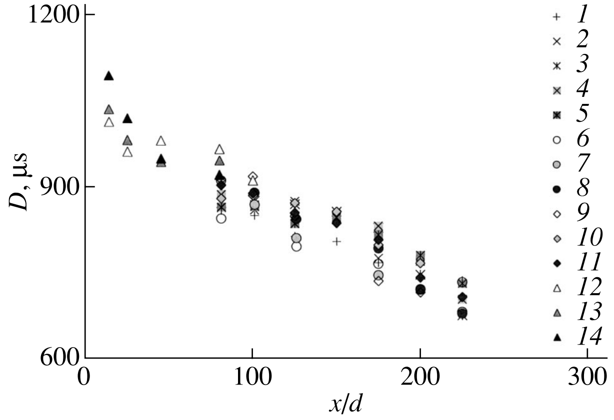

Fig. 5. A plot of the pulsed jet halfwidth D_i versus the distance to the skimmer entrance (for molecular beam mass spectrometry, *1*–*11*) or to the point of measurement (for electron-beam diagnostics, *12*–*14*) for various gases expanding from a nozzle with $d = 1$ mm at various fixed stagnation pressures: (*1*–*5*) He at $P_0 = 28$ (*1*), 70 (*2*), 100 (*3*), 225 (*4*), and 460 kPa (*5*); (*6*–*8*) Ar at $P_0 = 5$ (*6*), 15 (*7*), and 30 kPa (*8*), (*9*–*14*) N_2 at $P_0 = 5$ (*9*), 50 (*10*), 100 (*11*, *12*), 180 (*13*), and 350 kPa (*14*).

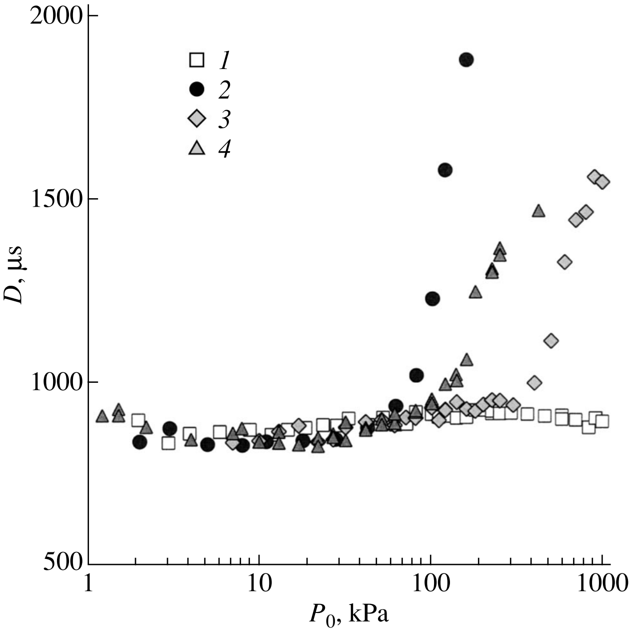

Fig. 6. A plot of the pulsed jet halfwidth D_i versus stagnation pressure P_0 for various gases expanding from the 1-mm nozzle and measured at $x/d = 175$: (*1*) He; (*2*) Ar; (*3*) N_2; (*4*) SiH_4.

Figure 6 shows a plot of the pulsed jet halfwidth D_i versus stagnation pressure P_0 for various gases. The measurements were performed under nearly identical conditions, including the same geometry and initial pulse duration, close background gas pressures in the expansion chamber, and the same nozzle–skimmer distance ($x/d = 175$). As can be seen, the D_i values for all gases at the same P_0 are equal to within the experimental error, except for the regions at high stagnation pressures, where D_i exhibits a sharp growth and the flow is accompanied by condensation [29].

The velocity of the leading front of an expanding gas jet was determined by measurements at various distances from the source. Table 2 presents data on the leading front velocities measured in helium, argon, nitrogen, and monosilane at a background gas pressure of $P_b \sim 10^{-1}$ Pa, together with the maximum velocities of steady (v_{ms}) and nonsteady (v_{mn}) flows in these gases calculated using formulas (1) and (2). A comparison of the calculated and experimental values shows that the leading front of a pulsed jet in all studied gases propagates at a velocity significantly smaller than the limiting value v_{ms} of steady expansion.

It should be noted that the leading front velocities reported in various papers for nonsteady jets are at first glance rather contradictory and disagree with our data. Indeed, the leading front velocities obtained in [18] for argon and nitrogen jets expanding into a space with low background gas pressure ($P_b \sim 10^{-4}$ Pa) were close to the limiting nonsteady flow velocity. The results of measurements for the pulsed jets of helium [30] performed at $P_b \sim 10^{-2}$ Pa showed that the leading front propagates at a velocity equal to the limiting value for steady expansion. On the other hand, the values obtained in [31] for the pulsed expansions of helium under conditions close to those used in our experiments ($P_b \sim 10^{-1}$ Pa) were close to our results for this gas.

DISCUSSION

Analysis of the experimental results obtained in this study leads to the following conclusions concerning the influence of the main flow parameters on the characteristics of pulsed gas jets:

(i) the length of the steady flow region decreases with increasing distance from the source;

(ii) under the conditions of fixed stagnation pressure, background gas pressure, and distance from the source, the length of the steady flow region is independent of the adiabatic exponent γ of the expanding gas;

(iii) as the stagnation pressure grows, the leading front velocity initially increases, passes through a maximum, and then decreases at a rate correlated with the increase in the background gas pressure;

Table 2. Comparison of the calculated steady (v_{ms}) and nonsteady (v_{mn}) gas expansion velocities and the experimental leading front propagation velocities (x_{exp}) for helium, argon, nitrogen, and monosilane expansions

He		Ar	N_2	SiH_4
v_{ms}, m/s	1770	560	790	970
v_{mn}, m/s	3060	970	1770	2930
v_{exp}, m/s	1230	380	420	440

(iv) the leading front velocity in the expanding gas jet is significantly smaller than the limiting steady flow velocity;

(v) the low value of the leading front velocity in the expanding gas jet and the fact that the width of this front depends neither on P_0 nor on the distance from the source indicate that no primary rarefaction wave is formed in the pulsed jet (therefore, the front boundary of the steady flow region under the conditions studied is determined by the leading front of the expanding gas jet).

When a supersonic jet expands into the space with low residual pressure, the expanding gas acts like a piston displacing the initially quiescent background gas. The energy of the expanding gas is spent predominantly for setting the displaced background gas into motion. Therefore, the law of motion of the leading front of the expanding gas is determined by the equality of the momentum flux densities of the expanding and background gases at the contact interface. Chekmarev [15] showed within the framework of the RISS model that the mechanism of pulsed jet expansion is determined by the ratio of masses of the expanding gas (m_e) and the displaced background gas (m_b). The case of expansion into vacuum corresponds to the condition $(m_b/m_e)^{1/2} \ll 1$, while nonsteady expansion into a flooded space is described by the relation $(m_b/m_e) \gg 1$. Let us estimate this ratio for the conditions under consideration.

The mass of the displaced gas can be evaluated under certain assumptions. Evidently, the background gas in the expansion chamber prior to measurements consists predominantly of residual nitrogen. However, under the conditions of a considerable rate of gas flow from the nozzle and a large number of pulses in experimental series, the composition of the background atmosphere changed: nitrogen was replaced by the expanding gas. In addition, the background gas composition could be influenced by selective pumping. For this estimation, it was assumed that expanding and background gas compositions are the same.

As is known [28], the angle of expanding current lines θ_m relative to the jet axis in the case of axisymmetric free expansion is determined by the adiabatic exponent γ of the expanding gas and the Mach number M_a at the nozzle aperture. For a monoatomic gas expanding from a supersonic nozzle ($M_a = 1$) into vacuum, the limiting expansion angle is $\theta_m \sim 85°$; for diatomic and triatomic gases, the corresponding values are $\theta_m \sim 130°$ and 165°, respectively. However, the main fraction of the expanding gas flows through a paraxial region within an angular interval of $0.5\theta_m$ [28]. Apparently, the expansion angles of polyatomic gases in a pulsed jet are also greater than those of monoatomic gases. For this reason, the mass of a displaced background gas was determined as a product of the mass density ρ_b of the background gas at the known background pressure P_b and the volume of a cone with an apical angle of $0.5\theta_m$.

The estimates were obtained for a background pressure of 0.1 Pa, typical of our experimental conditions.

The mass of the expanding gas was estimated as $m_e = \rho_a v_a st$, where ρ_a is the gas density at the nozzle exit, v_a is the gas velocity in this cross section, $s = \pi d^2$ is the area of the nozzle exit aperture, and t is the gas expansion time. The gas parameters at the nozzle exit were determined using isentropic relations. In order to compare the masses of the expanding gas and the gas displaced by the expanding jet, it is necessary to determine how the former mass gas varies in the course of gas expansion downstream from the nozzle. This variation was evaluated using the leading front velocity determined in the experiment (Table 2). Calculations were performed for the sonic nozzles with $d = 0.55$ and 1 mm and a stagnation pressure of $P_0 = 100$ kPa.

Figure 7 shows variation of the ratio of masses of the dispaced background gas (m_b) and the expanding gas (m_e) downstream from the nozzle for the pulsed jets of He, Ar, and N_2. At small distances from the source, the mass of the expanding gas is considerably greater than that of the displaced background gas, but the latter value rapidly grows for all gases as the jet propagates downstream from the nozzle. As a result, for $x/d > 100$ (i.e., for most regimes studied in our experiments), the mass of displaced background gas is comparable to the mass of expanding gas. Therefore, the background gas must significantly influence the expansion dynamics.

Our analysis suggests the following mechanism of pulsed jet expansion into the space with reduced background gas pressure. Since the density of the background gas is small, the velocity of expanding gas particles in the initial stage may reach the limiting value for the nonsteady flow. Interaction between the pulsed gas jet and the background gas leads to the formation of a continuous leading front separating the expanding gas and the displaced background gas. As this leading front propagates downstream from the nozzle, the mass of the displaced gas grows much faster than the mass of expanding gas. As a result, the expanding gas exhibits retardation at the leading front of the jet. However, the retarding effect of the background gas is not as large as in the case of expansion into a continuous medium and does not lead to the formation of shock waves at the jet front. Nevertheless, the velocity of propagation of the leading front of the expanding gas becomes significantly lower than the limiting steady flow velocity.

As a result, no primary rarefaction wave is formed in the course of expansion in front of the steady flow region under these conditions and the leading front determines the rear boundary of the steady flow region. Thus, the set time of a pulsed jet is determined by the motion of the leading front of the expanding gas. Note that a transition from the "shock" to "shockless" expansion regime was observed [23] during the investigation of nonsteady flows of shock-wave-heated gases in a flooded space under the condition of $n \sim 10^3$.

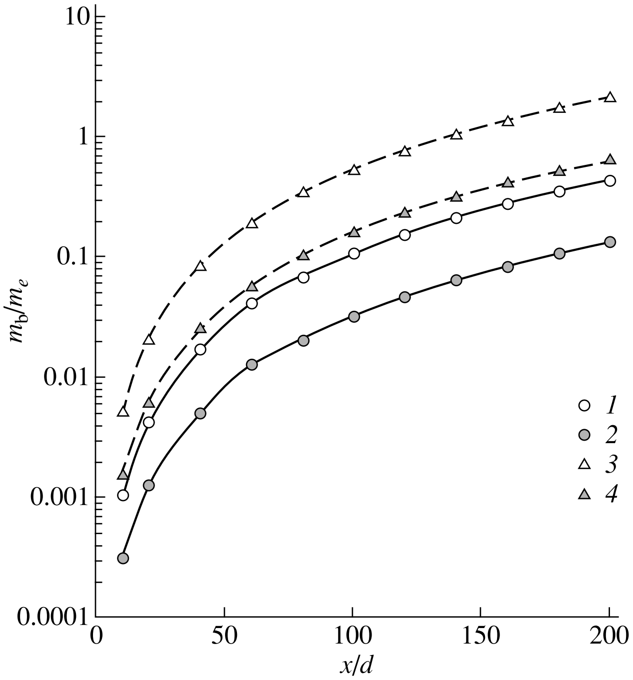

Fig. 7. Plots of the ratio of masses of the expanding (m_e) and displaced background (m_b) gases versus x/d for (*1, 2*) helium and argon and (*3, 4*) nitrogen expanding from the nozzles with $d = 0.55$ (*1, 3*) and 1 mm (*2, 4*) at a stagnation pressure of $P_0 = 100$ kPa and a backgropund pressure of $P_b = 0.1$ Pa.

In the final stage of expansion, the leading front slows down and reaches the limiting jet size L determined (as well as in the steady flow) by the ratio of stagnation and background pressures. The expanding gas retarded at the slowly propagating leading front forms the secondary rarefaction wave representing particles moving in the reverse direction. The existence of the reverse flow directed toward the source in a pulsed jet expanding into vacuum was demonstrated by the results of Monte Carlo simulations [20]. The intensity of this flow increased with the pulse duration. In our case, the presence of a slowly moving leading front must lead to an increase in the reverse flux of retarded particles.

An increase in the stagnation pressure leads to an increase in the density of the momentum flux from the source and, hence, to more intensive displacement of the background gas and accelerated propagation of the leading front of expanding gas. As a result, the length of the steady flow region increases (at a fixed initial pulse duration and the distance from the source).

As the pulsed jet propagates downstream from the source, an increasing fraction of expanding gas particles passes to the trailing rarefaction wave. This leads to a decrease in the length (duration) of the steady flow region with increasing distance from the source. At a fixed initial pulse duration and the same expanding and background gas compositions, the steady flow region

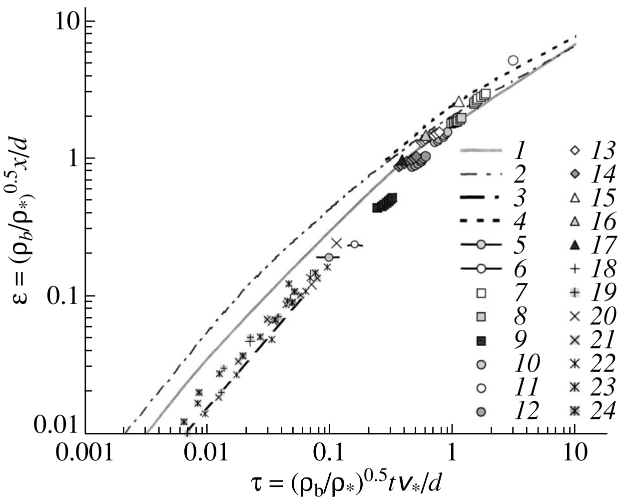

Fig. 8. Generalized plot of the jet set times in dimensionless coordinates for several gases measured in this study using (*7–17*) molecular beam mass spectrometry and (*18–24*) electron-beam diagnostics methods in comparison to published theoretical data for (*1*) Ar and (*2*) N_2 [15] and experimental data for (*3*) Ar [6], (*4*) N_2 [9], (*5*) He [30], (*6*) He [31]. Our data for He: (*7*) P_0 = 10 kPa, d = 1 mm; (*8*) 100 kPa, 0.55 mm; (*9*) 800 kPa, 1 mm; (*18*) 40 kPa, 0.55 mm; (*19*) 800 kPa, 0.55 mm; for Ar: (*10*) P_0 = 40 kPa, d = 1 mm; (*11*) 10 kPa, 0.55 mm; (*12*) 100 kPa, 1 mm; (*20*) 11 kPa, 0.55 mm; (*21*) 220 kPa, 0.55 mm; for N_2: (*13*) P_0 = 40 kPa, d = 1 mm; (*14*) 100 kPa, 1 mm; (*22*) 100 kPa, 1 mm; (*23*) 400 kPa, 0.55 mm; (*24*) 800 kPa, 0.55 mm; for SiH_4: (*15*) P_0 = 10 kPa, d = 1 mm; (*16*) 40 kPa, 1 mm; (*17*) 100 kPa, 1 mm.

length is independent of the adiabatic exponent γ of the expanding gas and is determined by the ratio of stagnation and background pressures.

In order to generalize the experimental spatiotemporal data, it is necessary to use dimensionless parameters including characteristics of the expanding gas and the expansion regimes. The dimensionless parameters introduced by Chekmarev [15] play the role of similarity criteria for the surfaces of strong discontinuity in the case of a pulsed gas expansion into a flooded space. For an axisymmetric flow, the dimensionless parameters are defined by the formulas

$$\tau\left(\frac{\rho_b}{\rho_a}\right)^{1/2}\frac{tv_a}{r_a}, \quad \xi = \left(\frac{\rho_b}{\rho_a}\right)^{1/2}\frac{r}{r_a}, \qquad (3)$$

where ρ_a is the density of the expanding gas at the nozzle exit and ρ_b is the density of the background gas.

Figure 8 presents data on the set times of pulsed jets obtained in our experiments with He, Ar, N_2, and SiH_4 using molecular beam mass spectrometry (upper array of points) and electron-beam diagnostics (lower array of points). In plotting the results of molecular beam mass spectrometry, we used an assumption based on the following considerations. As was noted above, the time-of-flight base for the pulsed flow behind the skimmer was significantly greater than the distance from the nozzle to skimmer. However, the background pressure on the molecular beam path is much lower than that in the expansion chamber: the pressure behind the skimmer was ~10^{-5} Pa and that in the detector was ~10^{-6} Pa against ~10^{-1} Pa in the expansion chamber. Obviously, the pressure behind the skimmer is sufficiently low and its effect on the pulsed jet can be ignored. In addition, estimates of the Knudsen number for the skimmer, Kn_S, showed that our measurements were performed mostly for $Kn_S > 1$. Therefore, the skimmer input aperture is the surface of last collisions of molecules in the flow. Under these conditions, the velocity of the leading front of the pulsed jet in the molecular beam region is determined by the leading front velocity at the skimmer entrance.

As can be seen, Fig. 8 generalizes the experimental data obtained for various stagnation pressures, background pressures, and nozzle diameters. However, the points corresponding to gases possessing different adiabatic exponents γ exhibit separation: the data for He and Ar are lying below those for N_2, while the data for SiH_4 are lying still higher (the results of electron-beam diagnostics are less scattered because of a lower accuracy of these measurements).

For the comparison, Fig. 8 shows the results of calculations for the moving contact interface in Ar and N_2 according to the RISS model [15]. Similar to the experimental data, the calculated jet set time increases with the γ value of the expanding gas. However, the theory [15] gives overstated estimates for the leading front velocity at small τ and ξ values (this discrepancy was explained by the author as being related to the use of a nonviscous gas model). Figure 8 also shows the experimental data for the leading front velocities reported by other researchers for the expansion of argon into vacuum [18], for a shock-wave-heated nitrogen jet [21], and for the free expansion of helium [30, 31]. As can be seen, these experimental data well agree with our results.

CONCLUSIONS

We have experimentally studied nonsteady expansion of gases into the space with reduced background pressure. It is established that the expansion dynamics is determined by the ratio of the momentum of the expanding gas to that of the background gas displaced from the flow region.

The jet set times were experimentally determined for the pulsed jets of helium, argon, nitrogen, and monosilane. It was found that, under the conditions studied, the leading front of a pulsed jet propagates at a velocity significantly smaller than the limiting steady value for a given gas. In contrast to the case of expansion into vacuum, the retarding action of the background gas leads to the absence of a primary rarefaction wave and makes the leading front of the expanding gas the boundary of a steady flow region.

Using the dimensionless similarity parameters, we obtained generalized data on the pulsed jet set times for various gases and expansion regimes. It is established that the length (duration) of the steady flow region in a pulsed jet at a fixed distance from the source is independent of the ratio of heat capacities of expanding gases and is determined by the pulse duration at the nozzle exit and the ratio of stagnation and background pressures. The length of the steady flow region in a pulsed jet monotonically decreases downstream from the source and drops with increasing background gas pressure because of the loss of jet particles in the trailing rarefaction wave; this length increases with the initial momentum because the background gas is more intensively displaced from the flow region.

The results of our experiments show that pulsed gas jets and molecular beams with a finite steady flow region can be successfully obtained for $\mathrm{Re}_L < 100$ in the presence of a background gas.

ACKNOWLEDGMENTS

This study was supported by the Federal Targeted Program Integration of Science and Higher Educational Schools in Russia: 2002–2006" (State Contract no. LO 126/805) and the Ministry of Industry, Science, and Technology of the Russian Federation within the framework of the Program of Support for Unique Research and Experimental Setups (project no. 06-05).

REFERENCES

1. G. Hall, K. Lin, M. J. McAuliffe, *et al.*, J. Chem. Phys. **74**, 5577 (1984).
2. L. Schnieder, K. Seekamp-Rahn, F. Liedeker, *et al.*, Faraday Discuss. Chem. Soc. **91**, 259 (1991).
3. M. G. Liverman, S. M. Beck, D. L. Monts, *et al.*, in *Proceedings of the 11th International Symposium on Rarefied Gas Dynamics, Paris, 1979*, Ed. by R. Campargue, Vol. 2, pp. 1037–1048.
4. H. Zacharias, M. M. T. Loy, P. A. Roland, *et al.*, J. Chem. Phys. **81**, 3148 (1984).
5. C. T. Rettner, E. E. Marinero, R. N. Zare, *et al.*, J. Phys. Chem. **88**, 4459 (1984).
6. G. N. Makarov, D. E. Malinovskiĭ, and D. D. Ogurok, Zh. Tekh. Fiz. **69** (1), 35 (1999) [Tech. Phys. **44**, 31 (1999)].
7. T. Hosokai, K. Kinoshita, T. Watanabe, *et al.*, in *Proceedings of European Particle Acceleration Conference, Paris, 2002*, pp. 981–983.
8. F. Luo, G. C. McBane, G. Kim, *et al.*, J. Chem. Phys. **98**, 3564 (1993).
9. M. Inutake and K. Kuriki, Rev. Sci. Instrum. **43**, 1670 (1972).
10. G. E. Derevyankin, V. G. Dudnikov, and P. A. Zhuravlev, Prib. Tekh. Éksp., No. 5, 168 (1975).
11. D. Eres, D. H. Lowndes, J. Z. Tischler, *et al.*, J. Appl. Phys. **67**, 1361 (1990).
12. R. Malik, E. Gulari, S. H. Li, *et al.*, J. Cryst. Growth **150**, 984 (1995).
13. *Atomic and Molecular Beam Methods*, Ed. by G. Scoles (Oxford Univ. Press, Oxford, 1988).
14. K. L. Saenger, J. Chem. Phys. **75**, 2467 (1981).
15. S. F. Chekmarev, *Pulsed Gas Flows in Supersonic Nozzles and Streams* (Inst. Teplofiz. Sib. Otd. Akad. Nauk SSSR, Novosibirsk, 1990) [in Russian].
16. S. F. Chekmarev and N. V. Stankus, Zh. Tekh. Fiz. **54**, 1576 (1984) [Sov. Phys. Tech. Phys. **29**, 920 (1984)].
17. K. L. Saenger and J. B. Fenn, J. Chem. Phys. **79**, 6043 (1983).
18. A. V. Eremin, V. A. Kochnev, A. A. Kulikovskiĭ, *et al.*, Zh. Prikl. Mekh. Tekh. Fiz., No. 1, 34 (1978).
19. V. A. Kochnev and I. M. Naboko, Zh. Prikl. Mekh. Tekh. Fiz., No. 1, 107 (1980).
20. N. Yu. Bykov and G. A. Luk'yanov, Teplofiz. Aeromekh. **9**, 247 (2002).
21. I. M. Naboko, V. V. Golub, A. V. Eremin, *et al.*, Arch. Mech. **29**, 69 (1977).
22. V. G. Maslennikov and B. M. Dobrynin, Zh. Tekh. Fiz. **51**, 1229 (1981) [Sov. Phys. Tech. Phys. **26**, 698 (1981)].
23. B. M. Dobrynin, V. G. Maslennikov, and V. A. Sakharov, Zh. Tekh. Fiz. **57**, 118 (1987) [Sov. Phys. Tech. Phys. **32**, 69 (1987)].
24. A. E. Zarvin, N. G. Korobeĭshchikov, V. Zh. Madirbaev, *et al.*, Prib. Tekh. Éksp., No. 5, 64 (2000).
25. G. G. Gartvich, V. A. Dudnikov, A. E. Zarvin, *et al.*, Prib. Tekh. Éksp., No. 2, 134 (1997).
26. G. G. Gartvich, A. E. Zarvin, V. V. Kalyada, *et al.*, Prib. Tekh. Éksp., No. 5, 160 (1996).
27. G. G. Gartvich, A. E. Zarvin, V. V. Kalyada, *et al.*, Zh. Prikl. Mekh. Tekh. Fiz. **34** (5), 150 (1993).
28. V. G. Dulov and G. A. Luk'yanov, *Gas Dynamics of Outflow Processes* (Nauka, Novosibirsk, 1984) [in Russian].
29. A. E. Zarvin, N. G. Korobeĭshchikov, V. Zh. Madirbaev, and R. G. Sharafutdinov, Zh. Tekh. Fiz. **71** (4), 141 (2001) [Tech. Phys. **46**, 503 (2001)].
30. B. D. Kay, T. D. Raymond, and J. K. Rice, Rev. Sci. Instrum. **57**, 2266 (1986).
31. W. K. Kang, E. J. Kim, C. J. Choi, *et al.*, Bull. Korean Chem. Soc. **16**, 238 (1995).

Translated by P. Pozdeev

Technical Physics, Vol. 49, No. 8, 2004, pp. 982–986. Translated from Zhurnal Tekhnicheskoĭ Fiziki, Vol. 74, No. 8, 2004, pp. 30–34.
Original Russian Text Copyright © 2004 by Tarasenko, Alekseev, Orlovskiĭ, Shpak, Shunaĭlov.

GAS DISCHARGES, PLASMA

Ultrashort Electron Beam and Volume High-Current Discharge in Air under the Atmospheric Pressure

V. F. Tarasenko*, S. B. Alekseev*, V. M. Orlovskiĭ*, V. G. Shpak, and S. A. Shunaĭlov****
** Institute of High-Current Electronics, Siberian Division, Russian Academy of Sciences, Tomsk, 634055 Russia*
e-mail: VFT@loi.hcei.tsc.ru
*** Institute of Electrophysics, Ural Division, Russian Academy of Sciences, Yekaterinburg, 620016 Russia*

Received April 3, 2003; in final form, December 9, 2003

Abstract—Conditions are studied under which an electron beam and a volume discharge with a subnanosecond rise time of a voltage pulse are produced in air under atmospheric pressure. It is shown that the electron beam appears in a gas-filled diode at the front of the voltage pulse in ~0.5 ns, has a half-intensity duration of ≤0.4 ns and an average electron energy of ~0.6 of the voltage across the gas-filled diode, and terminates when the voltage across the gap reaches its maximum value. The electron beam with an average electron energy of 60 to 80 keV and a current amplitude of ≥70 A is obtained. It is assumed that the electron beam is formed from electrons produced in the gap due to gas ionization by fast electrons when the intensity of the field between the front of the expanding plasma cloud and the anode reaches its critical value. A nanosecond volume discharge with a specific power input of ≥400 MW/cm^3, a density of the discharge current at the anode of up to 3 kA/cm^2, and specific energy deposition of ~1 J/cm^3 over 3 to 5 ns is created. © *2004 MAIK "Nauka/Interperiodica".*

Generation of accelerated electrons and X-rays in gas-filled diodes under elevated pressure was studied by many research groups (see, e.g., review [1] and monograph [2] and references cited therein). However, amplitudes of the electron beam currents obtained in molecular gases were no higher than a few fractions of an ampere [1]. Also, the parameters of the electron beam, the conditions for its formation, and the interpretation of this phenomenon were substantially different in different works. For example, the critical field reported in [1], which is sufficient for runaway of electrons in air under atmospheric pressure, differs from that attained in [2, 3] by a factor of 2 or more. The average energy of electrons in the beam in air under atmospheric pressure in [1] exceeds the maximum voltage across the gap by a factor of 1.5, while it is almost half the maximum voltage in [4, 5]. The effect of appearance of accelerated electrons in the discharge under elevated pressure and their influence on the discharge characteristics has not been adequately investigated and was disregarded in many monographs [6].

It was shown in 2002 [4, 5] that the amplitude of the electron beam produced in a diode filled with helium [4], molecular gases (air, nitrogen), or a CO_2–N_2–He mixture [5, 7] under atmospheric pressure can be substantially increased. In [4], an electron beam was obtained at average values of parameter E/p (E is the electric field strength and p is the gas pressure) that were above the critical values sufficient for creating the effect of electron runaway as well as at relatively small average values of parameter E/p, which were substantially lower than the critical values.

The purpose of this work is to determine the conditions under which a gas-filled diode produces an electron beam with the highest amplitude and to produce a volume discharge with a high specific power input in air under atmospheric pressure.

We used two RADAN-type nanosecond pulse generators, detailed in [8, 9]. Generator 1 (RADAN-303) had a wave impedance of 45 Ω and produced 50- to 170-kV pulses (with an open-circuit voltage of up to 340 kV) with a half-intensity width of ~5 and ~1-ns rise time under matched termination [8]. The voltage across the gas gap could be gradually changed by varying the width of the main discharge gap.

Generator 2 (RADAN-220) had a wave impedance of 20 Ω and formed a ~220-kV pulse with a half-intensity width of ~2 ns at an ~0.3-ns rise time across the discharge gap [9]. The design of the gas-filled diode was the same for both generators. As in the majority of works that study X rays and fast electrons in gas-filled diodes, we used a planar anode and a rod cathode. This gas gap geometry ensured field amplification near the cathode. The cathodes of both generators were designed as a tube made of a 50-μm-thick steel foil 6 mm in diameter, which was fixed on a metal rod of the same diameter, or had the form of a graphite rod 6 mm in diameter with rounded ends. The planar anode, through which the electron beam was extracted, was made of a 45-mm-thick AlBe foil, or a 10-mm-thick Al foil, or a grid with a 50–70% transparency to light. The distance between the cathode and the anode was varied from 13 to 20 mm.

1063-7842/04/4908-0982$26.00 © 2004 MAIK "Nauka/Interperiodica"

Signals picked off from a capacitance voltage divider, collectors, and shunts were observed on a TDS-684B oscilloscope with a bandwidth of 1 GHz and a 5-GS/s (5 samples per 1 ns) sampling rate. The glow of the discharge was photographed by a digital camera.

Based on the variation of voltage pulses across the gas-filled diode and the electron beam current and also on observations of the form of the discharge in the gap as a function of the anode-to-cathode gap length, the cathode type, and the voltage across the gas-filled diode, the following features were discovered.

The electron beam appears on the leading edge of the voltage pulse, its half-intensity duration being no longer than 0.4 ns (Fig. 1). The maximum of the beam current is usually observed after the voltage across the gap attains its maximum. Under optimal conditions, the amplitude of the current behind the foil is higher than 40 A for generator 1 and 70 A for generator 2 (Figs. 1b and 1c). As the voltage amplitude increases, the beam current maximum is displaced towards the beginning of the voltage pulse (Fig. 1a) and the beam terminates on its leading edge at maximal voltages. A decrease in the voltage increases the delay of the electron beam to ~1 ns, and the beam is observed at the beginning of the quasi-stationary phase of the voltage pulse, which is, however, accompanied by a substantial decrease in the beam current amplitude. Figure 2 plots the dependences of the beam current amplitude, the amplitude of the voltage across the gap at the first maximum, and the amplitude of the discharge current at the first maximum. At a fixed distance between the electrodes, the rise time of the voltage pulse, and the gas type and pressure (in our case, air at 1 atm), a rather narrow optimal generator voltage interval exists, in which the maximal amplitudes of the electron beam current behind the foil are observed. The dependences of the voltage across the gap and of the discharge current under these conditions are almost linear (Fig. 2, curves *2* and *3*) despite a noticeable variation in the beam current amplitude. The discharge current appears with a short delay after the voltage is applied to the gap and is 0.3 to 1 ns ahead of the electron beam current observed behind the foil. The magnitude and duration of the discharge current significantly exceed the amplitude and duration of the beam current: for example, for the first generator, at an open-circuit voltage of ~270 kV and a 17-mm-long gap, the current amplitudes are 2400 and 40 A, respectively. After the pulse of the electron beam current terminates, the discharge usually continues in its quasi-stationary phase and has a volume character. Photographs of the discharge glow (Fig. 3) are taken looking from the end for the mesh anode and from the side for the anode made of foil. It is seen that the discharge is of the volume type and bright spots are only seen near the cathode. With increasing generator voltage, bright filamentary channels appear against the background of the volume discharge and a dip in the voltage oscillogram (approximately to half the initial value) is observed (Fig. 1a, curve *2*). In generator 1, when the discharge

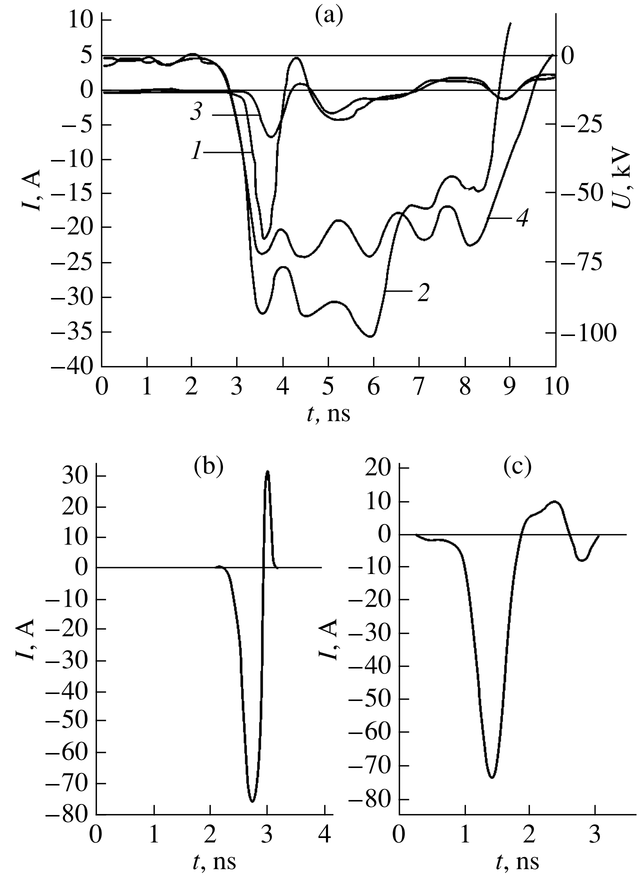

Fig. 1. (a) Oscillograms of (*1*, *3*) current pulses in an electron beam behind a 45-μm-thick AlBe foil and (*2*, *4*) of voltage pulses across the gas-filled diode produced by generator 1 at a diode gap width of d = 16 mm and a generator open-circuit voltage of (*1*, *2*) 260 and (*3*, *4*) 155 kV; (b, c) oscillograms obtained on generator 2 at a diode gap width of d = 16 mm and a collector diameter of (b) 20 and (c) 50 mm.

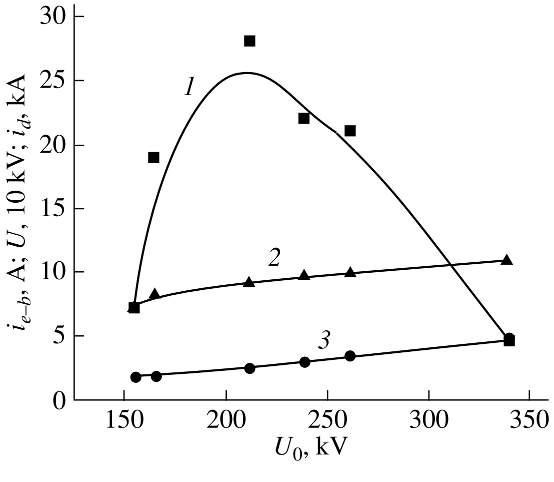

Fig. 2. (*1*) Current of the electron beam behind a 45-μm-thick AlBe foil, (*2*) voltage across the gap, and (*3*) discharge current versus open-circuit voltage for generator *1*.

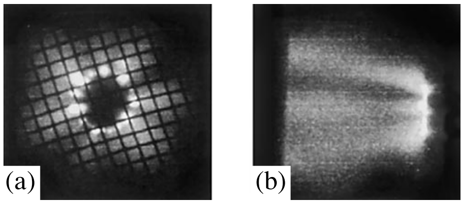

Fig. 3. Discharge glow in the gap photographed from the (a) end and (b) side for generator 2, the mesh size being 1 mm.

retains its volume character for 3 ns, the current density at the anode becomes as high as ~3 kA/cm^2, the specific energy deposition to the gas is ~1 J/cm^3, and the specific power input is ~400 MW/cm^3. At a volume phase duration of 5 ns, the current density at the anode reaches ~1.5 kA/cm^2, the specific power input is ~200 MW/cm^3, and the specific energy deposition to the gas is also ~1 J/cm^3. At the maximum voltage produced by generator 1, the average value of parameter E/p after the termination of the beam current is ~0.08 kV/cm Torr in the quasi-stationary phase. Note that, in the quasi-stationary phase of the volume discharge, which is observed after the breakdown of the gas gap, the voltage across the gap is typically lower than that in the course of the breakdown [2, 10]. Under the conditions of this experiment, a self-sustained discharge was observed in which the voltage across the gap is maximal in the quasi-stationary discharge phase operating in the single pulse mode without preliminary ionization (Fig. 1a, curves *2* and *4*).

Based on the experimental data obtained and an information about familiar processes in gas discharges [1, 2, 6], we believe that, under the conditions of our study, the gas discharge in the gap evolves as follows.

When a high-voltage pulse is applied, the process of avalanche electron multiplication must start on its leading edge, in which the electron concentration grows as $N = N_0\exp(\alpha d)$, where α is the volume ionization coefficient and d is the gap between the electrodes. The number of electrons in the avalanche can increase from a single initial electron by a factor of ~10^8 without forming a streamer [6]. Accordingly, the critical number of electrons in one avalanche is $N_c \approx 10^8$. To create a volume-discharge current of a few kiloamperes, which corresponds to the conditions of Fig. 1a, it is necessary to produce ~10^{14} electrons in the gap in 1 ns. Accordingly, the number N_0 of initial electrons must be ~10^6 or greater. However, the distance x_c at which the avalanche reaches the critical size in air under atmospheric pressure at an electric field strength of ~100 kV/cm, according to the formula $x_c = (\ln N_c)/\alpha$, is only 0.2 mm [2], which is substantially smaller than the length of the gap in the gas-filled diode used in the experiment. At the same time, using the method of interrupted discharge, we observed the entire gap glowing over ~1 ns. In the process of discharge formation over the entire gap in ~1 ns under the above conditions, amplification of the electric field at the cathode, which had the form of a rod with a sharp edge, plays the most important role. When a high-voltage pulse is applied, the electric field at the cathode is noticeably amplified and a part of the initial electrons, in our opinion, gain an energy of ~1 keV. The velocity v_e of an electron with an energy of ~1 keV will be ~1.9×10^9 cm/s. It is known [6] that $v_e = 5.93 \times 10^7(\varepsilon)^{1/2}$, where ε is the electron energy. Then, if the energy loss of electrons moving in the gas with an energy of ~1 keV is compensated by the increasing electric field, the electrons will fly through the gap in ~0.8 ns, which corresponds to the rise time of the current through the gap. It was shown [11] that fast electrons can cover long distances in gas gaps at a weak electric field as well. For this situation to occur, the electron energy must be higher than the energy corresponding to the maximum inelastic cross section for the gas that fills the gap. Moreover, it was shown [12] that the Paschen curve contains an additional upper branch, which describes the absence of the self-sustained discharge at strong electric fields.

The initial electrons are produced under these conditions at the cathode due to the electric field amplification and explosive electron emission. In experiments with an interrupted discharge, we observed a multitude of small bright points on the cathode at the beginning of the voltage pulse. The number of these points decreased with increasing operating time lag of the chopping gap, while their size and brightness increased. We think that part of the initial electrons are accelerated to an energy of ~1 keV due to the electric field amplification near the cathode. Further, as they move towards the cathode, these electrons ionize the gas in the gap and produce initial electrons, from which more and more avalanches evolve and contribute to the increase in the current across the gap. In this way, a plasma cloud is formed, which expands towards the anode with the velocity of electrons, which acquire an energy of ~1 keV. The electrons whose energy is substantially higher than 1 keV cross the discharge gap in fractions of a nanosecond and possess a lower ionizing power. As the plasma cloud expands, on the one hand, the space charge screens sharp edges of the cathode and, on the other hand, the positive charge of the ions, which remain at rest after the departure of electrons to the anode, amplifies the electric field near the cathode. To accurately account for the contribution of these processes and also to find the electron velocity distribution function and determine the dynamics of the electron distribution over the gap, a theoretical modeling is necessary. To cover the gap upon reaching the anode in ~1 ns under the conditions of this experiment, the plasma cloud must expand towards the anode at a rate of ~1.6×10^9 cm/s. Because the region occupied by the plasma expands towards the anode and its conductance is higher than that of the remaining part of the gap, the electric field between the plasma boundary and the anode will continuously grow. As a result, the expansion of the region occupied by the plasma will give rise to the field between the plasma cloud and the anode, which exceeds the critical value (equal to 0.8 to 3.5 kV/cm Torr high in air according to [2, 3]) so that an electron beam will be formed with an amplitude of a few tens of amperes. Since the field between the front of the moving plasma and the anode is strong, the gap will be "bridged" in a very short time (in fractions of a nanosecond) after the critical field is reached, which is precisely the circumstance that determines the duration of the beam current. Clearly, the energy of the electrons will be lower than that of the electrons accelerated in vacuum at the same voltage across the gap, because part of the voltage drops across the expanding plasma, which has a nonzero resistance. Figure 4 shows the energy distribution of electrons, where *I* is the number of electrons in a particular energy interval. The distribution was obtained from the amplitudes of the maximum current behind a set of Al foils with different thicknesses. One foil was 10 μm thick. The average energy of the electrons in the mode under study was 65 keV. If we take a number of electrons that comprise half the number of electrons with the average energy, their energy will be 30 to 95 keV. This mode of formation of the beam current in a gas under an increased pressure substantially differs from that described in [1], where the beam current under similar conditions was two orders of magnitude lower and the average electron energy was 1.5 times higher than the maximum voltage across the gap. Note that, when the avalanches grow, the plasma front consists of electrons. Due to this fact, the space charge of the electron cloud imparts an additional acceleration towards the anode to part of the electrons that are near the boundary of the electron cloud. The energy of some of the electrons may be higher than the voltage across the diode [1]. It is clear that the number of electrons in the beam must be much smaller than the number of electrons in the avalanches and the number of electrons with an energy higher than the voltage applied must be much smaller than the number of electrons with the average energy in the beam. The interruption of the beam current at the maximum voltage across the gap is due to the fact that, after the beam electrons reach the anode, the electric field in the gap becomes more uniform and the field gradient is insufficient for electron runaway. In the experiment (Fig. 1a), the beam current behind the foil on the flat part of the voltage pulse is observed only at the beginning of the flat top of the pulse.

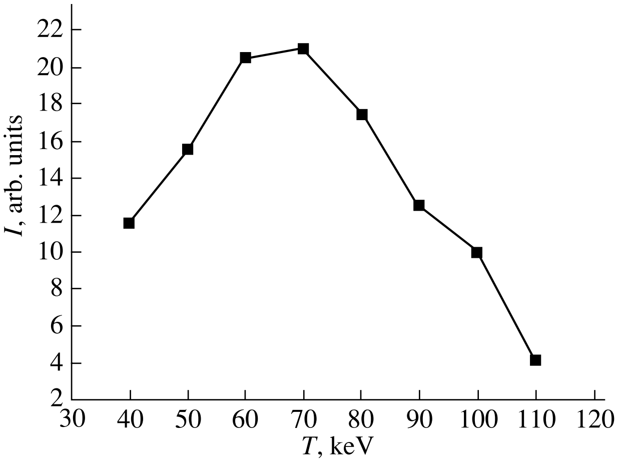

Fig. 4. Energy distribution of the beam electrons at an air pressure in the diode of 1 atm, obtained by the method of foils on generator 1 at an open-circuit voltage of 270 kV. The gap length in the diode is d = 17 mm.

The volume character of the discharge in the gap is preserved during the whole length of the voltage pulse (Fig. 1, curve *4*) due to the avalanche nature of the discharge in the gap in the first stage and to the preionization of the gap by fast electrons produced near the cathode. Stabilization of the discharge current amplitude at high average fields in the gap (E/p ~ 0.05–0.08 kV/cm Torr) is apparently due to the increase in energy loss of the electrons when they pass through the plasma produced in the course of the discharge evolution on the leading edge of the voltage pulse and also due to the recombination process. To our knowledge, the discharge mode studied has not been described in the literature [1, 2].

In conclusion, note that the experimental data obtained allow us to improve the understanding of the physics of the pulsed breakdown processes in gas gaps under high overvoltages. This mode of generating ultrashort electron beams in gas-filled diodes should find application in designing simple compact accelerators of subnanosecond electron beams and sources of subnanosecond X-ray pulses, while the space charge would be widely used in pulsed dense gas lasers and pulsed sources of high-power spontaneous radiation. At present, the Institute of High-Current Electronics of the Russian Academy of Sciences (Siberian Division) has an electron accelerator that forms an electron beam in air at atmospheric pressure with a beam current higher than 70 A, a half-intensity duration of ~0.3 ns, and an average electron power of ~70 keV. A small-size CO_2 laser with a radiation energy of 18 mJ, in which preionization is performed by a beam produced in the same gas mixture, was also developed.

ACKNOWLEDGMENTS

The authors are grateful to M.I. Yalandin and A.V. Fedenev for their help.

REFERENCES

1. L. P. Babich, T. V. Loĭko, and V. A. Tsukerman, Usp. Fiz. Nauk **160** (7), 49 (1990) [Sov. Phys. Usp. **33**, 521 (1990)].
2. Yu. D. Korolev and G. A. Mesyats, *The Physics of Pulsed Breakdown* (Nauka, Moscow, 1991) [in Russian].

3. Yu. E. Kolyada, Pis’ma Zh. Tekh. Fiz. **26** (16), 52 (2000) [Tech. Phys. Lett. **26**, 721 (2000)].
4. S. B. Alekseev, V. M. Orlovskiĭ, V. F. Tarasenko, *et al.*, Pis’ma Zh. Tekh. Fiz. **29** (16), 45 (2003) [Tech. Phys. Lett. **29**, 679 (2003)].
5. S. B. Alekseev, V. M. Orlovskiĭ, V. F. Tarasenko, *et al.*, Pis’ma Zh. Tekh. Fiz. **29** (10), 29 (2003) [Tech. Phys. Lett. **29**, 411 (2003)].
6. Yu. P. Raĭzer, *Gas Discharge Physics* (Nauka, Moscow, 1992; Springer-Verlag, Berlin, 1991).
7. V. F. Tarasenko, V. M. Orlovskiĭ, and S. A. Shunaĭlov, Izv. Vyssh. Uchebn. Zaved. Fiz. **46** (3), 94 (2003).
8. M. I. Yalandin and V. G. Shpak, Prib. Tekh. Éksp., No. 3, 5 (2001).
9. F. Ya. Zagulov, A. S. Kotov, V. G. Shpak, *et al.*, Prib. Tekh. Éksp., No. 2, 146 (1989).
10. V. V. Savin, V. F. Tarasenko, and Yu. I. Bychkov, Zh. Tekh. Fiz. **46** (1), 198 (1976) [Sov. Phys. Tech. Phys. **21**, 113 (1976)].
11. L. P. Babich, E. N. Donskoĭ, K. F. Zelenskiĭ, *et al.*, Dokl. Akad. Nauk **383**, 31 (2002) [Dokl. Phys. **47**, 1 (2002)].
12. A. N. Tkachev and S. I. Yakovlenko, Pis’ma Zh. Éksp. Teor. Fiz. **77**, 264 (2003) [JETP Lett. **77**, 221 (2003)].

Translated by A. Khzmalyan

Technical Physics, Vol. 49, No. 8, 2004, pp. 987–992. Translated from Zhurnal Tekhnicheskoĭ Fiziki, Vol. 74, No. 8, 2004, pp. 35–40.
Original Russian Text Copyright © 2004 by Kostyrya, Skakun, Tarasenko, Fedenev.

GAS DISCHARGES, PLASMA

Optical Characteristics of the Plasma of a Nanosecond Atmospheric-Pressure Volume Discharge in a Nonuniform Electric Field

I. D. Kostyrya, V. S. Skakun, V. F. Tarasenko, and A. V. Fedenev

Institute of High-Current Electronics, Siberian Division, Russian Academy of Sciences,
Akademicheskiĭ pr. 4, Tomsk, 634055 Russia

Received August 18, 2003; in final form, January 21, 2004

Abstract—Optical characteristics of the plasma of nanosecond volume discharges in air, nitrogen, krypton, argon, neon, and Ar/N_2 and Ar/Xe mixtures at elevated pressures are investigated. The discharges are excited in a gap with a cathode of small curvature radius. The waveforms and spectra of plasma emission from discharges in different gases in the 230- to 600-nm spectral range are measured. Optical generation in an Ar/Xe mixture is achieved at an active length of 1.5 cm. A comparison is performed of the spectral characteristics of the emission from nitrogen, krypton, argon, and neon excited by a volume discharge in a nonuniform electric field, by a nanosecond electron beam, and by a pulsed volume discharge in a uniform electric field at a high initial voltage. *© 2004 MAIK “Nauka/Interperiodica”.*

1. INTRODUCTION

Volume discharges in atomic and molecular gases at elevated pressures are usually excited by preionizing the discharge gap with a source of ionizing radiation [1]. The plasma of volume discharges is widely used in pulsed lasers [2]. It is well known [3, 4] that an atmospheric-pressure volume discharge in a nonuniform electric field can also be excited without preionization, by applying a nanosecond voltage pulse with a steep front (fractions of a nanosecond) to the discharge gap. In [5, 6], X-ray emission from nanosecond atmospheric-pressure discharges in air [5] and helium [6] was observed in a system with a point cathode and plain anode. Later, accelerated electron beams with energies from several tens to hundreds of kiloelectronvolts were observed under similar conditions [4, 7–12].

In systems with a cathode of small curvature radius, pulsed nanosecond volume discharges excited in atomic and molecular gases at elevated pressures in a nonuniform electric field have unique features and find wide application. In particular, such discharges are used for preionization in lasers pumped by a self-sustained discharge at an elevated pressure [13, 14] and for the generation of electron beams in gas diodes [9–12].

In [15], this type of volume discharge in nitrogen was used to create a UV radiation source with a short pulse duration (below 3 ns), and a total (into a solid angle of 4π) emission power of ~10 kW in the wavelength range of 340–400 nm (the second positive system of nitrogen) was achieved. However, the estimated efficiency of this source, which was obtained by us from the waveforms of the current and voltage presented in [15], turned out to be very low. The efficiency of converting the excitation power into spontaneous emission of the second positive system of nitrogen ($C^3\Pi_u$–$B^3\Pi_g$ transitions) is lower than 0.01%, i.e., more than one order of magnitude lower than the efficiency of an electric-discharge nitrogen laser [16], usually radiating at a single wavelength of 337.1 nm. It is well known that the total (into a solid angle of 4π) efficiency of spontaneous radiation sources is usually higher than the laser efficiency. Thus, the power and efficiency of the spontaneous emission of the second positive system of nitrogen in a pulsed source [17], excited by a transverse discharge with UV preionization, is more than one order of magnitude higher than the efficiency of the gas-discharge source described in [15].

The aim of this study was to investigate the optical characteristics of the plasma of a nanosecond volume discharge excited in a nonuniform electric field in air, nitrogen, krypton, argon, neon, and Ar/Xe and Ar/N_2 mixtures at elevated pressures and to compare the experimental data with the known optical characteristics of the plasma generated by a nanosecond electron beam [18–20], by a self-sustained discharge with UV preionization [18, 20], and by an RF discharge [21] with a duration from a few nanoseconds to a few tens of nanoseconds.

2. EXPERIMENTAL FACILITY AND TECHNIQUE

In experiments, we used two RADAN generators of nanosecond voltage pulses (see [22, 23] for details). The first generator (RADAN-303) with a wave resistance of 45 Ω generated 50- to 170-kV pulses at a matched load (the open-circuit voltage was up to 340 kV). The full width at half-maximum (FWHM) of

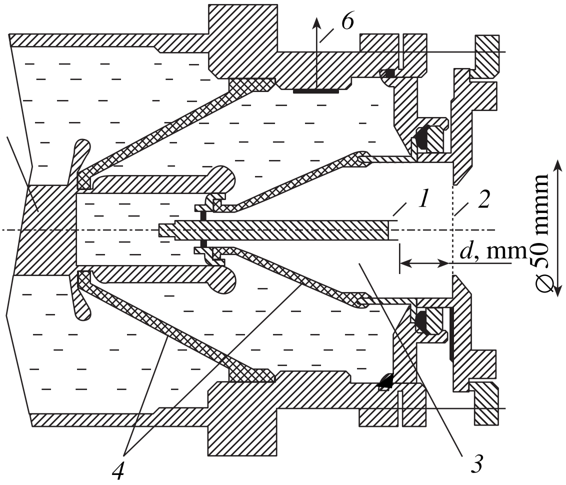

Fig. 1. Design of the high-voltage output of the generator and the gas diode: (*1*) cathode, (*2*) foil or grid, (*3*) gas diode, (*4*) insulators, (*5*) potential electrode of the generator, and (*6*) capacitive voltage divider.

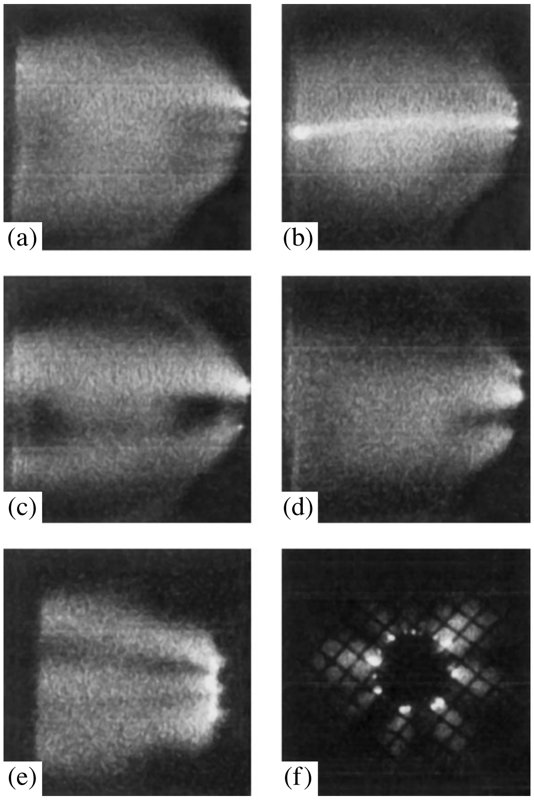

Fig. 2. Discharge glow from discharges in (a, b) argon, (c, d) krypton, and (e, f) air. Photographs (a–e) are taken in the transverse direction and photograph (f) is taken along the discharge axis (through the grid anode). The gas pressure is (a, c, e, f) 1, (b) 0.75, and (d) 0.25 atm. The second generator with an extended gas diode is used; the length of the discharge gap is 16 mm.

the voltage pulses was ~5 ns, the voltage rise time being ~1 ns [22]. The voltage across the discharge gap could be varied smoothly by varying the length of the main spark gap.

A second generator (RADAN-220) with a wave resistance of 20 Ω generated voltage pulses with an amplitude of up to 220 kV across the discharge gap. The FWHM of the voltage pulses was ~2 ns, the voltage rise time being ~0.3 ns [23]. The design of the gas diode was the same for both generators [24] (Fig. 1). As in most studies devoted to the generation of X rays and fast electrons in gas diodes, we used a plane anode and a cathode with a small curvature radius; this ensured an additional amplification of the field near the cathode. For both generators, we usually used a cathode shaped as a 6-mm-diameter tube made of a 50-μm steel foil. The tube was mounted on a metal rod of the same diameter. The plane anode, through which the electron beam produced in the gas diode was output [9–12, 24], was made of either a 45-μm AlBe foil or a grid with an optical transmittance of 20–70%. The distance between the cathode and anode was varied from 13 to 20 mm. When measuring the waveforms and spectra of plasma emission and photographing the discharge in the transverse direction to the cathode axis, the gas diode was extended by 3 cm toward the foil, which was also displaced by 3 cm. For this purpose, the cathode holder and the casing of the gas diode were lengthened and diagnostic holes were made in the side wall of the latter. In some experiments, the discharge gap was placed inside a gas chamber with windows or mirrors; this allowed us to pump out the gas and to vary the composition and pressure of the working gas in the gap.

To measure signals from capacitive voltage dividers, collectors, and shunts, we used a TDS-684B oscilloscope with a bandwidth of 1 GHz and time resolution of 5 GS/s (five spots per 1 ns) or a TDS-334 oscilloscope with a bandwidth of 0.3 GHz and time resolution of 2.5 GS/s (five spots per 2 ns). The discharge glow was photographed with a digital camera. The emission spectra were recorded on the RF-3 film with the help of an ISP-30 spectrograph.

3. EXPERIMENTAL RESULTS

The observations of the discharge glow and the measurements of the emission spectra, the discharge current, and the voltage pulses across the gas diode show the following:

Over a wide range of experimental conditions, a volume discharge in the form of diffuse cones or jets is excited between the anode and the sharp edge of the tubular cathode (Fig. 2). It can be seen that an atmospheric-pressure discharge is volume in character; bright spots are usually observed only near the cathode. When the length of the discharge gap was decreased, a point cathode was used, or the pressure was varied, we observed individual channels against the background of a diffuse discharge (Fig. 2b) and hot spots at both the cathode and the anode. Under nonoptimal conditions (e.g., at short gaps), the volume discharge can transform into a spark. As the generator voltage is increased at the optimal gap length, lighter filamentous channels also appear against the background of the volume discharge and a step appears in the waveform of the voltage pulse. However, a characteristic feature of a discharge excited in a nonuniform electric field in different gases at atmospheric pressure is that it is volume in character. Figures 2e and 2f show the photographs of the glow of a discharge in air. In the photographs, which were taken along the discharge axis in the case of a grid anode and in the transverse direction in the case of a foil anode, one can see characteristic volume jets.

Figure 3 shows the waveforms of the voltage and the beam current behind the foil (the time resolution is ~0.3 ns). The conditions for the formation of an electron beam in the gas diode are described in detail in [9–12, 24]. The discharge current signal appears at the leading edge of the voltage pulse with a very short time delay with respect to the instant at which the voltage is applied to the gap (the available equipment did not allow us to exactly measure this time delay). In some operating regimes, a capacitive spike in the waveform of the discharge current appeared at the leading edge of the voltage pulse during the charging of the interelectrode gap. The magnitude and duration of the discharge current depend on the pressure and the sort of the working gas, the interelectrode gap length, and the type and output voltage of the generator. The maximum discharge current is as high as a few kiloamperes in the case of a volume discharge. Thus, for the first generator, the current amplitude was ~4.7 kA at an open-circuit voltage of ~340 kV. With this generator, provided that a volume discharge lasts for 3 ns, the current density at the anode reaches 3 kA/cm^2, the specific energy deposited in a discharge is ~1 J/cm^3, and the specific deposited power is 400 MW/cm^3. When the volume stage of the discharge lasts for 5 ns, the current density at the anode reaches ~1.5 kA/cm^2, the specific deposited power is ~200 MW/cm^3, and the specific energy deposited in a discharge is ~1 J/cm^3. At the maximum voltage of the first generator, the mean value of the parameter E/p after the end of the beam current was ~0.08 kV/(cm torr) in the quasi-steady phase. Note that, for the quasi-steady phase of a volume discharge (which is established after the breakdown of the gas gap), the voltage across the gap is usually lower than before breakdown [16, 25]. In the case of a cathode with a small curvature radius, the discharge operated in a self-sustained regime. In this regime, in the case of single pulses and without gas preionization, the gap voltage was maximum in the quasi-steady phase of the discharge (Fig. 3). In [11], it was proposed to call this type of discharge the volume avalanche discharge initiated by an electron beam (VADIEB). When discussing the results obtained, we will explain the mechanism for the formation of a volume discharge.

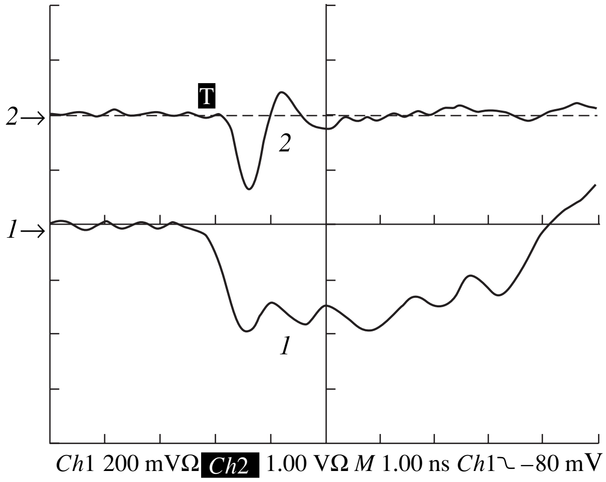

Fig. 3. Waveforms of (*1*) the voltage pulses at the gas diode and (*2*) the current of an electron beam behind the foil. The voltage scale is 45 kV/division, the current scale is 20 A/division, and the time scale is 1 ns/division. The first generator is used; the length of the discharge gap is 16 mm.

Figure 4 shows a typical waveform of the discharge current and the waveforms of the emission pulses in the 200- to 650-nm spectral range. The emission was recorded by an FÉK-22 photodiode for different gases at a pressure of ~1 atm. Figure 5 shows the dependences of the emission intensity on the gas pressure. An increase in the pressure results in an increase in the maximum emission power in all gases. Figure 5 (curve *5*) also shows the FWHM of the emission pulse as a function of the nitrogen pressure. The most powerful (Fig. 4d) and the shortest (Figs. 4, 5; curve *5*) emission pulses were observed in pure nitrogen. However, the efficiency of spontaneous emission from a VADIEB in the 200- to 600-nm spectral range both in nitrogen and other gases or gas mixtures was rather low. When nitrogen at a pressure of 1 atm was excited by the second generator, the emission power was ~36 kW, which was four times higher (due to the higher power of the generator) than in [15]. In this case, however, the emission efficiency of the second positive system of nitrogen (~0.01%) did not increase. In mixtures of nitrogen with argon, the duration of the emission pulses of the second positive system of nitrogen was substantially larger than in pure nitrogen, whereas the emission intensity was more than one order of magnitude lower (Figs. 4d, 4e).

Our spectral measurements (as well as those in [15]) show that, in nitrogen, the second positive nitrogen system is most intense (within this system, the most intense are the 337.1- and 358-nm bands). In argon/nitrogen mixtures, the second positive nitrogen system is also dominant and the less intense emission at a wavelength of 308 nm can be attributed to the emission of OH molecules and OH$^+$ ions.

In neon, the 600-nm emission, which is related to atomic transitions, is dominant. The wide near-UV

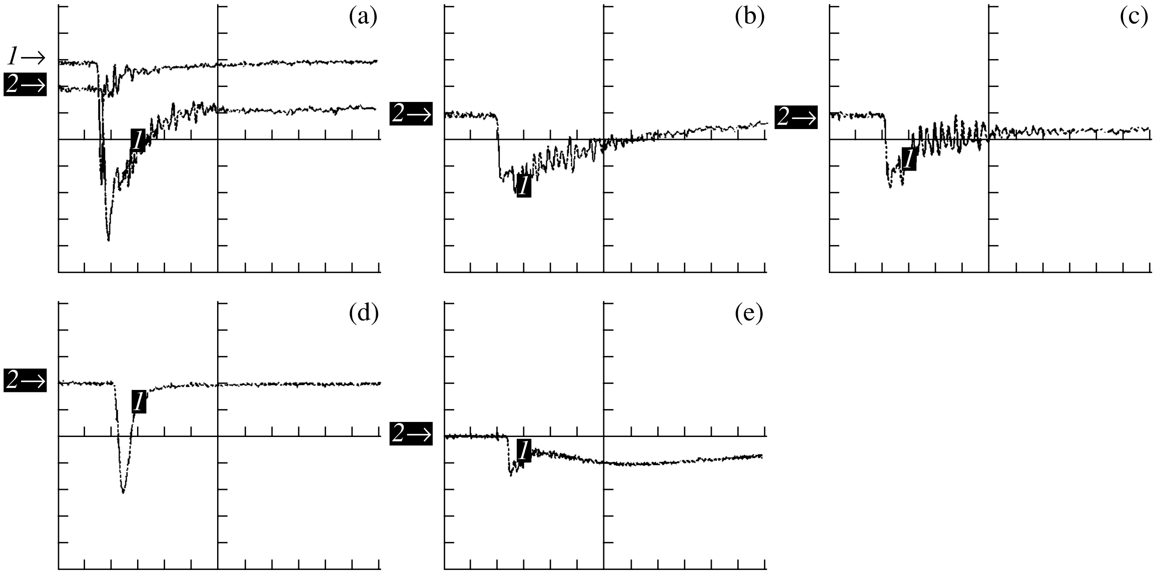

Fig. 4. Waveforms of (a) the discharge current (upper curve) and the emission intensity from a discharge in (a) neon (lower curve), (b) krypton, (c) argon, (d) nitrogen, and (e) the Ar : N_2 = 100 : 1 mixture at a pressure of ~1 atm: (a) the current scale is 3.4 kA/division, the voltage scale is 0.2 V/division, the time scale is 10 ns/division; (b, c) the voltage scale is 0.2 V/division and the time scale is 10 ns/division; (d) the voltage scale is 20 V/division and the time scale is 10 ns/division; and (e) the voltage scale is 0.5 V/division and the time scale is 20 ns/division. The second generator with an extended gas diode is used; the length of the discharge gap is 16 mm.

emission band that is clearly seen when neon is excited by an electron beam [19], a self-sustained discharge at high initial voltages [20], or an RF discharge [21] was not observed in a VADIEB at the same total deposited energies. We also observed no wideband emission from discharges in krypton and argon [18, 19]. The experiments show that the intensity of wideband emission from a VADIEB in krypton, argon, and neon is substantially lower than from discharges excited by an electron beam. The same follows from the comparison of the VADIEB emission spectrum with the emission spectrum of a self-sustained atmospheric-pressure discharge in neon with UV preionization at high initial voltages. Note that, in krypton and argon excited by a self-sustained discharge with UV preionization at high initial voltages, the discharge contracts at a pressure of 1 atm [18] and the emission of the third continua is not observed.

4. DISCUSSION OF THE RESULTS

An analysis of the measured VADIEB parameters allows us to answer the two main questions: (i) why is the volume discharge generated at elevated pressures and in the presence of cathode spots and (ii) why are the emission efficiency of the second positive nitrogen system in a VADIEB and the intensity of the wideband emission of the third continua in inert gases low?

We believe that, in the case of a cathode with a small curvature radius, the process of the formation of a volume discharge can be described as follows. When a high-voltage pulse is applied to the discharge gap, the electric field near the cathode is amplified as early as at the leading edge of the voltage pulse. The electric field is also amplified after cathode spots are formed from plasma bunches produced by explosive electron emission. In experiments with chopped discharges, we observed a lot of small plasma objects at the cathode during the leading edge of the voltage pulse. The number of these objects decreased as the time delay of the

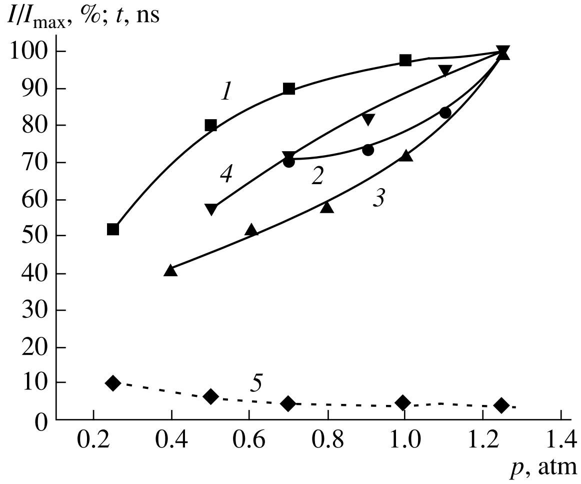

Fig. 5. Emission intensity from a discharge in (*1*) nitrogen, (*2*) neon, (*3*) krypton, and (*4*) argon as a function of the pressure and (*5*) the FWHM of the emission pulse as a function of the nitrogen pressure. The second generator with an extended gas diode is used; the length of the discharge gap is 16 mm.

operation of the chopping spark gap decreased, whereas their size and brightness increased. It is well known [1] that cathode spots can provide electron emission from the cathode that is sufficient to achieve discharge currents of 1–10 kA and higher.

Because of the field amplification and the rapid increase in the gap voltage at the leading edge of the voltage pulse, a fraction of electrons in the cathode region pass into the runaway regime; i.e., the electrons gain an energy that is larger than the energy corresponding to the maximum ionization cross section. Moving toward the anode, these electrons preionize the gas. Note that the fact that the amplification of the electric field at the point cathode and the high growth rate of the voltage lead to the generation of high-energy electrons was pointed out by us in [21]. Thus, the formation of a volume discharge in a nonuniform electric field is caused by the preionization of the working gas by fast electrons produced due to the field amplification at the cathode and cathode spots and by the overlap of the electron avalanches, whose density is maximum near the cathode. In this case, due to a rather intense preionization by fast electrons (by an electron beam), the gap voltage is maximum in the quasi-steady phase of a discharge ($E/p \sim 0.05$–0.08 kV/(cm torr)). A comparison of the quasi-steady values of the parameter E/p with the E/p values observed in a volume discharge at high initial overvoltages and high current densities [25] shows that they differ only slightly.

The low emission efficiency of the second positive system of nitrogen and the third continua in the case of excitation by a VADIEB in comparison to the excitation by a pulsed volume discharge with a high initial gap voltage is related to the lower maximum values of the reduced field, $E/p \sim 0.05$–0.08 kV/(cm torr), whereas a value of $E/p \sim 0.1$–0.2 kV/(cm torr) is needed for the efficient excitation of the second positive nitrogen system. Even higher values of E/p and higher electron energies are required to efficiently excite the upper levels that determine the emission of the third continua of noble gas ions [19].

Nevertheless, the electron temperature that is achieved in a VADIEB can be optimal for some pulsed lasers operating with dense gases, as well as for sources of spontaneous emission. In particular, it can be optimal for lasers operating on atomic xenon transitions; in this case, there is a channel of populating the upper laser level by step excitation and ionization [26]. To check this assumption, mirrors were placed in the chamber. The reflection coefficients of the mirrors at a wavelength of 1.73 μm were 99 and 98%. Accordingly, the transmittance of the second mirror was ~2%. The length of the active region was ~1.5 cm, which, however, was insufficient to achieve stable generation in an Ar/Xe mixture at a pressure of ~1 atm. Figure 6 shows waveforms of the discharge current and the emission pulses.

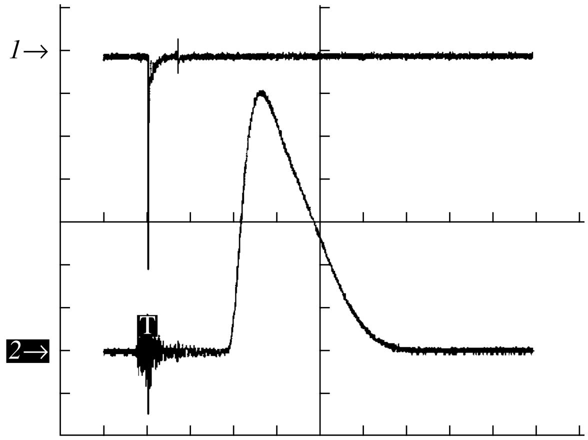

(*1*) [TDS-3032] *CH*1 10 V 200 ns
(*2*) [TDS-3032] *CH*2 50 V 200 ns

Fig. 6. Waveforms of the discharge current (upper curve) and the emission intensity (lower curve) in the Ar : Xe = 240 : 1 mixture at a pressure of ~1.2 atm. The time scale is 200 ns/division. The second generator with an extended gas diode is used; the length of the discharge gap is 16 mm.

Note that, in noble gases excited by an electron beam, it is easy to observe the emission of the third continua [19, 20]. This is explained by the fact that, in the case of excitation by an electron beam generated by a standard accelerator, the number of fast electrons in a plasma (at the same specific deposited energies) is substantially greater than in a VADIEB.

5. CONCLUSIONS

The results of our experiments allow us to draw the following conclusions:

(i) The optical characteristics of the plasma of a VADIEB differ substantially from those of a plasma produced in the same gases and gas mixtures excited by either an electron beam or a volume discharge with a high initial voltage (overvoltage) across the gap. The average electron temperature in a VADIEB is relatively low; this results in the low emission efficiency of the second positive system of nitrogen and the third continua of noble gases.

(ii) The quasi-steady phase of a VADIEB is established at relatively low initial voltages; this is caused by the generation of fast electrons near the cathode. The number of these electrons is sufficient to preionize the gap and to excite a volume discharge. However, at the same specific deposited energies, the number of fast electrons in a VADIEB is substantially smaller than in a plasma produced by an electron beam generated by a standard accelerator. As a result, the efficiency of the wideband emission of the third continua of krypton, argon, and neon is substantially lower.

(iii) VADIEBs can be used to achieve lasing in active media and to create spontaneous radiation sources that do not require too high average electron temperatures, e.g., radiation sources for pumping Ar/Xe lasers.

(iv) An important characteristic of the VADIEB is the possibility of achieving high specific deposited powers (up to 400 MW/cm^3), high current densities (up to 3 kA/cm^2 near the anode), and high specific deposited energies (~1 J/cm^3 over 3–5 ns). Note that these parameters are not limiting and can be increased.

In conclusion, we propose to use the term VADIEB for the regime of a pulsed volume discharge in a nonuniform electric field at elevated pressures. VADIEB is characterized by the high deposited energy and the high deposited pulsed power, which can be varied by varying the quasi-steady value of the parameter E/p and the discharge current density.

ACKNOWLEDGMENTS

We thank S.A. Shunaĭlov for his assistance in carrying out the experiments.

REFERENCES

1. Yu. D. Korolev and G. A. Mesyats, *The Physics of Pulsed Breakdown* (Nauka, Moscow, 1991) [in Russian].
2. G. A. Mesyats, V. V. Osipov, and V. F. Tarasenko, *Pulsed Gas Lasers* (Nauka, Moscow, 1991; Opt. Eng. Press, Washington, 1995).
3. L. V. Tarasova and L. N. Khudyakova, Zh. Tekh. Fiz. **39**, 1530 (1969) [Sov. Phys. Tech. Phys. **14**, 1148 (1969)].
4. L. P. Babich, T. V. Loĭko, and V. A. Tsukerman, Usp. Fiz. Nauk **160** (7), 49 (1990) [Sov. Phys. Usp. **33**, 521 (1990)].
5. Yu. L. Stankevich and V. G. Kalinin, Dokl. Akad. Nauk SSSR **177** (1), 72 (1967) [Sov. Phys. Dokl. **12**, 1042 (1967)].
6. R. C. Noggle, E. P. Krider, and J. R. Wayland, J. Appl. Phys. **39**, 4746 (1968).
7. L. V. Tarasova, L. N. Khudyakova, T. V. Loĭko, and V. A. Tsukerman, Zh. Tekh. Fiz. **44**, 564 (1974) [Sov. Phys. Tech. Phys. **19**, 351 (1974)].
8. L. P. Babich, T. V. Loĭko, and L. V. Tarasova, Zh. Tekh. Fiz. **48**, 1617 (1978) [Sov. Phys. Tech. Phys. **23**, 915 (1978)].
9. S. B. Alekseev, V. M. Orlovskiĭ, and V. F. Tarasenko, Pis'ma Zh. Tekh. Fiz. **29** (10), 29 (2003) [Tech. Phys. Lett. **29**, 411 (2003)].
10. S. B. Alekseev, V. M. Orlovskiĭ, V. F. Tarasenko, *et al.*, Pis'ma Zh. Tekh. Fiz. **29** (16), 45 (2003) [Tech. Phys. Lett. **29**, 679 (2003)].
11. V. F. Tarasenko, V. M. Orlovskiĭ, and S. A. Shunaĭlov, Izv. Vyssh. Uchebn. Zaved. Fiz. **46** (3), 94 (2003).
12. V. F. Tarasenko, S. I. Yakovlenko, V. M. Orlovskiĭ, *et al.*, Pis'ma Zh. Éksp. Teor. Fiz. **77**, 737 (2003) [JETP Lett. **77**, 611 (2003)].
13. A. I. Pavlovskiĭ, V. S. Bosamykin, V. I. Karelin, and V. S. Nikol'skiĭ, Kvantovaya Élektron. (Moscow) **3**, 601 (1976).
14. S. N. Buranov, V. V. Gorokhov, V. I. Karelin, *et al.*, Kvantovaya Élektron. (Moscow) **18**, 891 (1991).
15. L. P. Babich, T. V. Loĭko, and L. V. Tarasova, Prib. Tekh. Éksp., No. 1, 203 (1977).
16. V. F. Tarasenko, Kvantovaya Élektron. (Moscow) **31**, 489 (2001).
17. B. A. Koval', V. S. Skakun, V. F. Tarasenko, *et al.*, Prib. Tekh. Éksp., No. 4, 244 (1992).
18. V. S. Skakun, V. F. Tarasenko, and E. A. Fomin, Zh. Prikl. Spektrosk. **56**, 331 (1992).
19. A. M. Boĭchenko, V. F. Tarasenko, E. A. Fomin, and S. I. Yakovlenko, Kvantovaya Élektron. (Moscow) **20**, 7 (1993).
20. M. I. Lomaev, V. S. Skakun, V. F. Tarasenko, and A. V. Fedenev, Proc. SPIE **4071**, 291 (2000).
21. V. F. Tarasenko, A. S. Tobolkin, O. G. Bashagurov, *et al.*, Izv. Vyssh. Uchebn. Zaved. Fiz., No. 10, 32 (1995).
22. M. I. Yalandin and V. G. Shpak, Prib. Tekh. Éksp., No. 3, 5 (2001).
23. F. Ya. Zagulov, A. S. Kotov, V. G. Shpak, *et al.*, Prib. Tekh. Éksp., No. 2, 146 (1989).
24. V. F. Tarasenko, V. G. Shpak, S. A. Shunaĭlov, *et al.*, Pis'ma Zh. Tekh. Fiz. **29** (21), 1 (2003) [Tech. Phys. Lett. **29**, 879 (2003)].
25. V. V. Savin, V. F. Tarasenko, and Yu. I. Bychkov, Zh. Tekh. Fiz. **46**, 198 (1976) [Sov. Phys. Tech. Phys. **21**, 113 (1976)].
26. V. F. Tarasenko, A. V. Fedenev, and V. S. Skakun, Kvantovaya Élektron. (Moscow) **26**, 209 (1999).

Translated by E. Satunina

Technical Physics, Vol. 49, No. 8, 2004, pp. 993–997. Translated from Zhurnal Tekhnicheskoĭ Fiziki, Vol. 74, No. 8, 2004, pp. 41–44.
Original Russian Text Copyright © 2004 by G. Masharov, S. Masharov.

SOLIDS

Solubility of Substitutional Impurities in Decomposing Alloys

G. S. Masharov and S. I. Masharov
Ural State Technical University, ul. Mira 19, Yekaterinburg, 620002 Russia

Received May 22, 2003; in final form, January 29, 2004

Abstract—Solubility of substitutional impurities in decomposing alloys with a cubic structure is calculated. The effect of elastic lattice vibrations on the decomposition and solubility is taken into account. It is shown that the temperature that corresponds to the peak in the decomposition curve is increased and the range of the biphase states is widened if the phonon effects are taken into consideration. The dependence of solubility on the decomposition parameter is determined; several particular cases of this dependence are analyzed. © *2004 MAIK "Nauka/Interperiodica".*

At present, there is a well-developed theory of solubility of substitutional impurities in ordering alloys [1]; in terms of this theory, the dependences of the solubility on the temperature, the alloy composition, the degree of the long-range order, the value of spontaneous magnetization, and other parameters, were established. It is of interest to generalize this theory to the case of decomposing alloys, i.e., the systems in which precipitation of several phases (in the simplest case, of two phases) occurs with decreasing temperature.

In this study, we calculate the solubility of the substitutional impurity C in a binary decomposing alloy A–B with the cubic structure. We consider the simplest model: the A–B alloy is in contact with a donor crystal C that has the same structure as the solvent; the interaction is taken into account only within the first coordination sphere; it is assumed that the solubility of atoms C is not high, i.e., the content of atoms C in the phases is much smaller than unity; and is also assumed that two phases with the composition changed in comparison with the initial concentration of atoms A and B precipitate in the course of decomposition.

We represent the free energy of the entire system as the sum of the configuration-related (F_1) and phonon-related (F_2) terms, i.e.,

$$F = F_1 + F_2. \tag{1}$$

Designating the number of atoms of the α type in the ith phase ($i = 1, 2$) by $N_\alpha^{(i)}$ ($\alpha = A, B, C$), the total number of the lattice sites in the ith phase by N_i, and the negative energies of the pair of the nearest neighbors α–β by $v_{\alpha\beta}$, we obtain

$$\begin{aligned} F_1 = {} & -\frac{z}{2}(N - N_C^{(1)} - N_C^{(2)})v_{CC} - \frac{z}{2}\sum_{i=1}^{2}\frac{1}{N_i} \\ & \times (N_A^{(i)^2} v_{AA} + N_B^{(i)^2} v_{BB} + 2N_A^{(i)}N_B^{(i)} v_{AB} \\ & \times N_C^{(i)^2} v_{CC} + 2N_A^{(i)}N_C^{(i)} v_{AC} + 2N_B^{(i)}N_C^{(i)} v_{BC}) \\ & - kT\sum_{i=1}^{2}[N_i(\ln N_i - 1) - N_A^{(i)}(\ln N_A^{(i)} - 1) \\ & - N_B^{(i)}(\ln N_B^{(i)} - 1) - N_C^{(i)}(\ln N_C^{(i)} - 1)]. \end{aligned} \tag{2}$$

Here, v_{CC} is the energy of interaction between the pairs of nearest neighbors C–C in the crystal, z is the coordination number in the lattice, and N is the total number of atoms of type C. We use the following well-known high-temperature approximation for the phonon-related component of the free energy [2]:

$$F_2 = \frac{3}{2}N_0 kT \ln\frac{\hbar^2\overline{\omega^2}}{(kT)^2}. \tag{3}$$

Here, N_0 is the number of particles in the crystal and $\overline{\omega^2}$ is the squared frequency averaged over the spectrum.

In the case under consideration, formula (3) yields

$$\begin{aligned} F_2 = {} & \frac{3}{2}kT(N - N_C^{(1)} - N_C^{(2)})\ln\frac{\hbar^2\overline{\omega_C'^2}}{(kT)^2} \\ & + \frac{3}{2}kT\sum_{i=1}^{2}N_i\ln\frac{\hbar^2\overline{\omega_i'^2}}{(kT)^2}. \end{aligned} \tag{4}$$

In this formula, $\overline{\omega_C'^2}$ and $\overline{\omega_i'^2}$ are the spectrum-averaged squared frequencies of crystal C and the ith phase of the A–B–C alloy, respectively.

In order to calculate the latter quantity, we use the isotopic approximation and assume that the force constants of elastic interaction between the atoms in the alloy A–B–C are independent of composition. In this case, according to [3], vibrations of atoms in the alloy

1063-7842/04/4908-0993$26.00 © 2004 MAIK "Nauka/Interperiodica"

can be described assuming that lattice sites are occupied by effective atoms with masses $\bar{m}$ equal to

$$\left(\sum_{\alpha} c_{\alpha}/m_{\alpha}\right)^{-1},$$

where m_{α} and c_{α} are the mass and concentration of atoms α in the alloy.

At the same time, $\overline{\omega^2} = (1/2)A$ [2], where m is the mass of the crystal atom and A is the quantity expressed in terms of parameters of the elastic binding. Since A is independent of composition in the isotopic approximation and $m = \bar{m}$, we immediately obtain the following expression for $\overline{\omega'^2_i}$:

$$\overline{\omega'^2_i} = c_A^{(i)}\overline{\omega^2_A} + c_B^{(i)}\overline{\omega^2_B} + c_C^{(i)}\overline{\omega^2_C}. \tag{5}$$

We use the quantities $N_{\alpha}^{(i)}$ as thermodynamic variables. They satisfy two evident conditions; i.e.,

$$\sum_{i=1}^{2} N_A^{(i)} = N_A, \quad \sum_{i=1}^{2} N_B^{(i)} = N_B, \tag{6}$$

where N_{α} ($\alpha = A, B$) is the total number of atoms of the type α in the system.

In this case, the equilibrium values of $N_{\alpha}^{(i)}$ are determined from the condition for an extremum of the function

$$\Phi = F + \lambda_1\left(N_A - \sum_{i=1}^{2} N_A^{(i)}\right) + \lambda_2\left(N_B - \sum_{i=1}^{2} N_B^{(i)}\right), \tag{7}$$

where λ_1 and λ_2 are the Lagrangian multipliers.

The equilibrium equations are written as

$$\frac{\partial \Phi}{\partial N_{\alpha}^{(i)}} = 0; \quad \alpha = A, B, C; \quad i = 1, 2. \tag{8}$$

Using Eqs. (8) and taking into account conditions (6), we can, in principle, determine first the equilibrium values of $N_C^{(i)}$ and then the solubility

$$R = \frac{N_C^{(1)} + N_C^{(2)}}{N_1 + N_2}. \tag{9}$$

We now write the equations obtained as a result of differentiation of Φ with respect to $N_C^{(i)}$:

$$\begin{aligned}
&\frac{z}{2}\big(v_{CC} + c_A^{(i)^2} v_{AA} + c_B^{(i)^2} v_{BB} + 2c_A^{(i)}c_B^{(i)} v_{AB} \\
&+ c_C^{(i)^2} v_{CC} + 2c_A^{(i)}c_C^{(i)} v_{AC} + 2c_B^{(i)}c_C^{(i)} v_{BC}\big) \\
&- z\big(c_C^{(i)} v_{CC} + c_A^{(i)} v_{AC} + c_B^{(i)} v_{BC}\big) \\
&+ kT\ln c_C^{(i)} - \frac{3}{2}kT\ln\frac{\hbar^2\overline{\omega^2_C}}{(kT)^2} + \frac{3}{2}kT \\
&\times \ln\frac{\hbar^2\left(c_A^{(i)}\overline{\omega^2_A} + c_B^{(i)}\overline{\omega^2_B} + c_C^{(i)}\overline{\omega^2_C}\right)}{(kT)^2} + \frac{3}{2}kT \\
&\times \ln\frac{\overline{\omega'^2_C} - \left(c_A^{(i)}\overline{\omega^2_A} + c_B^{(i)}\overline{\omega^2_B} + c_C^{(i)}\overline{\omega^2_C}\right)}{c_A^{(i)}\overline{\omega^2_A} + c_B^{(i)}\overline{\omega^2_B} + c_C^{(i)}\overline{\omega^2_C}} = 0; \\
&i = 1, 2.
\end{aligned} \tag{10}$$

Since the case of low solubility is considered ($c_C^{(i)} \lll 1$), we solve Eqs. (10) discarding all terms with $c_C^{(i)}$ except for logarithmic terms. As a result, we obtain

$$\begin{aligned}
c_C^{(i)} &= \left(\frac{\overline{\omega'^2_C}}{c_A^{(i)}\overline{\omega^2_A} + c_B^{(i)}\overline{\omega^2_B}}\right)^{-\frac{3}{2}} \\
&\times \exp\left\{\frac{3}{2}\frac{c_A^{(i)}\overline{\omega^2_A} + c_B^{(i)}\overline{\omega^2_B} - \overline{\omega^2_C}}{c_A^{(i)}\overline{\omega^2_A} + c_B^{(i)}\overline{\omega^2_B}}\right\}\exp\left(-\frac{zE_i}{2kT}\right),
\end{aligned} \tag{11}$$

where

$$\begin{aligned}
E_i &= c_A^{(i)^2} v_{AA} + c_B^{(i)^2} v_{BB} + 2c_A^{(i)}c_B^{(i)} v_{AB} \\
&+ v_{CC} - 2c_A^{(i)} v_{AC} - 2c_B^{(i)} v_{BC}.
\end{aligned} \tag{12}$$

Expression (11) can be simplified if $\overline{\omega^2_A} \approx \overline{\omega^2_B}$, i.e., if the masses of atoms A and B are close to each other. Assuming that $\overline{\omega^2_A} = \overline{\omega^2_B} = \overline{\omega^2}$, we obtain the following expression instead of (11):

$$c_C^{(i)} = \left(\frac{\overline{\omega'^2_C}}{\overline{\omega^2}}\right)^{-\frac{3}{2}}\exp\left(\frac{3}{2}\frac{\overline{\omega^2} - \overline{\omega^2_C}}{\overline{\omega^2}}\right)\exp\left(-\frac{zE_i}{kT}\right). \tag{13}$$

It can be seen from (11) that only a small addition to $c_C^{(i)}$ results from consideration of the effect of dissolved atoms on the concentration of components A and B in the phases. Therefore, we calculate $c_{\alpha}^{(i)}$ ($i = 1, 2$) in the zeroth approximation with respect to $c_C^{(i)}$; however, we take into account the effect of the phonon contribution.

The equations obtained as a result of differentiation of Φ with respect to $N_A^{(i)}$ and $N_B^{(i)}$ have the following form if the terms that contain $N_C^{(i)}$ are discarded:

$$\frac{z}{2}(c_A^{(i)^2}v_{AA} + c_B^{(i)^2}v_{BB} + 2c_A^{(i)}c_B^{(i)}v_{AB}) - z(c_A^{(i)}v_{AA} + c_B^{(i)}v_{AB}) - \lambda_1 + kT\ln c_A^{(i)} + \frac{3}{2}kT\ln\frac{\hbar^2(c_A^{(i)}\overline{\omega_A^2} + c_B^{(i)}\overline{\omega_B^2})}{(kT)^2} + \frac{3}{2}kT\frac{(\overline{\omega_A^2} - \overline{\omega_B^2})c_B^{(i)}}{c_A^{(i)}\overline{\omega_A^2} + c_B^{(i)}\overline{\omega_B^2}} = 0, \quad (14)$$

$$\frac{z}{2}(c_A^{(i)^2}v_{AA} + c_B^{(i)^2}v_{BB} + 2c_A^{(i)}c_B^{(i)}v_{AB}) - z(c_B^{(i)}v_{BB} + c_A^{(i)}v_{AB}) - \lambda_2 + kT\ln c_B^{(i)} + \frac{3}{2}kT\ln\frac{\hbar^2(c_A^{(i)}\overline{\omega_A^2} + c_B^{(i)}\overline{\omega_B^2})}{(kT)^2} - \frac{3}{2}kT\frac{(\overline{\omega_A^2} - \overline{\omega_B^2})c_A^{(i)}}{c_A^{(i)}\overline{\omega_A^2} + c_B^{(i)}\overline{\omega_B^2}} = 0. \quad (15)$$

If the two last terms in Eqs. (14) and (15) are discarded, these equations transform into the well-known equations of the decomposition theory, which disregards the effect of elastic vibrations of atoms [4]. Subtracting (15) from (14), we obtain

$$z(v_{AB} - v_{BB} - c_A^{(i)}w) + kT\ln\frac{1 - c_A^{(i)}}{c_A^{(i)}} + \lambda_1 - \lambda_2 - \frac{3}{2}kT\ln\frac{\overline{\omega_A^2} - \overline{\omega_B^2}}{c_A^{(i)}\overline{\omega_A^2} + c_B^{(i)}\overline{\omega_B^2}} = 0, \quad (16)$$

where $w = 2v_{AB} - v_{AA} - v_{BB}$ is the ordering energy ($w < 0$ in decomposing alloys).

Assuming that the difference $\overline{\omega_A^2} - \overline{\omega_B^2}$ is small, we can represent the last term in (16) as

$$-\frac{3}{2}kT\ln\left(\frac{\overline{\omega_A^2} - \overline{\omega_B^2}}{\overline{\omega_B^2}}\right) + \frac{3}{2}kT\ln\left(\frac{\overline{\omega_A^2} - \overline{\omega_B^2}}{\overline{\omega_B^2}}\right)^2 c_A^{(i)}. \quad (17)$$

Substituting (17) into (16) and subtracting the resulting equality taken at $i = 1$ from that taken at $i = 2$, we obtain

$$-zw'(c_A^{(1)} - c_A^{(2)}) + kT\ln\frac{(1 - c_A^{(1)})c_A^{(2)}}{c_A^{(1)}(1 - c_A^{(2)})} = 0, \quad (18)$$

where

$$w' = w - \frac{3kT}{z}\left(\frac{\overline{\omega_A^2} - \overline{\omega_B^2}}{\overline{\omega_B^2}}\right)^2. \quad (19)$$

Equation (18) has exactly the same form as the equation in the static version of the decomposition theory [4] if w is replaced by w'. Consequently, we may introduce the decomposition parameter $\mu = c_A^{(1)} - c_A^{(2)}$; the equation for this parameter is written as

$$2\ln\frac{1 - \mu}{1 + \mu} = \left[\frac{zw}{kT} - \frac{3}{2}\left(\frac{\overline{\omega_A^2} - \overline{\omega_B^2}}{\overline{\omega_B^2}}\right)^2\right]\mu. \quad (20)$$

Let us study a variation in the shape of the decomposition curve due to elastic vibrations.

The value of μ is small if the initial-state composition is nearly equiatomic. Expanding the left-hand side of Eq. (20) into a series in terms of powers of μ, we derive the following expression for the temperature that corresponds to the peak of the decomposition curve:

$$T_0 = -\frac{zw}{2k\left[2 - \frac{3}{z}\left(\frac{\overline{\omega_A^2} - \overline{\omega_B^2}}{\overline{\omega_B^2}}\right)^2\right]}. \quad (21)$$

Thus, the highest decomposition temperature increases if lattice vibrations of atoms are taken into account.

We now calculate variations in the width of the biphase region. Assuming that $\mu = \mu_0 + \Delta\mu$ ($\Delta\mu \ll \mu_0$), where μ_0 is the decomposition parameter in the static variant, we use Eq. (20) to obtain

$$\Delta\mu = \frac{\frac{3}{2z}\left(\frac{\overline{\omega_A^2} - \overline{\omega_B^2}}{\overline{\omega_B^2}}\right)^2\mu_0}{\frac{2}{1 - \mu_0^2} + \frac{zw}{2kT}}, \quad (22)$$

which yields

$$\Delta\mu = \frac{3}{2z}\left(\frac{\overline{\omega_A^2} - \overline{\omega_B^2}}{\overline{\omega_B^2}}\right)^2\mu_0, \quad (23)$$

in the vicinity of T_0; i.e., the region of biphase states widens.

At temperatures below that of decomposition, we have

$$c_A^{(1)} = \frac{1 + \mu}{2}, \quad c_A^{(2)} = \frac{1 - \mu}{2}, \quad (24)$$

and, correspondingly,

$$N_1 = \frac{2c_A - 1 + \mu}{2\mu}\bar{N}, \quad N_2 = \frac{1 + \mu - 2c_A}{2\mu}\bar{N}, \tag{25}$$

where $\bar{N} = N_A + N_B$.

Formulas (24) and (25) make it possible to write the expressions for the number of atoms C dissolved in the first and second phases, respectively; i.e., we have

$$N_C^{(1)} = \bar{N}\frac{2c_A - 1 + \mu}{2\mu}\left(\frac{\overline{\omega_C^2}}{\overline{\omega^2}}\right)^{\frac{3}{2}}\exp\left(\frac{3}{2}\frac{\overline{\omega^2} - \overline{\omega_C^2}}{\overline{\omega^2}}\right) \times \exp\left(-\frac{z}{2kT}\left(E_0 - \frac{w\mu^2}{4} + \frac{\mu}{2}E_1\right)\right), \tag{26}$$

$$N_C^{(2)} = \bar{N}\frac{1 + \mu - 2c_A}{2\mu}\left(\frac{\overline{\omega_C^2}}{\overline{\omega^2}}\right)^{\frac{3}{2}}\exp\left(\frac{\overline{\omega^2} - \overline{\omega_C^2}}{\overline{\omega^2}}\right) \times \exp\left(-\frac{z}{2kT}\left(E_0 - \frac{w\mu^2}{4} + \frac{\mu}{2}E_1\right)\right). \tag{27}$$

Here,

$$E_0 = \frac{1}{4}(v_{AA} + v_{BB} + 2v_{AB}) + v'_{CC} - v_{AC} - v_{BC}, \tag{28}$$

$$E_1 = v_{AA} + 2v_{BC} - v_{BB} - 2v_{AC}. \tag{29}$$

It is easy to show that $E_1 = w_{BC} - w_{AC}$, where w_{BC} and w_{AC} are the energies of the ordered systems B–C and A–C. Substituting the obtained expressions for $N_C^{(1)}$ and $N_C^{(2)}$ into formula (10), we obtain the following expression for solubility:

$$R = R_0\exp\left(\frac{zw\mu^2}{8kT}\right) \times \left\{\cosh\left(\frac{zE_1\mu}{4kT}\right) + \frac{1 - 2c_A}{\mu}\sinh\left(\frac{zE_1\mu}{4kT}\right)\right\}, \tag{30}$$

where

$$R_0 = \left(\frac{\overline{\omega_C^2}}{\overline{\omega^2}}\right)^{\frac{3}{2}}\exp\left(\frac{3}{2}\frac{\overline{\omega^2} - \overline{\omega_C^2}}{\overline{\omega^2}}\right)\exp\left(-\frac{zE_0}{2kT}\right). \tag{31}$$

It can be easily shown by direct calculation that R_0 is the solubility in the monophase state in an alloy with equiatomic composition.

Let us consider the behavior of solubility in several particular cases. For an alloy with equiatomic composition ($c_A = 0.5$), we have

$$R = R_0\exp\left(\frac{zw\mu^2}{8kT}\right)\cosh\left(\frac{zE_1\mu}{4kT}\right). \tag{32}$$

In the vicinity of the decomposition temperature T_0 (i.e., at small values of μ), we use formula (32) to obtain

$$R = R_0\left[1 + \frac{1}{2}\left(\frac{E_1^2}{w^2} - 1\right)\mu^2\right]. \tag{33}$$

As can be seen, a variation in solubility as a result of decomposition is governed by the ratio between the energies E_1 and w: the solubility increases as a result of decomposition if $|E_1/w| > 1$ and decreases if $|E_1/w| < 1$.

We now study how the solubility changes as a result of decomposition of an alloy whose composition differs from stoichiometric. The smallest width of the biphase region in an alloy with $c_A \neq 0.5$, is equal to

$$\mu_0 = 2c_A - 1. \tag{34}$$

In the monophase state, the solubility in the alloy under consideration is given by

$$R' = R_0\exp\left(\frac{z(w\mu_0 - 2E_1)\mu_0}{8kT}\right). \tag{35}$$

It follows from formulas (30) and (35) that the ratio of solubilities in the biphase and monophase states can be written as

$$r = \frac{R}{R'} = \frac{1}{2}\exp\left[\frac{zw}{8kT}(\mu^2 - \mu_0^2)\right] \times \left\{\left(1 - \frac{\mu_0}{\mu}\right)\exp\left(\frac{zE_1(\mu_0 + \mu)}{4kT}\right) + \left(1 + \frac{\mu_0}{\mu}\right)\exp\left(\frac{zE_1}{4kT}(\mu_0 - \mu)\right)\right\}. \tag{36}$$

On transition to the biphase state, the value of μ_0 changes by $-2\delta c_A$, where $-\delta c_A$ is the variation in the concentration of component A in the first phase ($\delta c_A > 0$). In the vicinity of the decomposition temperature, $\delta c_A \ll 1$. Expanding then the right-hand side of (36) into a series in terms of powers of δc_A and retaining only the terms of the first order of smallness, we obtain

$$z = 1 + \left\{1 - \frac{zw}{2kT}\mu_0 + \frac{zE_1}{2kT} - \exp\left(\frac{zE_1\mu_0}{2kT}\right)\right\}\delta c_A. \tag{37}$$

In the region where δc_A is small, we can replace T by the decomposition temperature T_d of an alloy with the composition c_A; according to (20), this temperature is given by

$$T_d = \frac{2w\mu_0}{2\ln\frac{1 - \mu_0}{1 + \mu_0}}, \tag{38}$$

which finally yields

$$r = 1 + \left\{1 - \frac{1}{\mu_0}\ln\frac{1-\mu_0}{1+\mu_0}\left(1 - \frac{E_1}{w}\right) - \exp\left(\frac{E_1}{w}\ln\frac{1-\mu_0}{1+\mu_0}\right)\right\}\delta c_A. \quad (39)$$

Expression (37) can be simplified appreciably if $E_1/w \ll 1$. In this case,

$$r = 1 + \frac{1}{\mu_0}\ln\frac{1-\mu_0}{1+\mu_0}\delta c_A. \quad (40)$$

It follows from this formula that solubility is expected to increase as a result of decomposition.

There are binary systems that form a continuous series of solid solutions at high temperatures and decompose into two phases with the bell-shaped decomposition curve (the Au–Ni, Au–Pt, Ir–Pd, Ir–Pt, and W–Cr systems) [5]. As far as we know, experimental data on the solubility of substitutional impurities in the biphase state of aforementioned systems are lacking at present. The relevant experiments would make it possible to compare the results reported in this paper with experimental data.

REFERENCES

1. Z. A. Matysina and M. I. Milyan, *Theory of Solubility of Impurities in Ordered Phases* (DGU, Dnepropetrovsk, 1991).
2. G. Leibfrid, *Microscopic Theory of Mechanical and Thermal Properties of Crystals* (Fizmatgiz, Moscow, 1962) [in Russian].
3. S. I. Masharov, Fiz. Met. Metalloved. **17**, 176 (1964).
4. A. A. Smirnov, *Molecular-Kinetic Theory of Metals* (Nauka, Moscow, 1966) [in Russian].
5. A. E. Vul and I. K. Kagan, *The Structure and Properties of Double Metallic Systems* (Nauka, Moscow, 1976), Vol. 3 [in Russian].

Translated by A. Spitsyn

Technical Physics, Vol. 49, No. 8, 2004, pp. 998–1003. Translated from Zhurnal Tekhnicheskoĭ Fiziki, Vol. 74, No. 8, 2004, pp. 45–50.

On the Mechanism of Carbon Nanotube Formation: I. The Thermodynamics of Formation of Carbon Molten Drops in a Metallic Catalyst

N. I. Alekseev

Ioffe Physicotechnical Institute, Russian Academy of Sciences,
Politekhnicheskaya ul. 26, St. Petersburg, 194021 Russia
e-mail: g.dyuzhev@pop.ioffe.rssi.ru

Received September 22, 2003; in final form, January 5, 2004

Abstract—Carbon molten drops in a metallic catalyst are known to be nucleation centers for carbon nanotubes. The problem of the kinetics of condensation of such drops in wide concentration ranges of carbon and metal vapors is considered. The equilibrium distribution of the drops over the size and mole fraction of the components is obtained. The main result is the calculation of the quasi-steady-state rate of condensation of the molten drops in a supersaturated carbon vapor. This result forms the basis for the calculation of the characteristics of explosive and rapid condensation of the vapor upon its cooling. This calculation is performed in the next part of this work. *© 2004 MAIK "Nauka/Interperiodica".*

1. INTRODUCTION

Although carbon nanotubes (NTs) can be applied in many fields, none of the existing methods of their manufacture can produce them on an industrial scale. Advanced modifications of the chemical vapor decomposition (CVD) of hydrocarbons provide oriented high-quality multiwall NTs (bundles [1]); however, the quality of single-wall NTs produced by CVD is still low (apparently, CVD single-wall NTs produced using the catalytic decomposition of alcohol have the highest quality [2]). In many cases, this technique is sufficient to provide mass production; however, for a number of applications (primarily, in electronics) it is important to produce high-quality single-wall NTs. Moreover, CVD requires long-term and labor-consuming preparation of a substrate. Therefore, arc and laser methods for the deposition of NTs are still interesting despite their high energy consumption [3].

The disadvantages of both methods are related to the uncontrolled condensation of vapor, which initially consists of carbon and metal atoms, when it moves from its source and cools in the atmosphere of a buffer gas. During the condensation, NT nuclei (i.e., the drops of a metallic catalyst or a carbon melt in the catalyst) are formed. Then, in the cases of both arc and laser evaporation of a graphite target, NTs grow on these drops, which continue to move in a gas flow, as they are supersaturated with carbon [4–6]. Uncontrolled condensation results in the uncontrolled growth of chaotically oriented NTs. In this work and its continuation [7], we consider the condensation of a binary carbon–metal vapor when it cools, depending on the ratio of vapor concentrations. We discuss the possibility of controlled separation of the stages of NT growth, namely, the condensation of the drops and their deposition on a substrate and the growth of NTs from these drops. For definiteness, hereafter, we will discuss the arc method for the production of carbon nanotubes.

2. QUALITATIVE ANALYSIS

In the arc method of production of NTs, a metallic catalyst is introduced in a vaporized electrode (anode) in amounts of several fractions of a percent. As the metal content increases, the number of NTs produced decreases. However, taking into account that the modern arc method cannot be a commercial technology, it is important to analyze the variation of condensation with the component ratio.

When the metal content in the bulk of the anode is low (a few percent or several fractions of a percent), the vaporization temperature of the anode should be equal to that in a fullerene arc with a graphite electrode (about 4000 K) [8]. Under these conditions, the concentration of the carbon vapor over the surface can reach 10^{17} cm^{-3}, and that of the metal vapor, 10^{15}–10^{16} cm^{-3}. This concentration corresponds to a saturation temperature of 1700–1900 K for the metal vapor (Fig. 1).

On the contrary, when the metal content is high, the anode temperature is close to the melting temperature of the fusible catalytic metal (1600–1700 K). Then, the amount of the vaporized metal can even be smaller than in the case of an almost purely graphite electrode.

The temperature over the surface of the vaporized anode can be used to estimate the condensation temperature, i.e., the temperature in a certain region outside of the arc, where the real concentration of the metal vapor becomes equal to the concentration of saturated vapor.

(1) At a very low relative concentration of the metal, carbon clusters develop according to the "fullerene path" [9, 10]: condensation consists in the formation of dimers–chains–rings–fullerenes. The absence of more complex structures is due to the fact that the clusters that are formed upon coagulation are annealed in the time between collisions. An additional analysis shows that metal atoms trapped by clusters of the rings–chains type are at the periphery and, thus, can freely evaporate. This behavior ensures a relatively high concentration of free metal vapor and a high condensation temperature. The time it takes for condensed drops moving in a gas flow to become NT nuclei is found to be sufficient, and the yield of NTs is high.

(2) As the metal content in the anode increases, such evolution of carbon clusters is hindered. Frequent collisions between carbon clusters and metal atoms destroy the cluster structure. Such clusters can effectively trap and retain metal atoms inside them. Therefore, the concentration of free metal atoms, which can be condensed into drops, decreases. The condensation temperature also decreases. Then, the solubility of complex carbon structures in the drops formed is also low. As a result, neither fullerenes nor nanotubes are formed; however, a large quantity of amorphous carbon appears.

It is difficult to estimate the transition from case 1 to case 2, since (a) to the best of our knowledge, an arc discharge with a vaporizing graphite–metal anode in the vapor of a buffer gas has not been calculated; (b) it is extremely difficult to calculate the thermodynamics of clusters having a small amount of carbon and metal atoms.

(3) As the metal concentration increases further, the fullerene path becomes closed. Therefore, small iron–carbon clusters should have a topology that is similar to the topology of metallic clusters and acquire the properties of metallic drops when the number of atoms increases. This scenario can occur if we take into account the fact that the pressure of the saturated metal vapor is higher by four to five orders of magnitude (Fig. 1) and that the evaporation heat is half that of carbon. The temperature decreases with increasing distance from the source of arc, and the actual concentrations of metal and carbon vapors decrease according to what is approximately the same law. Therefore, the carbon vapor reaches saturation when the metal vapor is strongly undersaturated. In this case, condensation is delayed: it is prepared by carbon supersaturation but begins only at the instant when the metal vapor becomes saturated. According to the classic definition, the condensation is neither homogeneous nor heterogeneous, since the characteristics of each component of the material being condensed change with the environmental conditions.

A drop formed during the condensation is rapidly saturated with carbon and can become a nucleation center for a NT, provided the drop temperature at the condensation instant is sufficiently high and the NT has time to grow.

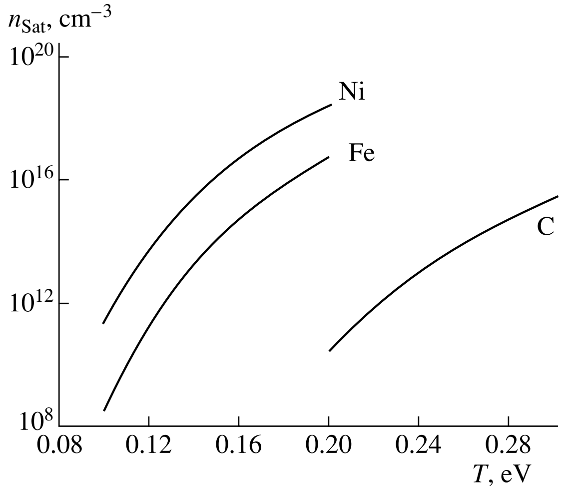

Fig. 1. Concentration of saturated vapors over the surfaces of iron, nickel, and graphite.

The condensation should be delayed at a low relative carbon concentration such that heterogeneous condensation terminates. Indeed, if the concentration and size of the drops that appear during this condensation are small, these drops cannot stop an increase in the supersaturation of the metal vapor, and, in a certain time, "secondary" condensation, which is similar to the homogeneous condensation of the metal vapor, takes place.

The considerations given above indicate that, in agreement with experiment, there is a certain optimal relative metal content in the electrode (less than one percent) above which the formation of NTs deteriorates.

However, there is another method to increase the efficiency of nanotube growth: vaporization of an electrode with a high metal content (e.g., an electrode made of conventional stainless steel). In this case, the arc serves only as the means for the formation of metallic nucleation centers during a given time. NTs can be grown on them but under different conditions. In principle, this approach is similar to that for the preparation of substrates in CVD techniques, and the realization of this approach can be simpler.

This approach raises the problem of the condensation of a binary carbon–metal gas mixture having a relatively high metal content and a low carbon content. The purpose is to answer the question: Is the presence of a metal an advantage or disadvantage from the standpoint of further growth of NTs? Moreover, it is of interest to consider the condensation of the gas mixture with various properties of its components.

The first stage of solving this problem is to obtain thermodynamic relations for a two-component cluster-(nucleus) of the liquid phase.

3. THERMODYNAMICS OF METAL–CARBON SOLUTION DROPS

In the classical Frenkel theory of condensation [11], a cluster of $g \gg 1$ atoms is considered as a drop with constant surface tension σ_0. In the case of a pure substance, the chemical potential of such a cluster is determined by the relation

$$\mu_g = T\ln(N_g\lambda_g^3) + (g-1)\mu_L + \ln Z_{\text{rot}}^{(g)} + 4\pi\sigma_0 R_g^2, \quad (1)$$

where N_g and R_g are the cluster concentration and radius, respectively; $\lambda = (h^2/2\pi mgT)^{1/2}$ is the thermal wavelength of the cluster and λ_1 is the similar quantity for an individual atom in the gas phase; m is the metal atom mass; $Z_{\text{rot}}^{(g)} = (8\pi^2 I_g T/h^2)^{3/2}$ is the rotational partition function of the cluster; $I_g = 2gmR_g^2/5$ is the moment of inertia of the cluster; $\mu_L = T\ln(N_S\lambda_1^3)$ is the chemical potential of an atom in the liquid phase; and N_S is the concentration of saturated vapor.

Using the law of mass action in the reaction of formation of a cluster, we have $\mu_g = g\mu_1 = (g-1)\mu_1 + \mu_1$; then, the number of atoms distribution function for clusters takes the form [11]

$$N_g = N_1 g^4 S^{g-1} A_{\text{rot}} \exp(-4\pi\sigma_0 R_g^2/T), \quad (2)$$

where $S = N_1/N_S$ is the vapor supersaturation; $A_{\text{rot}} = (16\pi^2 m r_L^2 T/5h^2)^{3/2}$; ρ_L is the liquid-phase density; and $r_L = (3m/4\pi\rho_L)^{1/3}$ has the meaning of the size of the cell per one particle, the drop radius being equal to $R_g = r_L g^{1/3}$.

Relations (1) and (2) can easily be generalized to the case of a melt. The free energy of the melt containing g atoms (hereafter, the Gibbs free energy) is defined by the relation [12]

$$G_g = G_{\text{mix}} + XG_C^{(0)} + (1-X)G_K^{(0)}, \quad (3)$$

where G_{mix} is the free energy of mixing; $X = c/(k + c)$ is the mole fraction of carbon; c and k are the numbers of carbon and metal atoms in the drop, respectively ($g = c + k$); and $G_C^{(0)}$ and $G_K^{(0)}$ are the free energies corresponding to pure carbon (subscript C) and a pure metal (subscript K) in the liquid phase.

In the case of carbon, we consider the energy of a hypothetical supercooled substance, as is usually done in the theory of alloys [12]. We neglect the effect of "separation" of the components of the binary mixture in Eq. (3); it is taken into account as a change in the surface tension. This problem is analyzed below in more detail.

As follows from the law of mass action, the chemical potential of an atom in the melt ($\mu_g = G_g/g$) is $\mu_g = k\mu_{K,1} + c\mu_{C,1}$, where $\mu_{K,1}$ and $\mu_{C,1}$ are the chemical potentials of the metal and carbon vapors, respectively.

By introducing the free energy of mixing per atom ($\mu_{\text{mix}} = G_{\text{mix}}/g$) and repeating the considerations given above, we can easily obtain

$$N_g = A_{\text{rot}} N_K^{1-X} N_C^X g^{9/2} A_{KC} (S_C^X S_K^{1-X})^{g-1} \times \exp\left(-\frac{(g-1)\mu_{\text{mix}}}{T} - \frac{4\pi\sigma_0 r_L^2 g^{2/3}}{T}\right), \quad (4)$$

where

$$A_{KC} = \left[\frac{A_C X + A_K(1-X)}{A_C^X A_K^{1-X}}\right]^{3/2},$$

$N_K^{(S)}$ and $N_C^{(S)}$ are the concentrations of the saturated metal and carbon vapors, respectively; and A_K and $A_C = 12$ are the atomic masses of the metal and carbon, respectively.

Except the multiplier A_{KC}, Eq. (4) can be written by analogy with Eq. (2) only from the considerations of the dimensions and symmetry of the solvent and solute.

Thus, the difference in the size distribution of the drops of the binary solution from the similar distribution of the pure drops consists in the energy of mixing μ_{mix} and the surface tension σ_0, which is a nontrivial quantity even for large drops because of a nonuniform component distribution in them. However, scarce experimental data on melts [13] indicate that, e.g., for liquid iron, the value of σ_0 varies from ~1800 erg/cm^2 for pure iron to ~1650 erg/cm^2 for the saturated melt ($T = 1600$°C), i.e., by less than 10%. Therefore, the dependence of σ_0 on the mole fraction can be assumed to be insignificant as compared to the size effects, which are of fundamental importance for the condensation of small drops.

The $\mu_{\text{mix}}(X)$ dependence that enters into Eq. (4) is unknown for almost all carbon–metal alloys, which is due to the fact that the alloys were mainly studied for metallurgy, where the heat of formation rather than the free energy is important. In the literature, we were able to find such data for a wide range of carbon concentration in the melt only for nickel [14], for which this dependence is close to the ideal dependence

$$\mu_{\text{mix}} = T(X\ln X + (1-X)\ln(1-X)) \quad (5)$$

up to $X \sim (0.7–0.8)X_{\text{Sat}}$.

For other materials, data on the correction to Eq. (5) are only available for low carbon concentrations; this case is described by the theory of regular solutions [12]. The regular correction has the form $(1-X)Q_{12}$; however, the data on the interchange energy Q_{12} are controversial. The most complete data on Q_{12} for various alloys are given in [15]. In this work, the regular correction was taken into account; however, for the sake of simplicity, all the formulas are written as if the drop is an ideal solution, at least, at $X \le (0.7–0.8)X_{\mathrm{Sat}}$. On the other hand, at $X > X_{\mathrm{Sat}}$, we have

$$\mu_{\mathrm{mix}} = T\ln(X/X_{\mathrm{Sat}}). \tag{6}$$

The curves of dependences (5) and (6) intersect at $X \sim 0.75X_{\mathrm{Sat}}$ (Fig. 2, curves *1, 3*). Therefore, taking into account the fact that the exact $\mu_{\mathrm{mix}}(X)$ dependence is unknown, we assume that the potential of mixing has a minimum at $X_m = \gamma X_{\mathrm{Sat}}$ ($\gamma = 0.75$), is determined at $X < X_m$ from Eq. (5), and is not considered to the right of point X_m.

The $X_{\mathrm{Sat}}(T)$ dependences for iron-group metals are available in the literature [16]. In this work, as an $X_{\mathrm{Sat}}(T)$ dependence for iron, we use the dependence $X_{\mathrm{Sat}} = \exp(–0.112/T – 0.8635)$, where the temperature T is expressed in eV.

The critical drop size g_* that is required for the onset of condensation depends on X and is determined from the condition $\partial N_g/\partial g = 0$:

$$g_*^{1/3} = \frac{8}{3}\frac{\pi r_L^2\sigma}{T} \times \frac{1}{X\ln S_C + (1-X)\ln S_K - \mu_{\mathrm{mix}}/T + 9/2g}, \tag{7}$$

which is analogous to the result for a pure material [11]:

$$g_*^{1/3} = \frac{8}{3T}\frac{\pi r_L^2\sigma}{\ln S + 4/g_*}.$$

The behavior of the drop distribution function $N_g(X)$ can easily be analyzed numerically by setting μ_{mix}/T in the form (5) up to the X_{Sat} point and, then, in the form (6), at $X > X_{\mathrm{Sat}}$.

The result is as follows. At large supersaturation of the carbon vapor ($S_C \gg S_K$), the carbon saturation of drops with $X = X^{(1)} \sim \gamma X_{\mathrm{Sat}}$ becomes thermodynamically favorable. Otherwise, at $S_K \gg S_C$, optimum drops have a low carbon content, $X = X^{(2)} \neq 0$. The difference of $X^{(2)}$ from zero is caused by the fact that the derivative $d\mu_{\mathrm{mix}}/dX$ behaves logarithmically at $X \longrightarrow 0$. Therefore, the dissolution of a very small amount of carbon in the drops is always favorable, even in the case of vapor almost free of carbon.

The curves that separate the first and second cases are plotted in the S_C, S_K coordinates for various temperatures (Fig. 3). The region with optimum drops having $X = X^{(1)}$ adjoins the S_C axis, and the region with optimum drops having $X = X^{(2)}$ adjoins the S_K axis. Along the boundary curves, $N_g(X)$ is almost independent of X; that is, the size distribution of the drops has a large dispersion.

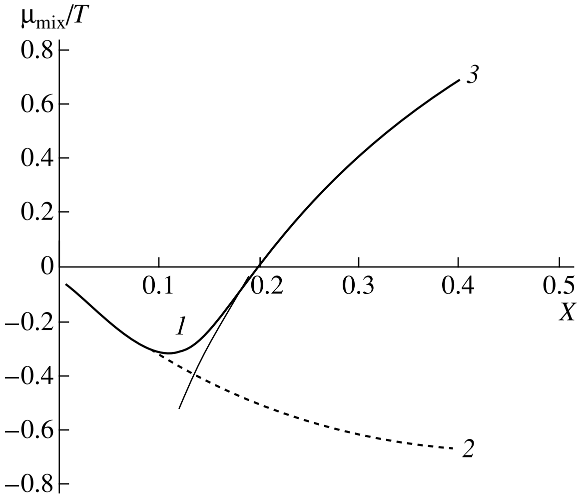

Fig. 2. Free energy of mixing per atom of a carbon melt in a metal as a function of the mole fraction of carbon: (*1*) the dependence used in the calculation (bold curve), (*2*) the case of an ideal solution (dashed curve), and (*3*) the dependence at $X > X_{\mathrm{Sat}}$.

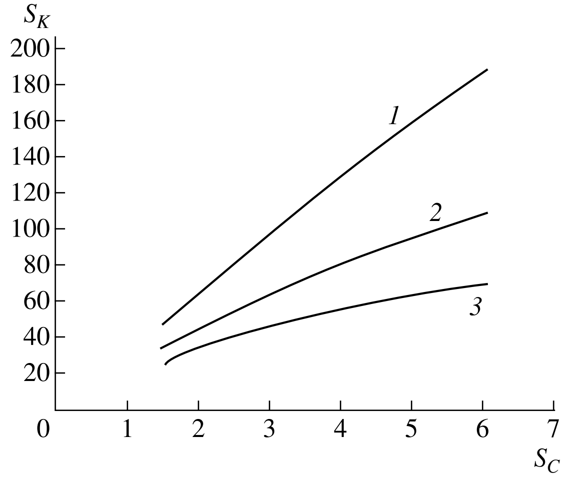

Fig. 3. Boundary curves for the regions with predominantly metallic drops and drops with a high carbon content for various temperatures T: (*1*) 0.12, (*2*) 0.16, and (*3*) 0.20 eV.

In the case of heterogeneous condensation, $S_C \gg S_K$, since, as noted in the Introduction, the evaporation heat of carbon ($q_C \sim 7.2$ eV) is almost twice as large as the evaporation heat of metals q_K. Therefore, as the gas mixture expands from the region where carbon and metal exist only as vapor, the concentration of the saturated carbon vapor

$$N_C^{(S)} = N_K^{(S)}(T_0)\exp\left[-\frac{q_C}{T}\left(\frac{1}{T} - \frac{1}{T_0}\right)\right] \tag{8}$$

decreases much faster than the analogous function for the metal vapor, and the partial supersaturation of the carbon vapor increases much faster.

4. SIZE EFFECTS

As was shown in [7], the critical cluster size required for the onset of condensation under typical arc conditions can consist of only a few tens of atoms. Under these conditions, the Frenkel theory is formally invalid and we have to estimate the effect of cluster sizes on the growth of NTs.

Small clusters of a pure substance ($g \leq 30$) seem to have been described most accurately in [17, 18]. For small clusters formed by atoms interacting through an additive pair potential, the partition function over internal degrees of freedom was related in [17, 18] to the equilibrium constant K_2 for the reaction of formation of a dimer:

$$Z_g = (\lambda_1^3 K_2)^{g-1}, \tag{9}$$

so that $\mu_g = T\ln(N_g\lambda_g^3) + (g-1)T\ln(\lambda_1^3 K_2) + T\ln Z_{\text{rot}}^{(g)}$.

For clusters that are intermediate between the small clusters and drops, the authors of [17] used the extrapolation

$$\begin{aligned}\mu_g &= T\ln(N_g\lambda_g^3) + (g-1)\mu_L \\ &+ \ln Z_{\text{rot}}^{(g)} + (g_0-1)[T\ln(K_2\lambda_1^3) - \mu_L]\end{aligned} \tag{10}$$

which is an analogue of Eq. (1), where the number of surface atoms g_0 is introduced. The relation of g_0 to the number of “bulk” atoms $g_1 = g - g_0$ has the form

$$g_0 = 3\omega g_1^{2/3} + 3\omega\Lambda g_1^{1/3} + \omega\Lambda^2. \tag{11}$$

The dimensionless parameter ω connects the macroscopic (surface tension) and microscopic (equilibrium constant K_2) characteristics,

$$\omega = \frac{4\pi}{3}\frac{\sigma_0 r_L^2}{T\ln(K_2 N_1^{(S)})}, \tag{12}$$

and the dimensionless length Λ has the meaning of the thickness of a surface atomic layer in units of r_L.

In this approach, the equilibrium distribution function of clusters with a small number of atoms takes the form

$$N_g = A_{\text{rot}} g^4 N_1 S^{g-1}\exp\left(-\frac{4\pi\sigma r_L^2}{3\omega}(g_0-1)\right). \tag{13}$$

For the group of metals studied in [18], we have $\omega \sim 0.8$ and $\Lambda \approx \omega/2 \approx 1.6$. However, the difference $\delta = \Lambda - 2\omega$, which makes it possible to take into account the size effects in the approach proposed, is a small difference of large numbers and cannot be estimated from general considerations even for a pure substance. Therefore, we have to vary the value of δ for the melt.

In the two-component case, the generalization of partition function (9) should take into account possible arrangements of unlike atoms in a given virtual chain. Such a calculation is similar to the calculation of the configuration integral in lattice models [19], and the result can be written as

$$\begin{aligned}\ln Z_g &= \ln\frac{g!}{k!c!} + (g-1)\left((1-X)^2\ln\frac{K_{KK}}{\lambda_K^3}\right. \\ &\left.+ X^2\ln\frac{K_{CC}}{\lambda_c^3} + 2X(1-X)\ln\frac{K_{KC}}{(\lambda_K\lambda_C)^{3/2}}\right),\end{aligned} \tag{14}$$

where K_{KK}, K_{CC}, and K_{KC} are equilibrium constants for dimers consisting of catalyst–catalyst, carbon–carbon, and carbon– catalyst atoms, respectively.

At $g = c$ ($X = 1$) or $g = k$ ($X = 0$) (a single-component drop), Eq. (14) is transformed into Eq. (9).

The expression for the chemical potential now has the form

$$\begin{aligned}\mu_g &= T\ln(N_g\lambda_g^3) + (g-1)\mu_L + \ln Z_{\text{rot}} + (g_0-1) \\ &+ (g_0-1)\left((1-X)^2\ln\frac{K_{KK}}{\lambda_K^3} + X^2\ln\frac{K_{CC}}{\lambda_C^2}\right. \\ &\left.+ 2X(1-X)\ln\frac{K_{KC}}{(\lambda_K\lambda_C)^{3/2}} + \frac{1}{g_0-1}\ln\frac{(g_0-1)!}{k!c!}\right).\end{aligned} \tag{15}$$

The constants K_{KK} and K_{KC} should be calculated from the interatomic interaction potentials with the participation of transition-metal atoms. These potentials are extremely complex, and a calculation result cannot be sufficiently reliable. On the other hand, if we assume that the parameters ω and Λ remain universal for alloys, then the generalization of Eq. (4) as a drop distribution function has the form

$$\begin{aligned}N_g &= A_{\text{rot}} N_K^{1-X} N_C^X g^{9/2} A_{KC}(S_X^X S_K^{1-X})^{g-1} \\ &\times \exp\left(-(g-1)\frac{\mu_{\text{mix}}}{T} - (g_0-1)\frac{4\pi\sigma_0 r_L^2}{3\omega T}\right).\end{aligned} \tag{16}$$

Apart from simpler formula (4), we used Eq. (16) to calculate the rate of explosive condensation of molten drops in [7].

5. STEADY-STATE CONDENSATION RATE

The steady-state condensation rate for drops can be calculated by Eqs. (4) and (16). The condensation rate is defined as the drop flux through the narrow site of condensation, namely, the neighborhood of the point (c^*, k^*) of the critical cluster size in the space of the number of atoms (c, k). The mole fraction of carbon in the subcritical region of the space of the number of atoms remains optimal and is several or even several tens of a percent, depending on temperature. In the case of condensation of the drops on neutral atoms, the flux of nucleating drops through the narrow region (Gibbs energy maximum) is determined, just as in the case of a pure substance, by the relation

$$J(g) = N_g^{(0)}\Omega V_T N_1\left|\frac{\partial y}{\partial g}\right|, \qquad (17)$$

where $\Omega = \pi r_L^2 g^{2/3}$ is the cross section of the reaction of addition of an atom to the cluster and y is the relative population of clusters with the number k of catalyst atoms. If g is assumed to be a continuous quantity, y and J can be determined from the steady-state diffusion equation

$$\frac{\partial}{\partial g}\left(N_1 N_g^{(0)}\frac{\partial y}{\partial g}\right) = 0$$

and has the form

$$y_g = \int_g^{\infty}\frac{dg'}{\Omega N_{g'}^{(0)}}\left(\int_1^{\infty}\frac{dg'}{\Omega N_{g'}^{(0)}}\right)^{-1},$$

$$J = V_T N_1\left(\int_1^{\infty}\frac{dg}{\Omega N_g^{(0)}}\right)^{-1}. \qquad (18)$$

If the size effects are not taken into account, after substituting Eq. (4), this result leads to the equations

$$J = \frac{N_C}{N_L}g_*^{9/2}B\sqrt{\frac{2\sigma}{\pi m}} \times \frac{(N_C X)^X(N_K(1-X))^{1-X}}{S_C^X S_K^{1-X}}\exp\left(-\frac{G_m}{T}\right), \qquad (19)$$

$$B = A_{\mathrm{rot}}\left(\frac{A_C X + A_K(1-X)}{A_C^X A_K^{1-X}}\right)^{3/2}, \qquad (20)$$

$$G_m = \frac{16\pi\sigma^3(x)}{3n_L^2T^3}\frac{1}{\left(X\ln\frac{S_C}{X} + (1-X)\ln\frac{S_K}{1-X}\right)^2}. \qquad (21)$$

The multiplier $(S_C^X S_K^{1-X})^{-1}$ in Eq. (19) is similar to the Courtney correction S^{-1} to the classic result of calculation of the condensation rate [20].

Making allowance for the size effects in Eqs. (19)–(21), we should perform the substitution

$$\sqrt{\frac{2\sigma}{\pi m}} \longrightarrow \sqrt{\frac{2\sigma}{\pi m}\frac{1-\delta/g_*^{2/3}}{1+\delta/g_*^{2/3}}}, \quad g_*^{9/2} \longrightarrow \frac{g_*^{9/2}}{1+\delta/g_*^{2/3}},$$

$$G_{\max} \longrightarrow \frac{G_{\max}}{(1+\delta/g_*^{2/3})^3}\left(1-\frac{6\delta}{g_*^{1/3}}+\frac{3\delta}{g_*^{2/3}}-\frac{1}{\omega g_*^{2/3}}\right).$$

CONCLUSIONS

The main result of the work is the derivation of expressions for the steady-state rate of condensation of molten drops in a supersaturated carbon vapor. These expressions form the basis for the calculation of the characteristics of explosive and rapid condensation to be performed in the next part of this work.

REFERENCES

1. Y. Tu, Z. P. Huang, D. Z. Wang, *et al.*, Appl. Phys. Lett. **80**, 4018 (2002).
2. S. Maruyama, R. Kojima, Y. Miyauchi, and S. Chiashi, Chem. Phys. Lett. **360**, 229 (2002).
3. D. T. Colbert and R. E. Smalley, *Perspectives of Fullerene Nanotechnology*, Ed. by E. Osawa (Academic, London, 2002), pp. 3–10.
4. Y. Saito, T. Koyama, and K. Kawalata, Z. Phys. D **40**, 421 (1997).
5. L. Alvarez, T. Guillard, J. L. Savajol, *et al.*, Chem. Phys. Lett. **342**, 7 (2001).
6. C. D. Scott, S. Arepalli, P. Nucolaev, and R. E. Smalley, Appl. Phys. A **72**, 573 (2001).
7. N. I. Alekseev, Zh. Tekh. Fiz. **74** (8), 51 (2004) [Tech. Phys. **49**, 1004 (2004)].
8. N. I. Alekseyev and G. A. Dyuzhev, Zh. Tekh. Fiz. **71** (10), 41 (2001) [Tech. Phys. **46**, 1247 (2001)].
9. J. M. Hunter, J. L. Fye, and M. F. Jarrold, J. Chem. Phys. **3**, 1785 (1993).
10. J. M. Hunter, J. L. Fye, E. J. Roskamp, and M. F. Jarrold, J. Phys. Chem. **3**, 1810 (1998).
11. Ya. I. Frenkel, *Kinetic Theory of Liquids* (Nauka, Leningrad, 1975; Clarendon, Oxford, 1946).
12. K. Vagner, *Thermodynamics of Alloys* (GNTI Chern. Metall., Moscow, 1957) [in Russian].
13. *Handbook of Physical Quantities*, Ed. by I. S. Grigoriev and E. Z. Meĭlikhov (Énergoatomizdat, Moscow, 1991; CRC, Boca Raton, 1997).
14. V. T. Vitusevich and A. K. Biletskiĭ, Izv. Akad. Nauk SSSR, Met., No. 4, 61 (1988).
15. B. P. Burylev, Izv. Vyssh. Uchebn. Zaved., Chern. Metall., No. 2, 5 (1963).
16. I. S. Kuznetsov, Izv. Akad. Nauk SSSR, Met., No. 1, 89 (1977).
17. D. I. Zhukhovitskiĭ, Zh. Fiz. Khim., No. 10, 1962 (1993).
18. D. I. Zhukhovitskii, J. Chem. Phys. **101**, 5076 (1994).
19. S. Ono and S. Kondo, *Molecular Theory of Surface Tension in Liquids* (Springer-Verlag, Berlin, 1960; Inostrannaya Literatura, Moscow, 1963).
20. Ya. B. Zel'dovich, Zh. Éksp. Teor. Fiz. **12**, 525 (1942).

Translated by K. Shakhlevich